

FACULDADE DE ENGENHARIA DA UNIVERSIDADE DO PORTO

Vibrations of fibre-reinforced composite beams and plates with carbon nanotubes

André Lello

DISSERTATION SUBMITTED TO FACULDADE DE ENGENHARIA DA UNIVERSIDADE DO PORTO FOR THE DEGREE OF MESTRE EM ENGENHARIA MECÂNICA



Mestrado Integrado em Engenharia Mecânica

Supervisor: Prof. Dr. Pedro Leal Ribeiro

Co-Supervisor: Prof. Dr. José Dias Rodrigues

July 31, 2020

The work presented in this dissertation was performed at the
Laboratory of Vibrations of Mechanical Systems
Department of Mechanical Engineering
Faculty of Engineering
University of Porto
Porto, Portugal

André Miguel Gomes Pereira Lello de Almeida
E-mail: up201506244@fe.up.pt

Faculdade de Engenharia da Universidade do Porto
Departamento de Engenharia Mecânica
Laboratório de Vibrações de Sistemas Mecânicos
Rua Dr. Roberto Frias s/n, Sala M206
4200-465 Porto
Portugal

Vibrations of fibre-reinforced composite beams and plates with carbon nanotubes

André Lello

Mestrado Integrado em Engenharia Mecânica

Laboratório de Vibrações de Sistemas Mecânicos
Departamento de Engenharia Mecânica
Faculdade de Engenharia da Universidade do Porto

July 31, 2020

Cofinanciado por:



UNIÃO EUROPEIA
Fundo Europeu
de Desenvolvimento Regional

Abstract

The use of carbon nanotubes on fibre-reinforced composites has been an intense field of study, in the past decades, due to their promising properties. Small additions of CNTs to these composite materials have shown significant improvements on the mechanical and vibration characteristics of dynamical systems, leading to the development of models that could encapsulate the effect carbon nanotubes have on these properties.

A brief bibliographic review is performed on the equivalent elastic properties of multiscale composites and a suitable model is described and some new features are added. This model is based on a hierarchic approach to the Halpin-Tsai equations and to an extension of Fu's model for the transverse Young's modulus of fibre-reinforced composites.

The hierarchic model for the equivalent elastic properties of multiscale composites is validated against experimental and numerical results by many authors. Some in-house tensile tests are analysed in order to validate further the previous model, for CNT-reinforced epoxy specimens.

The mechanisms of CNT interfacial slippage are discussed and a theoretical model to predict the loss of energy due to friction is deduced. This model is used to characterize the damping properties of CNT-reinforced composite beams, subjected to certain vibration modes of pure bending. The damping model is also validated, using experimental data by many authors.

To study the free vibrations of fibre-reinforced composite plates with carbon nanotubes, a p-version FEM model, based on the classical laminated plate theory, is employed. This numerical formulation is implemented on a computer program as to simulate the natural modes of vibration of such plates.

Finally, the damping model is extended to predict the modal damping ratios of multiscale composite plates, which consisted in a new improvement of the FEM model used previously. The predictions on the equivalent elastic properties, the natural frequencies and mode shapes of vibration and on modal damping ratios obtained through the models developed in this dissertation are compared with some experimental results, on these same properties, of some carbon fibre-reinforced epoxy laminated composite plates with CNTs.

Keywords: carbon nanotubes, hybrid composites, multiscale modelling, interfacial damping, classical laminated plate theory, p-FEM

Resumo

O uso de nanotubos de carbono em compósitos reforçados com fibras tem sido matéria de intenso estudo, nas últimas décadas, devido às suas promissoras propriedades. Pequenas adições de CNTs a estes materiais compósitos têm mostrado melhorias significativas nas características mecânicas e de vibração de sistemas dinâmicos, levando ao desenvolvimento de modelos que pudessem encapsular o efeito que os nanotubos de carbono têm nestas propriedades.

É realizada uma breve revisão bibliográfica sobre as propriedades elásticas equivalentes de compósitos multiescala e é descrito um modelo adequado, onde alguns aspetos novos são adicionados. Este modelo é baseado numa abordagem hierárquica às equações de Halpin-Tsai e a uma extensão do modelo de Fu para o módulo de Young transversal de compósitos reforçados com fibras.

O modelo hierárquico para as propriedades elásticas equivalentes de compósitos multiescala é validado em função de resultados experimentais e numéricos por vários autores. Além disso, alguns ensaios de tração são analisados a fim de validar o modelo anterior, para provetes de epóxi reforçada com CNTs.

São discutidos os mecanismos de escorregamento interfacial nos CNTs e é deduzido um modelo teórico para prever a perda de energia por fricção. Este modelo é usado para caracterizar as propriedades de amortecimento de vigas compósitas reforçadas com CNTs, sujeitas a certos modos de vibração à flexão pura. O modelo do amortecimento também é validado, usando dados experimentais por vários autores.

Para estudar as vibrações livres de placas compósitas reforçadas com fibras e nanotubos de carbono, é utilizado um modelo da versão p do método dos elementos finitos, baseada na teoria clássica de placas laminadas. Esta formulação numérica é implementada num programa de computador para simular os modos naturais de vibração dessas placas.

Finalmente, o modelo do amortecimento é estendido para prever as razões de amortecimento modais de placas de compósitos multiescala, consistindo numa nova melhoria ao modelo do método dos elementos finitos usado previamente. As previsões das propriedades elásticas equivalentes, das frequências naturais e das formas naturais de vibração e das razões de amortecimento modais obtidas através dos modelos desenvolvidos nesta dissertação são comparadas com alguns resultados experimentais, destas mesmas propriedades, nalgumas placas compósitas laminadas de epoxy reforçado com fibras de carbono e CNTs.

Palavras-chave: nanotubos de carbono, compósitos híbridos, modelos multiescala, amortecimento interfacial, teoria clássica de placas laminadas, p-FEM

To my grandfather Zeca.

Acknowledgements

I would like to express my gratitude to the many people, whom supported, in their own way, the development of the present dissertation. Also, I would like to acknowledge the great influence FEUP and INEGI had on my academic life and all the knowledge passed onto me through these institutions.

First of all, I would like to thank my advisor, Professor Pedro Leal Ribeiro, for the constant advice and for always being available to use his expertise on the improvement of the following work. Without his guidance, this dissertation would certainly not have been possible.

I also would like to thank my co-advisor, Professor José Dias Rodrigues, for all the knowledge in the area of dynamics and for explaining complex phenomena always in a simple, although comprehensive, way.

A special thank to the colleagues of UMEC, from INEGI, for providing the material specimens for the tensile tests and to LEMEC, from INEGI, and to LET, from FEUP, for performing these tests.

Not less important, I would like to mention and acknowledge the financial support provided by FCT (Fundação para a Ciência e Tecnologia) through Project POCI-01-0145-FEDER-030348 - "Laminated composite panels reinforced with carbon nanotubes and curvilinear fibres for enhanced vibration and flutter characteristics", supported by FCT/MCTES through national funds (PIDACC) and the European Regional Development Fund (FEDER), through the Competitiveness and Internationalization Operational Program (COMPETE 2020).

Finally, I want to thank all the people that have been in my life in the past five years and had a direct impact on my personal and academic growth.

To all the friends I have made in my passage through FEUP and Orfeão Universitário do Porto, for all the good times. To Francisca, for all the love and affection over the past years. To those whom I share a truly genuine friendship, through good moments and hardships, you have my gratitude and I hope I can return it someday.

Lastly, to my grandparents, for committing themselves, so selflessly, to my education as a great professional and, most importantly, as a human being. To the rest of my family, specially, to my parents and my brother, for always supporting me unconditionally, a warm and sincere thank.

“Fall in love with some activity, and do it! Nobody ever figures out what life is all about, and it doesn’t matter. Explore the world. Nearly everything is really interesting if you go into it deeply enough. Work as hard and as much as you want to on the things you like to do the best. Don’t think about what you want to be, but what you want to do. Keep up some kind of a minimum with other things so that society doesn’t stop you from doing anything at all.”

Richard P. Feynman

Contents

Abstract	i
Resumo	iii
Acknowledgements	vii
Contents	xi
List of Figures	xv
List of Tables	xix
List of Abbreviations	xxi
1 Introduction	1
1.1 CNT-reinforced multiscale composites	1
1.2 Objectives	3
1.3 Layout	3
2 Models for equivalent elastic properties of composites	5
2.1 Micromechanics based models for composites	5
2.1.1 Rule of mixtures	8
2.1.2 Hashin-Shtrikman bounds	10
2.1.3 Cox model	10
2.1.4 Chamis model	11
2.1.5 Fu model for transverse Young's modulus	12
2.1.6 Halpin-Tsai model	13
2.1.7 Non-dilute correction to Halpin-Tsai model	15
2.1.8 Mori-Tanaka model	16
2.2 Hierarchic model for multiscale composites	17
2.2.1 Equivalent properties of CNT/polymer matrix composites	17
2.2.2 Extended model for elastic moduli based on unit cell	19
2.2.3 Equivalent properties of CNT/fibre/polymer matrix composites	22
3 Validation of the hierarchic model	25
3.1 Prediction of elastic properties of CNT/polymer matrix composites	25
3.1.1 Formica et al (2010)	26

3.1.2	Tai et al (2008)	27
3.1.3	Yeh et al (2006)	29
3.1.4	Montazeri et al (2010)	30
3.2	Influence of CNT aspect ratio on the elastic properties of CNT/polymer matrix composites	30
3.3	Prediction of elastic properties of CNT/fibre/polymer matrix composites	32
3.3.1	Kulkarni et al (2010)	33
3.3.2	Gupta and Harsha (2014)	35
4	Tensile tests on CNT-reinforced epoxy resin	37
4.1	Experimental procedure	38
4.1.1	Standard EN ISO 527	38
4.1.2	Test specimens	40
4.2	Data analysis and results	44
4.2.1	Young's modulus	45
4.2.2	Poisson's ratio	48
4.2.3	Tensile strength	49
5	A model for damping in CNT nanocomposites	51
5.1	Micromechanics based vibration analysis of CNT-reinforced composites	51
5.1.1	Concept of "stick-slip" mechanism	52
5.1.2	Hysteretic damping in SDOF systems	59
5.1.3	Energy dissipation and loss factor	61
5.1.4	Effect of the material viscous damping and CNT orientation	66
5.1.5	Compatibility with the hierarchic model and the inclusion of fibres	67
5.2	Damping model for a composite cantilever beam	70
5.2.1	Modes of vibration of Euler-Bernoulli beams	71
5.2.2	"Stick-slip" damping model applied to beams	74
5.2.3	Brief analysis of the cantilever beam damping model	76
6	Validation of the damping model	81
6.1	Prediction of damping on CNT/polymer matrix composites	81
6.1.1	Bhattacharya et al (2014)	82
6.1.2	Zhou et al (2004)	83
6.1.3	Bórbon et al (2014)	86
6.1.4	Latibari et al (2013)	87
6.2	Prediction of damping on CNT/fibre/polymer matrix composites	89
6.2.1	DeValve and Pitchumani (2013)	90
6.2.2	Khan et al (2011)	93
7	Classical theory of laminated composite plates	97
7.1	Laminae and VSCL plates	97
7.1.1	Coordinate system	98
7.2	Assumptions of the CLPT	101
7.2.1	Kirchhoff's hypotheses	101
7.2.2	Displacement field	102
7.2.3	Strain-displacement relations	103
7.3	Constitutive relations	104

7.3.1	Stress-strain relations	104
7.3.2	Force and moment resultants	106
7.4	Equations of motion	107
7.4.1	p-version Finite Element Method	108
7.4.2	Application of the Principle of Virtual Work	110
7.4.3	Natural frequencies and modes of vibration	113
8	Damping in CNT-reinforced composite plates	115
8.1	Extension of the damping model to plates	116
8.1.1	Modes of vibration and deformation fields	116
8.1.2	"Stick-slip" damping model applied to plates	118
8.2	Comparison with an experimental modal analysis	120
8.2.1	Plates properties and experimental procedure	120
8.2.2	Equivalent elastic properties	122
8.2.3	Natural frequencies of vibration	124
8.2.4	Modal damping ratios	125
9	Conclusion	129
9.1	Conclusions	129
9.2	Future work	131
	References	133
A	Materials technical data sheets	139
A.1	Epoxy resin: SiPreg SR 121 / KTA 315 (Sicomini)	139
A.2	Single-walled carbon nanotube: SA-ML-2 (NANOSHEL)	143
A.3	Carbon fibre: Tenax®-E HTS45 12K (Teijin Carbon Europe GmbH)	145
B	Tensile tests: load - displacement curves	147
C	Tensile tests: stress - strain curves	155
D	Tensile tests: transversal - longitudinal strain curves	163
E	Numerical mode shapes	165

List of Figures

2.1	Schematic model of a nanotube (a) and an effective fibre (b) used to define the effective elastic properties of a CNT.	6
2.2	Schematic model of a discontinuous fibre composite and a corresponding representative volume element.	19
4.1	The two types of extensometers used in the tensile tests.	39
4.2	A typical fracture on a tensile test.	40
4.3	Examples of the samples used in the tensile tests.	41
4.4	Different specimen preparation: specimens 1 and 2 to the left for the clip-on extensometer and 5 and 6 to the right with the strain gauges already mounted on 5.	42
5.1	Stages of failure of the bonding between the inner layers of a MWCNT and the outer wall and the matrix of a nanocomposite.	54
5.2	Representative volume element of the dynamic analysis subjected to an alternating external load.	55
5.3	Micromechanical-based dynamical model of the representative volume element of the nanocomposite.	56
5.4	Force-displacement behaviour of the composite for $X \leq \delta_1$ (a), for $\delta_1 < X \leq \delta_2$ (b) and for $X > \delta_2$ (c).	59
5.5	Representation of the geometry of a cantilever beam.	72
5.6	Loss factor as a function of the amplitude of vibration for different weight fractions of CNT.	78
5.7	Loss factor as a function of the amplitude of vibration for different parameters of the cantilever beam.	79
6.1	Loss factor as a function of initial tip displacement for the experimental results obtained by Bhattacharya et al.	83
6.2	Damping ratio as a function of structural deformation, for 0.5% CNT weight fraction, for the experimental results obtained by Zhou et al.	84
6.3	Damping ratio as a function of structural deformation, for 1% CNT weight fraction, for the experimental results obtained by Zhou et al.	85
6.4	Influence of increasing the volume fraction in nanocomposites with SWCNTs with critical shear stress 0.95814 MPa by Latibari et al.	88
6.5	Loss factor as a function of strain for the numerical results obtained by Latibari et al.	89

6.6	Variation of the material damping loss factor, δ , with strain, ε , using (a) no CNTs and varying the fibre volume fraction of the composite material, as well as using various weight percentages of MWCNTs (15 nm in diameter, 5–20 μm in length) with constant vf values of (b) 0.00, (c) 0.46, and (d) 0.58 by DeValve and Pitchumani.	91
6.7	Loss factor of a nanocomposite without fibres as a function of structural deformation for the experimental results obtained by DeValve and Pitchumani.	91
6.8	Loss factor of a nanocomposite with fibres as a function of structural deformation for the experimental results obtained by DeValve and Pitchumani.	92
6.9	Loss factor of a nanocomposite with fibres, neglecting their effect on its stiffness, as a function of structural deformation for the experimental results obtained by DeValve and Pitchumani.	93
6.10	Damping ratio of (a) nanocomposites and (b) CFRP composites containing different CNT contents as a function of initial vibration amplitude by Khan et al.	94
6.11	Damping ratio as a function of initial tip displacement for the experimental results obtained by Khan et al.	94
6.12	Damping ratio, for a critical shear stress between CNTs and matrix of 75 MPa, as a function of initial tip displacement for the experimental results obtained by Khan et al.	95
7.1	A representation of a lamina with material and general coordinate systems.	99
7.2	General coordinate system and lamina numbering used for the composite laminated plate.	100
7.3	Orientation variation of a curvilinear fibre.	100
8.1	Graphical representation of the modal damping ratios predicted by the damping model and of those experimentally determined by Antunes.	126
8.2	Graphical representation of the component of the modal damping ratios, due to interfacial slippage, predicted by the damping model and of those calculated by the experimental values obtained by Antunes.	127
B.1	Load - displacement curves of the specimens of reference 1 (Epoxy Resin).	148
B.2	Load - displacement curves of the specimens of reference 2 (0.05 CNT Normal).	149
B.3	Load - displacement curves of the specimens of reference 3 (0.05 CNT SDBS).	150
B.4	Load - displacement curves of the specimens of reference 4 (0.05 CNT Triton).	151
B.5	Load - displacement curves of the specimens of reference 5 (0.05 CNT High).	152
B.6	Load - displacement curves of the specimens of reference 6 (0.1 CNT High).	153
B.7	Load - displacement curves of the specimens of reference 7 (0.2 CNT High).	154
C.1	Stress - strain curves of the specimens of reference 1 (Epoxy resin).	156
C.2	Stress - strain curves of the specimens of reference 2 (0.05 CNT Normal).	157
C.3	Stress - strain curves of the specimens of reference 3 (0.05 CNT SDBS).	158
C.4	Stress - strain curves of the specimens of reference 4 (0.05 CNT Triton).	159
C.5	Stress - strain curves of the specimens of reference 5 (0.05 CNT High).	160
C.6	Stress - strain curves of the specimens of reference 6 (0.1 CNT High).	161
C.7	Stress - strain curves of the specimens of reference 7 (0.2 CNT High).	162
D.1	Transversal - longitudinal strain curves of the specimens of reference 1 (Epoxy resin).	163
D.2	Transversal - longitudinal strain curves of the specimens of reference 2 (0.05 CNT Normal).	163
D.3	Transversal - longitudinal strain curves of the specimens of reference 3 (0.05 CNT SDBS).	164
D.4	Transversal - longitudinal strain curves of the specimens of reference 4 (0.05 CNT Triton).	164

D.5	Transversal - longitudinal strain curves of the specimens of reference 5 (0.05 CNT High).	164
E.1	Numerical mode shapes for the 0.01% SWCNTs plate.	166
E.2	Numerical mode shapes for the 0.05% SWCNTs plate.	167

List of Tables

2.1	Empirical parameter ξ for various equivalent elastic properties of the composite.	14
3.1	Comparison between the hierarchic model and the experimental values presented and the numerical ones obtained by Formica et al.	27
3.2	Comparison between the hierarchic model and the experimental values obtained by Tai et al.	28
3.3	Comparison between the hierarchic model and the experimental values obtained for network MWCNTs by Yeh et al.	29
3.4	Comparison between the hierarchic model and the experimental values obtained for untreated MWCNTs by Montazeri et al.	30
3.5	Comparison between the hierarchic model and the numerical values obtained by Tucker III and Liang.	31
3.6	Comparison between the hierarchic model and the numerical values obtained by Kulkarni et al.	33
3.7	Comparison between the hierarchic model and the experimental value of the transversal Young's modulus obtained by Kulkarni et al.	34
3.8	Comparison between the hierarchic model and the numerical values obtained by Gupta and Harsha.	36
4.1	Measured dimensions of the specimens.	43
4.2	Young's modulus of the specimens tested.	46
4.3	Comparison between the experimental values of the Young's modulus obtained by the tensile tests and the prediction of the hierarchic model.	47
4.4	Poisson's ratio of the specimens tested.	48
4.5	Comparison between the experimental value of the Poisson's ratio obtained by the tensile tests and the expected value of the Poisson's ratio of the epoxy resin.	48
4.6	Tensile strength of the specimens tested.	49
6.1	Comparison between the damping model and the experimental values for the sandwich beam obtained by Bórbon et al.	87
8.1	Properties of the plates used by Antunes.	121
8.2	Properties of the epoxy resin, the carbon fibres and the CNTs.	122
8.3	Comparison between the predictions of the hierarchic model for the equivalent elastic properties of the different plates and the experimental and theoretical values obtained by Antunes.	123

8.4	Comparison between the natural frequencies of vibration predicted by the numerical model developed for vibrating composite plates (CLPT) and those obtained experimentally (Exp) and numerically (Num) by Antunes.	124
8.5	Comparison between the modal damping ratios predicted by the damping model developed for vibrating composite plates and those obtained experimentally by Antunes.	125

List of Abbreviations

ASTM	American Society for Testing and Materials
CFRP	Carbon Fibre-Reinforced Polymer
CLPT	Classical Laminated Plate Theory
CNT	Carbon NanoTube
CSCL	Constant Stiffness Composite Laminated
DOF	Degree Of Freedom
DWCNT	Double Walled Carbon NanoTube
ESL	Equivalent Single Layer
FEM	Finite Element Method
FEUP	Faculdade de Engenharia da Universidade do Porto
FFFF	Plate boundary conditions, all edges free
FSDT	First-order Shear Deformation Theory
INEGI	Instituto de Ciência e Inovação em Engenharia Mecânica e Engenharia Industrial
ISO	International Organization for Standardization
MWCNT	Multi Walled Carbon NanoTube
RVE	Representative Volume Element
SDOF	Single Degree Of Freedom
SWCNT	Single Walled Carbon NanoTube
VSCL	Variable Stiffness Composite Laminated

Chapter 1

Introduction

Many civilian and military-oriented dynamical structures are subjected to vibratory motions and excitations. As it is well known, resonance and aeroelastic instability phenomena on these structural systems can lead to fatigue problems, aeroelastic flutter and, ultimately, to their failure. To avert these scenarios, the study of vibrations is of utmost importance in the fields of aerospace, mechanical and civil engineering [1].

The use of composite materials for structural components have been steadily rising for the past decades and, nowadays, investigation is being made in the behaviour of polymer nanocomposites and hybrid or multiscale composites [1]. Using low concentrations of nano-sized particles, fibres or tubes, the stiffness and strength of such composites increased substantially, compared to the base properties of the polymer matrix [1, 2]. Besides this, in recent years, there has been a lot of research on the damping characteristics of dynamical systems made of these nanocomposites and the mechanical damping capacity has been proven to also increase significantly, due to the high capacity of these nanoparticles to dissipate energy [1, 3].

Amongst these nanomaterials, the carbon nanotubes (CNTs), discovered in 1991 by Iijima [4], have been widely investigated, because of their promising mechanical and electrical properties. As such, a lot of effort has been put on the investigation of the advantages and disadvantages of using such CNT-reinforced composites in dynamical and structural applications, in the field of advanced and high-performance materials [5].

1.1 CNT-reinforced multiscale composites

Carbon nanotubes are long, slender fullerenes, which consist of a cylindrical wall with the crystal configuration of hexagonal carbon, the same as sheets of graphite. Many studies affirmed that the mechanical properties of CNTs have exceeded those of any other known material, which could result in a

new class of advanced composites in the future. The theoretical and experimental data have shown an extremely high Young's modulus, greater than 1 TPa, and a tensile strength between 10 and 100 times that of the strongest steel, at a much lower density [2]. They are also considered an efficient filler, as a very small load, typically less than 5% weight fraction, result in significant improvements in the mechanical properties of the composite [5].

In recent years, it has been also determined that for certain dynamical systems, a very small load of CNTs can increase their damping ratio, when such structures are subjected to vibrations. Due to their small size, the specific area of the nanotubes is extremely large and coupled with the fact that the main forces between the walls of a CNT and the composite's matrix are van der Waals forces, they are very prone to suffer from interfacial slippage with the base material [3]. The fraction when CNT debonding occurs is a very effective method for dissipating energy, so the damping of existing vibrations is encouraged [1, 3].

All these characteristics make the CNTs a prospective material for enhancing the dynamical behaviour of fibre-reinforced composite structural systems, such as beams or plates. By studying the mechanisms in which carbon nanotubes affect the properties of multiscale composites, it is possible to come up with theoretical models that can predict the behaviour of such materials, under different CNT loadings, with a good degree of accuracy. This in turn may allow the optimization of CNT-reinforced multiscale composites for certain special applications that require high stiffness and damping characteristics, leading to the creation of highly functionalized materials [6].

Although these astonishing improvements caused by the addition of little concentrations of CNTs in fibre-reinforced composites seem very appealing, some difficulties in the manufacturing process of these materials have been reported by several authors. One of the most difficult requirements that must be fulfilled for an efficient load transfer is a good dispersion of the nanotubes in the matrix. It is very hard to prevent the agglomeration of CNTs in bundles, however this condition must be successfully satisfied for a real improvement in the mechanical characteristics of the composite [2].

Besides this, there is, currently, a lack of techniques for direct property measurements of the properties of CNTs, being further complicated by the reduced size of nanomaterial. A lot of the available results have a non neglectable uncertainty, which translate into a large variance in the properties of the multiscale composites, rendering our current models inaccurate [2, 3].

In spite of these problems, CNTs remain a promising new nanomaterial, with incredible mechanical, electrical and thermal properties, that may revolutionize the application of composites for structural and dynamical systems [1].

1.2 Objectives

The main objective of this thesis is, as the title suggests, to study vibrations of fibre-reinforced composite beams and plates with carbon nanotubes, both numerically and experimentally. In order to study the effect of CNT loading on the vibrations of such composite systems, models regarding the stiffness and damping characteristics are to be developed. So, to achieve this goal, the following tasks were fulfilled:

- Study different theoretical models for the determination of the equivalent elastic properties of multiscale composites;
- Refine the existing models for the equivalent elastic properties of multiscale composite, based on a hierarchic approach, and validate it against experimental results by other authors;
- Perform tensile tests on CNT-reinforced epoxy resin to further validate the model for the equivalent elastic properties of multiscale composites with our own experimental data;
- Study the different models and mechanisms for explaining the interfacial slippage between nanotubes and matrix on CNT nanocomposites;
- Develop a damping model, based on the mechanism of CNT debonding, for CNT nanocomposites, apply it to composite cantilever beams and validate it against experimental results by other authors;
- Develop a numerical model for the analysis of VSCL plates, based on the p-version FEM and the classical laminated plate theory;
- Compare the predictions obtained by the models developed in this dissertation, for many relevant properties in the vibration of fibre-reinforced composite plates with CNTs, with experimental results obtained for the same plates.

It should be noted that the tensile tests were performed on specimens manufactured at INEGI, thus being the fabrication of these materials out of the scope of this thesis. This dissertation is a direct follow up on the work developed in another MEng. thesis, by Antunes [7], so some of the predictions of the theoretical models to be developed are compared to experimental data obtained in this previous work, such as the natural frequencies and mode shapes of vibration and the modal damping ratios of fibre-reinforced composite plates with CNTs. Also, the same numerical model for the analysis of VSCL plates was used, as it was already validated and the convergence study was also already performed.

1.3 Layout

This dissertation is divided in nine different chapters, with the following structure:

- Chapter 1 - "Introduction" - This chapter gives a brief introduction to the advantages of using carbon nanotubes in fibre-reinforced composites and displays the main objectives and layout of the thesis;

- Chapter 2 - "Models for equivalent elastic properties of multiscale composites" - In this chapter, a bibliographic review on the existing models for predicting the equivalent elastic properties of fibre-reinforced composites is performed, leading to the determination of the hierarchic model for CNT-reinforced multiscale composites;
- Chapter 3 - "Validation of the hierarchic model" - The hierarchic model is validated against experimental and numerical results obtained by many authors, for CNT-reinforced composites both with fibres and without them;
- Chapter 4 - "Tensile tests on CNT-reinforced epoxy resin" - Experimental tensile tests are performed on CNT-reinforced epoxy resin, with different CNT loadings and different dispersion methods, to further validate the hierarchic model and to gather experimental data on the elastic properties of such composites;
- Chapter 5 - "A model for damping in CNT nanocomposites" - In this chapter, the interfacial slippage mechanisms in CNT nanocomposites is discussed and a damping model, based on CNTs debonding from the matrix, is developed and applied to composite cantilever beams;
- Chapter 6 - "Validation of the damping model" - The damping model is, also, validated against experimental and numerical data obtained by many authors, using both FEM simulations and modal analysis of beams;
- Chapter 7 - "Classical theory of laminated composite plates" - In this chapter, a p-version FEM formulation, based on the classical laminated plate theory, for modelling the modes of vibration of laminated fibre-reinforced composite plates is presented, considering the possibility of curvilinear fibres;
- Chapter 8 - "Damping in CNT-reinforced composite plates" - All the models developed throughout this dissertation are used to predict the behaviour of the equivalent elastic properties, the natural frequencies and mode shapes of vibration and the modal damping ratios of fibre-reinforced composite plates with CNTs and these results are compared with some experimental values, in order to validate the extension of the damping model to composite plates;
- Chapter 9 - "Conclusion" - Lastly, the most important conclusions and some suggestions for future work are presented, in a summary way.

Chapter 2

Models for equivalent elastic properties of composites

The present chapter focus on the study of the elastic properties of multiscale composites. These so-called 'multiscale' composites refer to the fact that they are comprised of materials from different scale sizes. In this particular case, a polymer matrix reinforced with carbon fibres, at the microscale, and CNTs, at the nanoscale. As such, to predict accurately the bulk elastic properties of the composite, it is necessary the application of a micromechanics approach, rather than a macromechanics one [8, 9].

To provide a starting point for the elaboration of a micromechanics model, this section will concern itself with a review of the available analytical models for the equivalent elastic properties of multiscale composites. In this regard, two of the most widely used models are the Halpin-Tsai equations and the Mori-Tanaka model [5].

All the models studied can be divided into two main categories. The first one includes those who can predict the equivalent elastic properties of the composite material with the knowledge of the basic properties of each of its constituents and their relative quantities, whereas the second pertains to all models who give the stiffness matrix of the laminate based on the stiffness matrices of each of its constituents [10]. The focus of this section will be on the first category of models, with just a brief discussion, at the end, of the Mori-Tanaka model, which belongs to the second type, because of its precision and importance.

2.1 Micromechanics based models for composites

Many of the following models were first derived for fibre-reinforced composites. Although at a very smaller scale, where the continuum approach may not be valid, the CNTs can be thought of as an 'effective fibre' with equivalent properties, defined in such a way that they have the same effect in the

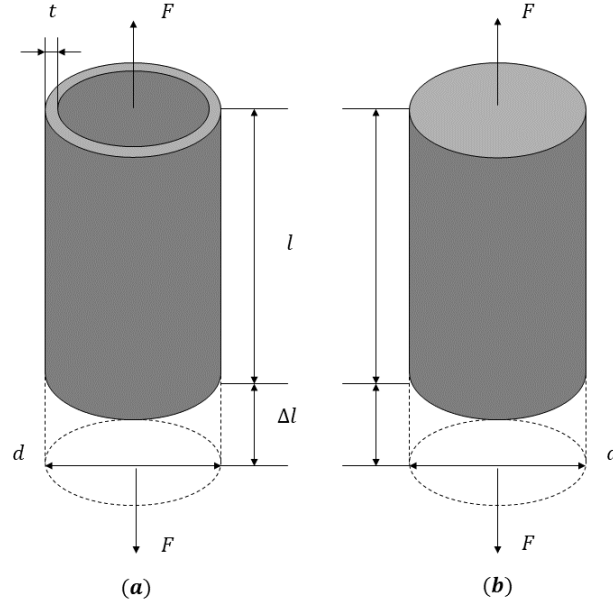


Figure 2.1: Schematic model of a nanotube (a) and an effective fibre (b) used to define the effective elastic properties of a CNT.

matrix. For low strains, it is reasonable to consider that the CNTs can support the interfacial stresses, because debonding does not occur [11].

In such conditions, we may derive these effective properties assuming a cylindrical 'effective fibre' that must behave in the same sense as the original structure. The elastic model of the CNT, modelled as a hollow cylinder, must give the same deformation as the effective model, if the applied force is the same. This establishes an iso-strain condition as shown in Figure 2.1 [11],

$$\varepsilon_{eff} = \varepsilon_{CNT} \quad (2.1)$$

The subscripts CNT and eff refer, respectively, to the carbon nanotube and the effective fibre. Then, using Hooke's Law and the fact that the same force is applied to each system, the following relationship is defined [11],

$$E_{eff} = \frac{\sigma_{eff}}{\sigma_{CNT}} E_{CNT} = \frac{A_{CNT}}{A_{eff}} E_{CNT} \quad (2.2)$$

For a hollow cylinder, the cross sectional area is given by

$$A_{CNT} = \frac{\pi}{4} (d^2 - (d - 2t)^2) = \pi (d - t) t \quad (2.3)$$

so, using (2.3) in (2.2) the relation between the CNT's Young's modulus and the effective fibre's is defined in the following way,

$$E_{eff} = \frac{4(d-t)t}{d^2} E_{CNT} \quad (2.4)$$

If higher order terms in the thickness are neglected, equation (2.4) reduces to the following form,

$$E_{eff} = \frac{4t}{d} E_{CNT} \quad (2.5)$$

which gives a valid approximation for $d/t < 25$ [11]. As described in Figure 2.1, E is the Young's modulus along the axis of the fibre or nanotube, t is the thickness of the CNT and d is its diameter. Many values of the geometrical properties of CNTs have been proposed in the literature. As such, for the thickness, it is normally considered to be equal to the interlayer spacing of graphite, $t = 0.34$ nm [12]. As for the diameter, it spans a large range of values at the nano scale (from 5 to 50 nm) [13], even reaching values as low as 0.43 nm [14]. At this extremely low value, although the thickness must be smaller than that described in [12], the error of the approximation made in (2.5) is very high. Even for a more reasonable value, $d = 5$ nm, the relative error is 7.3%, so it seems more conservative to consider the formula given in equation (2.4) rather than the latter, even if it introduces some complexity.

By the same logic, the effective density of the nanotube can be given as,

$$\rho_{eff} = \frac{4(d-t)t}{d^2} \rho_g \quad (2.6)$$

where ρ_g is the density of fully dense graphite $\rho_g = 2250$ kg/m³ [11]. Throughout the rest of the text, we will just refer to the effective density as the carbon nanotube density ρ_{CNT} , given that this quantity depends heavily on the thickness, which has a great uncertainty linked to it.

It should also be mentioned that all micromechanics models considered are based on the assumption that perfect bonding exists between the fibres, being them 'effective' CNT fibres or actual carbon fibres, and the matrix [10]. The fibres are considered well dispersed in the matrix and all of them share the same elastic properties and aspect ratio. Finally, the matrix must contain no voids and is considered isotropic [15].

If the fibres are unidirectional, instead of being randomly oriented, the resulting composite can be considered transversely isotropic, being described by five elastic properties. The compliance matrix for

such a material is defined as [10],

$$[S] = \begin{bmatrix} \frac{1}{E_{11}} & -\frac{\nu_{12}}{E_{11}} & -\frac{\nu_{12}}{E_{11}} & 0 & 0 & 0 \\ -\frac{\nu_{12}}{E_{11}} & \frac{1}{E_{11}} & -\frac{\nu_{23}}{E_{11}} & 0 & 0 & 0 \\ \frac{E_{11}}{\nu_{12}} & \frac{E_{22}}{\nu_{23}} & \frac{E_{22}}{1} & 0 & 0 & 0 \\ \frac{E_{11}}{\nu_{12}} & \frac{E_{22}}{\nu_{23}} & \frac{E_{22}}{1} & 0 & 0 & 0 \\ 0 & 0 & 0 & \frac{1}{G_{23}} & 0 & 0 \\ 0 & 0 & 0 & 0 & \frac{1}{G_{12}} & 0 \\ 0 & 0 & 0 & 0 & 0 & \frac{1}{G_{12}} \end{bmatrix} \quad (2.7)$$

where E_{11} and E_{22} are the longitudinal and transverse Young's modulus, ν_{12} and ν_{23} are the longitudinal and transverse Poisson's ratio and G_{12} and G_{23} are the longitudinal and transverse shear modulus. Besides, because of the isotropy in the transverse direction, the transverse shear modulus, the transverse Poisson's ratio and the transverse Young's modulus are related by [16],

$$G_{23} = \frac{E_{22}}{2(1 + \nu_{23})} \quad (2.8)$$

For our analysis we will consider the two Young's modulus, the major longitudinal Poisson's ratio and the two shear modulus as the defining mechanical properties of the composite. The minor longitudinal Poisson's ratio can be written as [17],

$$\nu_{21} = \frac{E_{22}}{E_{11}} \nu_{12} \quad (2.9)$$

2.1.1 Rule of mixtures

The simplest model for predicting the effective properties of the composite are the Voigt model and the Reuss's model, also known, respectively, as the rule of mixtures and the inverse rule of mixtures. For longitudinal loading, the Voigt model is considered, which leads to a condition of iso-strain in the composite. In fact, if we assume that the strain on the matrix is equal to that in the fibre and to the equivalent medium [10],

$$E_{11} = \nu_f E_{11f} + (1 - \nu_f) E_m \quad (2.10)$$

$$\nu_{12} = \nu_f \nu_{12f} + (1 - \nu_f) \nu_m \quad (2.11)$$

where the subscript f refers to the fibre and m to the matrix and ν_f is the fibre volume fraction. For transverse loading, the Reuss model is necessary, translating to an iso-stress condition across all the

sections of the composite. Using the fact that the stress in the matrix must equal the stress in the fibre, it is possible to determine that the transverse Young's modulus is [10],

$$\frac{1}{E_{22}} = \frac{v_f}{E_{22f}} + \frac{1-v_f}{E_m} \quad (2.12)$$

These two models, being quite the opposite of each other, give the upper and lower bounds of the possible space of mechanical properties the composite can have. As such, we can represent the upper bound of the shear modulus by considering the Voigt model [10],

$$G_{12} = v_f G_{12f} + (1-v_f) G_m \quad (2.13)$$

and the lower bound if the Reuss model is used [10],

$$\frac{1}{G_{12}} = \frac{v_f}{G_{12f}} + \frac{1-v_f}{G_m} \quad (2.14)$$

If one desires a better description of the lower bound for the effective shear modulus of the composite, we need to derive the equations considering shear and bending. For the case of parabolic shear stress distribution, typical of this situation [10],

$$\frac{1}{G_{12}} = \frac{v_f^2 (v_f + 3v_m)}{G_{12f}} + \frac{v_m^2 (3v_f + v_m)}{G_m} \quad (2.15)$$

giving a stricter lower bound on the effective shear modulus and where v_m is the matrix volume fraction.

The rule of mixtures works well for the determination of the longitudinal Young's modulus and the Poisson's ratio, but for the transverse Young's modulus and the shear modulus there are some discrepancies [10, 18]. The reason for this behaviour lies in the assumptions made while working in iso-strain or iso-stress conditions, which are not really true. Besides this, it is very difficult to determine accurately the mechanical properties of the fibres, so, usually, E_{22f} and G_{12f} are calculated with a great uncertainty [10].

A deeper analysis on the rule of mixtures led to the discovery of some inconsistencies in the compatibility of displacements on the fibre/matrix system. In fact, when proceeding to the derivation of the rule of mixtures, it was assumed that the sides with no forces applied had null stress boundary conditions. However, due to the difference in Poisson's ratios of the fibre and the matrix, the deformation perpendicular to those sides cannot possibly be equal, leading to the existence of a non-zero stress on them. To resolve this problem, some of the boundary conditions were changed, resulting in a modified

version of the inverse rule of mixtures for the transversal Young's modulus of the composite [17],

$$\frac{1}{E_{22}} = \frac{v_f}{E_{22f}} + \frac{v_m}{E_m} - v_f v_m \frac{v_f^2 \frac{E_m}{E_{22f}} + v_m^2 \frac{E_{22f}}{E_m} - 2v_f v_m}{v_f E_{22f} + v_m E_m} \quad (2.16)$$

2.1.2 Hashin-Shtrikman bounds

Using many concepts from variational principles in mechanics, Hashin and Shtrikman came up with an improved version of the bounds where the equivalent mechanical properties may lie. Applying the principle of minimum potential energy and the concept of stress polarization tensor, one can calculate the change in elastic strain energy by the addition of inclusions with different elastic properties [19].

For determination of the lower Hashin-Shtrikman bound, the variation of elastic strain energy must be maximized with respect to stress polarization tensor, being the matrix the reference material, while for the upper bound, the reference phase is the fibre. One particular feature of this model is the fact that it calculates the bounds for the shear modulus G_{12} and the bulk modulus, K . So, it is necessary to use the bulk modulus to determine the Young's modulus afterwards [10, 19].

2.1.3 Cox model

Until now, we have described a rather simplistic situation, where it is considered that the equivalent properties of the composite do not depend, in any way, on the geometry of placement of the fibres nor their aspect ratio. Of course this assumption may not be reasonable, as fibres with different sizes will impact differently the final properties of the material [20].

One of the main problems that emerge from fibre size considerations is the fact that they may not have the same length as the composite, which means, we need to readjust the equations for discontinuous fibres. Also, in short fibres, more often than not, the stress transfer between the matrix and the fibre is not perfect, so in fact, the effective reinforcement caused by the fibre is reduced [20].

To overcome this obstacle, the so-called 'shear lag' theory represents a very intuitive and reliable way to change the rule of mixtures into a more useful form when dealing with short fibres [21]. This important step, introduced by Cox, consists in a new parameter named the length efficiency factor, η_l , which reduces the fibre's Young's modulus in order to accommodate the incapacity to transfer perfectly the interfacial stresses between fibre and matrix [20, 22],

$$E_{11} = \eta_l v_f E_{11f} + (1 - v_f) E_m \quad (2.17)$$

$$\eta_l = 1 - \frac{\tanh\left(a \frac{l}{d}\right)}{\left(a \frac{l}{d}\right)} \quad (2.18)$$

$$a = \sqrt{\frac{-3E_m}{2E_{11f} \ln v_f}} \quad (2.19)$$

where a is also a new parameter named the stress transfer coefficient. As it is expected, the length efficiency factor approaches one with increasing aspect ratio of the fibre ($\frac{l}{d} > 10$), recovering the basic rule of mixtures. Although its apparent success, the Cox model suffer from a very discouraging problem: it can only be computed in the longitudinal direction, so it is only useful in predicting the longitudinal Young's modulus [21].

Finally, one more adjustment can be made to include another important factor in this analysis, the orientation of the fibres. With that in mind, it is possible to add another new factor, called the orientation efficiency factor, η_o , to change the reinforcement of the fibres based on their orientation distribution in space. We can adapt equation (2.17) to fit this last coefficient [20],

$$E_{11} = \eta_o \eta_l v_f E_{11f} + (1 - v_f) E_m \quad (2.20)$$

For aligned unidirectional fibres, $\eta_o = 1$, for randomly oriented fibres in a plane, $\eta_o = \frac{3}{8}$, and for randomly oriented fibres in space, $\eta_o = \frac{1}{5}$. The 'shear lag' theory is also useful to determine the yield strength of the composite, but this is out of the scope of this work [20].

2.1.4 Chamis model

As the Cox model tries to correct the rule of mixtures by incorporating the effect of fibre aspect ratio on the properties of the final composite, the Chamis model focus on the dependence of those properties with fibre-packing geometry. In fact, it was proposed that E_{22} and G_{12} might depend on fibre-packing, thus explaining the disparities observed in the inverse rule of mixtures [10].

This model utilizes the concept of a representative volume element (RVE) to demonstrate the whole behaviour of the composite, based on a square fibre-packing array. It equates the cross sectional area of a circular fibre to an equivalent square fibre and divides the RVE into two sub-regions: one composed only of matrix and another with a mixture of matrix and fibre [10, 23].

Using these concepts with the inverse rule of mixtures, one can derive relationships concerning the equivalent properties of the final composite. The resulting equations have been simplified by Chamis and

Hopkins to a simpler form [10, 23],

$$E_{22} = \frac{E_m}{1 - \sqrt{v_f} \left(1 - \frac{E_m}{E_{22f}}\right)} \quad (2.21)$$

$$G_{ij} = \frac{G_m}{1 - \sqrt{v_f} \left(1 - \frac{G_m}{G_{ijf}}\right)} \quad (2.22)$$

where G_{ij} can be G_{12} or G_{23} .

In fact, this simpler form give a more accurate description of the transverse properties than the Reuss model or the original equations obtained in Chamis's analysis. The prediction of the transverse Young's modulus and the longitudinal shear modulus are in good agreement with experimental values and the Chamis model offers more strict bounds on the values permitted by the composite. The principal disadvantage of this model is that it assumes square cross sectional fibres, which is not true, and completely neglects the effect of fibre aspect ratio [10].

2.1.5 Fu model for transverse Young's modulus

The model developed by Fu et al for the prediction of the transverse Young's modulus utilizes the same ideas as the Chamis model but present a better solution to this problem. It also utilizes a RVE in a square fibre-packing scheme, but considers circular cross sectional fibres, instead of the square ones. In addition to this, it considers the possibility of short fibres, which means that Fu's model is capable of predicting the dependence of the transverse Young's modulus with fibre-packing geometry and fibre aspect ratio, resolving both problems with Cox and Chamis models [10, 24].

Again, considering the division of the RVE into sub-regions that are only affected by the matrix or the matrix and the fibre and applying an approach based on continuum mechanics, rather than using only geometric parameters and fibre volume fraction, we obtain a more precise solution in very good agreement with experiment. For a continuous fibre the Fu model gives [10, 24],

$$\frac{1}{E_{22}} = \frac{\sqrt{\frac{4v_f}{\pi}}}{\sqrt{\frac{\pi v_f}{4}} E_{22f} + \left(1 - \sqrt{\frac{\pi v_f}{4}}\right) E_m} + \frac{1 - \sqrt{\frac{4v_f}{\pi}}}{E_m} \quad (2.23)$$

However, if we now consider an array of discontinuous fibres, characterised by some aspect ratio, the following correction to equation (2.23) is obtained [24],

$$\frac{1}{E_{22}} = \frac{\sqrt{\frac{4v_f(1+\lambda)}{\pi}}}{\sqrt{\frac{\pi v_f}{4(1+\lambda)}} E_{22f} + \left(1 - \sqrt{\frac{\pi v_f}{4(1+\lambda)}}\right) E_m} + \frac{1 - \sqrt{\frac{4v_f(1+\lambda)}{\pi}}}{E_m} \quad (2.24)$$

where λ represents the ratio between the interfibre spacing in the longitudinal direction and the fibre length. As it can easily be seen, for $\lambda = 0$, which means that the spacing between fibres is null or that the fibres are continuous, we recover equation (2.23).

Finally, because of the way the problem is stated in the Fu model, a maximum theoretical limit is imposed to the value of the fibre volume fraction, lower than 100%. This occurs as a consequence of the fibre-packing scheme and the fact that it is impossible to fill completely a square cross section with only objects of circular cross sectional area [24].

This model will be further studied in Section 2.2.2, because of its usefulness and rather good fitting with the existent experimental data.

2.1.6 Halpin-Tsai model

After some development on the elasticity models for the prediction of equivalent elastic properties of composites, Halpin and Tsai developed a set of equations that gives a better estimate of those parameters in comparison to all the models referred until now [25–27]. Based on the assumptions of theoretical elasticity theory, the Halpin-Tsai equations also utilizes some empirical parameters, obtained by curve-fitting, to acquire a better correlation with experimental data [10].

It has been proven to give better estimates for the transverse Young's modulus and the shear modulus. In their most generic form, the Halpin-Tsai equations can be written as [10, 25, 26],

$$\frac{P}{P_m} = \frac{1 + \xi \eta v_f}{1 - \eta v_f} \quad (2.25)$$

$$\eta = \left(\frac{P_f}{P_m} - 1 \right) \left(\frac{P_f}{P_m} + \xi \right)^{-1} \quad (2.26)$$

where P is a generic elastic property of the composite, P_m is a generic elastic property of the matrix, P_f is a generic elastic property of the fibres, η is a function defined by equation (2.26), that guarantees that $P = P_m$ if $v_f = 0$ and $P = P_f$ if $v_f = 1$, and ξ is an empirical parameter that varies with the geometry of the fibre phase and the type of loading applied to the composite [10, 25, 26].

P	P_m	P_f	ξ
E_{11}	E_m	E_{11f}	$2\frac{l}{d}$
E_{22}	E_m	E_{22f}	2
G_{12}	G_m	G_{12f}	1

Table 2.1: Empirical parameter ξ for various equivalent elastic properties of the composite.

The empirical parameter ξ depends on what property P you consider in the Halpin-Tsai model. For a square array fibre-packing and unidirectional fibres, Table 2.1 indicates what values to use in the case of the longitudinal and transverse Young's modulus and longitudinal shear modulus [10, 26].

Although the Halpin-Tsai equations are one of the most widely used models for the equivalent elastic properties of composite materials, due to its simplicity, it has the major shortcoming of using an empirical parameter that lacks physical meaning, offering no insights into the physical process involved. It also relies heavily on the experimental curve fitting of this parameter [10].

All the relations and factors described before are valid for a composite material with a unidirectional fibre phase. For the case of a random distribution of fibre orientations some adjustments must be made to account for the varying direction of the fibre's elastic properties [15, 28].

For a bidimensional random distribution of fibre orientations the material is considered isotropic in the plane of the fibres, so the in-plane Young's modulus of the composite is given by [28, 29],

$$\tilde{E}_{11} = \frac{3}{8}E_{11} + \frac{5}{8}E_{22} \quad (2.27)$$

where \tilde{E}_{11} represents the mean in-plane Young's modulus of the composite, due to the random distribution of fibres. Equation (2.27) is known in the literature as Tsai-Pagano equation. In turn, we can write the Halpin-Tsai and Tsai-Pagano equations in conjunction for the Young's modulus as [15],

$$\tilde{E}_{11} = \frac{E_m}{8} \left[5 \left(\frac{1 + 2\beta_{dd}v_f}{1 - \beta_{dd}v_f} \right) + 3 \left(\frac{1 + 2\frac{l}{d}\beta_{dl}v_f}{1 - \beta_{dl}v_f} \right) \right] \quad (2.28)$$

where β_{dd} represents the value a parameter η for the transversal Young's modulus E_{22} and β_{dl} the same parameter for the case of the longitudinal Young's modulus E_{11} .

Lavengood et al [28], also establish the relation of the mean Young's modulus of the composite for the case of a tridimensional random distribution of fibre orientation. In this case, the final material can

be thought of as isotropic and the Young's modulus is [28],

$$\tilde{E}_{11} = \frac{1}{5}E_{11} + \frac{4}{5}E_{22} \quad (2.29)$$

2.1.7 Non-dilute correction to Halpin-Tsai model

As discussed in the last Section 2.1.6, the Halpin-Tsai equations agree to a very good degree with the experimental data available. However, for large fibre volume fractions ($v_f > 70\%$), the non-linear behaviour of the mechanical properties tends to disagree with the theoretical model [10, 26].

To answer this problem, it was proposed a change to the value of ξ for the transverse Young's modulus and the shear modulus to better accommodate for the higher predicted values of the elasticity models. With this in mind, we have the following modifications [26, 30],

$$\xi_{E_{22}} = 2 + 40v_f^{10} \quad (2.30)$$

$$\xi_{G_{12}} = 1 + 40v_f^{10} \quad (2.31)$$

Also for the particular case of CNTs, it was noted that for sufficient high mass concentrations of the phase, the response curve of the longitudinal Young's modulus becomes highly non-linear. This non-linearity is attributed to the aggregation of nanotubes, causing our assumption of a good dispersion of the phase not valid [21, 31]. To address this problem, Yeh et al [31] introduce a non-linear factor in the empirical parameter ξ ,

$$\xi = 2 \frac{l}{d} e^{-av_f - b} \quad (2.32)$$

where a and b are coefficients that need to be determined by experimental means. This introduces more complexity in the model, requiring the determination of two additional constants [21].

Besides the correction introduced in equation (2.32), the Halpin-Tsai model benefits from the addition of another factor, called the orientation factor α , which describes the orientation of CNTs on the matrix. For CNTs randomly dispersed on a plane, $\alpha = \frac{1}{3}$, and for randomly dispersed in space, $\alpha = \frac{1}{6}$. Considering this factor, the Halpin-Tsai equation for the longitudinal Young's modulus can be written as equation (2.25) but with the adimensional factor η as [31],

$$\eta = \left(\frac{\alpha E_{11f}}{E_m} - 1 \right) \left(\frac{\alpha E_{11f}}{E_m} + \xi \right)^{-1} \quad (2.33)$$

2.1.8 Mori-Tanaka model

The Mori-Tanaka model is able to directly predict the final stiffness matrix of the composite through the use of a number of physical principles, having a definite physical meaning behind its equations. That is the reason it is considered a more elegant method than the Halpin-Tsai model, but it uses a rather complex mathematical formulation of the strain field on an inclusion surrounded by a medium [10, 32].

The original work of Mori and Tanaka concerned the calculation of the average internal stress of a medium containing inclusions with eigenstrains, which are constant interior strain fields [32, 33]. Using the idea of Eshelby's equivalent inclusion in conjunction with the eigenstrain theory, the Mori-Tanaka model was able to predict the equivalent elastic properties of composites, effects of cracks on a medium and void growth in viscous metals. Eshelby's idea is based on the following thought process: if a portion of an infinite homogeneous medium is replaced with an inclusion that has different elastic properties, a non-elastic strain will develop within that domain, which can be described as a fictitious eigenstrain. To relate the eigenstrain to the actual strain felt on the inclusion we use Eshelby's tensor [10, 32, 34].

Besides this, the Mori-Tanaka model also introduces the concentration tensor, that relates the mean strain felt on the fibre and the mean strain on the matrix, and the Mori-Tanaka tensor, which relates the mean stress on the fibre with that on the matrix. All this complex new identities are needed for the full description of the stiffness matrix of the final composite [10, 32, 35].

A detailed explanation of the Mori-Tanaka model is outside of the scope of this text, because although it fits well experimental data, we would rather not use methods that involve the direct computation of the stiffness matrix.

In spite of all the advantages the model has, it shares an assumption most other models also have: a dilute concentration of fibres. To solve this problem, two other methods were developed, based on this one, the self-consistent model and the differential scheme based model. The first one is based on the assumption that the matrix and the inclusion form an effective medium with some effective properties we want to determine. Many models studied until now share this consideration, but the self-consistent model was used to correct the Mori-Tanaka model for non-dilute dispersions, by stating that the inclusion is surrounded by an effective medium with the final properties of the composite. The latter one also tries to correct the non-dilute approximation of the Mori-Tanaka model by introducing a formulation based on successive iterations. The main shortcoming of the differential scheme based model is the heavy reliability on computational power to execute the iterations until meaningful results are achieved [10].

2.2 Hierarchic model for multiscale composites

In this section we will detail the chosen micromechanics model to represent a multiscale composite based on the CNT/fibre/polymer matrix mixture. First, it can be seen that most of the available models are only meant for two-phase mixtures, not being appropriate for our three-phase one. However, we can use an hierarchic model to represent a three-phase mixture as a sum a two-phase ones and that is the approach that will be used throughout this text [5, 15].

As mentioned before, the polymer matrix is to be considered as an isotropic material, contrasting with the CNTs and the carbon fibres which will be assumed as orthotropic. Then, by first "mixing" the polymer matrix with the nanotubes, an isotropic effective matrix material will be obtained, because of the random distribution of nanotube orientations. If after that the carbon fibres are finally added, it is possible to model the last mixture as a two-phase composite, with the effective CNT-reinforced matrix being one of the phases [5, 15].

Then, this hierarchic model will be subdivided into two steps: the two-phase mixture of the polymer matrix and the CNTs (resulting in a CNT/polymer matrix composite, which serves as an effective matrix for the next step) and the two-phase mixture of the CNT/polymer matrix composite and the carbon fibres (leading to the final CNT/fibre/polymer matrix composite) [5, 15]. The next Sections 2.2.1 and 2.2.3 will explain each of the steps described above.

2.2.1 Equivalent properties of CNT/polymer matrix composites

For the first step in the hierarchic model, the polymer will serve as the matrix and the CNTs will be the fibre. As already mentioned, the CNTs are well-dispersed in the isotropic matrix and their orientations are randomly distributed in space. This is a reasonable assumption, as the final composite will be used in the construction of a plate, but the plate's thickness will be orders of magnitude greater than the length of the nanotubes. It is also assumed a dilute fibre solution, so, as a rule of thumb, the mass concentration of CNTs should never be above 1% [5, 15].

Using the Halpin-Tsai model, for a tridimensional random distribution of fibre orientations and for a dilute solution, we have the Young's modulus of the combined CNT/polymer matrix composite E_{mCN} as,

$$E_{mCN} = \frac{E_m}{5} \left[4 \left(\frac{1 + 2\beta_{dd}v_{CNT}}{1 - \beta_{dd}v_{CNT}} \right) + \left(\frac{1 + 2\frac{l_{CNT}}{d_{CNT}}\beta_{dl}v_{CNT}}{1 - \beta_{dl}v_{CNT}} \right) \right] \quad (2.34)$$

with β_{dd} and β_{dl} defined as,

$$\beta_{dd} = \frac{4(d_{CNT} - t_{CNT})t_{CNT} \frac{E_{CNT}}{E_m} - d_{CNT}^2}{4(d_{CNT} - t_{CNT})t_{CNT} \frac{E_{CNT}}{E_m} + 2d_{CNT}^2} \quad (2.35)$$

$$\beta_{dl} = \frac{4(d_{CNT} - t_{CNT})t_{CNT} \frac{E_{CNT}}{E_m} - d_{CNT}^2}{4(d_{CNT} - t_{CNT})t_{CNT} \frac{E_{CNT}}{E_m} + 2l_{CNT} d_{CNT}} \quad (2.36)$$

where we used the relation defined in equation (2.4), between the effective fibre of the CNT and the actual CNT, unlike Rafiee et al that used equation (2.5) [5, 15]. In equations (2.34), (2.35) and (2.36), E_m is the Young's modulus of the matrix, E_{CNT} is the Young's modulus of the CNTs, l_{CNT} is the mean length of the CNTs, d_{CNT} is the mean diameter of the CNTs, t_{CNT} is the mean thickness of the CNTs and v_{CNT} is the volume fraction of CNTs.

Usually, we define the quantity of CNTs in a composite by their mass fraction, so we should convert from this quantity to their volume fraction to apply the Halpin-Tsai equation above. Then, for the volume fraction of CNTs we have,

$$v_{CNT} = \frac{w_{CNT}}{w_{CNT} + \frac{\rho_{CNT}}{\rho_m}(1 - w_{CNT})} \quad (2.37)$$

where w_{CNT} is the mass fraction of CNTs, ρ_{CNT} is the density of the CNTs and ρ_m is the density of the matrix [15]. It is also easily shown, based on the weight average of the components' mass densities, that the density of the CNT/polymer matrix composite ρ_{mCN} is [15],

$$\rho_{mCN} = v_{CNT} \rho_{CNT} + (1 - v_{CNT}) \rho_m \quad (2.38)$$

Finally, an isotropic material is defined by two elastic constants, so, in order to properly define the elastic properties of the CNT/polymer matrix composite, another must be given. Because the Poisson's ratio is usually dominated by the matrix in a dilute composite and the mass fraction of CNTs is very small, we can approximate the Poisson's ratio of the CNT/polymer matrix composite ν_{mCN} as equal to that of the matrix,

$$\nu_{mCN} = \nu_m \quad (2.39)$$

where ν_m is the Poisson's ratio of the matrix [5, 6, 15]. Also based on the assumption of isotropy, it is possible to calculate the shear modulus of the CNT/polymer matrix composite G_{mCN} by [5, 6],

$$G_{mCN} = \frac{E_{mCN}}{2(1 + \nu_{mCN})} \quad (2.40)$$

2.2.2 Extended model for elastic moduli based on unit cell

For the modelling of a fibre composite we could use the simple rule of mixtures as Rafiee et al, however to improve the hierarchic model used, the Fu model was chosen instead of the former [15]. The problem with the Fu model is that it only predicts the transversal Young's modulus, lacking the other important elastic properties needed. So, in this section, an extension of the Fu model for the longitudinal Young's modulus, Poisson's ratio and shear modulus is presented.

According to Fu et al, a fibre composite can be represented as in Figure 2.2, with a RVE with only a fibre surrounded by matrix present [24]. The fibres are modelled as full cylinders, all equal to each other, and the matrix around it as a hollow square prism. The stress transfer between the phases is perfect, as is their bonding. Although not the usual case with carbon fibres, it is going to be assumed that the fibres are discontinuous. This permits the most general case to be considered, so that the addition of continuity defects may be added in a latter experimental verification.

In this formulation, d_f is the diameter of the fibre, L_f is the length of the fibre, δ is the interfibre spacing in the yOz plane and L_1 is the gap between two end-to-end fibres in the longitudinal direction [24].

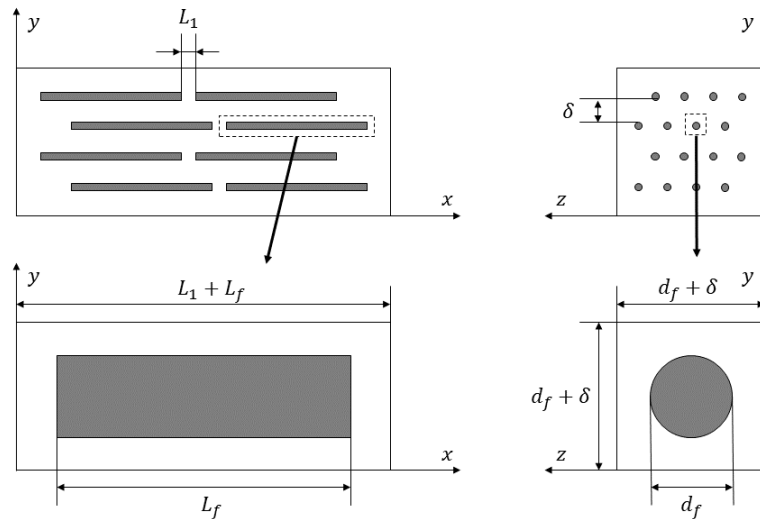


Figure 2.2: Schematic model of a discontinuous fibre composite and a corresponding representative volume element.

One of the first consequences of this fibre-packing scheme is that the volume fraction of fibres has a theoretical limit less than 100%. For the RVE shown, the fraction volume fraction is,

$$v_f = \frac{\pi d_f^2 L_f}{4(d_f + \delta)^2 (L_1 + L_f)} \quad (2.41)$$

where by reducing L_1 and δ to 0, hereby compacting to the fullest the matrix with fibres, it results in a maximum fibre volume fraction of about $v_{f_{max}} = 78.5\%$.

For the determination of the longitudinal Young's modulus of the composite E_{11} , equilibrium of forces and stresses along the x direction is computed. The method applied is similar to the one used by Fu in his analysis of the transverse modulus, however the direction of the force applied is changed [24].

This analysis can be divided in two zones: only matrix, A, and a mixture of matrix and fibre, B. For zone A, we have that the mean deformation is,

$$\tilde{\epsilon}_{xA} = \frac{\sigma_x}{E_m} \quad (2.42)$$

where σ_x is the applied stress on a RVE in the x direction and E_m is the Young's modulus of the matrix. However, for zone B, there exists a mixture of phases, so a stress equilibrium equation is necessary to calculate the effective Young's modulus of that zone. Then,

$$\frac{\pi d_f^2}{4(d_f + \delta)^2} \sigma_{xf} + \left(1 - \frac{\pi d_f^2}{4(d_f + \delta)^2}\right) \sigma_{xm} = \sigma_x \quad (2.43)$$

using an iso-strain condition and by the definition of equation (2.41),

$$v_f (1 + \lambda) E_{11f} \tilde{\epsilon}_{xB} + [1 - v_f (1 + \lambda)] E_m \tilde{\epsilon}_{xB} = \sigma_x \quad (2.44)$$

putting the mean deformation of zone B in evidence,

$$\tilde{\epsilon}_{xB} = \frac{\sigma_x}{v_f (1 + \lambda) E_{11f} + [1 - v_f (1 + \lambda)] E_m} \quad (2.45)$$

where E_{11f} is the longitudinal Young's modulus of the fibre and λ is a parameter defined by,

$$\lambda = \frac{L_1}{L_f} \quad (2.46)$$

as explained in Section 2.1.5.

Finally, to obtain the equivalent Young's modulus of the composite, we average the deformation of the two zones weighted by the corresponding volume fraction of each zone,

$$\varepsilon_x = \frac{L_1}{L_1 + L_f} \tilde{\varepsilon}_{xA} + \frac{L_f}{L_1 + L_f} \tilde{\varepsilon}_{xB} \quad (2.47)$$

expanding all the deformations with equations (2.42) and (2.45),

$$\frac{\sigma_x}{E_{11}} = \frac{L_1}{L_1 + L_f} \frac{\sigma_x}{E_m} + \frac{L_f}{L_1 + L_f} \frac{\sigma_x}{v_f (1 + \lambda) E_{11f} + [1 - v_f (1 + \lambda)] E_m} \quad (2.48)$$

and by rearrangement of the terms, we finally obtain,

$$E_{11} = E_m \frac{v_f E_{11f} + (1 - v_f) E_m + \lambda v_f (E_{11f} - E_m)}{E_m + \lambda v_f (E_{11f} - E_m)} \quad (2.49)$$

In equation (2.49) there is a lot of useful information that can be extracted about the fundamental ideas behind the Fu model. First in the limit $\lambda \rightarrow 0$, meaning only continuous fibres, it returns the basic rule of mixtures, which seems a valid evolution. For $\lambda \rightarrow \infty$, which means only the matrix is present, it returns E_m . Finally, for $v_f \rightarrow 0$, which means again that there is only matrix, it returns E_m .

For all the limiting cases and by its natural evolution, being discrepant with the rule of mixtures only for high fibre volume fractions, we may assume the validity of the equation. For all the other elastic properties, an analysis of the type shown above was used to obtain equations (2.50) to (2.52).

As established before, rearranging the result obtain by Fu et al to be in a similar form to that of E_{11} , the transversal Young's modulus is given by [24],

$$E_{22} = E_m \frac{E_m + \sqrt{\frac{\pi v_f}{4(1+\lambda)}} (E_{22f} - E_m)}{E_m + \left(\sqrt{\frac{\pi v_f}{4(1+\lambda)}} - v_f \right) (E_{22f} - E_m)} \quad (2.50)$$

where E_{22f} is the transversal Young's modulus of the fibres.

By a similar formulation as that done for the longitudinal Young's modulus, it is possible to obtain the longitudinal Poisson's ratio,

$$\nu_{12} = \frac{E_m [v_f \nu_{12f} + (1 - v_f) \nu_m] + \lambda v_f (E_{11f} - E_m) \nu_m}{E_m + \lambda v_f (E_{11f} - E_m)} \quad (2.51)$$

where ν_{12f} is the Poisson's ratio of the fibres and ν_m is the Poisson's ratio of the matrix.

Finally, using a method similar to the one described in detail throughout this section, but for the transverse direction, we can find the general expression for the longitudinal shear modulus,

$$G_{12} = G_m \frac{G_m + \sqrt{\frac{\pi v_f}{4(1+\lambda)}} (G_{12f} - G_m)}{G_m + \left(\sqrt{\frac{\pi v_f}{4(1+\lambda)}} - v_f \right) (G_{12f} - G_m)} \quad (2.52)$$

where G_{12f} is the longitudinal shear modulus of the fibres and G_m is the longitudinal shear modulus of the matrix.

2.2.3 Equivalent properties of CNT/fibre/polymer matrix composites

In this section we shall discuss the second step of the hierarchic model for the prediction of the CNT/fibre/polymer matrix composite. It is assumed that the CNT/polymer matrix composite is isotropic and that the carbon fibres are orthotropic and unidirectional. The fibres are also considered continuous throughout the complete length of the composite, rendering the λ parameter in the Fu model null [24].

Then, using the extended Fu model, detailed in Section 2.2.2, to predict the elastic properties of the multiscale composite, we have,

$$E_{11} = v_f E_{11f} + (1 - v_f) E_{mCN} \quad (2.53)$$

$$E_{22} = E_{mCN} \frac{E_{mCN} + \sqrt{\frac{\pi v_f}{4}} (E_{22f} - E_{mCN})}{E_{mCN} + \left(\sqrt{\frac{\pi v_f}{4}} - v_f \right) (E_{22f} - E_{mCN})} \quad (2.54)$$

$$\nu_{12} = v_f \nu_{12f} + (1 - v_f) \nu_{mCN} \quad (2.55)$$

$$G_{12} = G_{mCN} \frac{G_{mCN} + \sqrt{\frac{\pi v_f}{4}} (G_{12f} - G_{mCN})}{G_{mCN} + \left(\sqrt{\frac{\pi v_f}{4}} - v_f \right) (G_{12f} - G_{mCN})} \quad (2.56)$$

where E_{11f} and E_{22f} are, respectively, the longitudinal and the transversal Young's modulus of the fibres, ν_{12f} is the Poisson's ratio of the fibres, G_{12f} is the shear modulus of the fibres and v_f is the volume fraction of fibres. All the equations also admit that there exists no interaction between the fibres and the CNTs.

As the final CNT/fibre/polymer matrix composite is a mixture of an isotropic phase with an orthotropic one, it will also be an orthotropic material. Because the fibres are along a unique direction, it must be a transversely isotropic material, as described in Section 2.1. Then, using equation (2.9), it is possible to obtain the minor Poisson's ratio of the multiscale composite [17].

Finally, for a dynamic problem, another important property is the density of the multiscale composite. In analogy with Section 2.2.1, by calculating a weight average of the densities of the phases,

$$\rho = v_f \rho_f + (1 - v_f) \rho_{mCN} \quad (2.57)$$

being ρ_f the density of the fibres.

Only four of the necessary elastic constants were determined by the hierarchic model, so the complete stiffness matrix of the multiscale composite cannot be fully computed (it would need the transversal shear modulus G_{23} or the transversal Poisson's ratio ν_{23}). However, as there are not many models capable of predicting those properties and this work will only use bidimensional plates, the four constants will suffice to represent the elastic properties of the CNT/fibre/polymer matrix composite in study.

Chapter 3

Validation of the hierarchic model

Although theoretical models are a powerful method for gaining insights on the mechanics of a physical phenomenon, experimental facts must assert the validity of those models. With this in mind, this section aims to validate the hierarchic model of the equivalent elastic properties of multiscale composites, developed in the previous chapter.

For that purpose, many articles, listed in the references [16, 31, 36–40], were used to compare many numerical and experimental studies with the values obtain by the model in this text. First, the increase in Young's modulus of a resin matrix with the addition of CNTs is studied, as well as the relation between the CNT aspect ratio and the equivalent elastic properties. Finally, the effect of adding CNTs to a fibre-reinforced composite is compared, representing the final step in the validation of our model.

In some of the references, specially in Rafiee et al [15], there are experimental and numerical results on the natural frequencies of plates made of CNT/fibre/polymer matrix composites. However, as the introduction of the numerical model for the vibration of plates will only be done in a latter part of this text, these references will not be used in the current section.

3.1 Prediction of elastic properties of CNT/polymer matrix composites

In this section, the effect of adding CNTs to a polymer matrix is studied, to verify if the first step on the hierarchic model is valid or not. The first two papers concern the use of SWCNTs, while the others evidence the effect of adding MWCNTs.

Because our model is universal to the two kinds of nanotubes, some simplifying assumptions were made, for example the use of a constant thickness of 0.34 nm for all CNTs, representing the interlayer spacing of graphite [12]. However, even if this is a good approximation for SWCNTs of small diameter, for MWCNTs there is a linear relation between the diameter of a CNT and its thickness, as shown by

Thostenson and Chou [11].

As the thickness of a nanotube is a very difficult quantity to measure and one of the biggest inputs of error in the hierarchic model, this is the variable that will be most carefully analysed in each reference. All the quantities related to the thickness, like the effective Young's modulus and the effective density of the CNTs will also be taken carefully. In the remainder of this chapter, when the error in some result is mentioned, it refers to the relative error between our model and the comparison in analysis, being better described as an error of approximation, instead of a true error between some prediction and an experimental value.

3.1.1 Formica et al (2010)

In the first comparison model used [36], we are going to evaluate the use of SWCNTs on an epoxy resin. Almost all the variables used are described in the article. First of all, the nanotubes used had diameters of 1 to 2 nm and lengths of 5 to 15 μm [36]. With this information, it is reasonable to assume that all CNTs have the mean value of those intervals, so $d_{CNT} = 1.5 \text{ nm}$ and $l_{CNT} = 10 \mu\text{m}$.

About the mechanical properties it is known that for the CNTs, $E_{CNT} = 970 \text{ GPa}$ and $\rho_{CNT} = 1308 \text{ kg/m}^3$, and for the epoxy resin, $E_m = 2.35 \text{ GPa}$ and $\rho_m = 1200 \text{ kg/m}^3$ [36]. Also, for the case at hand, the weight fraction of SWCNT is 0.5%.

As the diameter of the CNTs is sufficiently small and we are working with single-walled nanotubes, it seems plausible that all nanotubes have a thickness of about 0.34 nm, as assumed in the original hierarchic model [11].

Finally, Formica et al [36] mention another article regarding the control of the micro-structure of the composite. There was a particular attention in achieving a homogeneous dispersion, efficient interfacial stress transfer and good alignment of the nanotubes inside the matrix [41]. Although all the important aspects mentioned were well fulfilled, it was possible to see images, using an electron microscope, that showed imperfectly aligned, but well-dispersed, chains of nanotubes [41].

To account for the imperfections in CNT alignment, we assumed in the hierarchic model a bidimensional random distribution of CNT orientations inside the epoxy resin. This conservative assumption showed very good results, even if it does not translate accurately the reality of the situation. In Table 3.1 it is possible to compare the values of the experimental test presented and the numerical model used by Formica et al [36] and our own obtained using the hierarchic model. The error in parenthesis is relative to the experimental value measured in the article.

$E_{[Formica,2010]_{exp}}$ /GPa	$E_{[Formica,2010]_{num}}$ /GPa	E_{mCN} /GPa
3.47	3.27	3.51 (1.15%)

Table 3.1: Comparison between the hierarchic model and the experimental values presented and the numerical ones obtained by Formica et al [36].

As it is described, the hierarchic model provided a better estimation for the Young's modulus of the composite than the value obtained using the numerical model of Formica et al. The fact that we used a bidimensional random distribution of CNT orientations, rather than a tridimensional one, imply some degree of alignment of the nanotubes, contributing to the good alignment criteria in obtaining the compared values.

The coefficients in the Tsai-Pagano equation (2.27) can be adjusted so that a greater preponderance is given to the longitudinal or the transversal Young's modulus, caused by the distribution of CNT orientations. For comparison, the weight that is given to the longitudinal Young's modulus in a tridimensional random distribution of orientations is $\frac{1}{5}$, against $\frac{4}{5}$ for the transversal one, whilst in an intermediate case of a bidimensional distribution the values are $\frac{3}{8}$ and $\frac{5}{8}$, respectively. Finally, at the extreme, the coefficients change to 1 and 0 for a fully aligned nanotube distribution, with all of the contribution to the Young's modulus from the longitudinal one, achieving an orthotropic material [28].

Following the trend established in the coefficients, we could expect a weight somewhat above $\frac{3}{8}$ for the longitudinal Young's modulus, due to a better alignment of nanotubes than a bidimensional random distribution of orientations, as can be seen in [41]. This implies that our model tends to overestimate the value of the nanocomposite's Young's modulus.

3.1.2 Tai et al (2008)

In this section, the improvement in the Young's modulus by the addition of SWCNTs on a phenolic resin was studied. The values used in the calculations performed by Tai et al [37] were more difficult to find, because there wasn't an extensive description of the computed variables. To that avail, other references were used in order to find all the missing information to run the hierarchic model for this case.

The mean value of the diameter of the CNTs was expressed as $d_{CNT} = 13.33$ nm and the phenolic resin had a Young's modulus of $E_m = 4.6$ GPa [37]. Also for the phenolic resin, the density is usually found in the range between 1200 and 1400 kg/m³ [42], so it was assumed the mean value of the interval as the density of the matrix, $\rho_m = 1300$ kg/m³.

According to Thostenson et al [11], there exists a relation between the diameter of a CNT and its effective density. Then, for a diameter of 13.33 nm the corresponding density is $\rho_{CNT} = 1600$ kg/m³, approximately [11]. Using equation (2.6) we get the thickness of the nanotubes, $t_{CNT} = 3.08$ nm, knowing

that $\rho_g = 2250 \text{ kg/m}^3$ [11].

Finally, Tai et al [37] mentions that the Young's modulus of the CNTs used is in the range of 988 and 1600 GPa and by using the mean value, we obtained $E_{CNT} = 1294 \text{ GPa}$. As in this work, there is no mention of the nanotubes' length, we will assume that their aspect ratio is a very big number, meaning that $l_{CNT} \rightarrow \infty$. This is a reasonable approximation due to the long chains of CNTs present in the phenolic resin [37].

Because an alignment process was not applied to the CNTs, our prediction was computed, considering a tridimensional random distribution of CNT orientations, resulting in Table 3.2, where the values of Tai et al [37] were taken from figure 3 in the reference. As it may be readily grasped, the relative error in some of the CNT weight fractions was noticeable, above 10%.

At first, Tai et al [37] used SWCNT with a fairly big diameter, making its effect on the phenolic resin much more relevant. Secondly, the weight fraction of CNT used was high enough for non-linear effects to be dominant at above $w_{CNT} = 0.75\%$. In fact, the reference tries to adjust the modified Halpin-Tsai equation, using Yeh empirical correction [31], to the experimental results. This implies an exponential curve-fitting, which our model is incapable of reproducing, giving a greater error for large values of CNT concentration.

For low values of CNT concentration, the error can be explained by the fact that the CNTs used have a quickly decaying augmentation factor on the mechanical properties of the composite, caused by the exponential decay of an initial highly steep linear curve [37]. This adds another layer of non linearity that our simple hierarchic model cannot capture fully.

The modified Halpin-Tsai equation used in Tai et al [37] suffers from this same problem in the initial part of the curve. In fact, the value of the Young's modulus for 0.25% CNT concentration is underestimated, giving the best results for 0.50% and 0.75%, just like our model.

$w_{CNT} / \%$	0.00	0.25	0.50	0.75	1.00	1.50	2.00
$E_{[Tai,2008]} / \text{GPa}$	4.60	5.65	5.85	5.90	5.70	5.70	5.50
E_{mCN} / GPa	4.60	4.99	5.39	5.78	6.18	6.97	7.77
	(0.00%)	(-11.68%)	(-7.86%)	(-2.03%)	(8.42%)	(22.28%)	(41.27%)

Table 3.2: Comparison between the hierarchic model and the experimental values obtained by Tai et al [37].

$w_{CNT} / \%$	0.0	0.5	1.0	1.5	2.0	3.0	4.0
$E_{[Yeh,2006]} / \text{GPa}$	5.13	5.71	6.49	7.08	7.52	7.69	8.21
E_{mCN} / GPa	5.13	5.68	6.24	6.79	7.35	8.47	9.60
	(0.00%)	(-0.53%)	(-3.85%)	(-4.10%)	(-2.26%)	(10.14%)	(16.93%)

Table 3.3: Comparison between the hierarchic model and the experimental values obtained for network MWCNTs by Yeh et al [31].

3.1.3 Yeh et al (2006)

Yeh et al [31] studied the effect of CNT concentration on the mechanical properties of a phenolic resin imbued with MWCNTs. Although our experiments will use only SWCNTs, the hierarchic model can be adapted to both types of nanotubes, so the comparison with this reference will help the establishment of a more general theory.

According to the reference, the mean diameter of the CNTs is $d_{CNT} = 23.63$ nm and the mean length is $l_{CNT} = 17.57$ μm . Yeh et al [31] used two different types of MWCNT microstructure in their experiments, namely a network structure and a dispersed one. The dispersed structure should be the preferred one in this work, however, as one can see in the microscope images shown in [31], the network MWCNTs seem a much more homogeneous medium, ideal for the application of the hierarchic model. As such, the values represented will also be about the network MWCNTs composite.

The paper also refers the mechanical properties used, of both the CNTs, $E_{CNT} = 953$ GPa and $\rho_{CNT} = 1300$ kg/m³, and the matrix, $E_m = 5.13$ GPa and $\rho_m = 1030$ kg/m³. The density of the CNTs is a correction to the real density considered by Yeh et al [31], $\rho_{CNT_{real}} = 1650$ kg/m³, however because voids near the crossings of MWCNTs cannot be filled by a nanotube, their effective density drops by a proportional amount.

This real CNT density will be used by the hierarchic model to calculate the thickness of the nanotubes used [11]. As such, the thickness of the CNTs is $t_{CNT} = 5.71$ nm. Table 3.3 represents the results obtain by the hierarchic model and those by Yeh et al [31].

As can be seen in the data presented, the hierarchic model has a very good agreement with the experimental results, never having an error greater than 5% for values of CNT weight fraction below 2.0%. For higher values of CNT concentration, as in the last analysis, the exponential behaviour of the real curve becomes evident.

$w_{CNT} / \%$	0.0	0.1	0.5	1.0	1.5	2.0	3.0
$E_{[Montazeri,2010]}$ /GPa	3.430	3.458	3.705	3.951	4.138	4.225	4.365
E_{mCN} /GPa	3.430	3.475	3.655	3.881	4.107	4.335	4.794
	(0.00%)	(0.49%)	(-1.35%)	(-1.77%)	(-0.75%)	(2.60%)	(9.83%)

Table 3.4: Comparison between the hierarchic model and the experimental values obtained for untreated MWCNTs by Montazeri et al [38].

3.1.4 Montazeri et al (2010)

In this last section regarding the study of MWCNTs, the hierarchic model is validated for the case of an epoxy resin with MWCNTs. Just as in the previous cases, the values of all the variables are discriminated in the text.

According to Montazeri et al [38], the mean diameter of the CNTs is $d_{CNT} = 20$ nm and the mean length is $l_{CNT} = 8.5$ μ m. In the reference, two types of MWCNTs were studied, one being the untreated case, while the other being treated with acid. As the microscope photographs show, the untreated MWCNTs seem to have a more random distribution of orientations, so this type of nanotubes will be compared to the hierarchic model for a tridimensional random distribution of CNT orientations [38].

The mechanical properties are also described fully in the reference. For the epoxy matrix we have a Young's modulus of $E_m = 3.430$ GPa and a density of $\rho_m = 1200$ kg/m³, whilst for the CNTs, the modulus is $E_{CNT} = 1000$ GPa and the effective density is $\rho_{CNT} = 1680$ kg/m³ [38]. The effective density of the nanotubes can be used to calculate their thickness, knowing their diameter. As such, the thickness of the CNTs will be $t_{CNT} = 1.67$ nm [11].

Finally, Table 3.4 represents the results obtained by the hierarchic model and those by Montazeri et al [38]. Again, the hierarchic model follows the experimental values with great accuracy, having an error below 2% for all values below 2% of CNT weight fraction. At this value of CNT concentration, the non linear aspect of the problem becomes more apparent, rendering our model less useful.

3.2 Influence of CNT aspect ratio on the elastic properties of CNT/polymer matrix composites

Another important effect that the CNTs have on the mechanical properties of a nanocomposite is the relation between their aspect ratio and the resulting elastic moduli. In fact, longer chains of CNT imply a greater improvement on the Young's modulus of the composite, rendering the aspect ratio of the CNTs an important parameter to control.

$\frac{l_{CNT}}{d_{CNT}}$	1	2	4	8	16	24	∞
$\frac{E_{[Tucker\ III,1999]}}{E_m}$	1.60	2.00	3.00	4.20	5.30	5.60	6.80
$\frac{E_{mCN}}{E_m}$	1.66	2.03	2.62	3.45	4.41	4.94	6.80
	(3.75%)	(1.50%)	(-12.67%)	(-17.86%)	(-16.79%)	(-11.79%)	(0.00%)

Table 3.5: Comparison between the hierarchic model and the numerical values obtained by Tucker III and Liang [16].

Tucker III and Liang [16] used a finite element microstructure analysis to study the effect of fibre aspect ratio on a matrix. Although the reference doesn't specifically concern CNTs, it may provide some insights in the evolution of the same properties for the nanotubes, using the concept of an effective CNT fibre [11].

As such, the hierarchic model must assume unidirectional full cylinders CNTs, with a fibre-packing arrangement of a regular square array. For dealing with the unidirectionality of the CNTs, the Tsai-Pagano equation may be used with a coefficient of 1 for the longitudinal Young's modulus and of 0 for the transversal. Besides that, for a full CNT, rather than a hollow one, the internal diameter must be null. With this in mind, it is possible to find a simple relationship between the thickness of such a CNT and its diameter,

$$t_{CNT} = \frac{d_{CNT} - d_i}{2} = \frac{1}{2}d_{CNT} \quad (3.1)$$

where t_{CNT} is the thickness of the CNT, d_{CNT} is the diameter of the CNT and d_i is the internal diameter of the CNT, which for the case of a full cylinder is 0.

Finally, the reference also mentions the relation between the mechanical properties of the fibre, which we are considering a CNT, and the matrix. It is considered that $E_{CNT} = 30E_m$ and the volume fraction of CNTs to be $v_{CNT} = 20\%$ [16]. The results are presented in Table 3.5, where the values were taken from figure 7 of Tucker III and Liang [16], considering the finite element analysis of a regular square array of representative volume elements.

There is a significant error on intermediate values of the aspect ratio of the CNTs, where the hierarchic model tends to underestimate the value of the Young's modulus. However, for low values or for very high ones, the model seems rather accurate, rendering errors below 5%. This fact was also noted by Tucker III and Liang [16] when he compared the behaviour of the Halpin-Tsai model to his numerical values. Because our hierarchic model is heavily based on the Halpin-Tsai model, it is possible to conclude that our model provides an accurate description for low values of the aspect ratio of the CNTs.

Besides this, it seems that for high aspect ratios, although more slowly growing, our model gives a precise description of the physical phenomenon at study, where at infinity the values coincide perfectly. For example, for a CNT aspect ratio of 1000, the error is only -1.03% , being even smaller for higher values [16]. As the aspect ratio of a CNT tends to be on the order of thousands, the diameter is usually on the nano scale, while the length is on the micro scale [13], the hierarchic model will provide almost for all considered applications a very good approximation of reality, because lower values of aspect ratio will not occur.

Although the results were not very promising, we must note some problems with the assumptions considered by Tucker III and Liang [16] in their analysis. First, his work deals mainly with the behaviour of fibres, not nanotubes, which can affect the outcome of this comparison. In fact, a Young's modulus of the fibres greater than that of the matrix by 30 times seems a plausible consideration for microfibrils in a composite, however for CNTs this number tends to be orders of magnitude greater [37].

Also, the reference in question considered the effect of fibre-packing geometry [16], which our own model ignores completely in the case of the nanotubes. Finally, one of the founding assumptions of the hierarchic model is the existence of a dilute mixture of CNTs in the composite matrix. With a volume fraction of CNTs of 20% it seems improbable, if not impossible, to achieve the dispersion required for a homogeneous distribution of properties along the composite, as well as the validity of the dilute approximation of the equations involved. As such, another base model, rather than the Halpin-Tsai one, should be used to approximate better this particular case, also noted by Tucker III and Liang [16].

3.3 Prediction of elastic properties of CNT/fibre/polymer matrix composites

Until now, we only studied the effect of adding CNTs to a medium on its mechanical properties, namely the Young's modulus. However, to fully verify the extent of the validity of the hierarchic model, we must include in our analysis the combined effect of the CNTs and the microfibrils in a multiscale composite.

To this avail, two references were used to compare the values predicted by our model with other experimental and numerical results. In the first one, all important mechanical properties will be compared [39], whilst on the second only the longitudinal Young's modulus will be verified [40].

As already noted, some references, like Rafiee et al [15], use vibrational analysis to predict the behaviour of a plate made up of a fibre-reinforced composite with embedded CNTs. Although this paper could be used to validate the hierarchic model, the dynamical model in effect for vibrational analysis in this text will only be described in a future section, leaving this comparison out.

3.3.1 Kulkarni et al (2010)

This reference studies the effect of CNT reinforcement on the mechanical properties of a fibre-reinforced epoxy resin composite. All properties of the phases are available in the text.

First, for the CNTs we have a Young's modulus of $E_{CNT} = 1000$ GPa, a diameter of $d_{CNT} = 10$ nm and a length of $l_{CNT} = 100$ nm [39]. Also, the reference considers all the nanotubes has full cylinders, so the relationship between the thickness and the diameter is presented as in equation (3.1).

For the epoxy resin, the Young's modulus is $E_m = 3$ GPa and the Poisson's ratio is $\nu_m = 0.3$, while for the carbon fibres we have a longitudinal Young's modulus of $E_{11f} = 294$ GPa and a transversal of $E_{22f} = 18.5$ GPa, a Poisson's ratio of $\nu_{12f} = 0.27$ and a longitudinal shear modulus of $G_{12f} = 25$ GPa [39].

It is possible to verify that Kulkarni et al [39] used a composite where the nanotubes grew outwards from the carbon fibres. This consists in a complex microstructure format which the hierarchic model cannot represent. However, because Kulkarni et al [39] assumes that the CNTs are isotropic, we may consider that the CNTs are unidirectional in every direction. Then, using the hierarchic model for a unidirectional dispersion of CNTs, we calculate the values represented in Table 3.6.

One important aspect in Table 3.6 is the volume fractions presented, which are respective to the total volume of material present in the composite. As the hierarchic model utilises a sequential approach to the mixture of the three phases, the volume fraction of CNTs must be first converted to their value in

	$\nu_{CNT} = 11\%$ and $\nu_f = 11\%$	$\nu_{CNT} = 2\%$ and $\nu_f = 41\%$
E_{11} [Kulkarni,2010] /GPa	42.80	83.60
E_{11} /GPa	43.58 (1.82%)	123.58 (47.82%)
E_{22} [Kulkarni,2010] /GPa	17.49	13.93
E_{22} /GPa	13.23 (-24.36%)	9.03 (-35.18%)
ν_{12} [Kulkarni,2010] ν_{12}	0.16 0.30 (87.50%)	0.16 0.29 (81.25%)
G_{12} [Kulkarni,2010] /GPa	7.88	9.36
G_{12} /GPa	6.12 (-22.34%)	5.31 (-43.27%)

Table 3.6: Comparison between the hierarchic model and the numerical values obtained by Kulkarni et al [39].

reference to the volume of epoxy resin, before being inserted in the equations.

Comparing the numerical results attained by Kulkarni et al [39], it is immediately noticed the enormous errors in all predictions by our model. However, this only happens because the hierarchic model is not well fitted to accurately represent the case at hand. In addition to that, the authors themselves make a comment on the unexpected progression of some of the values numerically obtained [39].

First, considering an iso-strain condition in the calculation of the longitudinal Young's modulus, instead of the numerical simulation by Kulkarni et al, we obtain a value of $E_{11} = 38.77$ GPa [39] for the first case and $E_{11} = 125.40$ GPa [39], which, for the second case, is much closer to the values obtained by the hierarchic model, with a relative error of just 1.45%.

Then, the Poisson's ratios obtained by Kulkarni et al [39] give a number much lower than any of the Poisson's ratios of the phases of the composite. This is a very strange behaviour mainly because for the Poisson's ratio, usually, the iso-strain model gives an accurate result.

Finally, Kulkarni et al [39] simulate the material assuming a cohesive phase between the CNTs and the epoxy matrix, which has its own properties different from any other material involved. This additional "material" makes a slight contribute to the overall elastic moduli having a great effect on the transversal Young's modulus and the longitudinal shear modulus, leading to very different values than those obtained by the hierarchic model.

The reference continues the analysis of the numerical model by comparing it to an experiment that measured the transversal Young's modulus of a fibre-reinforced composite with CNTs. Using all the above properties of the CNTs, carbon fibres and epoxy resin and noting that the real composite had volume fractions of $v_{CNT} = 2\%$ and $v_f = 40\%$ [39], the hierarchic model gives the value presented in Table 3.7.

The error compared to the experimental value is much lower than the errors on the numerical values of Table 3.6, meaning that our model, although less complex, gives a better estimate for the value of the transversal Young's modulus.

$E_{22} [Kulkarni,2010]_{exp}$ /GPa	E_{22} /GPa
10.02	8.88 (-11.38%)

Table 3.7: Comparison between the hierarchic model and the experimental value of the transversal Young's modulus obtained by Kulkarni et al [39].

In fact, we may try to adapt the hierarchic model to the particular geometry of this example for a better agreement between our prediction and the experimental value. First, we note that the CNTs sprouting around the carbon fibres may be represented as a bidimensional random distribution of CNT orientations in the transverse plane. As such, we may calculate the final transverse Young's modulus by considering the transverse Young's modulus of the fibre as the new longitudinal Young's modulus of the fibre, in the transverse plane. Finally, by utilizing the Young's modulus of the CNT distribution on the epoxy resin in the transverse plane and the modulus of the fibre in the transverse plane we obtain $E_{22} = 9.79$ GPa as the new value for the transverse Young's modulus of the composite. This new value is much closer to the experimental one, with an error of just -2.30% , because the packing geometry was taken in consideration.

In conclusion, although the reference used resulted in some predictive differences, the considerations taken in the final analysis of the comparison further assures the validity of the hierarchic model and the powerful algorithm it supplies.

3.3.2 Gupta and Harsha (2014)

Gupta and Harsha [40] used a finite element microstructure model to numerically evaluate the longitudinal Young's modulus of a carbon fibre-reinforced composite with CNTs embedded in an epoxy matrix. As in the last example, all the mechanical and geometrical properties were described in the reference.

The diameter of the CNTs is $d_{CNT} = 5.36$ nm, their thickness is $t_{CNT} = 0.68$ nm and the Young's modulus is $E_{CNT} = 1000$ GPa. For the carbon fibres we have a longitudinal Young's modulus of $E_{11f} = 380$ GPa and for the epoxy resin we have $E_m = 6$ GPa. Lastly, it is evident that for the numerical simulation performed by the reference, a hexagonal RVE was used with the fibres and the CNTs aligned and spanning the complete length of the element [40]. For this reason, we will assume an unidirectional distribution of CNTs and that the nanotubes have a high aspect ratio, which means that $l_{CNT} \rightarrow \infty$.

Using the values and assumptions discussed, the hierarchic model gives the results presented in Table 3.8. Like in the previous section, because the hierarchic model encapsulates a sequential mixture of the three phases, the volume fractions indicated in Table 3.8 are relative to the total volume of composite, leading to a need for converting the volume fraction of CNTs to their correct value with respect to the volume of epoxy matrix.

Another note on Table 3.8 is the use of an adimensional form of the longitudinal Young's modulus, E_{11} . The symbol E_0 represents the longitudinal Young's modulus for the case when no CNTs are introduced in the fibre-reinforced composite, for the same fibre volume fraction [40]. Then, the adimensional expression signifies the increase in longitudinal Young's modulus due to the addition of nanotubes, separating the effect from that of the carbon fibres.

$v_{CNT} / \%$	0.5	1.0	1.5	2.0	2.5	3.0	4.0	5.0
$v_f / \%$	59.6	59.9	60.3	60.7	61.1	61.4	62.2	63.0
$E_{11} [Gupta, 2014]$	1.022	1.052	1.080	1.108	1.137	1.162	1.220	1.277
$\frac{E_{11}}{E_0}$	1.010	1.020	1.029	1.040	1.050	1.061	1.082	1.105
	(-1.17%)	(-3.04%)	(-4.72%)	(-6.14%)	(-7.65%)	(-8.69%)	(-11.31%)	(-13.47%)

Table 3.8: Comparison between the hierarchic model and the numerical values obtained by Gupta and Harsha [40].

It can immediately be seen that the hierarchic model gives a fairly good approximation to the values obtained by Gupta and Harsha [40]. Until a CNT concentration of 2%, the error is less than 5%, which coincides with the usual threshold for the beginning of a non linear evolution [31, 38]. Even so, for higher CNT volume fractions the error doesn't grow much beyond acceptable values, indicating that when fibres are present the non linear effects introduced by the CNTs are attenuated.

With this last reference, the validation of the hierarchic model is concluded in all its depth. Although a simple and sometimes crude model, it led to good results in many cases and almost all the errors were explained by means of some particular detail that the hierarchic model could not represent faithfully. Besides this, it can also be the case that the references in question also contain some errors or approximations.

Chapter 4

Tensile tests on CNT-reinforced epoxy resin

The references used in Chapter 3 provided critical information in order to prove the validity and applicability of the hierarchic model to real world examples. However, to further provide evidence for this assertion, some experimental tests were done in order to measure the evolution of the Young's modulus and the Poisson's ratio with the addition of CNTs to an epoxy resin.

As the final nanocomposite will be an isotropic material, this two elastic properties are sufficient to characterize the elastic response of the material to any solicitation, namely the shear modulus. So, a simple experiment that can be performed to measure both of this properties is a tensile test.

Also, one of the main problems encountered when manufacturing the specimens used was achieving a satisfactory dispersion of the nanotubes in the matrix and reducing the number of bubbles in the curing process. In order to analyse the best methodology to approach an homogeneous distribution of CNTs, some specimens were made by different processes.

With this in mind, these experimental results have as an objective to determine the best CNT dispersion method inside the composite and to validate thoroughly the hierarchic model developed in this text. First, the experimental procedure is discussed, as well as the normalizations used in the tensile tests and a brief description of the specimens properties. In the last sections of this chapter, the results obtained in the tests will be presented and discussed. Some of the tensile tests were performed at LEMEC (Laboratório de Ensaios Mecânicos), INEGI and the rest at LET (Laboratório de Ensaios Tecnológicos), FEUP. All the specimens were manufactured at INEGI, by colleagues of UMEC involved in this research project.

4.1 Experimental procedure

This section will describe briefly the experimental procedure of the tensile tests executed on the CNT-reinforced composite specimens. The standard utilized is briefly discussed, mainly its limitations and its validity conditions, followed by a description of the specimens used.

The tensile tests were divided in two types, according to the measurement devices used and both utilized the EN ISO 527 standard [43, 44]. The first one used a clip-on extensometer which measures only the longitudinal displacement, as well as the load applied to the sample material. Although this only permits the computation of the specimen's Young's modulus, the clip-on extensometer can be reused and corrects many problems linked to misalignment of the specimen in the apparatus.

On the other hand, the second pair of tensile tests use a couple of strain gauges, longitudinally and transversally, to measure also the transversal displacement of the sample. This permits the calculation of the Poisson's ratio. However, this method requires a large supply of strain gauges and a greater assembly time than the first one.

There were seven types of specimens tested with the tensile tests. One of them is just the epoxy resin without nanotubes, serving as a reference for the rest of the tests. Four of the other types share the same weight fraction of CNTs, 0.05%, differing only on the degree of dispersion in the epoxy matrix, as well as on the process used to achieve such a dispersion. Some of the dispersion methods involve the use of chemical agents, while others consist of only a physical mechanism for separation of the carbon nanotubes. Finally, the other two types have, respectively, weight fractions of CNTs of 0.1% and 0.2% and were produced using only mechanical dispersion of nanotubes.

4.1.1 Standard EN ISO 527

The tensile tests were performed in six different samples of each kind of specimen. The first four tests used the clip-on extensometer, represented in Figure 4.1a, giving four values for the Young's modulus. The last two tests used strain gauges, shown in Figure 4.1b, which translated in two other values for the Young's modulus and all the results for the Poisson's ratio. For the two last types of specimens, all the tests used the clip-on extensometer, giving only six values for the Young's modulus, as we did not consider that the Poisson's ratio would change significantly.

The standard requires a minimum of five tests for the results to be considered relevant [43], however there were only executed two tests for the Poisson's ratio of each specimen. This might result in this value to not be statistically relevant, due to its variance, however, as we shall see, the value of the Poisson's ratio did not vary much, so we opted to consider only two tests.

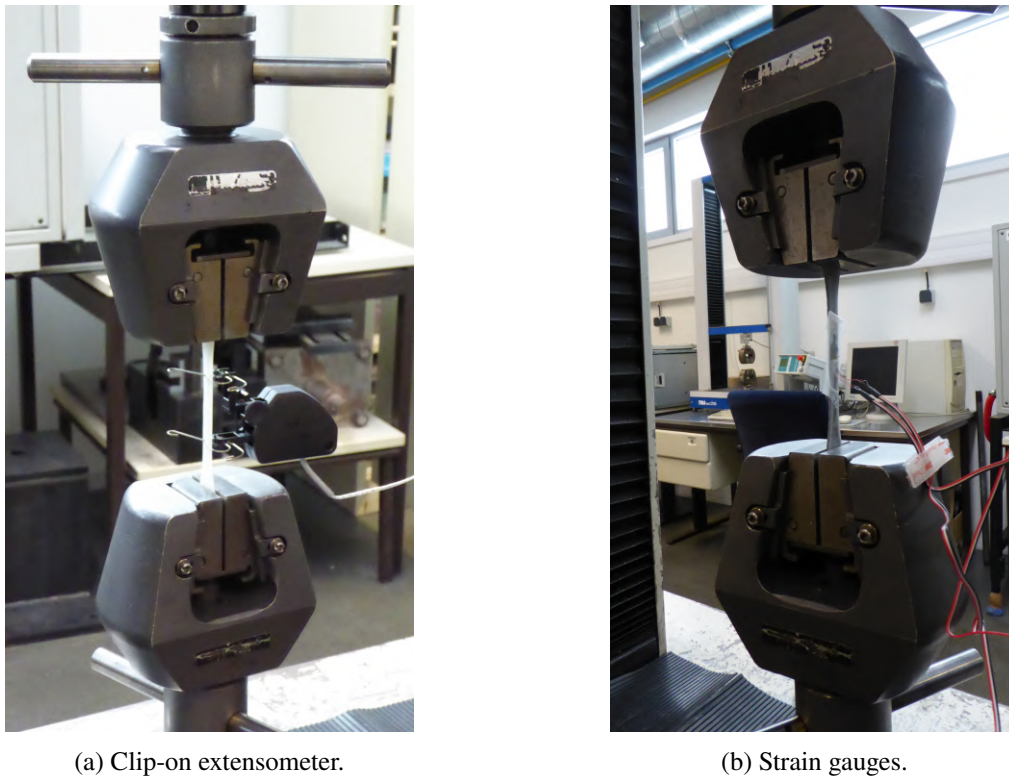


Figure 4.1: The two types of extensometers used in the tensile tests.

The specimens fabricated in the laboratory suffered from a cooling problem that resulted in an exothermal chemical reaction that damaged the material and altered its properties [45]. As such, samples with lower thickness were produced in an attempt to reduce this problem. All the other dimensions were fulfilled, with the said exception of the nominal value of the thickness, which was lowered to 2 mm, instead of the original 4 mm [44]. For the last two types of samples, due to their higher content of CNTs, the curing process was more stable, so specimens with 4 mm of thickness were possible.

Finally, the ISO standard states that the Young's modulus is the ratio of the stress difference between two points, to the corresponding strain difference. These two points are defined by a strain of 0.0005 and of 0.0025 [43]. For the case of the Poisson's ratio, the standard defines it as the ratio of the transversal strain difference between two points, to the corresponding longitudinal strain difference. These points are the same as those for the computation of the Young's modulus. However, if for some reason the interval described is firmly non linear, another interval in the linear region must be used to account for such an irregularity.

The standards also determine that the place where the fracture occurs can invalidate the test. Fractures inside the grip or too much close to it should not be considered in the evaluation of the properties [43], even if no substantial change should be apparent in the elastic moduli, as they are measured in the range



Figure 4.2: A typical fracture on a tensile test.

of small strains. Only one of the tests had a fracture inside the grip, so almost all of them were considered valid, even if the fracture didn't occur on top of the gauge. Figure 4.2 shows a typical fracture on a tensile test, near the gauge.

All the other conditions imposed by the ISO standard [43, 44] were accomplished with success. The specimens used were dumb-bell-shaped of type 1B of the ISO 527 standard [44], for all of the tensile tests.

4.1.2 Test specimens

Before the realization of the tests, the specimens were prepared accordingly and all the necessary dimensions for the computation of the final properties were measured. All the nanocomposites were made using the following materials:

- Epoxy resin SiPreg SR 121 / KTA 315 (Sicomini) [46]
- Single-walled carbon nanotubes SA-ML-2 (NANOSHEL) [47]

These technical data sheets can be found in Appendix A. One of the epoxy resin samples and two of the CNT-reinforced epoxy are presented in Figure 4.3. In the images it is very noticeable the small voids and bubbles that exist near the outer walls of the specimens. Those defects, caused by the air dissolved



Figure 4.3: Examples of the samples used in the tensile tests.

in the resin before the curing process, can change considerably the real sectional area of the samples, therefore inducing an error in the computation of the stresses in the material. Also, the bigger the bubble, the bigger the probability of occurrence of a fracture due to a stress concentration in the nearby zone, leading to a premature failure.

As already mentioned, seven types of specimens were tested, based on their material and CNT dispersion method. The seven samples can be categorized as:

- Epoxy resin
- Epoxy resin + 0.05% CNTs (Normal dispersion)
- Epoxy resin + 0.05% CNTs (Ionic surfactant SDBS)
- Epoxy resin + 0.05% CNTs (Non-ionic surfactant Triton X-100)
- Epoxy resin + 0.05% CNTs (High dispersion)
- Epoxy resin + 0.1% CNTs (High dispersion)
- Epoxy resin + 0.2% CNTs (High dispersion)



Figure 4.4: Different specimen preparation: specimens 1 and 2 to the left for the clip-on extensometer and 5 and 6 to the right with the strain gauges already mounted on 5.

The first one shall function as a reference for the values of Young's modulus and Poisson's ratio. The normal dispersion refers to samples that were mixed in 16 passages in the three roller machine [45], used to prepare the composite before the curing process. The high dispersion specimens were also mixed in the three roller machine, but with a much greater number of passages, in our case 50. Although the only difference between these two methods were the number of passages, purely a physical separation, this tested for the effect on the global dispersion of the sample with increasing mixing.

Finally, there was the possibility of using chemical agents to facilitate the process of CNT dispersion. These chemicals are called surfactants and they act as to oppose the van der Waals forces that tend to aggregate CNTs in bundles [48]. As such, two types of surfactants were used, ionic and non-ionic. Both the specimens that used the surfactants also were subjected to the normal dispersion, isolating the effect that these chemicals had on the CNT dispersion.

Before executing the preparation of the specimens, all of their relevant dimensions were measured with a micrometer. The thickness and the width of the samples were measured in three different points along their length, to account for variability in these variables. The mean value of the measured quantities are presented in Table 4.1.

After the measurements took place, the specimens were prepared for the tensile tests. Specimens 1 and 2 of all the references were just marked for the evaluation of the place where the failure should happen, unlike specimens 5 and 6, on which were mounted the strain gauges. Image 4.4 shows the two different setups needed for each of the standards tensile tests. In the image, one can see a different numbering

Reference	Specimen	w /mm	t /mm
Ref 1 (Epoxy Resin)	1	10.21	2.43
	2	10.15	2.32
	3	10.20	2.17
	4	10.20	1.90
	5	10.20	2.13
	6	10.20	2.63
Ref 2 (0.05 CNT Normal)	1	10.14	1.92
	2	10.13	2.13
	3	10.30	2.57
	4	10.23	2.27
	5	10.15	2.21
	6	10.15	2.11
Ref 3 (0.05 CNT SDBS)	1	10.18	2.58
	2	10.18	2.36
	3	10.10	1.30
	4	10.17	1.73
	5	10.20	2.33
	6	10.19	2.34
Ref 4 (0.05 CNT Triton)	1	10.18	2.35
	2	10.20	2.23
	3	10.20	2.70
	4	10.20	2.27
	5	10.20	2.48
	6	10.19	2.21
Ref 5 (0.05 CNT High)	1	10.20	2.57
	2	10.19	2.55
	3	10.23	2.67
	4	10.23	2.57
	5	10.21	2.63
	6	10.24	2.36
Ref 6 (0.1 CNT High)	1	10.30	4.00
	2	10.40	4.23
	3	10.33	3.50
	4	10.23	4.10
	5	10.27	3.80
	6	10.33	4.37
Ref 7 (0.2 CNT High)	1	10.30	4.23
	2	10.30	4.10
	3	10.23	3.87
	4	10.30	4.20
	5	10.20	4.00
	6	10.27	4.40

Table 4.1: Measured dimensions of the specimens.

for specimens 5 and 6, which was a result of a different numbering scheme used in the beginning of the tensile tests. Due to the confusion that could arise in the analysis of the tensile tests, performed in two different laboratories, the current numbering for such specimens is 5 and 6. Besides this, specimens 3 and 4 of all the references used the same preparation as specimens 1 and 2.

Almost all of the specimens had a small curvature on one of the sides, however, because we used mean values of thickness, the error in considering a rectangular cross section instead of a curved one was neglected in this analysis.

During the tensile tests at LEMEC, INEGI, some of the specimens fractured in invalid locations, such as the grips, and a defective extensometer did not record the strain data of the experiment, leading to a lack of experimental tests for having sufficient statistically valid data. As such, some of the tests, with and without glued extensometers on the specimens, were performed at LET, FEUP, for completion of the minimum required number of tests, according to the ISO standard [43].

For future reference, specimens 1 and 2 of reference 1, specimens 1, 5 and 6 of reference 4 and specimens 1, 2, 5 and 6 of references 2, 3 and 5 were tested at LEMEC, INEGI. All the other tests were performed at LET, FEUP.

4.2 Data analysis and results

With the analysis of the experimental procedure concluded we can proceed to the discussion of the data obtained in the tensile tests. For the computation of the Young's modulus and the Poisson's ratio the definitions for those properties by the ISO [43] standard were used. In this section, the tensile strength of each of the specimens will also be calculated, even if it is not a necessary variable for our analysis. This will further help to confirm the real effect of the CNTs on the nanocomposite.

We will use the ISO standard to calculate the Young's modulus. According to it, the Young's modulus is computed by the following definition [43],

$$E = \frac{\sigma_2 - \sigma_1}{\varepsilon_2 - \varepsilon_1} \quad (4.1)$$

where σ_i refers to the stress on point i of the stress - strain curve and ε_i to the strain on point i . For the ISO standard [43], the points used should be such that they are the closest available to $\varepsilon_1 = 0.0005$ and to $\varepsilon_2 = 0.0025$.

On the other hand, for the Poisson's ratio we must use,

$$\nu = -\frac{\varepsilon_{l_2} - \varepsilon_{l_1}}{\varepsilon_{l_2} - \varepsilon_{l_1}} \quad (4.2)$$

where ε_{l_i} is the transversal strain at point i in the transverse - longitudinal strain curve and ε_{l_i} is the longitudinal strain. As in the previous case, the limits discussed in the ISO standard should be applied to

the longitudinal strain.

Finally, for the tensile strength, according to the ISO standard, it shall be equal to the maximum value of stress measured in each test. The standard also allow for the computation of such properties to be achieved with a linear regression, however we will use equations (4.1) and (4.2) for their simplicity. All the curves representative of the tests can be consulted in the appendixes: the load - displacement curves in Appendix B, the stress - strain curves in Appendix C and the transversal strain - longitudinal strain curves in Appendix D.

4.2.1 Young's modulus

In this section the results obtained in the tensile tests regarding the Young's modulus will be discussed. The Young's modulus calculated in each test, the mean values for each reference and their respective standard deviation is shown in Table 4.2.

First of all, a brief comment on the results obtained in the two different laboratories. All the specimens of references 6 and 7 were tested at LET, while for the other references, the results shown are a mixture of values attained at LEMEC and LET. Besides this, some more tests were performed, but were immediately discarded due to malfunctions in the extensometers or due to fracturing in the grips, as indicated by the ISO standard [43].

Before the analysis of the results, it is noted that the tests executed with strain gauges yielded higher values of the Young's modulus than those that used the clip-on extensometers, consistently. This is an experimental bias that needs to be carefully taken in consideration, however in this preliminary comparison we will not concern ourselves with this question, however, all future tensile tests should use only one of these methods to avoid this unnecessary problem. Also, this bias could be related to an irregular calibration of the transducers, so, in the future, additional care should be given to the experimental preparation.

Also, the tests performed at the LEMEC laboratory yielded higher values for the Young's modulus, when compared with the ones performed at LET. This is another systemic bias that should be accounted for when analysing the results and is, in conjunction with the differences between the extensometers used, the main factor that influenced the high standard deviation of all the values.

It is apparent that all references had a value of the Young's modulus higher than that of the epoxy resin. This fact was expected because the addition of CNTs should increase the stiffness of the material. Besides that, for the high dispersion references, the sixth one gave a number bigger than the fifth, which was also expected due to the higher concentration of CNTs. Because of the great variability of all the results, the decrease in Young's modulus from 0.1% to 0.2% CTN concentration cannot be fully accepted

Reference	Specimen	E /GPa	\bar{E} /GPa	σ_E /GPa
Ref 1 (Epoxy Resin)	1	3.14	2.97	0.56
	2	3.32		
	3	2.81		
	4	2.60		
	5	3.01		
	6	2.94		
Ref 2 (0.05 CNT Normal)	1	3.20	3.30	0.87
	2	3.54		
	3	2.85		
	4	2.85		
	5	3.73		
	6	3.62		
Ref 3 (0.05 CNT SDBS)	1	3.32	3.20	0.95
	2	3.24		
	3	2.59		
	4	2.83		
	5	3.73		
	6	3.51		
Ref 4 (0.05 CNT Triton)	1	3.27	3.20	0.56
	2	2.91		
	3	3.28		
	4	2.87		
	5	3.46		
	6	3.40		
Ref 5 (0.05 CNT High)	1	3.02	3.17	0.83
	2	3.17		
	3	2.89		
	4	2.71		
	5	3.63		
	6	3.57		
Ref 6 (0.1 CNT High)	1	3.01	3.25	0.48
	2	3.60		
	3	3.09		
	4	3.34		
	5	3.31		
	6	3.12		
Ref 7 (0.2 CNT High)	1	3.00	3.18	0.38
	2	3.47		
	3	3.03		
	4	3.19		
	5	3.24		
	6	3.16		

Table 4.2: Young's modulus of the specimens tested.

as true, as the expected behaviour should be an increase in this value, assuming the specimens have a good dispersion of nanotubes in the resin.

Also interesting to note is the fact that the reference that showed a greater increase in the Young's

Reference	E_{exp} /GPa	E_{mCN} /GPa
Ref 5	3.17	3.02 (-4.73%)
Ref 6	3.25	3.07 (-5.54%)
Ref 7	3.18	3.18 (0.00%)

Table 4.3: Comparison between the experimental values of the Young's modulus obtained by the tensile tests and the prediction of the hierarchic model.

modulus, for the same CNT concentration, is the normal dispersion, followed by the ionic and the non-ionic surfactant. It was expected that the greater increase should be on the high dispersion reference or one of the references that received chemical treatment. However, because the standard deviations are so high, it is impossible to safely declare that one of the values is greater than the other one. For further evidence of this evolution more tensile tests needed to be taken, to lessen the variability in the mean values.

Even so, it would be an important discovery to contradict the fact that a greater dispersion of CNTs lead to a higher stiffness of the nanocomposite [11]. In fact, maybe the bundles of CNTs on a poorly dispersed distribution in a matrix act as obstacles to the propagation of displacements, as impurities and different sized atoms do in a crystal lattice, increasing the overall stiffness of the composite.

To verify our experimental results, it is possible to use the hierarchic model developed in subsequent sections to guess what would be the increase in Young's modulus, due to the addition of a certain weight fraction of carbon nanotubes. We will use the experimental Young's modulus of the epoxy resin, instead of the value from the technical data sheet, has to approximate better the experimental results, so $E_m = 2.97$ GPa.

Using the data sheet of the epoxy resin [46], we find a density of $\rho_m = 1176 \text{ kg/m}^3$. Also using the specification certificate of the CNTs [47], we have a length of the CNTs between 8 and 15 μm and a diameter between 1 and 2 nm. Considering the mean values of these quantities, $l_{CNT} = 11.5 \mu\text{m}$ and $d_{CNT} = 1.5 \text{ nm}$. A reasonable value for the Young's modulus of a CNT is $E_{CNT} = 968 \text{ GPa}$ [49].

Finally, we may use a thickness of $t_{CNT} = 0.34 \text{ nm}$ [11] for the CNTs. This gives a density of the CNTs $\rho_{CNT} = 1578 \text{ kg/m}^3$, using the formula elaborated by Thostenson et al [11]. With all the variables defined, the comparison between the experimental values and the prediction achieved with the hierarchic model is presented in Table 4.3.

The values used as the experimental comparisons were those of the high dispersion reference. Besides being the closest value to the theoretical prediction, it also satisfies better the constraints placed by our model, by having the best CNT dispersion amongst all specimens. The very small error further encourages the validity of our hierarchic model and provides another foundation for the acceptance of the experimental

results obtained.

4.2.2 Poisson's ratio

The results of the tensile tests regarding the Poisson's ratio are presented in Table 4.4. Only specimens 5 and 6 of each reference collected data relative to the transversal strain during the test, so they are the only tests capable of computing a value for the Poisson's ratio.

As expected, the variation of the Poisson's ratio was almost non-existent, confirming the constant Poisson's ratio prediction of the hierarchic model. Because this property is heavily dominated by the matrix's properties, it should not vary with CNT concentration or dispersion. For the epoxy resin, we have a value of $\nu_m = 0.35$. Taking the expected value of the Poisson's ratio of the epoxy resin to be 0.35 [50], we have the comparison shown in Table 4.5.

It can be noted that it is exactly the same value, meaning that our experimental results are correct. This also reiterates the validity of the theoretical model used. Because the Poisson's ratio of references 1 to 5 did not vary much, we assumed that the assumption of constant Poisson's ratio with increasing CNT loading was correct and, thus, we did not try to find this value for references 6 and 7.

Reference	Specimen	ν	$\bar{\nu}$	σ_ν
Ref 1 (Epoxy Resin)	5	0.34	0.35	0.02
	6	0.36		
Ref 2 (0.05 CNT Normal)	5	0.33	0.35	0.03
	6	0.36		
Ref 3 (0.05 CNT SDBS)	5	0.37	0.35	0.04
	6	0.32		
Ref 4 (0.05 CNT Triton)	5	0.34	0.35	0.01
	6	0.35		
Ref 5 (0.05 CNT High)	5	0.27	0.31	0.05
	6	0.34		

Table 4.4: Poisson's ratio of the specimens tested.

$\nu_{[Shan,1995]}$	ν_m
0.35	0.35 (0.00%)

Table 4.5: Comparison between the experimental value of the Poisson's ratio obtained by the tensile tests and the expected value of the Poisson's ratio of the epoxy resin [50].

4.2.3 Tensile strength

In Table 4.6, the values for the tensile strength obtained in the tensile tests are shown. Just like the other values obtained in the tensile tests, the tensile strength also showed a great variation, due to the fact that

Reference	Specimen	σ_r /MPa	$\bar{\sigma}_r$ /MPa	σ_{σ_r} /MPa
Ref 1 (Epoxy Resin)	1	58.50	53.05	15.08
	2	50.18		
	3	51.71		
	4	41.48		
	5	58.81		
	6	57.60		
Ref 2 (0.05 CNT Normal)	1	53.08	55.63	12.22
	2	46.57		
	3	62.01		
	4	55.24		
	5	59.90		
	6	56.95		
Ref 3 (0.05 CNT SDBS)	1	68.30	58.85	25.14
	2	70.17		
	3	50.26		
	4	41.99		
	5	56.40		
	6	65.96		
Ref 4 (0.05 CNT Triton)	1	51.41	54.74	12.86
	2	57.98		
	3	60.69		
	4	49.00		
	5	60.83		
	6	48.54		
Ref 5 (0.05 CNT High)	1	56.95	48.51	22.52
	2	49.52		
	3	44.88		
	4	30.22		
	5	52.62		
	6	56.89		
Ref 6 (0.1 CNT High)	1	61.03	63.19	18.08
	2	52.81		
	3	55.97		
	4	74.11		
	5	66.14		
	6	69.07		
Ref 7 (0.2 CNT High)	1	64.48	64.60	8.45
	2	66.43		
	3	65.71		
	4	70.05		
	5	59.28		
	6	61.64		

Table 4.6: Tensile strength of the specimens tested.

the experiments were performed in different laboratories.

The specimens with higher concentrations of CNTs showed some improvement on the tensile strength of the nanocomposite. In fact, this was expected, because the CNTs should increase the tensile strength of the matrix [37]. However, the great variability of the results cannot confirm this fact, as this increase may be due to random fluctuations, which prevent us from confirming it. More tests should be done to reaffirm this or a greater CNT load should be implemented in the specimens to increase the effect on the mechanical properties of the samples.

Although it can also be attributed to random variations, the dispersion method which showed a greater increase in the tensile strength of the specimens was the one that used the SDBS surfactant, for 0.05% CNT weight fraction. Maybe the chemical interaction between the composite and this chemical favoured a microstructure capable of withstanding greater loads, leading to a greater tensile strength.

Chapter 5

A model for damping in CNT nanocomposites

Besides the use of nanotubes to reinforce composites and increase their stiffness, the greatest advantage of using CNT nanocomposites may stand on their promising improvement of the damping characteristics it imparts on a structure. This effect has been studied and it seems to be the greatest claim towards the use of CNTs on multiscale composites [51].

This chapter will introduce a model, based on the works of Bhattacharya et al [52] and Lin and Lu [1], which utilizes a micromechanics approach to analyse the vibration response of a RVE to an external solicitation. The advantage of this theory is that it requires only the elastic moduli of both phases and their concentrations, which have already been studied in previous sections of this text, the amplitude of the imposed vibration and a quantity that characterizes the interfacial bonding strength between the CNT and the resin.

It is also relevant to mention the existence of models that use the stiffness matrices of both phases to predict the damping caused by CNT debonding [3], that exist almost as an extension of the Mori-Tanaka model and Eshelby's equivalent inclusion idea. There are also models that use molecular dynamics [53], where the individual atoms of the nanotube are represented as separate entities and all the van der Waals interactions between them and the matrix and also the covalent bonds between the atoms themselves are included. However, as interesting as they are, we will focus our attention on a model based on a micromechanics vibration analysis of the CNTs on the resin.

5.1 Micromechanics based vibration analysis of CNT-reinforced composites

In this first part of the chapter, the theoretical model that will serve as the foundation for the prediction of the damping ratio of CNT-reinforced composite beams and plates will be discussed in detail. As for the

second part, because many articles use vibrating cantilever beams to experimentally measure the damping introduced by the nanotubes [3, 52, 54–56], the model will be applied to a practical case of a cantilever beam.

Even though our experimental materials involve only the use of SWCNTs, the damping model will be developed for MWCNTs so that it can be as general as possible. As soon as this model is defined, the hierarchic model will also be introduced to accommodate the elastic model used throughout this work.

There are two main approaches that can be used to attain the damping model described in the next sections: energetic methods, used by Bhattacharya et al [52], and nonlinear system analysis, contemplated on the work of Lin and Lu [1]. Because of its simplicity and physical insight provided, the energetic method was chosen as the final damping model used throughout the rest of the text. The nonlinear analysis involved the use of the Describing Function method, which is an extension of the concept of transfer functions for nonlinear systems [1, 57], and resulted in a description of the response of the system that depended on the assumed waveform of the excitation [57]. This method resulted in a more complex set of equations and relied heavily on the use of complex numbers, so the energetic method was preferred.

After the exposition of the theory, some corrections regarding the effect of inherent viscous damping of the matrix and of CNT orientation are presented in Section 5.1.4. Those two factors can account for the remaining offset between the practical cases shown in Chapter 6 and the predictions made by the developed damping model.

5.1.1 Concept of "stick-slip" mechanism

When an external force acts upon a CNT-reinforced composite, its effect is transmitted through the resin to the nanotubes, as it cannot be directly applied to them. As such, there must be a mechanism of load transfer between the matrix and the CNTs. It is widely accepted that because of their small size and the fact that they are hollow, the ratio between their surface area to their mass, also called the specific surface area, is extremely large [3, 53]. This fact implies that the major means of load transfer cannot be by normal stresses on the extremities of the CNT, but instead by interfacial shear stresses around the outer wall of the nanotube [54]. Also, its high aspect ratio and cylindrical geometry promote the load transfer through the outer wall.

It is easy to picture that this type of interfacial load transfer also occurs between successive walls on the inside of a MWCNT. In fact, it is possible to consider a MWCNT as just a bundle of SWCNTs concentric to one another, with increasing diameter [1, 11]. The only force that keeps the different layers of a MWCNT together is the van der Waals force, which is very weak compared to the covalent bonds between carbon atoms in the cylindrical configuration of carbon nanotubes [1, 11, 53]. Then, it is possible to conceive that the load transfer worsens as it goes through the inner walls of a MWCNT and,

in reality, it has been proven that the outer wall of a MWCNT carries almost the entire load transfer of the nanotube/matrix interface [11, 58]. Because of this experimental fact, we will consider that a MWCNT can be modelled by just two concentric SWCNTs, where the outermost one represents the SWCNT that supports almost all the load and the innermost one represents the inner SWCNTs, which do not contribute that much to the overall load transfer capacity of the MWCNT.

As mentioned before, the van der Waals forces are the only effect responsible for the cohesion of a MWCNT and the bonding between itself and the resin surrounding it [53]. However, because these forces are relatively weak, if a sufficiently high load is applied to the interface, these bonds may break, resulting in the debonding between the MWCNT and the matrix or the "sword and sheath" telescoping failure of the MWCNT, which occurs when the SWCNTs inside of the MWCNT start sliding with respect to one another, in analogy to the extension of a telescope [2]. The established criteria for the occurrence of the failures mentioned are called the critical shear stresses. When the shear stress reaches the critical shear stress for a particular interface, there is no more capacity to accommodate further load transfers, so the interface fails and sliding between the phases occurs [1, 52, 53].

Obviously, because, at the molecular level, the critical shear stress of an interface is a result of the complex interactions between atoms of both phases, this value will depend heavily on the interface in question. It has been noticed, that the critical shear stress between SWCNTs inside a MWCNT is lower than that between the outer wall of a MWCNT and epoxy resin [52]. This infers that as a growing force is applied to a MWCNT nanocomposite, first the inner SWCNTs of the MWCNTs start sliding with respect to each other, as a result of not being able to transfer the excessive load amongst themselves, followed by the debonding of the outer SWCNT of the MWCNT from the matrix [52, 59]. After this point, the remaining load is supported only by the matrix, reducing the effective stiffness of the composite.

Figure 5.1 shows a step by step evolution of the progressive failure of the bonding between the different walls of the phases in a nanocomposite. The light grey object represents the inner SWCNTs of the MWCNT, the dark grey object represents the outer wall of the MWCNT and, finally, the white rectangle represents the matrix of the composite. As such, τ_1 refers to the shear stress between the inner walls of the MWCNT, τ_2 refers to the shear stress between the outer wall of the MWCNT and the resin, caused by the external applied force, and τ_{cr1} and τ_{cr2} refer to the critical shear stresses of each interface, respectively. It is possible to express the fact that the critical shear stress for CNT/matrix debonding is higher than that for failure of the bonding between the internal SWCNTs of a MWCNT by a simple equation [52],

$$\tau_{cr1} < \tau_{cr2} \quad (5.1)$$

Many values have been proposed for both critical shear stresses, however, because it is such a difficult property to measure, there exists a consensus only on an interval of possible values. Bhattacharya et

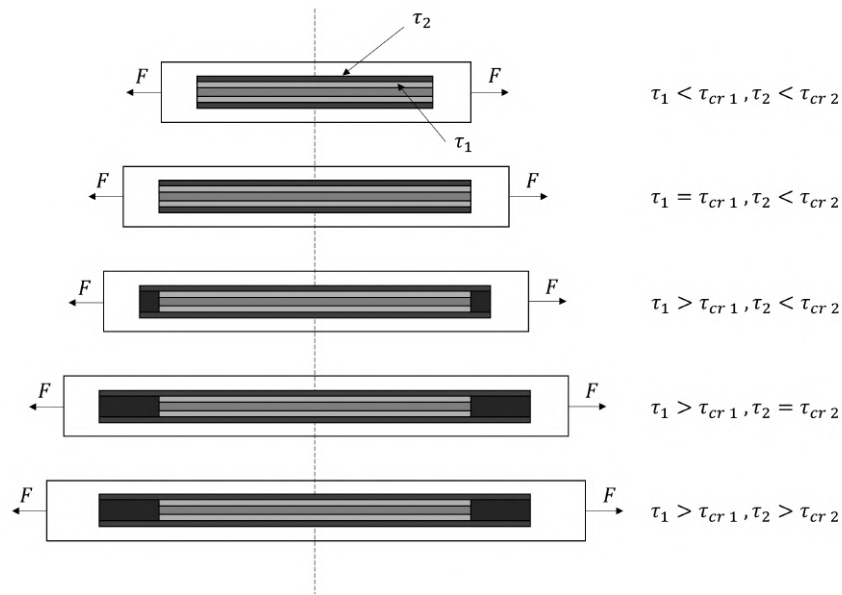


Figure 5.1: Stages of failure of the bonding between the inner layers of a MWCNT and the outer wall and the matrix of a nanocomposite.

al [52] proposed a value of 0.3 MPa for the critical shear stress between SWCNTs and of 1 MPa for the critical shear stress between CNTs and epoxy resin. Zhou et al [3] used a value of 0.2 MPa for the critical shear stress between CNTs and epoxy resin, however it has been reported in pullout simulations and experiments that the critical shear stress could reach values of 75 MPa [60].

If instead of an increasing static load, an alternating force is applied to the matrix, as in the study of vibrations, the response of the system will depend on the strength of this solicitation. However, if the load is high enough, debonding may occur and the phenomenon known as "stick-slip" will take place. In fact, let us describe briefly what happens to the system as a vibration is induced in the matrix. First, as the load increases, the steps described in Figure 5.1 will occur in order, hence promoting a "slip" behaviour on the individual phases of the composite, in reference to one another. Then, after the force reaches its maximum, it starts to decrease, releasing the accumulated elastic energy present in the system, as the individual parts stay "stuck" to one another, because the plastic deformation induced by the previous slippage is not undone. Finally, after the load turns direction and starts increasing in the opposite orientation, the slippage between different parts is promoted again and so on, hence the name "stick-slip".

Before describing the model used to analyse the dynamic response of the nanocomposite, we must determine the system that will be subjected to that analysis. As such, we will use a RVE as described in Figure 5.2. As usual, the white prism represents the matrix of the composite, the light grey hollow

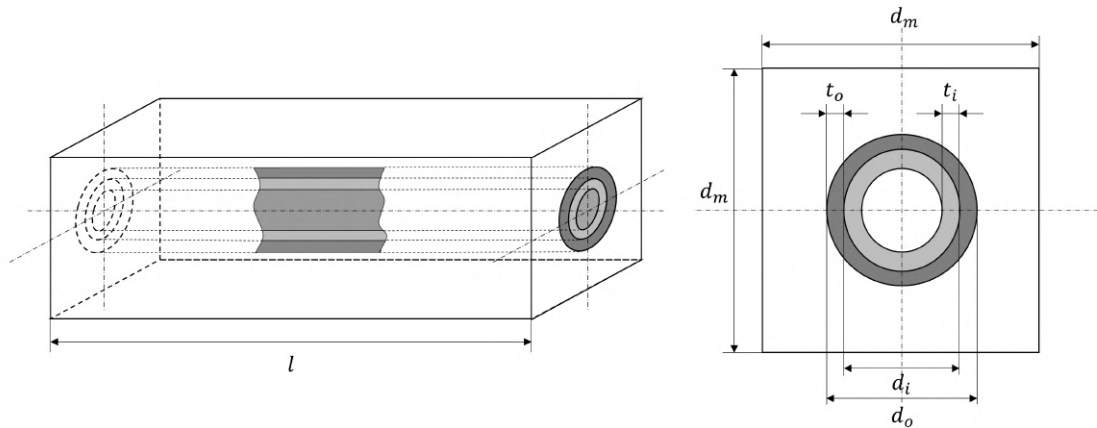


Figure 5.2: Representative volume element of the dynamic analysis subjected to an alternating external load.

cylinder represents the inner SWCNTs of the MWCNT and the dark grey one the outermost SWCNT. The MWCNT will be studied as an equivalent DWCNT, where the outer tube has the same properties as the outer SWCNT of the original MWCNT and the inner tube as the rest of the SWCNTs of the MWCNT. In the representation, d_m is the length of the square cross section of the matrix, d_o and d_i are the diameters of the outer nanotube and the inner one, respectively, t_o and t_i are the thickness of the outer nanotube and the inner one, respectively, and l is the length of the RVE, whereas for an aligned distribution of nanotubes, it is the same as the length of the CNT, l_{CNT} [1, 52].

Then, it can be easily seen in the RVE that a simple model that simulates the behaviour of such a system can be the one represented in Figure 5.3. In this micromechanical-based model, the resin, the outer nanotube and the inner one are represented as separate masses, bonded together by coulombic friction [59]. This friction force is a representation of the shear stress that transfers the load from the matrix to the inner SWCNT. As all the components have a stiffness associated, these are represented as springs, clamped on one of the sides. Throughout the rest of the presentation of the model, we will assume that the external load on the resin F acts only in the axial direction and that the RVE is fixed on one of its sides.

In analogy to the explanation of the "stick-slip" mechanism in previous paragraphs, let us first study the evolution of the system to an increasing static force and only then will we analyse a dynamic one. On a static analysis the masses of the objects involved are unimportant, however we need to establish the

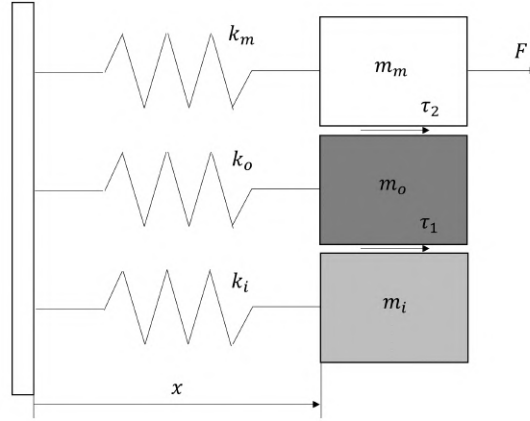


Figure 5.3: Micromechanical-based dynamical model of the representative volume element of the nanocomposite.

equivalent axial stiffness of each component. It is known that for a linear material the axial stiffness is given by [61],

$$k = \frac{EA}{l} \quad (5.2)$$

where k is the axial stiffness, E is the Young's modulus, A is the cross sectional area and l is the length. Then, using equation (5.2) we may derive the stiffness of each component as,

$$k_i = \frac{E_{CNT} A_i}{l} = \frac{\pi E_{CNT}}{4l} (d_i^2 - (d_i - 2t_i)^2) \quad (5.3)$$

which simplifies to a somewhat familiar result,

$$k_i = \frac{\pi(d_i - t_i)t_i E_{CNT}}{l} \quad (5.4)$$

where E_{CNT} is the Young's modulus of the carbon nanotube. For the outer nanotube the resulting equation is completely analogous,

$$k_o = \frac{\pi(d_o - t_o)t_o E_{CNT}}{l} \quad (5.5)$$

For the stiffness of the matrix, the process is a little more complex, as the cross sectional area depends on the volume concentration of CNTs present in the composite. Let us first relate the volume concentration

of CNTs with the length of the square cross sectional area of the resin,

$$v_{CNT} = \frac{V_{CNT}}{V_{CNT} + V_m} = \frac{\frac{\pi}{4}d_o^2 l}{d_m^2 l} \quad (5.6)$$

which simplifies to,

$$d_m^2 = \frac{\pi d_o^2}{4v_{CNT}} \quad (5.7)$$

where v_{CNT} is the volume fraction of CNTs in the composite. Finally, we are in a position to derive the stiffness of the matrix,

$$k_m = \frac{E_m A_m}{l} = \frac{E_m}{l} \left(d_m^2 - \frac{\pi}{4} d_o^2 \right) \quad (5.8)$$

that can be ultimately reduced to,

$$k_m = \frac{\pi d_o^2 E_m}{4l} \left(\frac{1}{v_{CNT}} - 1 \right) \quad (5.9)$$

where E_m is the Young's modulus of the matrix.

Now that all the components' stiffnesses are determined, we may advance for the analysis of the static problem described. As the force increases, all the springs act in opposition to the solicitation, deforming the system by a certain amount to balance the load. However, if the shear stress in the internal DWCNT interface reaches the critical value, no more load can be transferred to the inner nanotube, rendering the sliding of the outer tube and the resin over the inner one. After some time, the same phenomenon happens to the outer interface, leaving the matrix as the only load supporter. The forces at which the critical shear stresses are reached shall be called the critical loads. As it is described in [62], the relationship between a force and the stresses it sustains is given by,

$$\tau = \frac{F}{A} \quad (5.10)$$

where τ is the shear stress, F is the applied force and A is the surface area where the stresses are applied. With this in mind, both critical loads can be calculated by [52],

$$F_1 = \pi d_i l \tau_1 \quad (5.11)$$

$$F_2 = \pi d_o l \tau_2 \quad (5.12)$$

where F_1 and F_2 are the critical forces of each interface, respectively, and τ_1 and τ_2 are the critical shear stresses (from now onwards, we will drop the subscript *cr*).

The fact that we can determine a critical force for interfacial debonding and that we know the stiffness of each phase, allow us to compute a critical displacement where debonding occurs. This critical displacement can be used to separate the deformations before and after interfacial debonding. Before the internal debonding of the inner layers of the CNT, all the phases contribute to the overall stiffness of the composite so [52],

$$\delta_1 = \frac{F_1}{k_m + k_o + k_i} \quad (5.13)$$

and because we know the relationship between the inner and outer nanotube diameter,

$$d_i = d_o - 2t_o \quad (5.14)$$

this allows us to arrive at the final expression,

$$\delta_1 = \frac{4v_{CNT} d_i l^2 \tau_1}{d_o^2 E_m (1 - v_{CNT}) + 4v_{CNT} [d_o - (t_o + t_i)] (t_o + t_i) E_{CNT}} \quad (5.15)$$

where δ_1 is the critical displacement for the inner interface debonding. As the load continues to increase, the composite stiffness is only mediated by those of the matrix and the outer SWCNT, so the second critical displacement is given by,

$$\delta_2 = \frac{F_2 - F_1}{k_m + k_o} + \delta_1 \quad (5.16)$$

where it simplifies to,

$$\delta_2 = \frac{4v_{CNT} l^2 (d_o \tau_2 - d_i \tau_1)}{d_o^2 E_m (1 - v_{CNT}) + 4v_{CNT} (d_o - t_o) t_o E_{CNT}} + \delta_1 \quad (5.17)$$

and δ_2 represent the critical displacement for debonding between the matrix and the CNT.

Finally, we must perform the dynamical analysis to study the behaviour of the system when an alternating axial load is applied to the resin. When analysing vibrating systems, inertial effects should not be neglected unless the analysis uses very small frequencies of excitation. However, the mass of the CNTs are very small when compared to the mass of the matrix that contains them and, as our work utilizes mass fractions of CNTs on the order of 1%, we shall neglect all inertial effects that are caused by m_o or m_i . This consideration implies that the mass of the CNTs will not have an effect on the natural modes and frequencies of vibration of the nanocomposite, which seems a reasonable approximation.

There are three possible situations that must be accounted separately [52] the amplitude of vibration of the matrix is smaller than the critical displacement for both types of debonding; the amplitude of vibration is greater than the critical displacement for the internal debonding of the CNT, but lesser than that for CNT/matrix debonding; the amplitude of vibration is greater than any of the critical displacements. The

force-displacement behaviour of the composite in all of these situations is represented in Figure 5.4, where X represents the amplitude of the imposed vibration.

It is immediately noticed that the system is nonlinear, because it contains hysteresis, although it is stepwise linear. As such, we must solve a problem that revolves around hysteretic damping, also called structural damping. So, before we continue to determine the damping model based on the mechanisms of CNT debonding, we will discuss briefly hysteretic damping in a simple single DOF system.

5.1.2 Hysteretic damping in SDOF systems

When analysing vibrating systems, we usually assume that a viscous damper is in action, as well as a spring. For a SDOF system, such as a single mass excited by a force, the equation of motion is [61, 63],

$$m\ddot{x}(t) + c\dot{x}(t) + kx(t) = f(t) \quad (5.18)$$

where m is the mass of the system, c is the damping coefficient of the viscous dashpot, k is the stiffness of the spring, $f(t)$ is the external force applied on the system and $x(t)$ and its derivatives are, respectively, the displacement, velocity and acceleration of the system. Obviously, we can also represent the equation of motion based on modal parameters, such as the natural frequency of vibration and the damping ratio

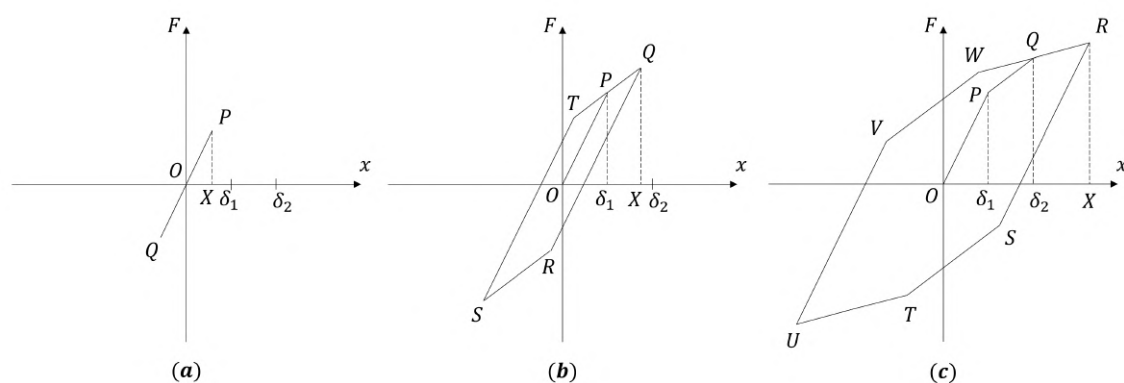


Figure 5.4: Force-displacement behaviour of the composite for $X \leq \delta_1$ (a), for $\delta_1 < X \leq \delta_2$ (b) and for $X > \delta_2$ (c).

[61, 63],

$$\omega_n = \sqrt{\frac{k}{m}} \quad (5.19)$$

$$\xi = \frac{c}{2m\omega_n} \quad (5.20)$$

with ω_n as the natural frequency of vibration and ξ as the damping ratio. Using equations (5.19) and (5.20), we may write the equation of motion of the system in the form [61],

$$\ddot{x}(t) + 2\xi\omega_n\dot{x}(t) + \omega_n^2x(t) = f(t) \quad (5.21)$$

To solve the previous equation, for a sinusoidal excitation, it is possible to use complex numbers to represent the solution in a very simple form. The excitation will be considered of the form, $f(t) = Fe^{j\omega t}$, and the response as well, $x(t) = Xe^{j\omega t}$. With this solution in mind, we can also determine the velocity and acceleration as $\dot{x}(t) = j\omega Xe^{j\omega t}$ and $\ddot{x}(t) = -\omega^2Xe^{j\omega t}$, respectively. So, substituting these results into equation (5.21) and rearranging [61, 63],

$$1 - \left(\frac{\omega}{\omega_n}\right)^2 + j\left(\frac{2\xi\omega}{\omega_n}\right) = \frac{F}{X} \quad (5.22)$$

where F is the amplitude of the excitation load, X is the amplitude of the displacement response and j is the imaginary unit. It can be readily seen, that the imaginary part of the left member of equation (5.22), pertaining to the damping of the system, has a linear dependence with the frequency of the excitation. It is evident that the effect of hysteretic damping on the system cannot depend on the frequency of the excitation, because the same energy is dissipated in each cycle.

Then, to account for this frequency-independence of the energy dissipated by the damping mechanism, there exists an elegant and simple way to modify the previous equations. To that avail, let us consider a viscous dashpot which has a variable damping coefficient, such that it is inversely proportional to the frequency of excitation [63],

$$c(\omega) = \frac{d}{\omega} \quad (5.23)$$

where d is called the hysteretic damping coefficient and is directly proportional to the dissipated energy per cycle of vibration. Then, substituting this relation on the equation of motion for viscous damping, it is possible to obtain the equation of motion for structural damping [63],

$$m\ddot{x}(t) + \frac{d}{\omega}\dot{x}(t) + kx(t) = f(t) \quad (5.24)$$

and if we assume the same sinusoidal excitation and, consequently, the same sinusoidal response, we attain an equation akin to (5.22) but for hysteretic damping [63],

$$1 - \left(\frac{\omega}{\omega_n}\right)^2 + j\left(\frac{d}{k}\right) = \frac{F}{X} \quad (5.25)$$

where the imaginary part of the left member of the previous equation is independent of the frequency, as desired.

The constant factor that appears on the imaginary factor is called the loss factor η , so it is apparent that [63],

$$\eta = \frac{d}{k} \quad (5.26)$$

but, as the hysteretic damping factor is proportional to the dissipated energy per cycle and the stiffness is proportional to the maximum elastic energy stored in the system, the loss factor may be determined by a more physical meaningful way [52],

$$\eta = \frac{W}{2\pi U} \quad (5.27)$$

where W is the energy dissipated in each cycle and, for the case of hysteretic damping, can be calculated by the area inside the force-displacement diagram of the system and U is the maximum elastic energy stored in the system.

It may be apparent in equations (5.22) and (5.25) that there exists a simple relationship between the damping ratio and the loss factor, which is [63],

$$\eta = \frac{2\xi\omega}{\omega_n} \quad (5.28)$$

and for frequencies close to that of the resonance we may simply assume that $\eta = 2\xi$. This relationship will be important in latter parts of this text, because it is much more frequent to measure the damping ratio than the loss factor in experimental assemblies.

5.1.3 Energy dissipation and loss factor

For the analysis of a hysteretic damping mechanic, it was discussed in the previous section that the best quantity to describe the grade of damping is the loss factor. For that reason, we will now turn to the determination of the loss factor for the "stick-slip" mechanism studied before. As the three cases, mentioned early, have three different force-displacement diagrams, as can be seen in Figure 5.4, they will have different dissipated energies per cycle and also different maximum elastic energies stored. For that reason, we will separate this analysis for each of those cases.

Case 1: $X \leq \delta_1$

When the amplitude of vibration is sufficiently small, the forces involved are not enough to cause any debonding effect on any interface [1, 52]. Because of this, the composite will behave according to Hooke's Law and hysteresis will not be present (see Figure 5.4a):

$$\text{OP: } F(x) = (k_m + k_o + k_i)x \quad (5.29)$$

$$\text{PQ: } F(x) = (k_m + k_o + k_i)x \quad (5.30)$$

Without the presence of hysteresis in the force-displacement diagram, the dissipated energy will be null and, as a consequence, the system will not manifest any damping, leading to $\eta = 0$.

Case 2: $\delta_1 < X \leq \delta_2$

Increasing the amplitude of vibration may trigger the interfacial debonding between inner SWCNTs of the MWCNT and, as such, damping is introduced in the system. Let us first describe analytically the force-displacement diagram of Figure 5.4b [52]:

$$\text{OP: } F(x) = (k_m + k_o + k_i)x \quad (5.31)$$

$$\text{PQ: } F(x) = (k_m + k_o)x + k_i\delta_1 \quad (5.32)$$

$$\text{QR: } F(x) = (k_m + k_o + k_i)x - k_i(X - \delta_1) \quad (5.33)$$

$$\text{RS: } F(x) = (k_m + k_o)x - k_i\delta_1 \quad (5.34)$$

$$\text{ST: } F(x) = (k_m + k_o + k_i)x + k_i(X - \delta_1) \quad (5.35)$$

$$\text{TQ: } F(x) = (k_m + k_o)x + k_i\delta_1 \quad (5.36)$$

Then, to evaluate the energy dissipated per cycle of oscillation, we need to integrate the area inside the force-displacement diagram. As the curve displayed is symmetric about the origin O, we may compute the integral with only two of the piecewise functions and then multiply by two. Let us choose TQ and QR as half the evolution to calculate the integral. We know that the horizontal coordinates of those points are,

$$\text{T: } x = 2\delta_1 - X \quad (5.37)$$

$$\text{Q: } x = X \quad (5.38)$$

$$\text{R: } x = X - 2\delta_1 \quad (5.39)$$

so, the energy dissipated per cycle is given by,

$$W = 2 \int_{2\delta_1 - X}^X (k_m + k_o)x + k_i\delta_1 dx + 2 \int_X^{X - 2\delta_1} (k_m + k_o + k_i)x - k_i(X - \delta_1) dx \quad (5.40)$$

which simplifies to,

$$W = 4k_i(X - \delta_1)\delta_1 \quad (5.41)$$

We may compute the maximum elastic energy stored using the maximum elongation of the phases when a static displacement X is applied to the matrix. This formulation does not need the use of integrals and is much more direct. It can be noted that because of the debonding, the matrix and the outer SWCNT have a elongation equal to the imposed displacement, however the inner nanotubes only elongated by the same amount as the critical displacement for their debonding. Because of this, the maximum elastic energy stored is [52],

$$U = \frac{1}{2}(k_m + k_o)X^2 + \frac{1}{2}k_i\delta_1^2 \quad (5.42)$$

Finally, we can determine the loss factor that is introduced by the debonding of the inner nanotubes, using equation (5.27), as,

$$\eta = \frac{4k_i(X - \delta_1)\delta_1}{\pi(k_m + k_o)X^2 + \pi k_i\delta_1^2} \quad (5.43)$$

Case 3: $X > \delta_2$

For amplitudes greater than the required critical displacement for the interfacial debonding between the CNT and the resin, there is even more damping introduced, as all the individual parts slide past each other during a cycle of vibration. For the force-displacement diagram presented in Figure 5.4c, the equations of all the stepwise functions are [52]:

$$\text{OP: } F(x) = (k_m + k_o + k_i)x \quad (5.44)$$

$$\text{PQ: } F(x) = (k_m + k_o)x + k_i\delta_1 \quad (5.45)$$

$$\text{QR: } F(x) = k_mx + k_i\delta_1 + k_o\delta_2 \quad (5.46)$$

$$\text{RS: } F(x) = (k_m + k_o + k_i)x - k_i(X - \delta_1) - k_o(X - \delta_2) \quad (5.47)$$

$$\text{ST: } F(x) = (k_m + k_o)x - k_i\delta_1 - k_o(X - \delta_2) \quad (5.48)$$

$$\text{TU: } F(x) = k_mx - k_i\delta_1 - k_o\delta_2 \quad (5.49)$$

$$\text{UV: } F(x) = (k_m + k_o + k_i)x + k_i(X - \delta_1) + k_o(X - \delta_2) \quad (5.50)$$

$$\text{VW: } F(x) = (k_m + k_o)x + k_i\delta_1 + k_o(X - \delta_2) \quad (5.51)$$

$$\text{WR: } F(x) = k_mx + k_i\delta_1 + k_o\delta_2 \quad (5.52)$$

Let us perform exactly the same analysis as in the previous case, where we choose, in this case, three of the piecewise functions to perform the integration and then multiply by two to have the total area of the hysteresis. We choose the VW, WR and RS to perform the integrals, which means we need to establish the coordinates of the points,

$$\text{V: } x = 2\delta_1 - X \quad (5.53)$$

$$\text{W: } x = 2\delta_2 - X \quad (5.54)$$

$$\text{R: } x = X \quad (5.55)$$

$$\text{S: } x = X - 2\delta_1 \quad (5.56)$$

this results in the following integral for the energy dissipated per cycle,

$$W = 2 \int_{2\delta_1 - X}^{2\delta_2 - X} (k_m + k_o)x + k_i\delta_1 + k_o(X - \delta_2) dx + 2 \int_{2\delta_2 - X}^X k_mx + k_i\delta_1 + k_o\delta_2 dx + 2 \int_X^{X - 2\delta_1} (k_m + k_o + k_i)x - k_i(X - \delta_1) - k_o(X - \delta_2) dx \quad (5.57)$$

that, in its simpler form, reduces to,

$$W = 4k_i(X - \delta_1)\delta_1 + 4k_o(X - \delta_2)\delta_2 \quad (5.58)$$

In the same way as before, let us compute the maximum elastic energy stored in the system by noting how it responds to a static displacement applied on the matrix. Just as before, and noting that the second

interface as already debonded as well, we have [52],

$$U = \frac{1}{2}k_m X^2 + \frac{1}{2}k_i \delta_1^2 + \frac{1}{2}k_o \delta_2^2 \quad (5.59)$$

and for the loss factor of this last case, using again equation (5.27), we get,

$$\eta = \frac{4k_i(X - \delta_1)\delta_1 + 4k_o(X - \delta_2)\delta_2}{\pi k_m X^2 + \pi k_i \delta_1^2 + \pi k_o \delta_2^2} \quad (5.60)$$

With this last equation, the loss factor associated with the "stick-slip" mechanism for energy dissipation is completely determined, for any amplitude of vibration. It is interesting to note the similarities between equations (5.43) and (5.60): there seems to be a term on the numerator of the type $4k(X - \delta)\delta$ for all of the debonding interfaces present in the system. Also, if we rearrange the denominator of both equations such that,

$$\eta = \frac{4k_i(X - \delta_1)\delta_1}{\pi(k_m + k_o + k_i)X^2 - \pi k_i(X^2 - \delta_1^2)} \quad (5.61)$$

$$\eta = \frac{4k_i(X - \delta_1)\delta_1 + 4k_o(X - \delta_2)\delta_2}{\pi(k_m + k_o + k_i)X^2 - \pi k_i(X^2 - \delta_1^2) - \pi k_o(X^2 - \delta_2^2)} \quad (5.62)$$

it is evident that for each debonding that occurred, the maximum elastic energy stored, if debonding had not happened, is decreased by a factor of $\frac{1}{2}k(X^2 - \delta^2)$.

Although the loss factor is completely determined by now, it is only defined as a piecewise function of the amplitude of vibration, which is not a very elegant way to describe the system. Besides this, we noted in the previous paragraph that the new terms that appear on the expression of the loss factor always contains a subtraction between the amplitude and the correspondent critical displacement, $(X - \delta)$ or $(X^2 - \delta^2)$. With this in mind, if a certain interface had been affected by debonding, their correspondent terms in the equation of the loss factor will be positive, because X must be higher than δ for debonding to occur. On the other hand, if debonding has not occurred, the corresponding terms will be negative, however they will not appear in the final form of the loss factor, because their physical contribution to the damping is null.

It is apparent that only positive terms can appear in the loss factor expression, so we will use an important mathematical property to nullify those terms when they are negative. If we take the square root of those terms, if they are positive, they stay positive real numbers, but if they are negative, they will became pure imaginary numbers. Then, by taking the real part of the term and squaring off the result, we obtain the original number if it was positive, because it was a pure real number and we squared the square root, or we get zero if it was negative, because the real part of a pure imaginary number is zero.

To conclude this analysis, it is obvious that an expression for the loss factor of the system that is valid for any amplitude of vibration is,

$$\eta = \frac{\left[\Re \left(\sqrt{4k_i(X - \delta_1)\delta_1} \right) \right]^2 + \left[\Re \left(\sqrt{4k_o(X - \delta_2)\delta_2} \right) \right]^2}{\pi(k_m + k_o + k_i)X^2 - \left[\Re \left(\sqrt{\pi k_i(X^2 - \delta_1^2)} \right) \right]^2 - \left[\Re \left(\sqrt{\pi k_o(X^2 - \delta_2^2)} \right) \right]^2} \quad (5.63)$$

or if a cleaner equation is desired,

$$\eta = \frac{4k_i\delta_1C_1 + 4k_o\delta_2C_2}{\pi(k_m + k_o + k_i)X^2 - \pi k_i(X + \delta_1)C_1 - \pi k_o(X + \delta_2)C_2} \quad (5.64)$$

where C_1 and C_2 represent the length that the parts involved in a debonded interface have slipped past one another, from 0 to ∞ , and can be calculated by,

$$C_1 = \left[\Re \left(\sqrt{X - \delta_1} \right) \right]^2 \quad (5.65)$$

$$C_2 = \left[\Re \left(\sqrt{X - \delta_2} \right) \right]^2 \quad (5.66)$$

With these last equations the model for CNT debonding induced damping is complete, for the case of aligned nanotubes excited by an alternating load in the direction of alignment. Of course, to account for other types of geometry or other types of damping mechanisms, some corrections must be made to this model.

5.1.4 Effect of the material viscous damping and CNT orientation

Until now, all the work done regarding the establishment of a model for damping in CNT nanocomposites only focused on the friction between interfaces where debonding has occurred. Although an important contribution, the damping introduced by the "stick-slip" mechanism cannot account for all of the damping measured on experiments. The inherent viscous damping of the polymer matrix also contributes effectively to the overall damping experienced by the composite [1].

It was proposed first by Gu et al [64] that the overall loss factor of a composite, η_{comp} , has two components,

$$\eta_{comp} = \eta_{mat} + \eta_I \quad (5.67)$$

a contribution from the interfacial interactions between the phases, η_I , and another from the material damping of each phase, η_{mat} [3, 52]. The contribution from interfacial interactions is exactly the loss factor we have determined from the "stick-slip" mechanism, for the case of a CNT nanocomposite. As for the viscous material damping, it is normally derived through strain energy methods applied to composites

[3]. However, as a rigorous stress/strain analysis of the composite is not possible, we will assume that the law of mixtures is valid and so, the material viscous damping is just the weighted average, by the volume fractions, of the viscous damping of the matrix and the CNTs [3].

Finally, neglecting the viscous contribution to damping inherent to the nanotubes, we may define the overall loss factor of the composite as [3, 52],

$$\eta_{mCN} = \eta_m(1 - v_{CNT}) + \eta_I \quad (5.68)$$

where η_{mCN} is the loss factor of the CNT nanocomposite and η_m is the loss factor of the matrix due to viscous damping mechanisms.

Another problem that arises from the initial assumptions of our model is the necessity of an aligned distribution of CNTs inside the resin. This requirement often does not hold true in practical examples, so there is a need to find a correction that incorporates the dependence on CNT orientation on our model.

During the discussion about models for the equivalent elastic properties of multiscale composites in Chapter 2, it was noticed that some corrections to the Halpin-Tsai equation, regarding the orientation of the nanotubes, can be achieved through multiplication by an orientation factor, α [31, 38]. Then, it was also discussed that, for a tridimensional random distribution of nanotube orientations, the best fit for the value of the orientation factor was $\frac{1}{6}$ [31, 38]. So, to account for the reduced stiffness of the composite, because of the random orientation of the CNTs it contains, in the damping model we will multiply the Young's modulus of the CNTs by $\frac{1}{6}$ [31].

Besides this, if the nanotubes are oriented in a random fashion, instead of the considered axially aligned distribution, the imposed displacements caused by a vibration will not, in general, be aligned with the direction of the axis of the RVE used in the dynamic analysis. To account for this effect, Bhattacharya et al [52] proposed the use of the orientation factor on the length of the RVE, giving,

$$l = \frac{1}{6}l_{CNT} \quad (5.69)$$

and this was proven to be a statistically accepted value [38]. Both of these corrections together let us describe more complex situations, such as a nanocomposite with a random distribution of CNT orientations excited by a unidirectional alternating load.

5.1.5 Compatibility with the hierarchic model and the inclusion of fibres

One of the assumptions required when we derived the damping model in previous sections was that the dynamical model of the RVE was the one depicted in Figure 5.3. In this description of the composite, all the parts are separate masses that have separate springs attached to them and it is readily seen that the

stiffnesses associated with each one can be summed up to give the global stiffness of the nanocomposite. This fact collides with the established model for the equivalent elastic properties of a composite, because it is more akin to the rule of mixtures, than to the Halpin-Tsai equations.

To account for these discrepancies we need to modify the way that the stiffness at each moment is computed. Instead of summing the contribution from each phase before debonding occurs, let us think of the stiffness as a global quantity. First, for very low amplitudes, the stiffness of the composite can be calculated by the hierarchic model as we normally would. After debonding has occurred between the inner nanotubes of the MWCNT, only the outer SWCNT will contribute to the stiffness, so we may calculate the equivalent stiffness of the composite by the hierarchic model, substituting the initial MWCNT by this new equivalent SWCNT. Finally, for larger amplitudes of oscillation, all of the nanotube debonds from the resin, leaving the matrix to act as the only contribution to the nanocomposite's stiffness.

If we think of the stiffness of the composite as a global quantity, like we just described in the previous paragraph, the inclusion of the hierarchic model is a natural extension to the established damping model. Even the addition of fibres, resulting in a multiscale composite, becomes trivial, by the use of the hierarchic model to calculate the three stiffnesses at each stage of the evolution of debonding.

As noted before, in the first stage, where debonding has not occurred yet, the composite acts as a MWCNT/fibre/polymer matrix multiscale composite, so the equivalent Young's modulus, E_{11} , is calculated normally through the use of equations (2.34) to (2.36) and (2.53). We will admit that the alternating load acts along the longitudinal direction of the fibres and, if not, we may also compute E_{22} and G_{12} and use a transformation of coordinates to account for this factor.

For the second stage, the only contribution the MWCNTs provide to the stiffness is through its outermost nanotube, so it is possible to model the nanocomposite as a SWCNT/fibre/polymer matrix mixture, where the SWCNT has the same diameter as the original MWCNT, but a thickness of only, $t_{SW} = 0.34$ nm. With this little alteration, we will still calculate the equivalent Young's modulus, E_{11SW} , by using exactly the same equations as before, with, however, the new thickness of the nanotube, t_{SW} .

Finally, in the last stage of the "stick-slip" mechanism, the CNTs are all debonded from the matrix, so we have an effective fibre/polymer matrix composite and we may calculate the equivalent Young's modulus, E_{11mf} , as if the nanotubes do not exist. For this, we may consider $w_{CNT} = 0\%$ in the hierarchic model and use only equation (2.53), the rule of mixtures, with the Young's modulus of the matrix, instead of the CNT/polymer matrix composite's.

With the diverse equivalent Young's modulus computed with the hierarchic model, we may advance

for the determination of the stiffness of each stage. As the CNTs are always converted to a full cylinder "effective fibre" by the hierarchic model, both the first and second stiffnesses will act upon the full square cross section of the RVE, whereas, the third one will only act on the area outside of the CNT. Because of this, we may define the three stiffnesses as,

$$k_{mf\ CN} = \frac{\pi d_{CNT}^2 E_{11}}{4v_{CNT}l} \quad (5.70)$$

$$k_{mf\ SW} = \frac{\pi d_{CNT}^2 E_{11SW}}{4v_{CNT}l} \quad (5.71)$$

$$k_{mf} = \frac{\pi d_{CNT}^2 E_{11mf}}{4l} \left(\frac{1}{v_{CNT}} - 1 \right) \quad (5.72)$$

$k_{mf\ CN}$ is the equivalent stiffness of the first stage, $k_{mf\ SW}$ is the equivalent stiffness of the second stage and k_{mf} is the equivalent stiffness of the final stage of the "stick-slip" mechanism.

The redefinition of each stiffness is the major modification needed to adapt the existing model to the already in use, hierarchic stiffness model. However, for the sake of completeness and consistency of notation, all the other equations of the model will be adapted below, but without their derivation, because it is very similar to those done in Sections 5.1.1 and 5.1.3.

In this new notation, the critical loads and the critical displacements will be described as,

$$F_1 = \pi(d_{CNT} - 2t_{SW})l\tau_1 \quad (5.73)$$

$$F_2 = \pi d_{CNT}l\tau_2 \quad (5.74)$$

$$\delta_1 = \frac{F_1}{k_{mf\ CN}} \quad (5.75)$$

$$\delta_2 = \frac{F_2 - F_1}{k_{mf\ SW}} + \delta_1 \quad (5.76)$$

and, consequently, the energy dissipated per cycle and the maximum elastic energy stored are,

$$W = 4(k_{mf\ CN} - k_{mf\ SW})\delta_1 C_1 + 4(k_{mf\ SW} - k_{mf})\delta_2 C_2 \quad (5.77)$$

$$U = \frac{1}{2}k_{mf\ CN}X^2 - \frac{1}{2}(k_{mf\ CN} - k_{mf\ SW})(X + \delta_1)C_1 - \frac{1}{2}(k_{mf\ SW} - k_{mf})(X + \delta_2)C_2 \quad (5.78)$$

with C_1 and C_2 still defined by equations (5.65) and (5.66).

Just as in the previous model, we obtain the loss factor by its definition, equation (5.27), which gives the final expression,

$$\eta = \frac{4(k_{mf\,CN} - k_{mf\,SW})\delta_1 C_1 + 4(k_{mf\,SW} - k_{mf})\delta_2 C_2}{\pi k_{mf\,CN} X^2 - \pi(k_{mf\,CN} - k_{mf\,SW})(X + \delta_1)C_1 - \pi(k_{mf\,SW} - k_{mf})(X + \delta_2)C_2} \quad (5.79)$$

and with this last equation, we have a perfectly defined damping model, compatible with the hierarchic model in use to predict the equivalent elastic properties of the multiscale composite.

It is obvious that one of the corrections made in Section 5.1.4 is not needed any more, as the stiffness is corrected automatically for random CNT orientation distributions by the hierarchic model. However, we still need to take into account the reduction of the length of the RVE made by equation (5.69). Besides that, the material viscous damping will now include also the effect of the fibres, which we can add to the loss factor of the viscous damping of the resin to reduce to a simple equation, analogous to (5.68),

$$\eta_{mf\,CN} = \eta_{mf}(1 - \nu_{CNT}) + \eta_I \quad (5.80)$$

where $\eta_{mf\,CN}$ is the loss factor of the CNT/fibre/polymer matrix composite, η_{mf} is the loss factor due to viscous damping in the matrix and the fibres and η_I is the loss factor due to interfacial interactions, now given by equation (5.79). Throughout the rest of this text, this last model will be referred as the damping model for CNT/fibre/polymer matrix multiscale composites.

Although we derived a general model for all types of CNTs, this text focus, specially, on the influence of SWCNTs on the characteristics of multiscale composites. As such, we may at any time reduce the general model to a simplified version capable of representing SWCNTs inside a polymer matrix. First, we notice that the biggest difference between the damping mechanism in MWCNTs against SWCNTs is that, in the latter, debonding between inner nanotubes does not occur, because there is only one. As such, to simplify the general model to account for the effect of SWCNTs we need only to nullify the first critical shear stress τ_1 , as this type of debonding never happens.

5.2 Damping model for a composite cantilever beam

We will continue our discussion of theoretical models for describing the damping behaviour of CNT nanocomposites by applying the aforementioned model to a practical example. In fact, to validate the damping modal established in previous sections we wish to compare the theoretical predictions it provides to the experimental data collected in several works. However, usually the damping tests are made on a CNT composite beam, so, before advancing to the validation, we need a theory capable of predicting the

damping ratio of an oscillating cantilever beam made of the nanocomposite in question.

Our current model depends heavily on the amplitude of the imposed vibration, so, as the beam possess a different oscillation at any point, we expect a variation from point to point of the loss factor, unlike the damping model already derived. This additional complexity requires an understanding of the dynamics of beams, in particular of the natural modes of vibration when one side is cantilevered and the other is free. For that reason, we will discuss briefly the modes of oscillation of Euler-Bernoulli beams.

After the dynamics of the cantilever beam are reviewed, the current damping model will be applied and the global loss factor of the beam will be derived, to provide us with a means to compare the theoretical predictions to the experimental results. At last, some of the peculiarities of the cantilever beam damping model are described, to gain a better understanding of the dependences involved in the computation of the loss factor.

5.2.1 Modes of vibration of Euler-Bernoulli beams

When a beam is vibrating, there is a transversal displacement that varies in time and with its position along the beam. This displacement causes the appearance of internal normal stresses and strains along the longitudinal axis of the beam, that, if high enough, start the debonding mechanism extensively studied in the previous discussion of the damping model. Because of this, the main goal of this analysis of the modes of vibration of beams is to obtain the maximum deformation field as a function of position along the beam.

Because the loss factor is dependent on the amplitude of vibration, as the beam loses energy by damping, its amplitude of movement will decrease, hence its global loss factor will also decrease with time. However, we will consider only the loss factor at the initial moment when the beam starts to oscillate.

For a Euler-Bernoulli beam, the general equation of motion can be expressed as [61],

$$\frac{\partial^2}{\partial x^2} \left(EI(x) \frac{\partial^2 v(x,t)}{\partial x^2} \right) + \rho S(x) \frac{\partial^2 v(x,t)}{\partial t^2} = f(x,t) \quad (5.81)$$

however, for a free vibration of a constant cross sectional beam, as shown in Figure 5.5, we may write the equation of motion as [1, 61],

$$E_{11} I \frac{\partial^4 v(x,t)}{\partial x^4} + \rho S \frac{\partial^2 v(x,t)}{\partial t^2} = 0 \quad (5.82)$$

where E_{11} is the Young's modulus of the composite, I is the second moment of the cross sectional area, ρ is the density of the composite, S is the area of the cross section and $v(x,t)$ is the transversal displacement, as a function of position and time, caused by the vibration of the beam.

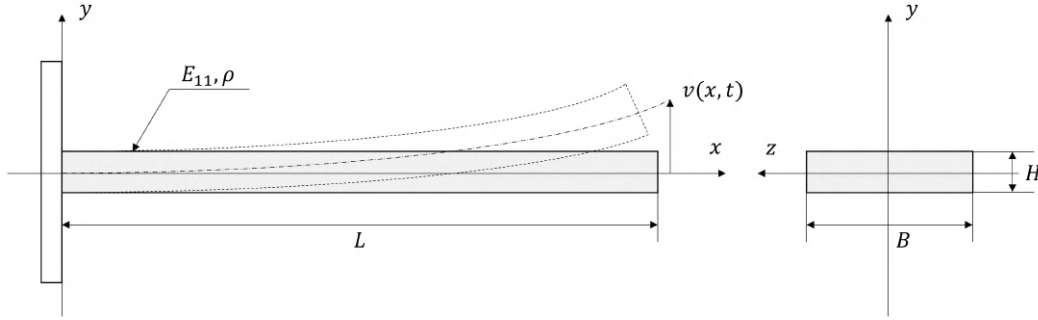


Figure 5.5: Representation of the geometry of a cantilever beam.

As vibrating beams have been extensively studied in the past, we will not present a rigorous derivation of the following equations, however for a detailed explanation it is possible to consult the work by Rodrigues [61]. For a rectangular cross section, the area and the second moment of the area can be computed by [62],

$$S = HB \quad (5.83)$$

$$I = \frac{H^3 B}{12} \quad (5.84)$$

where H is the height of the beam in the direction of oscillation and B is the width of the beam in the direction transverse to the plane of oscillation.

Then, solving the partial differential equation of motion by the method of separable variables, we obtain the characteristic problem [61],

$$E_{11} I \frac{d^4 V(x)}{dx^4} = \omega_n^2 \rho S V(x) \quad (5.85)$$

being ω_n the natural frequency of vibration and $V(x)$ the function representing the variation of amplitudes of vibration along the beam, because [61],

$$v(x, t) = V(x) [C \cos(\omega t) + D \sin(\omega t)] \quad (5.86)$$

where C and D are constants depending on the initial conditions of the motion.

Finally, we may solve equation (5.85) by determining ω_n and $V(x)$, which gives [61],

$$\omega_n = \lambda^2 \sqrt{\frac{E_{11} I}{\rho S}} = \lambda^2 \sqrt{\frac{E_{11}}{12 \rho}} H \quad (5.87)$$

$$V(x) = A_1 \cosh(\lambda x) + A_2 \sinh(\lambda x) + A_3 \cos(\lambda x) + A_4 \sin(\lambda x) \quad (5.88)$$

where λ is a parameter that depends on the boundary conditions of the beam and A_1 , A_2 , A_3 and A_4 are constants that must satisfy the boundary conditions as well. For a clamped-free beam, such as our case, the parameter λ is defined by the following transcendental equation [1, 61],

$$\cosh(\lambda L) \cos(\lambda L) + 1 = 0 \quad (5.89)$$

being L the length of the beam in the longitudinal direction. Every solution of the equation (5.89) results in a different value for λ , which in turn gives a different natural frequency of oscillation and a different shape for the amplitude function. Each solution is, thus, called a mode of vibration of the beam [61].

Knowing the equality from the last equation and the specific boundary conditions of the beam, $V(0) = 0$, $\frac{dV}{dx}\big|_{x=0} = 0$, $V(L) = A$ and $\frac{d^2V}{dx^2}\big|_{x=L} = 0$, we can simplify equation (5.88) to give [1, 61],

$$V_i(x) = \frac{A}{2} \left[\cosh(\lambda_i x) - \cos(\lambda_i x) - \frac{\sinh(\lambda_i L) - \sin(\lambda_i L)}{\cosh(\lambda_i L) + \cos(\lambda_i L)} (\sinh(\lambda_i x) - \sin(\lambda_i x)) \right] \quad (5.90)$$

where we used A , the tip amplitude displacement of the free side of the beam, as the normalization constant for the shape of the mode and i indicates the mode of vibration.

Finally, having attained an expression for the transversal amplitude displacement of vibration as a function of the position along the beam, we can proceed to the derivation of the normal deformation field that exists in the beam.

The transversal displacement the beam undertakes when vibrating is caused by a bending moment that acts along all its length. The bending moment can be related to the transversal displacement by the following expression [62],

$$\frac{d^2v(x,t)}{dx^2} = \frac{M(x,t)}{E_{11}I} \quad (5.91)$$

where $M(x,t)$ represent the bending moment acting on the beam at each point x and for each time t . It is also possible to use continuum mechanics to relate the normal stress developed in the beam to the bending moment that produced it by [62],

$$\sigma_{xx}(x,y,t) = -\frac{M(x,t)y}{I} \quad (5.92)$$

where $\sigma_{xx}(x,y,t)$ is the normal stress along the longitudinal direction developed at a certain point (x,y) of the beam and at some time t . By using Hooke's law, we can join equations (5.91) and (5.92) to obtain

the relation between the deformation field and the transversal displacement so [1, 62],

$$\varepsilon_{xx}(x, y, t) = -y \frac{d^2 v(x, t)}{dx^2} \quad (5.93)$$

being $\varepsilon_{xx}(x, y, t)$ the normal deformation field along the direction of the axis of the beam. Obviously, as this is a dynamic problem, the deformation field is dependent on the time passed from the initial instant. To simplify this dependence, let us focus on the maximum deformation field, corresponding to the time where all points are at their maximum displacement. Explicitly for our case, the maximum deformation field for a certain mode of vibration i is [1],

$$\varepsilon_{xxi}^{max}(x, y) = -y \frac{\lambda_i^2 A}{2} \left[\cosh(\lambda_i x) + \cos(\lambda_i x) - \frac{\sinh(\lambda_i L) - \sin(\lambda_i L)}{\cosh(\lambda_i L) + \cos(\lambda_i L)} (\sinh(\lambda_i x) + \sin(\lambda_i x)) \right] \quad (5.94)$$

With the maximum deformation field completely described for every mode of vibration, it is possible to implement the damping model at each point and integrate for the entirety of the volume of the beam to attain a global loss factor, also for each mode of the system.

5.2.2 "Stick-slip" damping model applied to beams

The application of the damping model to the case of a cantilever beam is very simple, provided the maximum deformation field at any point. First, we should note that the longitudinal amplitude of vibration, X , required by the damping model, varies from point to point in a beam and is directly related to the normal deformation.

As such, noting that we need the longitudinal deformation of the RVE, that amplitude of vibration is given by,

$$X_i(x, y) = |\varepsilon_{xxi}^{max}(x, y)|l \quad (5.95)$$

where $X_i(x, y)$ is the amplitude of vibration for the i th mode of oscillation of the beam and for point (x, y) and l is the length of the RVE.

All the coefficients of stiffness, the critical loads and the critical displacements are independent of the amplitude of vibration, so these variables will not change for a beam, being calculated by the same equations developed in Section 5.1.5. Therefore, the only parameters that are still missing for the computation of the loss factor are the dissipated energy per cycle and the maximum elastic energy stored, however they will vary from point to point, just as the amplitude of oscillation.

For the energy dissipated per cycle and the maximum elastic energy stored we arrive at the following fields,

$$W_i(x, y) = 4(k_{mf\ CN} - k_{mf\ SW})\delta_1 C_{1i}(x, y) + 4(k_{mf\ CN} - k_{mf\ SW})\delta_2 C_{2i}(x, y) \quad (5.96)$$

$$C_{1i}(x, y) = \left[\Re \left(\sqrt{X_i(x, y) - \delta_1} \right) \right]^2 \quad (5.97)$$

$$C_{2i}(x, y) = \left[\Re \left(\sqrt{X_i(x, y) - \delta_2} \right) \right]^2 \quad (5.98)$$

$$U_i(x, y) = \frac{1}{2}k_{mf\ CN} [X_i(x, y)]^2 - \frac{1}{2}(k_{mf\ CN} - k_{mf\ SW})(X_i(x, y) + \delta_1)C_{1i}(x, y) - \frac{1}{2}(k_{mf\ SW} - k_{mf})(X_i(x, y) + \delta_2)C_{2i}(x, y) \quad (5.99)$$

where $W_i(x, y)$ is the dissipated energy per cycle for a certain mode of vibration i and a point (x, y) and $U_i(x, y)$ is defined in the same way, but is the maximum elastic energy stored.

Now, we could compute the loss factor at each point [1], using its definition, however as the energies can be summed up to account for the global energetic balance of the beam, we will prefer to compute first the total energy dissipated per cycle and the total maximum elastic energy stored, before calculating the global loss factor.

Then, let us compute a volume integral of those quantities through all the volume of the beam and find the total energy quantities,

$$\bar{W}_i = \frac{1}{V} \iiint_V W_i(x, y) dV = \frac{2}{LH} \int_0^L \int_0^{\frac{H}{2}} W_i(x, y) dy dx \quad (5.100)$$

$$\bar{U}_i = \frac{1}{V} \iiint_V U_i(x, y) dV = \frac{2}{LH} \int_0^L \int_0^{\frac{H}{2}} U_i(x, y) dy dx \quad (5.101)$$

where \bar{W}_i is the total dissipated energy per cycle, \bar{U}_i is the total maximum elastic energy stored and V is the volume of the beam, $V = LBH$. Finally, the global loss factor of the beam is computed by,

$$\eta_i = \frac{\bar{W}_i}{2\pi\bar{U}_i} \quad (5.102)$$

with η_i being the global loss factor of the i th mode of vibration. These last couple of equations involve complicated integrals that may even not have an analytical solution, so all the equations were solved

numerically for the comparisons made in subsequent chapters.

Often, in vibration analysis, the fundamental mode has a major contribution on the complex motion of a vibrating system, being the greatest concern in structural design [1]. Besides this, in particular to the study of vibrating cantilever beams, we have established the previous equations having in mind that the excitation was achieved by imposing a displacement on the free tip of the beam, which implies a transversal displacement very similar to that of the fundamental mode of the beam. Therefore, it does not seem a bad approximation to reduce our study to the loss factor of the fundamental mode, substituting $i = 1$ in all of the equations. Because of this, from now on, unless especially specified, if the variables do not appear with a subscript it is because they are relative to the fundamental mode of oscillation of the system.

In accordance with the last paragraph, for a clamped-free beam, the parameter λ for the fundamental mode is given by,

$$\lambda = \frac{1.8751}{L} \quad (5.103)$$

being L the length of the beam. This leaves the model completely defined and functional to be applied on a numerical software.

In this last section of this chapter we will produce a numerical analysis of the model to gain some insights on its dependence with some of the most relevant parameters. It is almost certainly not possible to obtain an analytical form of the loss factor of the beam, so this may be the only way to understand the mathematical formulation, behind all the equations.

5.2.3 Brief analysis of the cantilever beam damping model

The damping model established in this chapter results in the loss factor being a convoluted mathematical function of many variables. Amongst them are the initial magnitude of vibration, the mechanical properties of the composite and, in the case of the cantilever beam, the dimensions of the beam. Instead of studying, independently, all the possible dependencies of the loss factor in each variable, let us group them in three separate groups to facilitate the analysis of the function.

First of all, we have the characteristics of the imposed free vibration, which involve some kind of displacement amplitude at a point. In the case of the beam, we developed the model based on an imposed amplitude at the free tip. Furthermore, the geometric properties of the beam also fit this group, as the only influence they have is on the shape of the modes of vibration, resulting in a different distribution of amplitudes and, consequently, in a different deformation field at any point.

Then, we have the mechanical properties of the composite, which are directly related to the type and quantity of fibres and CNTs, as these phases influence heavily the global stiffness and damping of the composite. Finally, the last group will consist in the defining properties for the occurrence of debonding, namely the critical shear stresses.

To access the dependence of the loss factor on each of these groups we will choose some of the most important properties from each and graph their evolution. All the graphics will be representations of the loss factor as a function of the amplitude of vibration, because it is a property that varies much from case to case, therefore it profits from being represented as the dependent variable. Besides this, the influence of the weight fraction of the nanotubes and the volume fraction of fibres must be plotted separately, to see how the concentration of CNTs and the global stiffness of the multiscale composite affect the damping. At last, the dependence with the critical shear stresses will also be graphed, to understand the implications of bonding strength between the phases. All the other properties will be defined beforehand.

For the mechanical properties of the epoxy and the nanotubes we will use the values taken from Bhattacharya et al [52], so we have for the epoxy resin, $E_m = 3.3$ GPa and $\rho_m = 1200$ kg/m³, and for the MWCNTs, $E_{CNT} = 650$ GPa, $l_{CNT} = 4.5$ μ m, $d_{CNT} = 12$ nm and $t_{CNT} = 2$ nm, which give an effective density of, according to equation (2.6), $\rho_{CNT} = 1167$ kg/m³. The properties of the carbon fibres will be given by Khan et al [56], so, $E_{11f} = 234$ GPa and $\rho_f = 1800$ kg/m³. Finally, the geometric properties of the beam will be chosen as $L = 100$ mm and $H = 2$ mm, because those seem reasonable values.

Then, by plotting the loss factor as a function of tip displacement amplitude of the imposed vibration, for different weight fractions of CNTs, we obtain the graphic from Figure 5.6a, where we considered $v_f = 0\%$, $\tau_1 = 0.3$ MPa and $\tau_2 = 1$ MPa, based on the debonding properties used by Bhattacharya et al [52]. It can be noted, that the loss factor starts as zero, before debonding as occurred, and as soon as the critical threshold is crossed, it has an accentuated increase with increasing amplitude of vibration. Then, it reaches a maximum and starts to decrease, because the increase in dissipated energy caused by an increase in the amplitude of vibration is surpassed by the increase in the maximum elastic energy stored, thus reducing their ratio, which is the loss factor.

As far as the concentration of CNTs is concerned, an increase in its weight fraction results in an increase of the loss factor, which was easy to predict, because there are more CNTs to debond and dissipate energy. The weight fraction also increases the critical displacement for debonding, because in a stiffer material it is more difficult to start the "stick-slip" mechanism, as noted by the later start of the curve for higher concentrations of nanotubes.

Another feature of the curves shown in Figure 5.6a is that they are smooth with the appearance of only a single maximum. This contrasts with the functions described in Figure 5.6b, which represent the

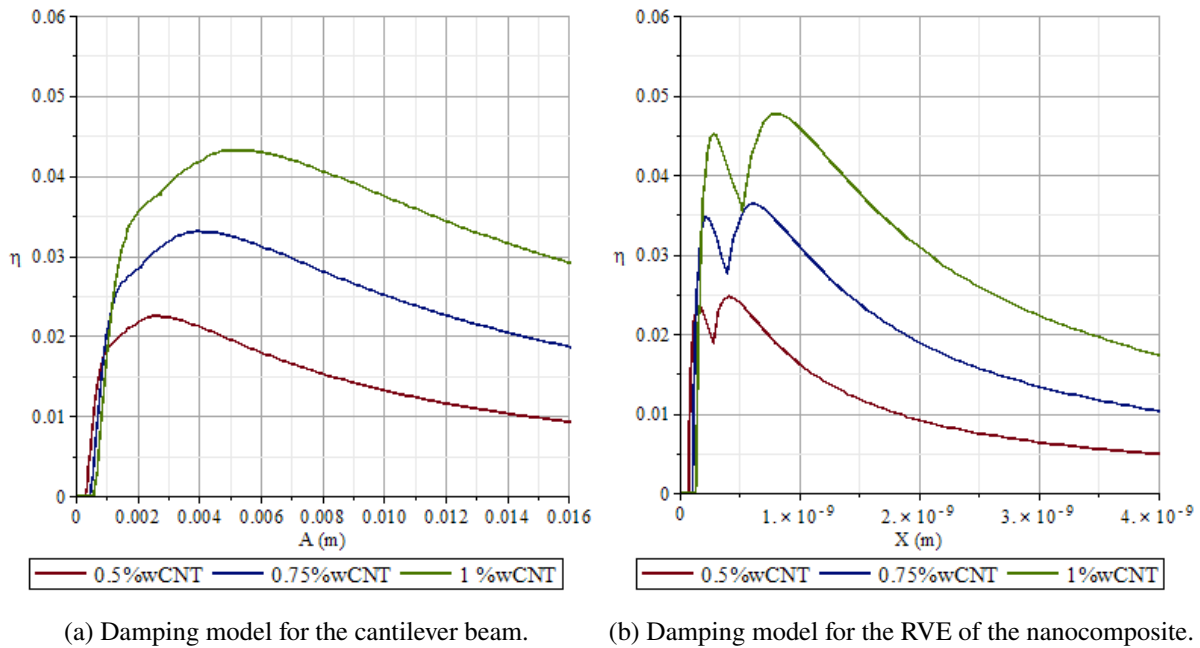


Figure 5.6: Loss factor as a function of the amplitude of vibration for different weight fractions of CNT.

loss factor when calculated for the composite excited axially in the direction of the RVEs, using the model from Section 5.1.5. In fact, it should be expected, since we have two different critical displacements for debonding, that the loss factor would have two maxima, corresponding to each different type of debonding, between the inner parts of the MWCNT and between the MWCNT and the matrix. However, since the loss factor presented in the left figure corresponds to the global loss factor of the beam, even if each point, throughout the beam, obeys to a function closer to that of the right figure, the volume average of all points of the beam should make the final relation more smooth, as shown in Figure 5.6a.

In Figure 5.7a and 5.7b we present the loss factor of the beam as a function of the tip displacement for different volume fractions of fibres and different critical shear stresses, respectively. For both plots, the concentration of CNTs was $w_{CNT} = 0.5\%$. It is evident, from the left plot, that an increase in the concentration of fibres, which translates to an increase in the equivalent stiffness of the composite, results in an overall decrease of the loss factor of the beam and also a decrease of the critical displacement necessary for the mechanism of debonding to take place.

This behaviour was expected since an increase in stiffness leads to a decrease in the displacement needed to achieve the same load. Also, because the reaching of the critical load is the reason for debonding between phases to occur and, since these loads are achieved with smaller amplitudes of vibration, the length of sliding between the debonded parts is severely reduced, which translates to a reduced loss factor.

It is also evident that even a small concentration of fibres reduces heavily the loss factor of the

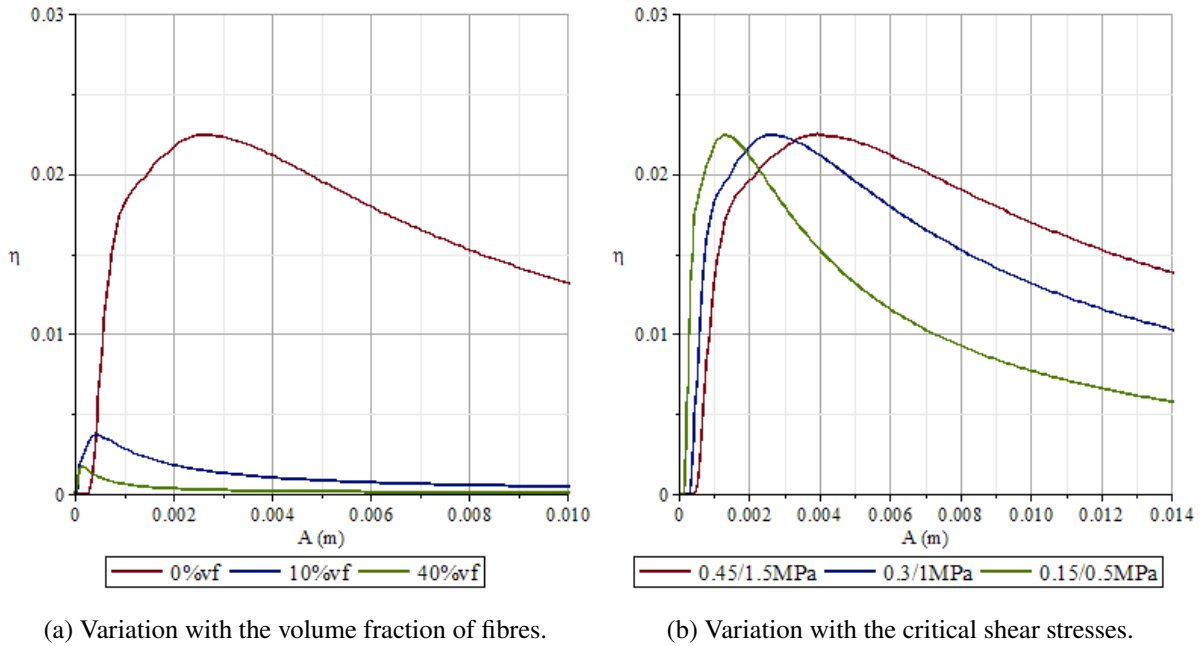


Figure 5.7: Loss factor as a function of the amplitude of vibration for different parameters of the cantilever beam.

material, since it usually increases considerably the stiffness of the composite. As most multiscale CNT-reinforced composites have a volume fraction of fibres between 40% and 60% [39, 40, 55, 56], it seems that for most such composites, the loss factor will be very small, in comparison to only CNT-reinforced polymers.

Finally, on the right graphic, the effect of altering the critical shear stresses, the criteria for debonding, is apparent. To access the influence from both critical stresses, the same proportion between them was maintained such that $\frac{\tau_1}{\tau_2} = 0.3$. It is visible that they did not influence the maximum loss factor that can be achieved, however the shape of the curves was strongly modified. For lower critical shear stresses, debonding occurs earlier and the peak of the loss factor function is more narrow and also appears for lower amplitudes of vibration.

With this final analysis of the loss factor as a function of many of the relevant variables, we close off the detailed presentation of the damping model used to predict the loss factor of CNT/fibre/polymer matrix multiscale composites.

Chapter 6

Validation of the damping model

After the description of the hierarchic model for the equivalent elastic properties of composites, a numerical and experimental validation was performed with the aid of results from many articles. Likewise, to verify the validity of the damping model established in a previous part of this text, some articles with experimental and numerical results are presented throughout this chapter [3, 52–56].

In the first part of the chapter we will discuss some numerical and experimental results obtained for CNT nanocomposites, without the inclusion of fibres. As stated previously, almost all of the articles regard experimental damping ratios of the free vibration of a cantilever beam, so we will focus on the study of our damping model applied to beams. Besides this, one of the works [53] provide numerical results for the damping model applied to the usual RVE excited axially, which gives a great opportunity to test the fundamental model of the "stick-slip" mechanism.

Lastly, we will delve into articles that include the effect of the usage of fibres in the nanocomposite. We expect a great decrease in the loss factor with this addition, as studied in Section 5.2.3. All these comparisons will give a base for the acceptance of the theoretical model used to describe the damping associated with CNT debonding.

6.1 Prediction of damping on CNT/polymer matrix composites

This first section will concern itself with the comparison between our model and experimental assemblies that measured the damping ratio of systems made of CNT nanocomposites. Whenever the values used are not defined, we will try to adjust the missing ones to the experimental results or we will use another source to obtain them.

Instead of plotting the variation of the loss factor with the amplitude of vibration, many works graph it against a quantity called the structural deformation [3], in cantilever beam systems. So, before advancing

we should define this new variable and show how to compute it. Usually, the structural deformation is the average maximum surface strain of the beam, when subject to a certain displacement [3]. As such, it can be given by the integral of the deformation field over one of surfaces,

$$\varepsilon_i = \frac{1}{S} \iint_S \left| \varepsilon_{xxi}^{max} \left(x, \frac{H}{2} \right) \right| dS = \frac{1}{L} \int_0^L \left| \varepsilon_{xxi}^{max} \left(x, \frac{H}{2} \right) \right| dx \quad (6.1)$$

where ε_i is the structural deformation for the i th mode of vibration of the beam and S is the area of the top surface, $S = LB$. This expression can be solved numerically, just as the equations of the damping model, and then a parametric plot can be used to graph the loss factor as a function of the structural deformation.

Besides this, one of the problems with our theoretical model is its dependence on variables that are very difficult to measure, such as the critical shear stresses. Wherever it functions well, the values $\tau_1 = 0.3$ MPa and $\tau_2 = 1$ MPa [52] will be preferred, but, as need arises, these should be adjusted to the experimental values. This will allow us, at least, to take some conclusions on these variables and to understand better how they should behave. Even if we adjust the values of the critical shear stresses, we will maintain their ratio for MWCNTs, $\frac{\tau_1}{\tau_2} = 0.3$, for the sake of simplicity, because it is easier to adjust just one value, than two variables.

6.1.1 Bhattacharya et al (2014)

The first article [52] for comparison was the main inspiration for the determination of the damping model, as it is. As such, we expect a reasonable approximation of our prediction of the loss factor to the experimental values measured. In this work we are evaluating the loss factor of a cantilever beam made of a MWCNT nanocomposite.

For the epoxy resin used we know that, $E_m = 3.3$ GPa and $\rho_m = 1200$ kg/m³, and for the nanotubes we have, $E_{CNT} = 650$ GPa, $l_{CNT} = 4.5$ μ m, $d_{CNT} = 12$ nm and $t_{CNT} = 2$ nm [52]. It also mentions that the density of the CNTs is 2100 kg/m³, however using the equation that determines the effective density of the nanotubes and this value as the density of fully dense graphite we arrive at, $\rho_{CNT} = 1167$ kg/m³ [11].

Bhattacharya et al [52] also defines the concentration of nanotubes, $w_{CNT} = 0.5\%$, and the critical shear stresses used for each type of debonding, $\tau_1 = 0.3$ MPa and $\tau_2 = 1$ MPa. The CNTs are assumed to be uniformly dispersed in the matrix and their orientations randomly distributed in three dimensions.

Finally, the only missing values are the geometrical properties of the beam used for the experiment and the contribution of the viscous damping of the matrix. However, we know that the experimental procedure used was the one from the standard ASTM E 756-05 [65], that explains how to measure damping related properties on vibrating beams. In this standard the geometrical properties of an uniform beam must be contained in the interval of 180 to 250 mm for its length and of 1 to 3 mm for its height

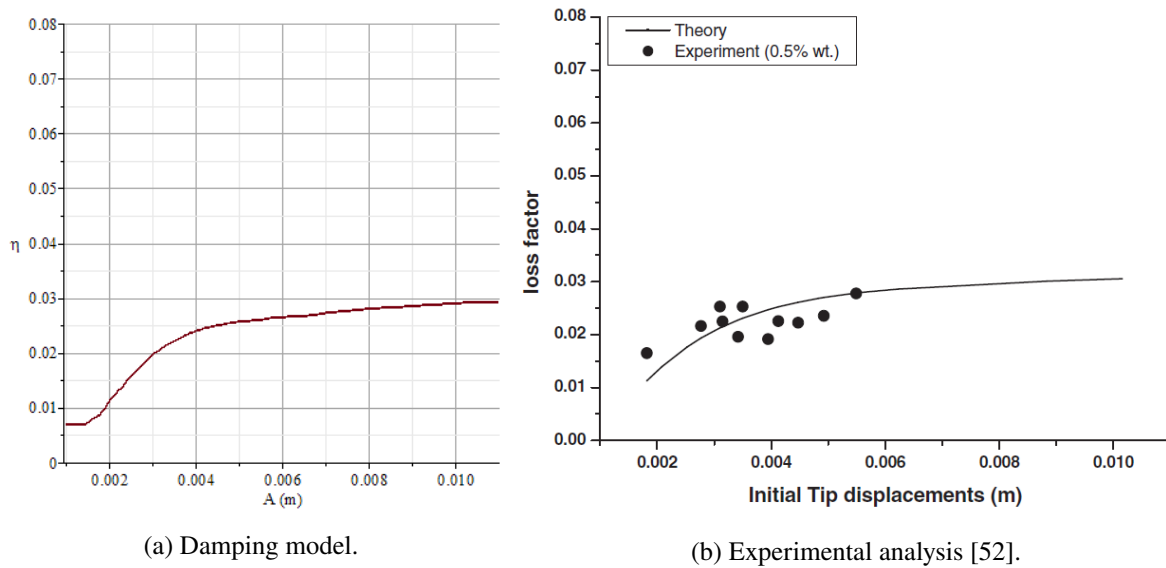


Figure 6.1: Loss factor as a function of initial tip displacement for the experimental results obtained by Bhattacharya et al [52]. Reprinted with permission from *International Journal for Computational Methods in Engineering Science and Mechanics*, 15, Bhattacharya S, Alva A, Raja S, "Modeling and Characterization of Multiwall Carbon Nanotube Reinforced Polymer Composites for Damping Applications", 258-264, 2014. © Taylor & Francis. Reproduced with permission. All rights reserved.

[65]. As we do not know the true magnitude of these properties, we will chose the mean value of each interval to be the used value, so $L = 215$ mm and $H = 2$ mm.

For the viscous damping, we may adjust its value so that the curve predicts a better estimate for the experimental values. In this case we will consider, $\eta_m = 0.007$. With all the necessary variables defined, we obtained the graphic of Figure 6.1a, that is to be compared to the plot of figure 5 on the article [52], shown in Figure 6.1b.

It can be readily seen that the curve obtained follows exceptionally well the theoretical prediction of Bhattacharya et al [52], which was expected, and, in turn, they follow the experimental data with a very reasonable proximity. This first article served as a validation test for the implemented equations, because if the theoretical predictions differed much, probably it would be because of an error in the calculations, as the theoretical damping models are not very different.

6.1.2 Zhou et al (2004)

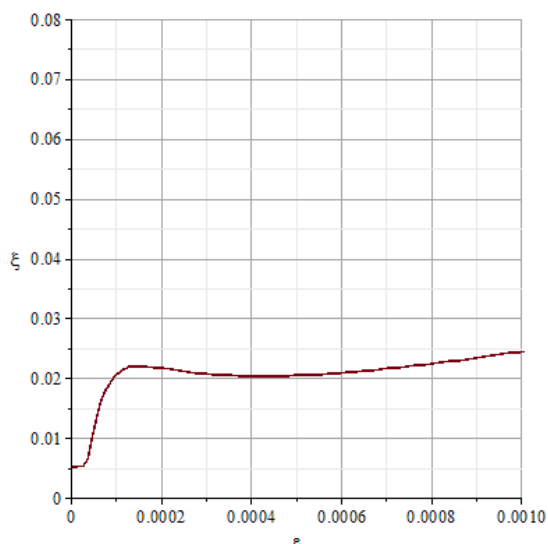
In this article, the effect of SWCNTs on the damping of a nanocomposite beam was studied [3]. As such, to adapt our model for this situation we defined $\tau_1 = 0$ and computed the rest of the equations normally.

The epoxy resin used had $E_m = 3.3$ GPa and $\rho_m = 1170$ kg/m³ and the nanotubes had $E_{CNT} = 1030$ GPa, $l_{CNT} = 1$ μ m, $d_{CNT} = 1.34$ nm and $t_{CNT} = 0.34$ nm [3]. The density of the CNTs was also mentioned to be 1313 kg/m³, however the sample of SWCNTs was not pure and corrections to the volume fraction of actual nanotubes on the matrix were needed. Zhou et al [3] performed these corrections and considered the effective density of the CNTs to be $\rho_{CNT} = 2172$ kg/m³.

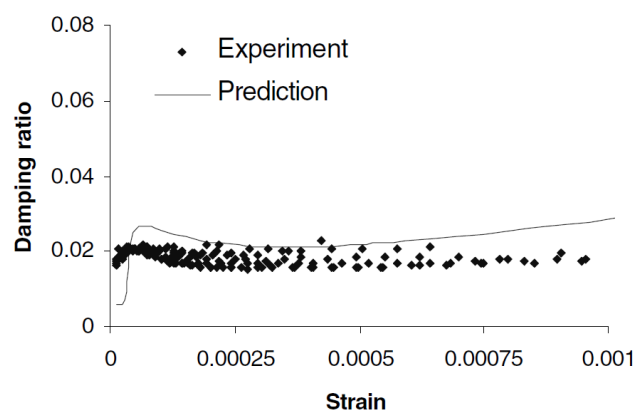
Also, the CNTs were assumed to be perfectly dispersed in the matrix and their orientations were randomly distributed in three dimensions. The dimensions of the cantilever beam used by Zhou et al [3] were $L = 165.1$ mm and $H = 1.5$ mm.

Finally, the critical shear stress for CNT/matrix debonding was $\tau_2 = 0.2$ MPa and the inherent viscous damping of the resin was measured to be $\eta_m = 0.01 + 30\varepsilon$, where ε is the structural deformation of the beam [3]. For these parameters, the damping ratio as a function of the structural deformation is presented in Figures 6.2a and 6.3a, for $w_{CNT} = 0.5\%$ and $w_{CNT} = 1\%$, respectively. These plots should be compared to figures 9 and 10 of the article [3], shown in Figures 6.2b and 6.3b, respectively.

The first aspect to be noticed is the fact that our model captured very well the shape of the curve, even showing the slight increase in damping ratio, when the viscous damping starts to dominate over the "stick-slip" mechanism. Then, it is also apparent that both curves show an almost horizontal plateau and



(a) Damping model.



(b) Experimental analysis [3].

Figure 6.2: Damping ratio as a function of structural deformation, for 0.5% CNT weight fraction, for the experimental results obtained by Zhou et al [3]. Reprinted from *Composites Science and Technology*, 64, Zhou X, Shin E, Wang KW, Bakis CE, "Interfacial damping characteristics of carbon nanotube-based composites", 2425–2437, Copyright (2004), with permission from Elsevier.

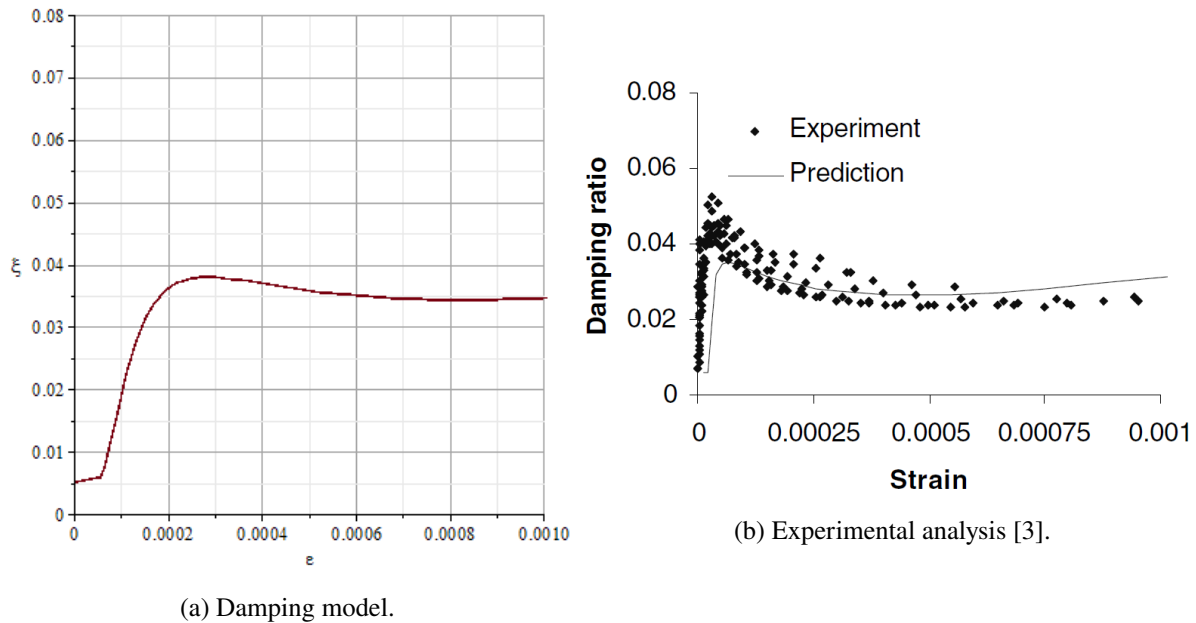


Figure 6.3: Damping ratio as a function of structural deformation, for 1% CNT weight fraction, for the experimental results obtained by Zhou et al [3]. Reprinted from *Composites Science and Technology*, 64, Zhou X, Shin E, Wang KW, Bakis CE, "Interfacial damping characteristics of carbon nanotube-based composites", 2425–2437, Copyright (2004), with permission from Elsevier.

these values correlate very well with the ones from the experimental measures. For the specimen with 0.5% CNT concentration, the value stagnated a little above 0.02, while for the higher weight fraction of 1%, it reached a value above 0.03 [3].

One of the worst problems our model have is its poor capability to represent the great increase in damping associated with the initial part of the curve, near the critical displacement for debonding. Specially in the case for 1% CNT concentration, some experimental values reached 0.05, for very low strains, while our model peaked just below 0.04 and for a strain above 0.0002. Even the theoretical model established by Zhou et al [3] could not capture fully the extent of this initial increase.

We may explain this effect by noting that, the damping model of the cantilever beam smooths greatly the curve in its initial part, in spite the maxima shown when only an axial load is applied to the composite, as demonstrated in Section 5.2.3. This is caused by the gradual debonding in different parts of the beam, starting in the clamped section, where the deformation is higher, and propagating all the way to the free end of the beam. During this motion, even if some parts have already passed the peak and have a decreasing damping ratio, the global loss factor will continue to rise, until almost the full volume of beam as been subjected to displacements higher than the critical displacement for debonding.

6.1.3 Bórbon et al (2014)

Bórbon et al [54] studied the effect of different types of MWCNTs on the damping behaviour of sandwich and Oberst beams [65]. Because of its many layers of complexity, added by the kind of experimental assembly used, we will only use the results that can be adapted, with a minimum rigour, to our model.

First of all, there were used four types of MWCNTs, designated as SM5, MC7, MH7 and aligned, but some of them were chemically functionalized with hydroxyl or carboxyl groups [54]. Because our model is not able to predict how these chemical changes will affect the adhesion between the matrix and nanotubes, we will not consider these CNTs, namely the MC7 and MH7. Then, the beams used were made of two different materials: the CNT nanocomposite and aluminium. The sandwich beams consisted of two plates of aluminium with the composite in the middle, while the Oberst beam [65], also called simple beam, was made of a plate of aluminium with the composite on top [54]. Such beams do not exactly meet the criteria used in our model, however because the sandwich beam has a symmetric deformation field, we can think of it as an equivalent beam made only of the nanocomposite layer, but with the added stiffness of the aluminium plates.

As the thickness of the aluminium plates are half that of the composite, which means $A_{Al} = \frac{1}{2}d_m^2$, the stiffness of the aluminium part of the sandwich beam can be computed as,

$$k_{Al} = 2 \frac{E_{Al} \frac{1}{2} d_m^2}{l} = \frac{\pi d_{CNT}^2 E_{Al}}{4 \nu_{CNT} l} \quad (6.2)$$

where k_{Al} is the stiffness of both aluminium plates and E_{Al} is the Young's modulus of aluminium. Now, we just need to correct the stiffnesses in the damping model with this additional factor, which in reality will have the same effect as the addition of carbon fibres: just an increase in the overall stiffness.

For the epoxy resin we will consider, $E_m = 3.3$ GPa and $\rho_m = 1200$ kg/m³, and for both MWCNTs, $E_{CNT} = 650$ GPa [52]. Then, for the SM5 we have, $d_{CNT} = 25$ nm, $t_{CNT} = 8.75$ nm and $l_{CNT} = 1.25$ μ m, and for the aligned, $d_{CNT} = 15$ nm, $t_{CNT} = 5.25$ nm and $l_{CNT} = 10$ μ m, where we used the mean values of each quantity [54]. With these values, the density of both types of nanotubes is $\rho_{CNT} = 2048$ kg/m³ [11].

Besides this, we also have the other variables as, $w_{CNT} = 5\%$, $L = 300$ mm, $H = 2$ mm and $A = 5.5$ mm [54]. It is to be noted that the value for the concentration of CNTs is very high and almost certainly the hierarchic model and, consequently, the damping model will not give an accurate description, as it is not recommended to use it beyond 1%. Even though this is true, we will continue this comparison. For the aluminium, we have $E_{Al} = 73.1$ GPa [66].

	$\xi_{[B\acute{o}rbon,2014]}$	$\xi_{0.6/2\text{MPa}}$	$\xi_{0.15/0.5\text{MPa}}$
SM5	0.0124	0.0107 (-13.7%)	0.0092 (-25.8%)
Aligned	0.0123	0.0097 (-21.1%)	0.0129 (4.9%)

Table 6.1: Comparison between the damping model and the experimental values for the sandwich beam obtained by Bórbon et al [54].

Finally, knowing that the damping ratio of the epoxy inside the sandwich beam is $\xi_m = 0.0092$, the critical shear stresses were adjusted, within reasonable values, as to achieve the least error in the prediction of the model, compared to the experimental values measured by Bórbon et al [54]. Using $\tau_1 = 0.6$ MPa and $\tau_2 = 2$ MPa for the SM5 and $\tau_1 = 0.15$ MPa and $\tau_2 = 0.5$ MPa for the aligned MWCNTs and noting that the first type have a random distribution of orientations, whilst the latter are unidirectional, we get Table 6.1.

It is apparent that the addition of the aluminium will make the stiffness of the beam dominated by these plates, thus reducing the global damping ratio of the beam, as noted when the effect of adding fibres was studied in Section 5.2.3. Besides this, the values obtained from our model were not very accurate, even while using different critical shear stresses, close to what we have been considering.

These results clearly mark another big problem with the damping model: its dependence on the critical shear stresses, which can vary widely. In fact, the values obtained suggest that these stresses can vary with CNT type and orientation. For the SM5, a higher critical stress was needed to achieve the correct damping ratio, which means that, maybe, for SM5 CNTs the debonding energy is higher than for aligned ones. It could also mean that aligned CNTs debond from the resin more easily than random oriented ones, as their specific surface areas are comparable and so are their damping potential [54]. The orientation of the principal stresses should matter to the debonding mechanism, giving an explanation to the behaviour described.

If the critical shear stresses are not constant, it may be difficult to obtain good results with our model, as these properties are very hard to measure accurately. We will continue to use the values admitted by Bhattacharya et al [52] as a good approximation to the real values.

6.1.4 Latibari et al (2013)

Lastly, on the comparison with articles that studied nanocomposites that did not have fibres, we have Latibari et al [53], which executed a finite element analysis of a SWCNT/matrix RVE system. To perform the comparison with the numerical results obtained by this work we must use the model for axial excited

CNT nanocomposites, instead of the damping model for beams.

For this article we will consider, $E_m = 3.3$ GPa for the epoxy resin and $E_{CNT} = 1250$ GPa for the nanotube, taking the mean value of the interval considered [53]. Besides this, we also have $d_{CNT} = 10$ nm, $t_{CNT} = 0.34$ nm and $\tau_2 = 0.95814$ MPa [53]. The other critical shear stress will be null, because we are considering a SWCNT in this example.

By adjusting the length of the CNT to $l_{CNT} = 0.25$ μm , we obtained the plots of Figure 6.5a, for several volume fractions of CNTs. This graphic should be compared to that of figure 12 in the article [53], shown in Figure 6.4. Just as in the previous section, the concentration of the nanotubes is too high for the hierarchic model to be an accurate representation of reality. As such, it was expected that the stiffness should be overestimated and, likewise, the loss factor. This inaccuracy in the hierarchic model is, by extension, another of the biggest flaws in the damping model, rendering it imprecise for large concentrations of CNTs.

Let us try to solve this problem by considering an exponential evolution of the stiffness of the composite with the volume fraction of CNTs. Using the values, according to the hierarchic model, for 0.5% and 1% of nanotube concentration we obtain the following exponential law,

$$E_{exp} = 4.48 \left(1 - e^{-254v_{CNT}} \right) \quad (6.3)$$

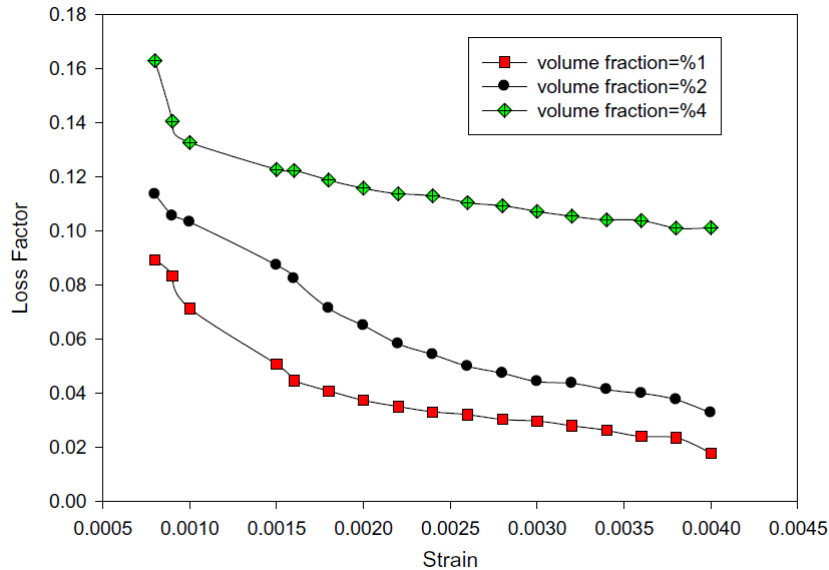


Figure 6.4: Influence of increasing the volume fraction in nanocomposites with SWCNTs with critical shear stress 0.95814 MPa by Latibari et al [53]. Reprinted from *Composites: Part B*, 50, Latibari ST, Mehrali M, Mottahedin L, Fereidoon A, Metselaar HSC, "Investigation of interfacial damping nanotube-based composite", 354–361, Copyright (2013), with permission from Elsevier.

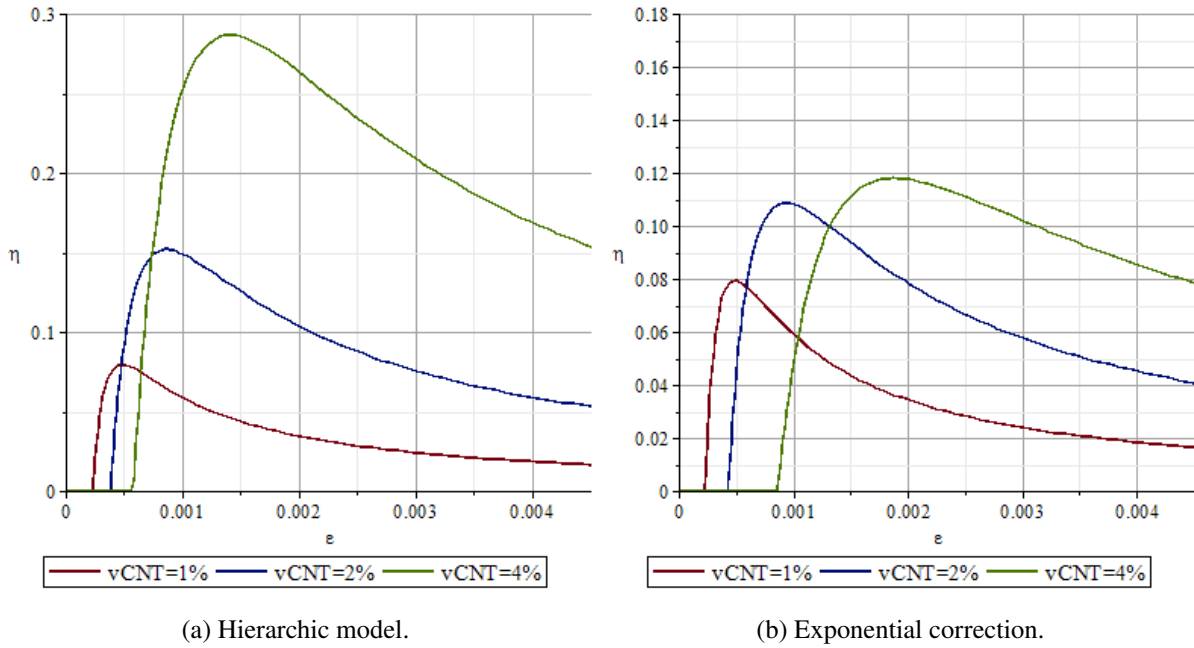


Figure 6.5: Loss factor as a function of strain for the numerical results obtained by Latibari et al [53].

where E_{exp} is the correction to the Young's modulus of the composite, the parameter -254 on the exponent was taken out of the work from Yeh et al [31] and the rest of the equation was obtained by adjustment.

Using the exponential law from equation (6.3), it is possible to obtain a better approximation to the numerical results, in Figure 6.5b. The peaks move to the right as we increase the CNT concentration, giving a bad estimate for higher volume fractions, however it is possible to see a lot of similarities in the tendencies of the two graphs. The peak for 1% happens at around 0.08 and for 2% at around 0.1 and 0.12, which are very close to the ones from Latibari et al [53]. Also, at a strain of 0.004, for the 1% curve we have 0.02 for both, for 2% we have values around 0.04 and, finally, for 4% we have loss factors around 0.09, which is just a little lower than that obtained in the article.

This correction helped us to understand that the damping model gives reasonable results, for its field of validity, which is also restricted by the hierarchic model. Although a great part of the curve is close to that attained in the article, the peaks usually happen too much to the right of the graphic and below the actual experimental or numerical data.

6.2 Prediction of damping on CNT/fibre/polymer matrix composites

After the references studied until now, it is only logical to advance to the case of multiscale composites that include fibres and CNTs. We already declared that the inclusion of fibres mainly affects the overall

stiffness of the composite, which means it will decrease considerably the damping characteristics of the system, as noted in Section 5.2.3.

For that reason a parallel could be made with the work of Bórbon et al [54], as the aluminium plates also serve only to increase the global stiffness of the beam. The references in this section both perform experiments on MWCNT nanocomposite cantilever beams [55, 56] and in both the concentration of nanotubes never exceeds 2% volume fraction, which seems a value somewhat inside the limits of validity of the hierarchic model.

When the references alone do not provide enough information about the properties used, we will consider other sources for those values. For the case of the critical shear stresses, as noted on the section regarding the work of Bórbon et al [54], the fact that we have a great increase in stiffness, somehow disrupt the usual values [52]. Therefore, these are the main variables where an adjustment to the experimental values will be performed.

6.2.1 DeValve and Pitchumani (2013)

DeValve and Pitchumani [55] executed an extensive research on the effect CNT type and concentration and fibre reinforcement have on the damping characteristics of composite cantilever beams. In this section we are particularly interested in the addition of fibres to a CNT nanocomposite, so we will restrict our comparison to the analysis of this specific effect. For that, we will study a system consisting of MWCNT/fibre/polymer matrix multiscale composites with a varying volume fraction of fibres.

For this article we have, $E_m = 3.3$ GPa and $\rho_m = 1200$ kg/m³ for the epoxy resin and $E_{CNT} = 650$ GPa for the nanotubes [52]. It is also defined in the reference that $d_{CNT} = 15$ nm, $t_{CNT} = 5$ nm and $l_{CNT} = 12.5$ μ m [55], which means that the density can be calculated as $\rho_{CNT} = 2000$ kg/m³ [11]. For the carbon fibres used, we will consider $E_{11f} = 234$ GPa and $\rho_f = 1800$ kg/m³ [67].

Also, it is considered $L = 292$ mm and $H = 2$ mm for the geometric properties of the beam [55]. Finally, the results obtained by the damping model are presented in Figures 6.7 and 6.8, to be compared to figure 6 in the reference [55], shown in Figure 6.6. We have used different material viscous loss factors for each volume fraction of fibres: $\eta_m = 0.16 + 20\varepsilon$, for 0%, $\eta_m = 0.025 + 30\varepsilon$, for 46% and $\eta_m = 0.020 + 10\varepsilon$, for 58% [55]. Also, we have adjusted the critical shear stresses as to approximate better the results, so $\tau_1 = 0.03$ MPa and $\tau_2 = 0.1$ MPa for the case with no fibres and $\tau_1 = 0.9$ MPa and $\tau_2 = 3$ MPa for the others.

It can be visualised that the introduction of fibres heavily reduced the loss factor of the beams, as predicted by our analysis in Section 5.2.3. Although the results from the case with no fibres are mimicked well by our model, when the fibres are included, our prediction for the loss factor is very underestimated [55]. Besides that, from this comparison it may be possible to conclude that for composites reinforced

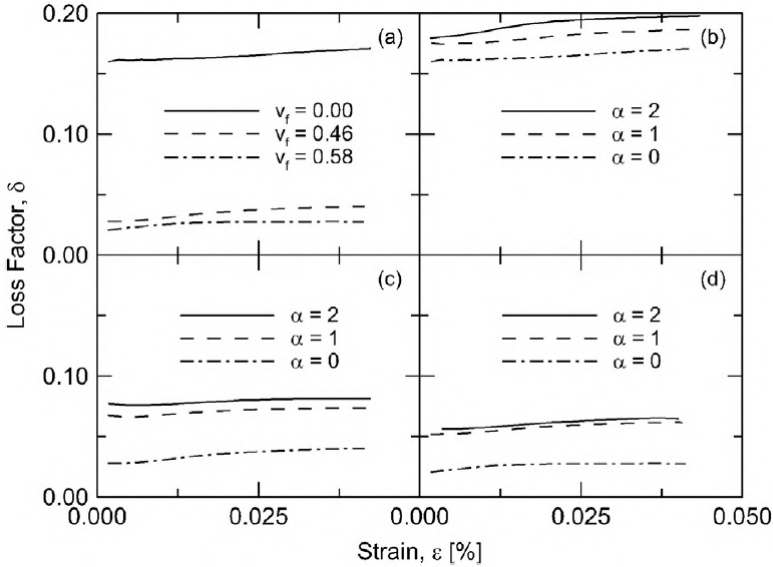


Figure 6.6: Variation of the material damping loss factor, δ , with strain, ϵ , using (a) no CNTs and varying the fibre volume fraction of the composite material, as well as using various weight percentages of MWCNTs (15 nm in diameter, 5–20 μm in length) with constant v_f values of (b) 0.00, (c) 0.46, and (d) 0.58 by DeValve and Pitchumani [55]. Reprinted from *Carbon*, 63, DeValve C, Pitchumani R, "Experimental investigation of the damping enhancement in fiber-reinforced composites with carbon nanotubes", 71–83, Copyright (2013), with permission from Elsevier.

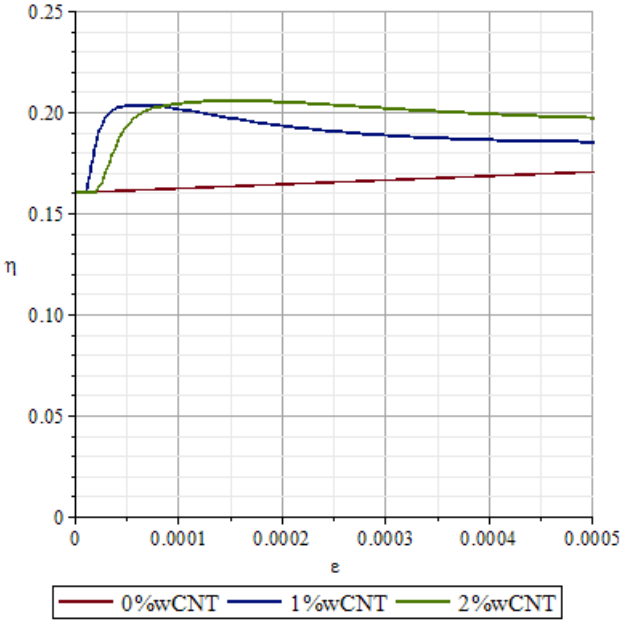


Figure 6.7: Loss factor of a nanocomposite without fibres as a function of structural deformation for the experimental results obtained by DeValve and Pitchumani [55].

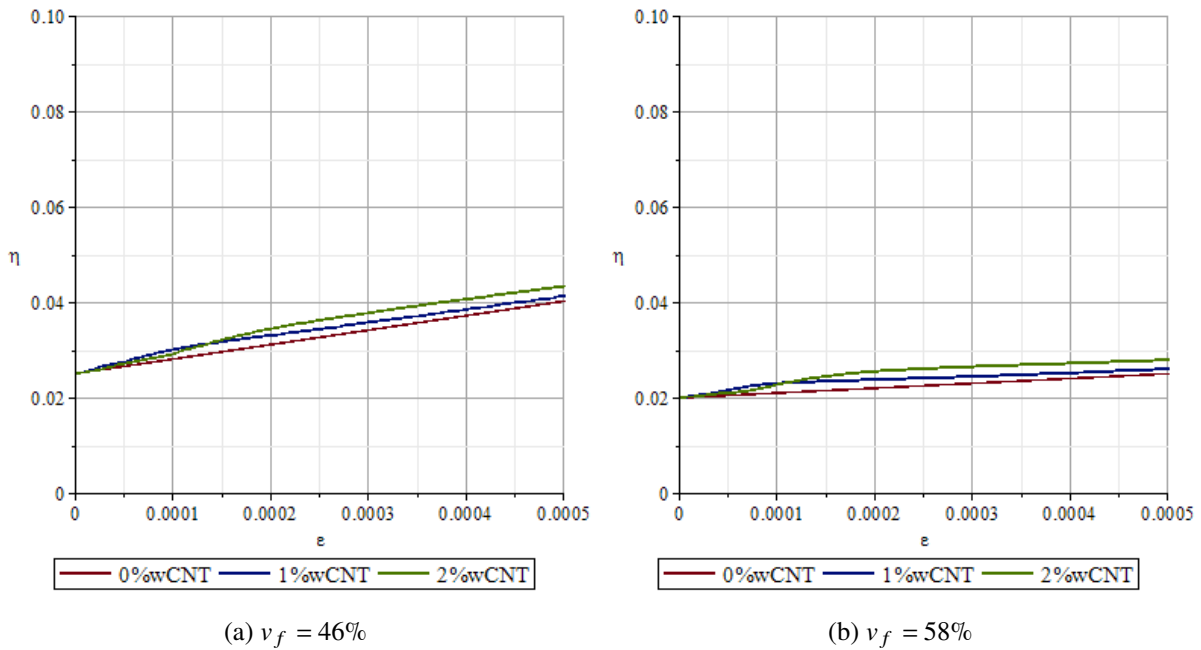


Figure 6.8: Loss factor of a nanocomposite with fibres as a function of structural deformation for the experimental results obtained by DeValve and Pitchumani [55].

with fibres, the critical shear stresses are, usually, higher, which would imply that the fibres help sustain the bonding between the nanotubes and the matrix.

However, let us plot, in Figure 6.9, the loss factor given by the damping model, for the cases with fibres, but neglecting their effect on the stiffness of the composite and using the critical shear stresses when no fibres are present. The results shown have a very solid correspondence to the experimental graphics attained by DeValve and Pitchumani [55].

Maybe, as the matrix is the only phase that is responsible for the load transfer to the CNTs, the damping behaviour inherent to the "stick-slip" mechanism is not affected by the existence of fibres. Such a phenomenon would explain the previous results on why neglecting the stiffness introduced by the fibres makes a better approximation to the experimental values.

Although it would be important to conclude how the fibres affect the damping characteristics of a multiscale composite beam, it seems that we still have no definitive proof of any of the aforementioned behaviour. Therefore, this leads to the last major limitation of the damping model: its limited predictive power when fibres are present in the composite.

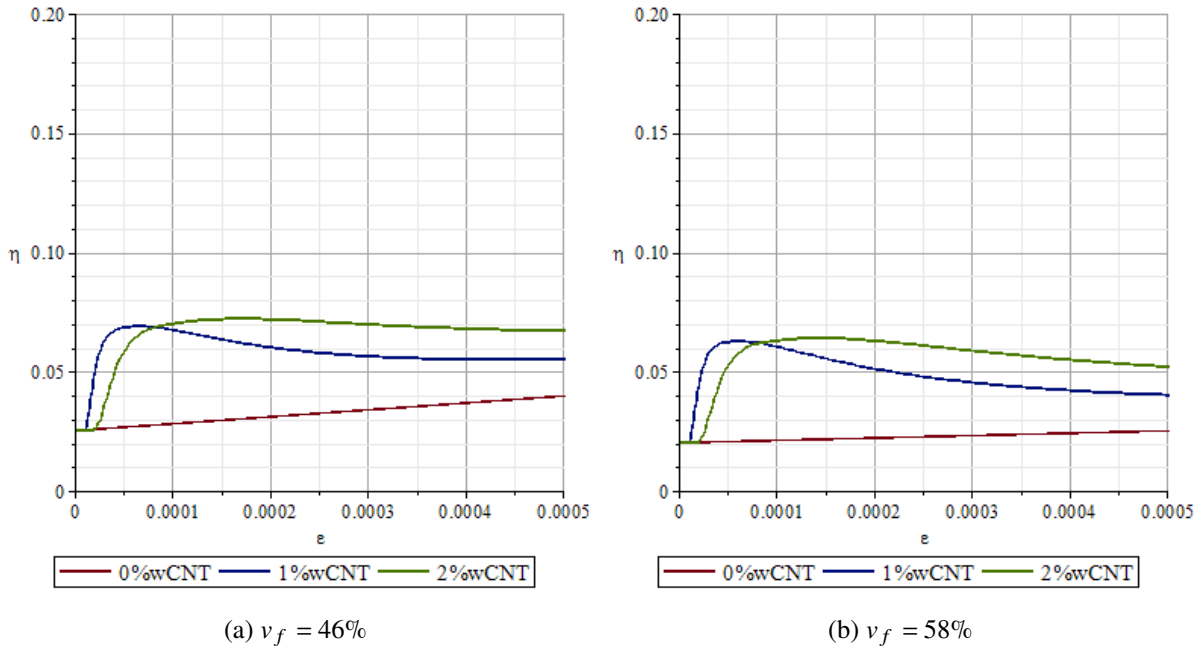


Figure 6.9: Loss factor of a nanocomposite with fibres, neglecting their effect on its stiffness, as a function of structural deformation for the experimental results obtained by DeValve and Pitchumani [55].

6.2.2 Khan et al (2011)

In this last article, we will study the effect of increasing MWCNT concentration on a neat polymer composite against the same effect on a fibre-reinforced multiscale composite [56]. Before making any comparisons, it is easy to predict that the same problem that occurred in the previous reference, will also happen here, leading to an underestimated value of the damping ratio for the composite with fibres [55].

For the epoxy resin we will use $E = 3.3$ GPa and $\rho_m = 1200$ kg/m³, while for the nanotubes we have $E_{CNT} = 650$ GPa [52]. According to the reference [56], the MWCNTs have $d_{CNT} = 50$ nm, using the mean value of this quantity, and $l_{CNT} = 20$ μ m, leading to $t_{CNT} = 20$ nm and $\rho_{CNT} = 2160$ kg/m³, by Thostenson et al [11]. The values for the carbon fibres are taken as the same from the previous reference [55], $E_{11f} = 234$ GPa, $\rho_f = 1800$ kg/m³ and $v_f = 46\%$.

Using the following values for all the remaining variables, $L = 185$ mm, $H = 3$ mm, $\tau_1 = 0.3$ MPa and $\tau_2 = 1$ MPa [52, 56] we arrive at the graphs of Figure 6.11, to be compared with those from figure 7 of the article [56], shown in Figure 6.10. The material viscous damping ratio was $\xi_m = 0.0085$ for the epoxy nanocomposite and $\xi_m = 0.0075$ for the CFRP with CNTs [56].

Again, it is obvious that the plot from Figure 6.11b is a very poor picture of the experimental curves found by Khan et al [56]. The graphic from the epoxy nanocomposite also did not correctly depict

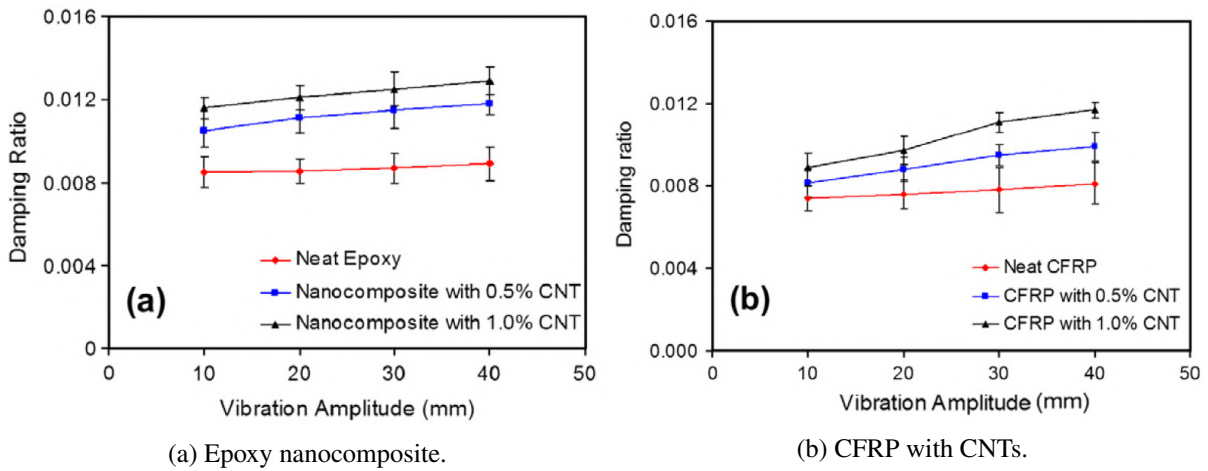


Figure 6.10: Damping ratio of (a) nanocomposites and (b) CFRP composites containing different CNT contents as a function of initial vibration amplitude by Khan et al [56]. Reprinted from *Composites Science and Technology*, 71, Khan SU, Li CY, Siddiqui NA, Kim J-K, "Vibration damping characteristics of carbon fiber-reinforced composites containing multi-walled carbon nanotubes", 1486–1494, Copyright (2011), with permission from Elsevier.

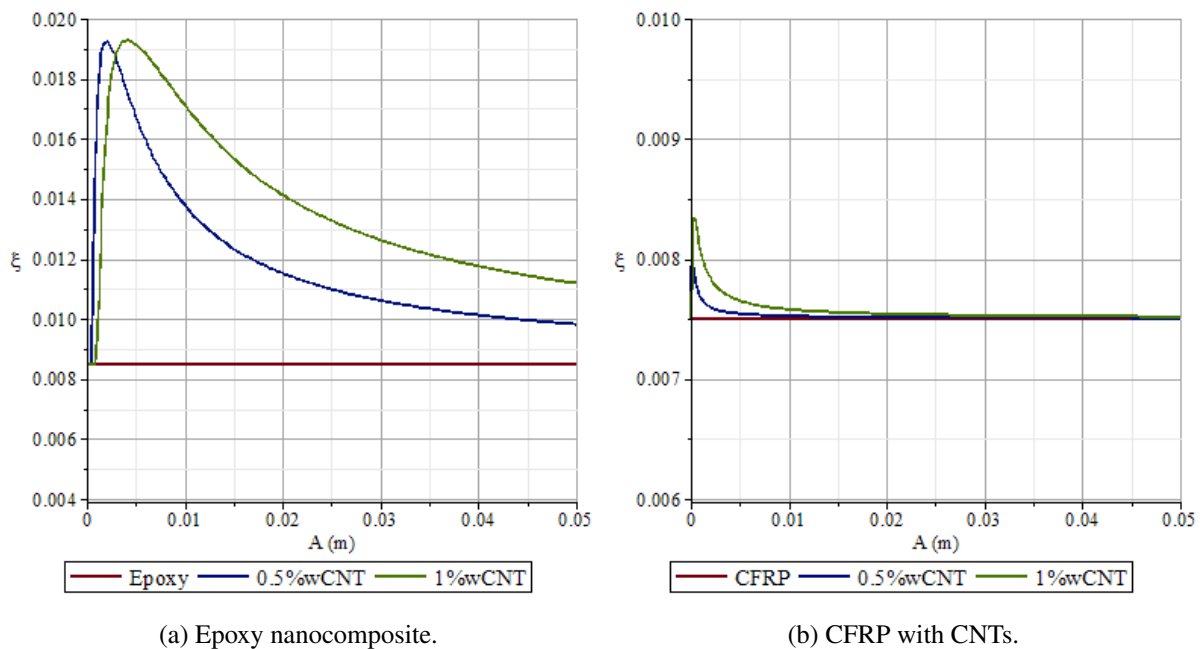


Figure 6.11: Damping ratio as a function of initial tip displacement for the experimental results obtained by Khan et al [56].

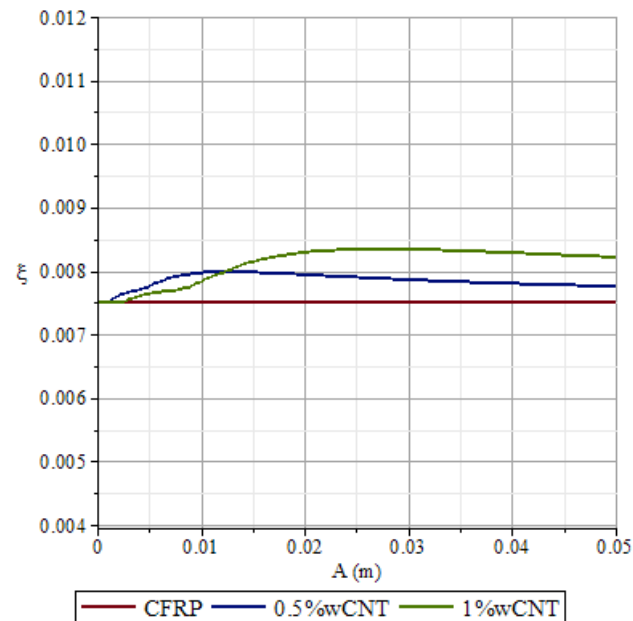


Figure 6.12: Damping ratio, for a critical shear stress between CNTs and matrix of 75 MPa, as a function of initial tip displacement for the experimental results obtained by Khan et al [56].

the increasing evolution of the damping ratio with initial tip displacement apparent in the article [56], however, for such a representation to be correct, we should have increased and adjusted the critical shear stresses. However, as we have been using $\tau_1 = 0.3$ MPa and $\tau_2 = 1$ MPa [52] for many of the previous examples, it was chosen not to proceed with a change to these values.

If we correct the values of the critical shear stresses to $\tau_1 = 22.5$ MPa and $\tau_2 = 75$ MPa we attain a somewhat better representation of the experimental results, depicted in Figure 6.12. Although it is still a heavily underestimated prediction for the damping ratio of the CFRP with CNTs, the decrease is not so apparent in this case and the evolution is increasing, in accordance with the reference [56].

As in the work by DeValve and Pitchumani [55], this result might imply that either the presence of fibres influence greatly the bonding strength between the matrix and the nanotubes, resulting in an enormous increase in the critical shear stresses, or the fibres do not affect at all the damping characteristics of the composite beams and should not be taken into account when calculating the stiffness used in the damping model. For all of the above, we believe the latter explains better the behaviour of the model, when considering the effect of the fibres on a multiscale composite.

Chapter 7

Classical theory of laminated composite plates

The increase in stiffness and damping caused by the addition of nanotubes to a composite can improve the response of the material, in a variety of structural dynamic systems, that can undertake vibratory motions [1]. In fact, many of those systems, such as machine elements, manufacturing tools, turbo-machinery and aircraft structures [1], can be modelled as beams or plates subjected to some periodic excitation.

To study the performance of CNT multiscale composites when an oscillating load is applied, we will use a p-version finite element model to obtain numerical results, predicting their dynamical behaviour. In this chapter, this model for CNT-reinforced composite plates will be described in detail.

First, the geometrical model used to represent a laminated composite plate and its associated coordinate system is discussed, followed by the assumptions required by the CLPT. Finally, the constitutive relations and the equations of motion are determined, using a p-version of the FEM.

7.1 Laminae and VSCL plates

To understand the behaviour of a plate made of a laminated composite it is important to have a clear notion of how it is constructed. A laminated composite is constituted by several layers of fibre-reinforced composites, called laminae or plies, and each behave as an orthotropic elastic medium [68]. These layers, usually with unidirectional fibres [69], are stacked on top of each other, possibly with different fibre angles between them. This sequence of orientations is termed lamination scheme or stacking scheme [68].

By using a symmetric lamination scheme with many different orientations, it is possible to obtain almost an isotropic laminated composite, in the plane of the composite [68]. For these kinds of laminae, which have unidirectional fibres, we call the final product a constant stiffness composite laminated (CSCL)

plate. However, many studies have shown that using curvilinear fibres, thus changing the stiffness of the ply from point to point, we may optimise the plate for certain applications, improving its structural response. This type of laminated composites are considered variable stiffness laminated composite (VSCL) plates, being amongst the methods used to achieve such a non constant behaviour [70, 71]. For the sake of generality, we will develop our model considering curvilinear fibres in the laminae.

It may be apparent that, because our system is composed of a number of laminae, each of them may be represented as individual mechanical systems with their own dynamical responses to an excitation. This would require three-dimensional elasticity theories or layerwise type approaches, which would make our model a lot more complex, but much more close to reality. Although it is better to describe the detailed distribution of stresses and strains in the laminate, we are mainly interested in the natural frequencies and modes of vibration of VSCL plates, which are given with a fairly good approximation by the so called equivalent single layer (ESL) theories [71].

The ESL theories can be derived from three-dimensional elasticity by using suitable simplifications that allow us to reduce the problem to just a bidimensional one. This usually involves the use of stress averages in the thickness direction of the plate, by comparing the contributions of the many plies to that of a single layer, with an equivalent behaviour [68].

Before advancing to the description of the actual equations used by the computational model, let us determine the coordinate system used and the definition of most geometrical quantities.

7.1.1 Coordinate system

To characterise the coordinate system of the laminate, we first need to describe that of each individual lamina. For simplicity, let us describe the coordinate system for rectilinear fibres and then extend it to curvilinear ones. Each lamina is taken as an orthotropic material whose principal coordinate axes are along the direction defined by the fibres. These principal axes, which coincide with the axes of material symmetry, are called material axes and vary from lamina to lamina [68].

As mentioned before, the stacking sequence of a laminate can be represented by the successive orientation of the fibres in each ply. From this, it is apparent that a general coordinate system must be used and the material coordinate system of each lamina should be related to the general one by its fibre orientation angle [68], as shown in Figure 7.1.

Using the notation from Figure 7.1, (x, y, z) represent the general coordinate system of the composite laminated plate and (x_1^k, x_2^k, x_3^k) is the material coordinate system for the k th lamina. Also, the angle θ_k represent the fibre orientation with respect to the general coordinate system of the k th ply [68].

For the complete laminate, we will use the coordinate system depicted in Figure 7.2, where only straight fibres are represented. Each ply will be represented by its fibre orientation, as well as its z_k coordinate with respect to the middle plane. The thickness of the composite plate is h and there are L layers stacked on top of each other. The z axis is represented downwards so that, when we have a downwards load applied, the displacement field in the z direction is positive [68].

Using this notation, each ply will have a thickness of h_k , given by [68],

$$h_k = z_{k+1} - z_k \quad (7.1)$$

where z_{k+1} and z_k are the z coordinates of the upper faces of the k th and the $(k+1)$ th lamina and the lamination scheme is counted from the top of the plate to the bottom [68].

Finally, for the case of VSCL plates, the orientation of the fibres will vary throughout all points of the same lamina. In spite of its simplicity, we will assume a linear variation of the fibre orientation along the x axis, which allows the generation of plates with a large range of properties. The curvilinear fibre path in analysis is shown in Figure 7.3 [69, 71, 72].

Using the notation of Figure 7.3, the fibre orientation along the x coordinate will be [72],

$$\theta_k(x) = \frac{2(T_1^k - T_0^k)}{a} |x| + T_0^k \quad (7.2)$$

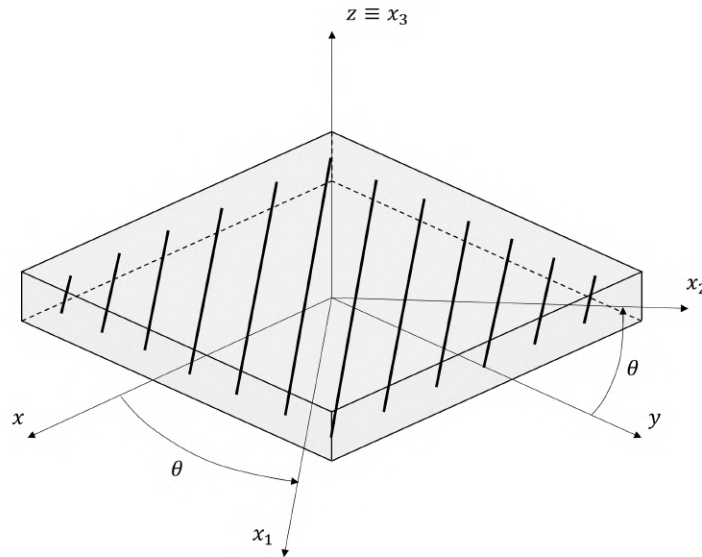


Figure 7.1: A representation of a lamina with material and general coordinate systems.

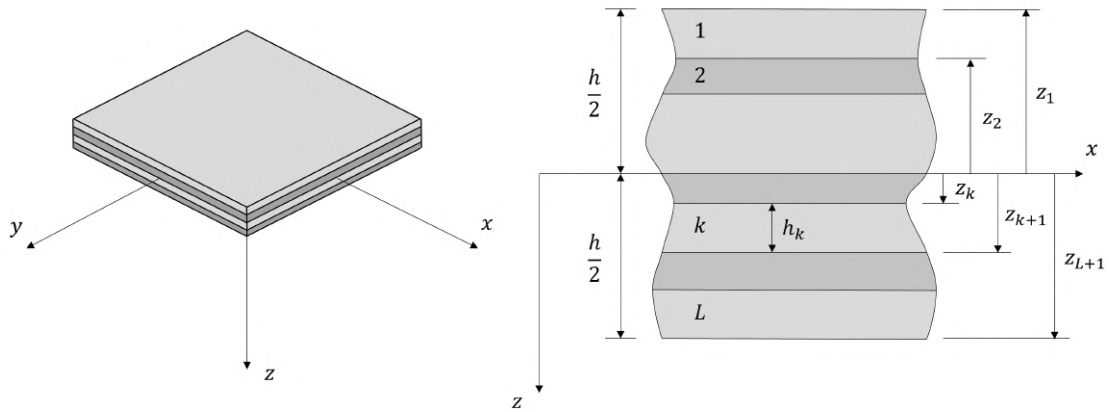


Figure 7.2: General coordinate system and lamina numbering used for the composite laminated plate.

where T_0^k is the fibre orientation of the k th lamina at the centre, $x = 0$, and T_1^k is the fibre orientation of the k th lamina at the edges, $x = \frac{a}{2}$ and $x = -\frac{a}{2}$ [72].

Also, the length of the plate in the x direction is a , while the length along the y direction is b . These quantities should be significantly bigger than the thickness h as we shall soon explain [68].

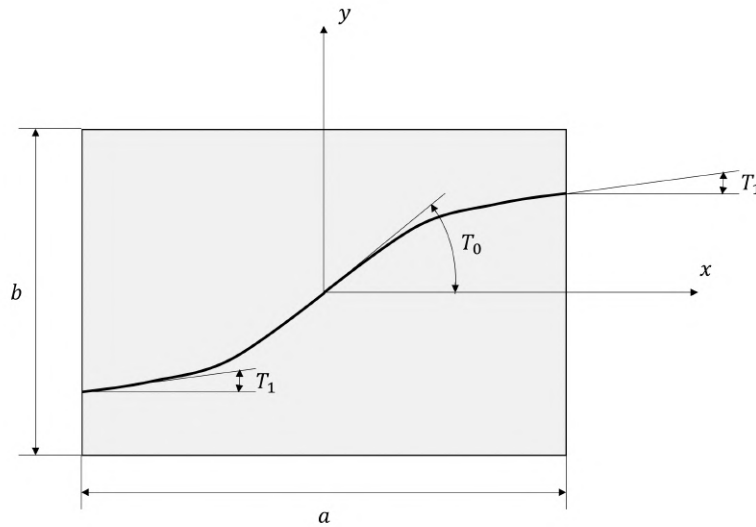


Figure 7.3: Orientation variation of a curvilinear fibre.

7.2 Assumptions of the CLPT

As stated in the previous section, ESL theories rely on the reduction of the complex multilayered mechanical system that constitutes a laminate to an equivalent bidimensional plate problem. As such, ESL theories are developed by assuming that the displacement field is of the form [68],

$$u_i(x, y, z, t) = \sum_{j=0}^n (z)^j u_i^j(x, y, t) \quad (7.3)$$

where $u_i(x, y, z, t)$ is the i th component of the displacement field, t the time and $u_i^j(x, y, t)$ a set of functions that describe the particular problem at hand. These undetermined functions can be explicitated with the aid of the Principle of Virtual Work or another dynamical principle [68].

Because of the form assumed by the displacement field in equation (7.3) and the rectangular cross sectional geometry of a plate, being symmetric about its midplane, all the integrations performed on variables directly related to the displacement field can be reduced to [68],

$$\iiint_V (\cdot) dV = \int_{-\frac{h}{2}}^{\frac{h}{2}} \iint_{\Omega} (\cdot) d\Omega dz \quad (7.4)$$

where V is the volume of the plate and Ω is the area of the undeformed midplane. Equation (7.4) implies that the Euler-Lagrange equations of this model will contain differential equations involving the displacement field and thickness-average stress resultants [68].

Two of the most used ESL theories are the classical laminated plate theory (CLPT), which is an extension of the Kirchhoff plate theory to laminated composite plates, and the first-order shear deformation theory (FSDT), which is an extension of the Reissner-Mindlin plate theory to laminates [68, 73]. Both are first-order theories, meaning that the displacement field is of the form assumed in equation (7.3), for $n = 1$ [68].

Although technically, the FSDT is a better representation of a real composite laminated plate, because the CLPT neglects the existence of transverse shear stresses, for the case of thin plates, the latter gives a fairly good description of their behaviour. As we will only study thin plates and because the CLPT is a much simpler theory, this is the one we will consider in the following text [68].

7.2.1 Kirchhoff's hypotheses

The CLPT is an extension to the classical plate theory, so the Kirchhoff's hypothesis should also hold in this case. These assumptions state that [68]:

1. Straight lines perpendicular to the midsurface, also called transverse normals, before deformation remain straight after deformation;

2. The transverse normals do not experience elongation, that is, they are inextensible;
3. The transverse normals rotate such that they remain perpendicular to the midsurface after deformation.

The first assumption implies that the transverse displacement is independent of the thickness coordinate, which means $n = 0$ in equation (7.3). Also, the transverse normal strain is zero, $\varepsilon_{zz} = 0$, by the second assumption of transverse inextensibility. Finally, the last one results in a non existence of transverse shear strains, $\varepsilon_{xz} = 0$ and $\varepsilon_{yz} = 0$, which is one of the main differences from the assumptions of the FSDT [68].

Other assumptions and restrictions are also made in order to simplify the resulting model, namely [68]:

- The layers are perfectly bonded together;
- The material of each layer is linearly elastic and is an orthotropic medium;
- Each layer is of uniform thickness;
- The strains and displacements are small, meaning we are in the linear regime;
- The transverse shear stresses on the top and bottom surfaces of the laminate are zero, which is a redundant restriction, because we assumed they were zero everywhere.

7.2.2 Displacement field

For the case of a first-order theory, the displacement field will be a sum of only two terms, according to equation (7.3). The displacements of a point on the plate for the CLPT are assumed to be described by [68],

$$u(x, y, z, t) = u_0(x, y, t) - z \frac{\partial w_0(x, y, t)}{\partial x} \quad (7.5)$$

$$v(x, y, z, t) = v_0(x, y, t) - z \frac{\partial w_0(x, y, t)}{\partial y} \quad (7.6)$$

$$w(x, y, z, t) = w_0(x, y, t) \quad (7.7)$$

where (u, v, w) is the displacement field along the corresponding axes (x, y, z) and (u_0, v_0, w_0) is the displacement field of a point on the midplane of the plate, $z = 0$.

As expected from an ESL theory, the displacements at any point of the plate can be computed once the displacements at the midplane are determined, reducing the tridimensional problem to, effectively, a bidimensional one [68]. Also, although our objective is the analysis of linear bending of composite laminated plates, we will consider the membrane displacements u_0 and v_0 just for the sake of completeness of the mathematical model, as these components will be null for our case.

7.2.3 Strain-displacement relations

Throughout the development of this model, we will assume that the strain components are sufficiently small and that the rotations and displacements involved are also small, so that our analysis results in a linear model. With this simplification in mind, the finite Green-Lagrange strain tensor will reduce to the infinitesimal strain tensor and the second Piola-Kirchhoff stress tensor will be equal to the Cauchy stress tensor. Then, the strain tensor will simply be [68],

$$[\boldsymbol{\varepsilon}] = \begin{bmatrix} \varepsilon_{xx} & \varepsilon_{xy} & \varepsilon_{xz} \\ \varepsilon_{xy} & \varepsilon_{yy} & \varepsilon_{yz} \\ \varepsilon_{xz} & \varepsilon_{yz} & \varepsilon_{zz} \end{bmatrix} = \begin{bmatrix} \frac{\partial u}{\partial x} & \frac{1}{2} \left(\frac{\partial u}{\partial y} + \frac{\partial v}{\partial x} \right) & \frac{1}{2} \left(\frac{\partial u}{\partial z} + \frac{\partial w}{\partial x} \right) \\ \frac{1}{2} \left(\frac{\partial u}{\partial y} + \frac{\partial v}{\partial x} \right) & \frac{\partial v}{\partial y} & \frac{1}{2} \left(\frac{\partial v}{\partial z} + \frac{\partial w}{\partial y} \right) \\ \frac{1}{2} \left(\frac{\partial u}{\partial z} + \frac{\partial w}{\partial x} \right) & \frac{1}{2} \left(\frac{\partial v}{\partial z} + \frac{\partial w}{\partial y} \right) & \frac{\partial w}{\partial z} \end{bmatrix} \quad (7.8)$$

where ε_{xx} , ε_{yy} and ε_{zz} are the normal strains and ε_{xy} , ε_{xz} and ε_{yz} are the shear strains. The tensorial shear strains relate to the engineering shear strains by a multiplication by 2, $\gamma_{xy} = 2\varepsilon_{xy}$ [62]. To distinguish both strains, we shall call the latter shear deformation.

Substituting the displacement field of equations (7.5) to (7.7) in the definitions from equation (7.8) and noting that the transverse shear strains, ε_{xz} and ε_{yz} , and the normal strain along the thickness of the plate, ε_{zz} , are zero, by the Kirchhoff's hypothesis, we have the following strain-displacement relations [68],

$$\varepsilon_{xx}(x, y, z, t) = \frac{\partial u_0(x, y, t)}{\partial x} - z \frac{\partial^2 w_0(x, y, t)}{\partial x^2} \quad (7.9)$$

$$\varepsilon_{yy}(x, y, z, t) = \frac{\partial v_0(x, y, t)}{\partial y} - z \frac{\partial^2 w_0(x, y, t)}{\partial y^2} \quad (7.10)$$

$$\gamma_{xy}(x, y, z, t) = \frac{\partial u_0(x, y, t)}{\partial y} + \frac{\partial v_0(x, y, t)}{\partial x} - 2z \frac{\partial^2 w_0(x, y, t)}{\partial x \partial y} \quad (7.11)$$

Finally, it can be noted that we may write the previous equations in a more intuitive form, separating the strain field into two components. The first one will represent the deformations resulting from the application of in-plane forces on the plate, called the membrane strains in the midplane, $\boldsymbol{\varepsilon}_m$, and the other the deformations due to bending, $z\boldsymbol{\varepsilon}_b$ [68]. With such a separation, we may define,

$$\boldsymbol{\varepsilon} = \boldsymbol{\varepsilon}_m + z\boldsymbol{\varepsilon}_b \quad (7.12)$$

or, clarifying the vector components,

$$\begin{Bmatrix} \varepsilon_{xx} \\ \varepsilon_{yy} \\ \gamma_{xy} \end{Bmatrix} = \begin{Bmatrix} \frac{\partial u_0}{\partial x} \\ \frac{\partial v_0}{\partial y} \\ \frac{\partial u_0}{\partial y} + \frac{\partial v_0}{\partial x} \end{Bmatrix} + z \begin{Bmatrix} -\frac{\partial^2 w_0}{\partial x^2} \\ -\frac{\partial^2 w_0}{\partial y^2} \\ -2\frac{\partial^2 w_0}{\partial x \partial y} \end{Bmatrix} \quad (7.13)$$

where ε_b are commonly called the curvatures [68]. Hence, for a certain displacement field, the strains at any point of the plane can be calculated, using equation (7.13).

7.3 Constitutive relations

The constitutive relations of a body relate the stresses applied to it to the deformations it will undertake. These equations allow us to describe mathematically the mechanical behaviour of the material, being the simplest one the Hooke's law, for linear elastic media [68]. According to the CLPT, a laminated composite plate will not have any of the three transverse strain components, ε_{xz} , ε_{yz} and ε_{zz} , which is a result of the assumed displacement field. Identically, the transverse shear stresses, τ_{xz} and τ_{yz} , will be zero and, although the transverse normal stress, σ_{zz} , will not necessarily be null, it will not be considered in the equations of motion, because there is no deformation in that direction [68].

For these reasons, the transverse normal stress can be neglected and, thus, we are in the presence of a state of both plane stress and plane strain. However, from practical experience, a plate can be considered in a state of plane stress, as the thickness is, usually, very small when compared to the in-plane dimensions. Therefore, in the subsequent analysis, the constitutive relations will be computed with the assumption of a state of plane stress [68].

7.3.1 Stress-strain relations

The constitutive equations for the k th lamina of a laminate with curvilinear fibres relative to the principal material axes and assuming a state of plane stress are [68],

$$\begin{Bmatrix} \sigma_{11} \\ \sigma_{22} \\ \tau_{12} \end{Bmatrix}^{(k)} = \begin{bmatrix} Q_{11} & Q_{12} & 0 \\ Q_{12} & Q_{22} & 0 \\ 0 & 0 & Q_{66} \end{bmatrix}^{(k)} \begin{Bmatrix} \varepsilon_{11} \\ \varepsilon_{22} \\ \gamma_{12} \end{Bmatrix} \quad (7.14)$$

where σ_{ij} and τ_{ij} are the normal and shear stresses in the material coordinates, ε_{ij} and γ_{ij} are the normal and shear strains in the material coordinates and Q_{ij} are the plane stress reduced stiffnesses, which for an orthotropic material are given by [68],

$$Q_{11} = \frac{E_{11}}{1 - \nu_{12}\nu_{21}} \quad (7.15)$$

$$Q_{12} = \frac{\nu_{12}E_{22}}{1 - \nu_{12}\nu_{21}} \quad (7.16)$$

$$Q_{22} = \frac{E_{22}}{1 - \nu_{12}\nu_{21}} \quad (7.17)$$

$$Q_{66} = G_{12} \quad (7.18)$$

where E_{11} and E_{22} are the longitudinal and transverse Young's modulus, ν_{12} and ν_{21} are the longitudinal major and minor Poisson's ratio and G_{12} is the longitudinal shear modulus. All these quantities should be calculated for each lamina, in our case, using the hierarchic model developed in previous chapters.

As the laminae can have different orientations with respect to the general coordinate system of the plate and even between different points in the same ply, because of the variable stiffness introduced by the curvilinear fibres, a coordinate transformation should be performed in order to transfer these equations to the general system, as shown in Figure 7.1. This transformation is defined by the fibre orientation angle, θ , and is given by [68],

$$\begin{Bmatrix} \sigma_{xx} \\ \sigma_{yy} \\ \tau_{xy} \end{Bmatrix}^{(k)} = \begin{bmatrix} \cos^2 \theta & \sin^2 \theta & -\sin(2\theta) \\ \sin^2 \theta & \cos^2 \theta & \sin(2\theta) \\ \sin \theta \cos \theta & -\sin \theta \cos \theta & \cos^2 \theta - \sin^2 \theta \end{bmatrix}^{(k)} \begin{Bmatrix} \sigma_{11} \\ \sigma_{22} \\ \tau_{12} \end{Bmatrix}^{(k)} \quad (7.19)$$

resulting in the following stress-strain relations [68, 69, 71],

$$\begin{Bmatrix} \sigma_{xx}(x, y, z, t) \\ \sigma_{yy}(x, y, z, t) \\ \tau_{xy}(x, y, z, t) \end{Bmatrix}^{(k)} = \begin{bmatrix} \bar{Q}_{11}(\theta_k(x)) & \bar{Q}_{12}(\theta_k(x)) & \bar{Q}_{16}(\theta_k(x)) \\ \bar{Q}_{12}(\theta_k(x)) & \bar{Q}_{22}(\theta_k(x)) & \bar{Q}_{26}(\theta_k(x)) \\ \bar{Q}_{16}(\theta_k(x)) & \bar{Q}_{26}(\theta_k(x)) & \bar{Q}_{66}(\theta_k(x)) \end{bmatrix}^{(k)} \begin{Bmatrix} \varepsilon_{xx}(x, y, z, t) \\ \varepsilon_{yy}(x, y, z, t) \\ \gamma_{xy}(x, y, z, t) \end{Bmatrix} \quad (7.20)$$

where \bar{Q}_{ij} are the transformed plane stress reduced stiffnesses, which are, in general, a function of the fibre orientation θ_k of the k th lamina, being itself a function of the general coordinate x , as defined in equation (7.2).

These transformed reduced stiffnesses can be calculated by applying the transformation from equation (7.19) to the stiffness tensor of equation (7.14), which give [8],

$$\bar{Q}_{11}(\theta_k(x)) = U_1 + U_2 \cos(2\theta_k(x)) + U_3 \cos(4\theta_k(x)) \quad (7.21)$$

$$\bar{Q}_{12}(\theta_k(x)) = U_4 - U_3 \cos(4\theta_k(x)) \quad (7.22)$$

$$\bar{Q}_{22}(\theta_k(x)) = U_1 - U_2 \cos(2\theta_k(x)) + U_3 \cos(4\theta_k(x)) \quad (7.23)$$

$$\bar{Q}_{16}(\theta_k(x)) = \frac{1}{2} U_2 \sin(2\theta_k(x)) + U_3 \sin(4\theta_k(x)) \quad (7.24)$$

$$\bar{Q}_{26}(\theta_k(x)) = \frac{1}{2}U_2 \sin(2\theta_k(x)) - U_3 \sin(4\theta_k(x)) \quad (7.25)$$

$$\bar{Q}_{66}(\theta_k(x)) = U_5 - U_3 \cos(4\theta_k(x)) \quad (7.26)$$

with the coefficients U_i defined as [8],

$$U_1 = \frac{1}{8}(3Q_{11} + 3Q_{22} + 2Q_{12} + 4Q_{66}) \quad (7.27)$$

$$U_2 = \frac{1}{2}(Q_{11} - Q_{22}) \quad (7.28)$$

$$U_3 = \frac{1}{8}(Q_{11} + Q_{22} - 2Q_{12} - 4Q_{66}) \quad (7.29)$$

$$U_4 = \frac{1}{8}(Q_{11} + Q_{22} + 6Q_{12} - 4Q_{66}) \quad (7.30)$$

$$U_5 = \frac{1}{8}(Q_{11} + Q_{22} - 2Q_{12} + 4Q_{66}) \quad (7.31)$$

7.3.2 Force and moment resultants

By performing an integration of the stresses over the thickness of the plate, we obtain the membrane force resultants, N , and the bending moment resultants, M , through the following equations [68],

$$\begin{aligned} \begin{Bmatrix} N_{xx}(x, y, t) \\ N_{yy}(x, y, t) \\ N_{xy}(x, y, t) \end{Bmatrix} &= \sum_{k=1}^L \int_{z_k}^{z_{k+1}} \begin{Bmatrix} \sigma_{xx}(x, y, z, t) \\ \sigma_{yy}(x, y, z, t) \\ \tau_{xy}(x, y, z, t) \end{Bmatrix} dz \\ &= \sum_{k=1}^L \int_{z_k}^{z_{k+1}} \begin{bmatrix} \bar{Q}_{11}(\theta_k(x)) & \bar{Q}_{12}(\theta_k(x)) & \bar{Q}_{16}(\theta_k(x)) \\ \bar{Q}_{12}(\theta_k(x)) & \bar{Q}_{22}(\theta_k(x)) & \bar{Q}_{26}(\theta_k(x)) \\ \bar{Q}_{16}(\theta_k(x)) & \bar{Q}_{26}(\theta_k(x)) & \bar{Q}_{66}(\theta_k(x)) \end{bmatrix}^{(k)} \begin{Bmatrix} \varepsilon_{xx}(x, y, z, t) \\ \varepsilon_{yy}(x, y, z, t) \\ \gamma_{xy}(x, y, z, t) \end{Bmatrix} dz \end{aligned} \quad (7.32)$$

$$\begin{aligned} \begin{Bmatrix} M_{xx}(x, y, t) \\ M_{yy}(x, y, t) \\ M_{xy}(x, y, t) \end{Bmatrix} &= \sum_{k=1}^L \int_{z_k}^{z_{k+1}} \begin{Bmatrix} \sigma_{xx}(x, y, z, t) \\ \sigma_{yy}(x, y, z, t) \\ \tau_{xy}(x, y, z, t) \end{Bmatrix} z dz \\ &= \sum_{k=1}^L \int_{z_k}^{z_{k+1}} \begin{bmatrix} \bar{Q}_{11}(\theta_k(x)) & \bar{Q}_{12}(\theta_k(x)) & \bar{Q}_{16}(\theta_k(x)) \\ \bar{Q}_{12}(\theta_k(x)) & \bar{Q}_{22}(\theta_k(x)) & \bar{Q}_{26}(\theta_k(x)) \\ \bar{Q}_{16}(\theta_k(x)) & \bar{Q}_{26}(\theta_k(x)) & \bar{Q}_{66}(\theta_k(x)) \end{bmatrix}^{(k)} \begin{Bmatrix} \varepsilon_{xx}(x, y, z, t) \\ \varepsilon_{yy}(x, y, z, t) \\ \gamma_{xy}(x, y, z, t) \end{Bmatrix} z dz \end{aligned} \quad (7.33)$$

however, we may represent both these equation in a more elegant format, using the definitions of equation (7.12). Using the membrane strains, $\boldsymbol{\varepsilon}_m$, and the curvatures, $\boldsymbol{\varepsilon}_b$, we have [68],

$$\begin{Bmatrix} \mathbf{N}(x, y, t) \\ \mathbf{M}(x, y, t) \end{Bmatrix} = \begin{bmatrix} [A](x) & [B](x) \\ [B](x) & [D](x) \end{bmatrix} \begin{Bmatrix} \boldsymbol{\varepsilon}_m(x, y, t) \\ \boldsymbol{\varepsilon}_b(x, y, t) \end{Bmatrix} \quad (7.34)$$

where the coefficients of the matrices $[A](x)$, $[B](x)$ and $[D](x)$ are, respectively, the membrane stiffnesses, the membrane-bending coupling stiffnesses and the bending stiffnesses. It is apparent from equations (7.32) through (7.34) that these stiffnesses are calculated by [68],

$$(A_{ij}, B_{ij}, D_{ij}) = \sum_{k=1}^L \int_{z_k}^{z_{k+1}} \bar{Q}_{ij}(\theta_k(x))(1, z, z^2) dz, \quad (i, j) = 1, 2, 6 \quad (7.35)$$

For symmetric laminates, that is laminates with a symmetric stacking sequence, the membrane-bending coupling matrix, $[B]$, is null, which simplifies equation (7.35) and allow us to consider the membrane problem as separate from the pure bending one [68]. With all the relations between the strains and stresses determined we may proceed to the description of the equations of motion of the system.

7.4 Equations of motion

To obtain the equations of motion of the laminated composite plate, using the CLPT model established in previous sections, a dynamical principle should be used, such as the Principle of Minimum Total Potential Energy, the Principle of Virtual Work or Hamilton's Principle [68]. Amongst these, we will apply the Principle of Virtual Work, which states that [74]:

For all admissible infinitesimal displacement fields that take place, the total work done by all the forces acting on a body, including inertial ones, is zero.

This principle can be written mathematically as [74],

$$\delta W_e + \delta W_i + \delta W_j = 0 \quad (7.36)$$

where δW_e is the virtual work done by external forces, δW_i is the virtual work done by internal forces, which in our case represent the stored elastic energy in the deformation field, and δW_j is the virtual work done by inertial forces.

To proceed with the application of the Principle of Virtual Work, we first need a displacement field to compute the virtual work done by all forces through that specific virtual displacement field. Instead of resorting to a complex mathematical function, describing the exact distribution of displacements for all points of the plate, a method known as the p-version FEM will be used, which equate the displacement field to a series of polynomial space and time functions, termed shape functions [69, 71].

7.4.1 p-version Finite Element Method

There are two main approaches to improve the accuracy of solutions obtained by the FEM: increasing the number of elements of the mesh, which is usually termed the h-version of the method, or increasing the order of the polynomials used to approximate the displacement field, which is named the p-version. The latter allow us to use only one element, for simple structures such as a plate, which can save up computational power, because an assemblage of the global stiffness and mass matrices is not needed [75–77]. Also, the p-version FEM performs better in terms of computational efficiency, requiring, in many problems, the use of less DOFs than the h-version [78].

The partial differential equations that result by the application of the assumptions of the CLPT are of fourth-order in space and of second-order in time for the bending part and of second-order in space and time for the membrane part, requiring continuity of the displacement field for both components, but requiring, as well, the continuity of the first derivative of the displacement for the bending component, at all points of the plate. As such, to fulfil the previous conditions, we should use at least cubic polynomials to interpolate the displacement field, where bending effects are concerned. The shape functions used were derived by Rodrigues' form of Legendre's orthogonal polynomials, which guarantee the continuity of both the displacements and the rotations of the plate, as required [77].

For the in-plane displacements, u_0 and v_0 , the shape function are defined as [76, 79, 80],

$$g_r(\xi) = \sum_{n=0}^{\lfloor r/2 \rfloor} \frac{(-1)^n (2r-2n-5)!!}{2^n n! (r-2n-1)!} \xi^{r-2n-1}, \quad r > 2 \quad (7.37)$$

and for the out of plane shape functions, related to the transverse displacement, w_0 , we have [76, 79, 80],

$$f_r(\xi) = \sum_{n=0}^{\lfloor r/2 \rfloor} \frac{(-1)^n (2r-2n-7)!!}{2^n n! (r-2n-1)!} \xi^{r-2n-1}, \quad r > 4 \quad (7.38)$$

where g_r and f_r are the shape functions of order r , respectively for the in-plane displacements and the transverse one, $r!! = r(r-2) \cdots (2 \text{ or } 1)$ depending on the parity of the integer r , $0!! = (-1)!! = 1$ and $\lfloor \cdot \rfloor$ denote the integer part of a real number. Also, whenever a factorial of a negative number appears in the previous expressions, the respective term is ignored.

The geometric boundary conditions must be satisfied by any valid shape function used in the FEM. The in-plane shape functions have zero values at their limits, $\xi = -1$ and $\xi = 1$, while the out of plane ones have zero value at their limits, but also zero slope, being appropriate for clamped edges. For simply-supported or free edges, the in-plane shape functions should also be used to approximate the transverse displacement, thus, in general, a specific set of the shape functions described above and other cubic and linear functions described by Bardell [79] should be used to accurately represent any type of

boundary condition of the plate [75, 76].

If we represent the entire plate as an unique element, the transformation of coordinates from the local system to the global will be very straightforward and, as previously stated, there will be no need to assemble local matrices into a global one. Then, being ξ and η the local coordinates, their relation with the global ones can be depicted as [75, 76],

$$x = \frac{a}{2}\xi \quad (7.39)$$

$$y = \frac{b}{2}\eta \quad (7.40)$$

allowing the midplane displacements to be written as functions of these local coordinates [75, 76],

$$u_0(\xi, \eta, t) = \sum_{r=1}^{p_i} \sum_{s=1}^{p_i} g_r(\xi) g_s(\eta) q_{rs}^u(t) \quad (7.41)$$

$$v_0(\xi, \eta, t) = \sum_{r=1}^{p_i} \sum_{s=1}^{p_i} g_r(\xi) g_s(\eta) q_{rs}^v(t) \quad (7.42)$$

$$w_0(\xi, \eta, t) = \sum_{r=1}^{p_o} \sum_{s=1}^{p_o} f_r(\xi) f_s(\eta) q_{rs}^w(t) \quad (7.43)$$

where p_i and p_o are the number of in-plane and out of plane shape functions used, respectively, and q_{rs}^i are the generalized coordinates of each displacement i , which are continuous functions of time. It is apparent that the displacement field will be a linear combination of bidimensional polynomial functions, $g_r g_s$ or $f_r f_s$, multiplied by time dependent functions, q_{rs}^i .

The previous equations (7.41) to (7.43) can also be written in matrix form, for a more compact presentation [76],

$$\begin{Bmatrix} u_0(\xi, \eta, t) \\ v_0(\xi, \eta, t) \\ w_0(\xi, \eta, t) \end{Bmatrix} = \begin{bmatrix} \mathbf{g}\mathbf{g}^T(\xi, \eta) & \mathbf{0} & \mathbf{0} \\ \mathbf{0} & \mathbf{g}\mathbf{g}^T(\xi, \eta) & \mathbf{0} \\ \mathbf{0} & \mathbf{0} & \mathbf{f}\mathbf{f}^T(\xi, \eta) \end{bmatrix} \begin{Bmatrix} \mathbf{q}^u(t) \\ \mathbf{q}^v(t) \\ \mathbf{q}^w(t) \end{Bmatrix} \quad (7.44)$$

where $\mathbf{g}\mathbf{g}(\xi, \eta)$ and $\mathbf{f}\mathbf{f}(\xi, \eta)$ are column vectors that represent the products between unidimensional shape functions, generating a bidimensional spatial distribution of displacements [76],

$$\mathbf{g}\mathbf{g}(\xi, \eta) = \begin{pmatrix} gg_{11} \\ gg_{12} \\ \vdots \\ gg_{rs} \\ \vdots \\ gg_{p_i p_i} \end{pmatrix} = \begin{pmatrix} g_1(\xi)g_1(\eta) \\ g_1(\xi)g_2(\eta) \\ \vdots \\ g_r(\xi)g_s(\eta) \\ \vdots \\ g_{p_i}(\xi)g_{p_i}(\eta) \end{pmatrix} \quad (7.45)$$

$$\mathbf{f}\mathbf{f}(\xi, \eta) = \begin{pmatrix} ff_{11} \\ ff_{12} \\ \vdots \\ ff_{rs} \\ \vdots \\ ff_{p_o p_o} \end{pmatrix} = \begin{pmatrix} f_1(\xi)f_1(\eta) \\ f_1(\xi)f_2(\eta) \\ \vdots \\ f_r(\xi)f_s(\eta) \\ \vdots \\ f_{p_o}(\xi)f_{p_o}(\eta) \end{pmatrix} \quad (7.46)$$

and $\mathbf{q}^i(t)$ are the column vectors that contain the generalized coordinates of each displacement i [76],

$$\mathbf{q}^u(t) = \begin{pmatrix} q_{11}^u(t) \\ q_{12}^u(t) \\ \vdots \\ q_{rs}^u(t) \\ \vdots \\ q_{p_i p_i}^u(t) \end{pmatrix}, \quad \mathbf{q}^v(t) = \begin{pmatrix} q_{11}^v(t) \\ q_{12}^v(t) \\ \vdots \\ q_{rs}^v(t) \\ \vdots \\ q_{p_i p_i}^v(t) \end{pmatrix}, \quad \mathbf{q}^w(t) = \begin{pmatrix} q_{11}^w(t) \\ q_{12}^w(t) \\ \vdots \\ q_{rs}^w(t) \\ \vdots \\ q_{p_o p_o}^w(t) \end{pmatrix} \quad (7.47)$$

The approximation used for the displacement field of the composite laminated plate, displayed in equations (7.41) through (7.43), imply the existence of a finite number of DOFs, represented by each of the generalized coordinates. As such, there are p_i^2 for the in-plane displacement u , p_i^2 more for the in-plane displacement v and, finally, p_o^2 for the transverse displacement, w . The total number of DOFs of the model will be $2p_i^2 + p_o^2$, however, if the membrane deformations are neglected, such that we consider only pure bending, the final number of degrees of freedom reduces to p_o^2 , resulting in less computations performed and a lighter numerical problem [7].

7.4.2 Application of the Principle of Virtual Work

Using the displacements described in the previous section and applying the Principle of Virtual Work, through equation (7.36), we can determine the equations of motion that model the system. The first term in equation (7.36) refers to the virtual work done by all the external forces that act on the body.

Considering that both distributed forces, $P_d(x, y, t)$, and punctual ones, $P_p(t)$, that act on a single point, (x_P, y_P) , are acting on the body, we may express their virtual work by [7],

$$\delta W_e = \left\{ \delta q^{uT} \quad \delta q^{yT} \quad \delta q^{wT} \right\} \left(\iint_{\Omega} \begin{Bmatrix} P_d^x \mathbf{g} \mathbf{g}(x, y) \\ P_d^y \mathbf{g} \mathbf{g}(x, y) \\ P_d^z \mathbf{f} \mathbf{f}(x, y) \end{Bmatrix} d\Omega + \begin{Bmatrix} P_p^x \mathbf{g} \mathbf{g}(x_P, y_P) \\ P_p^y \mathbf{g} \mathbf{g}(x_P, y_P) \\ P_p^z \mathbf{f} \mathbf{f}(x_P, y_P) \end{Bmatrix} \right) \quad (7.48)$$

where δq^i are the virtual generalized coordinates of each displacement i and Ω is the area in which the distributed forces are acting. Compacting the previous equation to matrix form we have [7],

$$\delta W_e = \delta \mathbf{q}^T \mathbf{P} \quad (7.49)$$

being $\delta \mathbf{q}$ the vector of virtual generalized coordinates and \mathbf{P} the external forces vector.

The second term of the equation of the Principle of Virtual Work is concerned with the virtual work done by all internal forces, which for our case, as previously stated, is equal to the elastic energy stored in the deformation field of the body. As such, we may write [7, 68],

$$\delta W_i = - \iiint_V \sigma_{ij} \delta \varepsilon_{ij} dV = - \iint_{\Omega} \delta \boldsymbol{\varepsilon}^T(x, y, t) \begin{Bmatrix} \mathbf{N}(x, y, t) \\ \mathbf{M}(x, y, t) \end{Bmatrix} d\Omega \quad (7.50)$$

where we must perform a sum for all possible i and j of $\sigma_{ij} \delta \varepsilon_{ij}$, $\boldsymbol{\varepsilon}$ and $\delta \boldsymbol{\varepsilon}$ are, respectively, the vector of deformations and of virtual deformations, $\boldsymbol{\varepsilon}^T = \{\boldsymbol{\varepsilon}_m^T \quad \boldsymbol{\varepsilon}_b^T\}$, and $d\Omega$ represent the area of the midsurface of the plate $dxdy$.

By including the constitutive relations in the previous equation, we get [7],

$$\begin{aligned} \delta W_i &= - \iint_{\Omega} \delta \boldsymbol{\varepsilon}^T(x, y, t) \begin{bmatrix} [A](x) & [B](x) \\ [B](x) & [D](x) \end{bmatrix} \boldsymbol{\varepsilon}(x, y, t) d\Omega \\ &= - \iint_{\Omega} \delta \boldsymbol{\varepsilon}_m^T(x, y, t) [A](x) \boldsymbol{\varepsilon}_m(x, y, t) d\Omega - \iint_{\Omega} \delta \boldsymbol{\varepsilon}_b^T(x, y, t) [D](x) \boldsymbol{\varepsilon}_b(x, y, t) d\Omega \end{aligned} \quad (7.51)$$

where we have considered $[B](x)$ to be null, restricting our model to symmetric laminates. We can simplify further by denoting the separate parts concerned with membrane or bending effects and assigning a specific stiffness matrix to each of them. Therefore, the stiffness matrix associated with the in-plane

displacements is given by [7],

$$\begin{aligned}
[K_m] &= \begin{bmatrix} [K_m]^{uu} & [K_m]^{uv} \\ [K_m]^{vu} & [K_m]^{vv} \end{bmatrix} \\
&= \iint_{\Omega} \begin{bmatrix} \frac{\partial \mathbf{g}\mathbf{g}}{\partial x} & \mathbf{0} & \frac{\partial \mathbf{g}\mathbf{g}}{\partial y} \\ \mathbf{0} & \frac{\partial \mathbf{g}\mathbf{g}}{\partial y} & \frac{\partial \mathbf{g}\mathbf{g}}{\partial x} \end{bmatrix} \begin{bmatrix} A_{11}(x) & A_{12}(x) & A_{16}(x) \\ A_{12}(x) & A_{22}(x) & A_{26}(x) \\ A_{16}(x) & A_{26}(x) & A_{66}(x) \end{bmatrix} \begin{bmatrix} \frac{\partial \mathbf{g}\mathbf{g}^T}{\partial x} & \mathbf{0} \\ \mathbf{0} & \frac{\partial \mathbf{g}\mathbf{g}^T}{\partial y} \\ \frac{\partial \mathbf{g}\mathbf{g}^T}{\partial y} & \frac{\partial \mathbf{g}\mathbf{g}^T}{\partial x} \end{bmatrix} d\Omega \quad (7.52)
\end{aligned}$$

whereas the part of the stiffness matrix related to the bending and the transverse displacement is [7],

$$[K_b] = [K_b]^{ww} = \iint_{\Omega} \begin{bmatrix} \frac{\partial^2 \mathbf{f}\mathbf{f}}{\partial x^2} & \frac{\partial^2 \mathbf{f}\mathbf{f}}{\partial y^2} & 2\frac{\partial^2 \mathbf{f}\mathbf{f}}{\partial x\partial y} \end{bmatrix} \begin{bmatrix} D_{11}(x) & D_{12}(x) & D_{16}(x) \\ D_{12}(x) & D_{22}(x) & D_{26}(x) \\ D_{16}(x) & D_{26}(x) & D_{66}(x) \end{bmatrix} \begin{bmatrix} \frac{\partial^2 \mathbf{f}\mathbf{f}^T}{\partial x^2} \\ \frac{\partial^2 \mathbf{f}\mathbf{f}^T}{\partial y^2} \\ 2\frac{\partial^2 \mathbf{f}\mathbf{f}^T}{\partial x\partial y} \end{bmatrix} d\Omega \quad (7.53)$$

These definitions of the stiffness matrices allow us to assemble a global stiffness matrix for all DOFs of the system, which gives the virtual work done by all internal forces as a function of the virtual generalized coordinates and of the generalized coordinates [7],

$$\delta W_i = - \left\{ \begin{matrix} \delta \mathbf{q}^{uT} & \delta \mathbf{q}^{vT} & \delta \mathbf{q}^{wT} \end{matrix} \right\} \begin{bmatrix} [K_m]^{uu} & [K_m]^{uv} & [0] \\ [K_m]^{vu} & [K_m]^{vv} & [0] \\ [0] & [0] & [K_b]^{ww} \end{bmatrix} \left\{ \begin{matrix} \mathbf{q}^u \\ \mathbf{q}^v \\ \mathbf{q}^w \end{matrix} \right\} \quad (7.54)$$

and compacting in the same way as equation (7.49), we obtain [7],

$$\delta W_i = -\delta \mathbf{q}^T [K] \mathbf{q} \quad (7.55)$$

where \mathbf{q} is the vector of generalized coordinates and $[K]$ the global stiffness matrix.

Finally, the virtual work done by the inertial forces, which is the only term still undetermined, can be given by [7, 68],

$$\begin{aligned}
\delta W_j &= - \iiint_V \rho \left(\frac{\partial^2 u}{\partial t^2} \delta u + \frac{\partial^2 v}{\partial t^2} \delta v + \frac{\partial^2 w}{\partial t^2} \delta w \right) dV \\
&= - \int_{-\frac{h}{2}}^{\frac{h}{2}} \iint_{\Omega} \rho \left[(\delta \mathbf{q}^{uT} \mathbf{g}\mathbf{g}) \cdot (\mathbf{g}\mathbf{g}^T \ddot{\mathbf{q}}^u) + (\delta \mathbf{q}^{vT} \mathbf{g}\mathbf{g}) \cdot (\mathbf{g}\mathbf{g}^T \ddot{\mathbf{q}}^v) + \right. \\
&\quad \left. + (\delta \mathbf{q}^{wT} \mathbf{f}\mathbf{f}) \cdot (\mathbf{f}\mathbf{f}^T \ddot{\mathbf{q}}^w) \right] d\Omega dz \quad (7.56)
\end{aligned}$$

where $\ddot{\mathbf{q}}^i$ are the generalized accelerations and where we have neglected the rotational inertia, which does not translate to a very rough approximation of our problem, since we are dealing with thin plates.

Because we are also assuming geometric and material symmetry about the midplane of the plate, the global mass matrix, $[M]$, can be determined from the previous equation as [7],

$$[M] = \begin{bmatrix} [M]^{uu} & [0] & [0] \\ [0] & [M]^{vv} & [0] \\ [0] & [0] & [M]^{ww} \end{bmatrix} = \rho h \begin{bmatrix} \iint_{\Omega} \mathbf{g} \mathbf{g} \mathbf{g} \mathbf{g}^T d\Omega & [0] & [0] \\ [0] & \iint_{\Omega} \mathbf{g} \mathbf{g} \mathbf{g} \mathbf{g}^T d\Omega & [0] \\ [0] & [0] & \iint_{\Omega} \mathbf{f} \mathbf{f} \mathbf{f} \mathbf{f}^T d\Omega \end{bmatrix} \quad (7.57)$$

which allows equation (7.56) to be written in the form of equations (7.49) and (7.55) [7],

$$\delta W_j = -\delta \mathbf{q}^T [M] \ddot{\mathbf{q}} \quad (7.58)$$

where $\ddot{\mathbf{q}}$ is the vector of the generalized accelerations.

Substituting each expression of the virtual works on the equation of the Principle of Virtual Work, we arrive at the following [7, 68],

$$\delta \mathbf{q}^T \mathbf{P} - \delta \mathbf{q}^T [K] \mathbf{q} - \delta \mathbf{q}^T [M] \ddot{\mathbf{q}} = 0 \quad (7.59)$$

which must be a valid expression for any arbitrary admissible virtual displacement, hence the equations of motion for a thin plate are, according to the CLPT [7, 68],

$$[M] \ddot{\mathbf{q}} + [K] \mathbf{q} = \mathbf{P} \quad (7.60)$$

It can be immediately seen that the damping was not taken into consideration in this derivation of the equations of motion. In fact, the damping introduced through our damping model is assumed to not have a significant effect on the modes and frequencies of vibration, thus this dynamical model will not consider it.

7.4.3 Natural frequencies and modes of vibration

To analyse the natural frequencies and modes of vibration, the equations of motion should be solved for the case of zero external forces applied, since we are considering that free vibrations are being sustained on the structure. Then, the equations of motion for a free vibrating plate are given by [61, 68],

$$[M] \ddot{\mathbf{q}} + [K] \mathbf{q} = \mathbf{0} \quad (7.61)$$

The characterization of the oscillatory motion requires a solution of the equations of motion. With that in mind, let us establish another hypothesis, which states that the free vibration of a plate consists in

a harmonic synchronous movement with a definite frequency. This implies that the vector of generalized coordinates will have the following form [61],

$$\mathbf{q} = \mathbf{U} \cos(\omega t - \phi) \quad (7.62)$$

where \mathbf{U} is the vector that contains the amplitudes undertaken by each generalized coordinate, ω is the frequency of vibration and ϕ is the phase of the vibration. This definition can be used in the equations of motion (7.61) to give [61],

$$\left(-\omega^2[\mathbf{M}] + [\mathbf{K}]\right)\mathbf{U} \cos(\omega t - \phi) = \mathbf{0} \quad (7.63)$$

For equation (7.63) to be verified for any instant in time, t , being $\cos(\omega t - \phi)$ in general non zero, a generalized eigenvalue problem must be solved. Therefore, these equations can be written in the form [61, 68],

$$\omega^2[\mathbf{M}]\mathbf{U} = [\mathbf{K}]\mathbf{U} \quad (7.64)$$

being ω the natural frequencies of vibration, ω^2 the eigenvalues of the problem and \mathbf{U} the amplitude of the mode shapes of vibration and the eigenvectors of the problem.

Finally, the natural modes of vibration can be computed for each of the calculated frequencies and mode shapes [61],

$$\mathbf{q}_i = \mathbf{U}_i \cos(\omega_i t - \phi_i) \quad (7.65)$$

where i is called the order of the mode of vibration.

A convergence study of this model was performed by Antunes [7] and it was numerically validated, based on the CLPT. It presented good convergence and the results for the vibration modes of thin plates were in very good agreement with the ones found in literature and experimentally determined. Since it was defined that the order of the polynomial used for the out of plane shape functions should be 11 or higher, so that the relative error could be neglected, we will use, throughout the rest of this text polynomials of the order 12, $p_o = 12$.

Now that we have implemented a numerical model for the determination of the mode shapes of vibration of composite laminated plates, we may introduce CNTs to evaluate their effect on the damping characteristics of the system.

Chapter 8

Damping in CNT-reinforced composite plates

One of the main goals of this text is the evaluation of the effect the addition of CNTs has on the damping properties of a fibre-reinforced laminated composite plate. In Chapter 5, a model capable of predicting the increase in damping ratio due to CNT debonding in a nanocomposite was developed and it was applied to the case of a cantilever beam. The model required the mode shapes of vibration of the beam in order to predict the modal damping ratios [1], so, it is evident that to extend the model to the case of plates, their modes of vibration should also be determined.

For that reason, in the previous Chapter 7, a numerical model based on the classical laminated plate theory was implemented to establish the mode shapes of vibration of the system being studied. This dynamical model used a p-version approach of the finite element method to approximate the displacement field of the plate, using a linear combination of polynomials of higher orders. Because we are interested in vibrations caused by the bending of the plate, the membrane components will not have an impact on the final result, for symmetric laminates, with uncoupled equations. Therefore, the only displacement present will be the transverse one, simplifying a lot of the equations developed in that model [68].

We will start our discussion of the damping caused by CNT debonding in CNT-reinforced composite plates by depicting briefly how to extend the damping model developed for beams to plates. Then, we will compare the predictions that our model can produce with experimental results obtained by a modal analysis of such plates in the work of Antunes [7]. This will allow the validation of the model for composite plates, which will facilitate the optimization process of such laminates in future works.

Until the date of submission of this dissertation, to the best knowledge of the author, there was no model developed for predicting the damping properties caused by CNT debonding of CNT-reinforced composite plates. A successful validation of such a model would be very helpful for a future optimization

process that better tailors the desired characteristics of CNT-reinforced composite plates for specific applications and purposes.

8.1 Extension of the damping model to plates

Using the finite element model developed for laminated composite plates, the mode shapes of each DOF are contained in the vector \mathbf{q}_i [61]. These mode shapes are continuous functions, which are to be denoted by $\Phi_i(\xi, \eta)$, throughout the rest of this chapter.

The modal shapes will be used to compute the in-plane strains, due to bending of the plate, which will determine the displacements the RVEs have sustained. By comparing these displacements with the critical displacements for debonding, the hysteretic "stick-slip" damping model may be applied [1], where we should calculate the energy loss per cycle and the maximum elastic energy stored in the entire volume of the plate [52].

As with the other cases, the loss factor relative to a certain mode of vibration is the ratio between the energy lost and the maximum energy stored, for that same mode shape [52]. These modal loss factors are twice the modal damping ratios, for frequencies sufficiently close to the respective natural frequencies of oscillation [63]. At the fundamental level, the theory for plates is just a bidimensional extension of that for beams.

8.1.1 Modes of vibration and deformation fields

In general, the mode shapes of vibration will be given as the eigenvectors of the eigenvalue problem that describe free vibrations on the plate. As such, if we multiply the mode shapes by a constant value, we still have a valid solution to equation (7.64) [61]. This normalization must be performed in order for the functions describing the mode shapes to have the correct amplitude of vibration at each point of the plate, because our damping model is dependent on this amplitude.

As such, we should expect that the maximum transverse displacement for each mode of vibration is given by,

$$w_i^{max}(x, y) = \frac{A}{N} \Phi_i \left(\frac{2x}{a}, \frac{2y}{b} \right) \quad (8.1)$$

where $w_i^{max}(x, y)$ is the maximum transverse displacement for each mode of vibration i and for every point of the plate, A is the amplitude of vibration at a certain point (x, y) and N is a normalization constant, which is the value of the mode shape at that same point of the plate. Also, it is necessary to perform a change of coordinates from the local to the general ones on the mode shapes.

Then, using the strain-displacement relations developed for the CLPT, equations (7.9) through (7.11), we arrive at the maximum deformation field [68],

$$\varepsilon_{xxi}^{max}(x, y, z) = -z \frac{\partial^2 w_i^{max}(x, y)}{\partial x^2} \quad (8.2)$$

$$\varepsilon_{yyi}^{max}(x, y, z) = -z \frac{\partial^2 w_i^{max}(x, y)}{\partial y^2} \quad (8.3)$$

$$\gamma_{xyi}^{max}(x, y, z) = -2z \frac{\partial^2 w_i^{max}(x, y)}{\partial x \partial y} \quad (8.4)$$

where the exponent *max* denotes that these deformations are correspondent to the instant in time when the transverse displacement is maximum.

As we have a biaxial strain condition in the plate, instead of uniaxial, like in the beam case, we could use a criteria, analogous to that of Tresca or von Mises for yield failure [62], to consider the different components of the debonding mechanism. One could exploit the properties of the second invariant of the deviatoric stresses or strains [62] to develop a debonding failure criteria that could model cases where the deformation field act on different directions, based on energetic methods. For the sake of simplicity, this problem will be approached in a different way in this work.

It has been noted that the plate is both in a state of plane stress and of plane strain, so it is possible to find the in-plane principle strains, using Mohr's circle. Then, the maximum principal strains of the plate will be given by [62],

$$\varepsilon_{1i}^{max}(x, y, z) = \left(\frac{\varepsilon_{xxi}^{max} + \varepsilon_{yyi}^{max}}{2} \right) + \sqrt{\left(\frac{\varepsilon_{xxi}^{max} - \varepsilon_{yyi}^{max}}{2} \right)^2 + \left(\frac{\gamma_{xyi}^{max}}{2} \right)^2} \quad (8.5)$$

$$\varepsilon_{2i}^{max}(x, y, z) = \left(\frac{\varepsilon_{xxi}^{max} + \varepsilon_{yyi}^{max}}{2} \right) - \sqrt{\left(\frac{\varepsilon_{xxi}^{max} - \varepsilon_{yyi}^{max}}{2} \right)^2 + \left(\frac{\gamma_{xyi}^{max}}{2} \right)^2} \quad (8.6)$$

where $\varepsilon_{1i}^{max}(x, y, z)$ and $\varepsilon_{2i}^{max}(x, y, z)$ are the principal strains for each mode of vibration and for every point, corresponding to the instant in time where the transverse displacement is maximum.

The principal strains are two normal strains that also contain the effect of the shear deformation, γ_{xy} , and can be applied directly with the criteria of the critical displacement, used in previous chapters. As the normal displacements caused by these two principal strains are perpendicular at every point, simply by the definition of principal strains [62], we can perform a vector addition to obtain a single displacement for every point of the plate, which is a compound addition of each component from each principal strain.

The amplitude of the normal displacements caused by each principal strain will be described by,

$$X_{1i}(x, y, z) = |\varepsilon_{1i}^{max}(x, y, z)|l \quad (8.7)$$

$$X_{2i}(x, y, z) = |\varepsilon_{2i}^{max}(x, y, z)|l \quad (8.8)$$

being $X_{1i}(x, y, z)$ and $X_{2i}(x, y, z)$ the amplitude of the displacements caused by the principal strains, for each mode of vibration i and for every point of the plate, and l is the length of the representative volume element of the damping model. Then, using vector addition of the previous displacements we obtain,

$$X_i(x, y, z) = \sqrt{[X_{1i}(x, y, z)]^2 + [X_{2i}(x, y, z)]^2} \quad (8.9)$$

where $X_i(x, y, z)$ is the amplitude of the vector displacement field at each point of the plate. It is evident that this quantity will have a tridimensional and convoluted distribution of orientations throughout all (x, y, z) .

This undetermined distribution of orientations could be regarded as an additional problem, however, for CNTs homogeneously dispersed in the matrix and with a tridimensional random distribution of orientations, it is possible to overcome this easily. For this case, the orientation of the displacement field is irrelevant, as soon as we use the orientation factor considered in equation (5.69).

The approach described above only works for the specified conditions of a good dispersion of CNTs in the matrix and a random distribution of orientations, however this simplifies immensely the analysis that we would need to perform, if we considered the biaxial state of strain of the original general coordinate system.

8.1.2 "Stick-slip" damping model applied to plates

Now that we have the expression for a unique displacement field to compare with the critical displacement for debonding, we may apply the equations for the energy loss per cycle and the maximum elastic energy stored to compute the modal loss factors. For those we have,

$$W_i(x, y, z) = 4(k_{mf\,CN} - k_{mf\,SW})\delta_1 C_{1i}(x, y, z) + 4(k_{mf\,CN} - k_{mf\,SW})\delta_2 C_{2i}(x, y, z) \quad (8.10)$$

$$C_{1i}(x, y, z) = \left[\Re \left(\sqrt{X_i(x, y, z) - \delta_1} \right) \right]^2 \quad (8.11)$$

$$C_{2i}(x, y, z) = \left[\Re \left(\sqrt{X_i(x, y, z) - \delta_2} \right) \right]^2 \quad (8.12)$$

$$U_i(x, y, z) = \frac{1}{2}k_{mfCN} [X_i(x, y, z)]^2 - \frac{1}{2}(k_{mfCN} - k_{mfSW})(X_i(x, y, z) + \delta_1)C_{1i}(x, y, z) - \frac{1}{2}(k_{mfSW} - k_{mf})(X_i(x, y, z) + \delta_2)C_{2i}(x, y, z) \quad (8.13)$$

where $W_i(x, y, z)$ is the dissipated energy per cycle for a certain mode of vibration i and a point (x, y, z) , $U_i(x, y, z)$ is defined in the same way, but is the maximum elastic energy stored as determined in Chapter 5, and $C_{1i}(x, y, z)$ and $C_{2i}(x, y, z)$ are the functions that show if debonding is happening.

The main difference between these equations and those of the model for cantilever beams is the volume of integration. So, for the case of the plate, the total modal energies are given by,

$$\bar{W}_i = \frac{1}{V} \iiint_V W_i(x, y, z) dV = \frac{2}{abH} \int_{-\frac{a}{2}}^{\frac{a}{2}} \int_{-\frac{b}{2}}^{\frac{b}{2}} \int_0^{\frac{H}{2}} W_i(x, y, z) dz dy dx \quad (8.14)$$

$$\bar{U}_i = \frac{1}{V} \iiint_V U_i(x, y, z) dV = \frac{2}{abH} \int_{-\frac{a}{2}}^{\frac{a}{2}} \int_{-\frac{b}{2}}^{\frac{b}{2}} \int_0^{\frac{H}{2}} U_i(x, y, z) dz dy dx \quad (8.15)$$

where \bar{W}_i is the total dissipated energy per cycle, \bar{U}_i is the total maximum elastic energy stored and V is the volume of the plate, $V = abH$. Finally, just as in the previous systems, the global loss factor of the plate is calculated by,

$$\eta_i = \frac{\bar{W}_i}{2\pi\bar{U}_i} \quad (8.16)$$

with η_i being the global loss factor of the i th mode of vibration. Just as in the case of the beam, these last equations also need to be programmed and solved numerically by a computer.

Finally, we may use equation (5.68) to compute the loss factor of the entire plate, with the effect of the inherent material damping of the matrix and the fibres, and equation (5.28) to determine the modal damping ratio correspondent to each loss factor. For each mode, at resonance, the relation between the loss factor and the damping ratio simplifies to $\eta_i = 2\xi_i$, which we will use throughout the rest of text.

These last equations mark the end of the determination of the damping model for laminated composite plates, caused by CNT debonding in a CNT-reinforced composite. In the next section, we will perform a validation of this model based on the results of an experimental modal analysis of fibre-reinforced composite plates with carbon nanotubes.

8.2 Comparison with an experimental modal analysis

In this section, we will compare all the models developed in this dissertation with the experimental results obtained by Antunes [7] in tensile tests and in an experimental modal analysis of composite plates performed last year. We will compare the predictions of the hierarchic model with the experimental values obtained in the tensile tests, of the CLPT model with the natural frequencies of vibration and of the damping model for plates with the modal damping ratios.

Not all the values for the input variables are described in the work of Antunes [7], since a model for damping caused by CNT debonding was not established by then. This implies that certain quantities, like the critical shear stresses for debonding, τ_1 and τ_2 , and the amplitude of vibration at a certain point of the plate, A , that influence heavily the outcome of the damping model will be estimated, based on previous validations in Chapter 6, or simply tuned, until the prediction fits the experimental data with a reasonable approximation.

First, a discussion of the properties of the plates used is presented, followed by a brief analysis of the experimental apparatus that measured the dynamical behaviour of the system. In the last sections, we will compare the three models, respectively, with each of the relevant experimental measurements that were obtained by Antunes [7].

8.2.1 Plates properties and experimental procedure

The experimental modal analysis was performed in three different composite plates. The first, called the reference plate, was made up of carbon fibre-reinforced epoxy, with no addition of CNTs, while the other two, the 0.01% SWCNTs plate and the 0.05% SWCNTs plate, had a reinforcing of carbon nanotubes of, respectively, 0.01% and 0.05% weight fraction. Although all the plates were fabricated with the aim that the only different between them was the CNT loading, there was some variability in the geometric properties and in the concentration of fibres [7].

All the plates were fabricated as laminates with 30 layers, all stacked at an angle of 0° . This is equivalent to having a single layer with its material coordinates coincident with the global plate coordinate system, so we will model this system as such, for simplicity of the mathematical formulation. Also, for every plate, the fibres are considered rectilinear, being CSCL plates [7]. The geometrical properties of the three plates and their respective concentrations of CNTs and carbon fibres are displayed in Table 8.1.

The mechanical properties of the material that constitutes the plates were determined using tensile tests performed on specimens of the same material as that of the plates [7], however, as we are interested in the predictive power of the theoretical models developed in previous chapters, we should use the properties referenced in the technical reports of the epoxy resin, the fibres and the nanotubes. These

properties are taken from [46, 47, 49, 81–83] and are compiled in Table 8.2. They can also be found in the technical data sheets of Appendix A.

In the work of Antunes [7], the density of the nanotubes is described as the density of graphene, so it is necessary to use the conversion established in a previous part of this text to compute the effective density of the CNTs [11]. Using equation (2.6), we get the density of the nanotubes as $\rho_{CNT} = 1736.0 \text{ kg/m}^3$.

There are also two other elastic properties that are needed to fully define the mechanical properties of the fibres: the transverse Young's modulus and the longitudinal shear modulus. As no information was provided, regarding these values, we will use the experimental results of the tensile tests on the material of the reference plate to tune these quantities, using the hierarchic model. The value of the transverse Young's modulus of the reference plate was $E_{22} = 9.45 \text{ GPa}$ and the longitudinal shear modulus was $G_{12} = 3.56 \text{ GPa}$ [7]. Then, using equations (2.54) and (2.56) and noting that the shear modulus for isotropic media, like the epoxy matrix, is given by an equation analogous to equation (2.40), we have,

$$E_{22f} = 20.9 \text{ GPa}; G_{12f} = 7.88 \text{ GPa}$$

leading to a complete definition of all the important mechanical and geometric variables of the problem.

The dynamical behaviour of all the plates was studied using the same experimental apparatus, which consisted in a frame that supported the hanging plate and the electromagnetic shaker. This provided a FFFF boundary condition, which indicate that the plate was free in all borders. The force transducer was mounted on the point of the plate of coordinates $x = -\frac{a}{10}$ and $y = \frac{b}{10}$, because it was capable of exciting all the relevant modes of vibration for this work, namely the first seven modes [7].

For the plate damping model, two other properties, undefined in the work of Antunes [7], because it lacked a model for predicting CNT induced damping, are needed: the critical shear stresses and the amplitude of vibration at a point of the plate. As there is not a consensus on the values the critical shear stresses for debonding should take, we will adopt the ones from the work of Bhattacharya et al [52], because we have previously used them in some of the validations performed in chapter 6 and they closely approximated the experimental results. With this in mind, we will consider $\tau_1 = 0.3 \text{ MPa}$ and $\tau_2 = 1 \text{ MPa}$

Plate	a /mm	b /mm	H /mm	w_{CNT} /%	v_f /%
Reference	349.5	247.0	2.60	0.00	55
0.01% SWCNTs	349.3	249.0	2.43	0.01	55
0.05% SWCNTs	349.5	249.0	2.74	0.05	52

Table 8.1: Properties of the plates used by Antunes [7].

Property	Value	Units
E_m [Sicomin]	3.30	GPa
ν_m [Pilling]	0.33	-
ρ_m [Sicomin]	1166.9	kg/m ³
E_{CNT} [Lu,1997]	968	GPa
l_{CNT} [NANOSHEL]	11.5	μm
d_{CNT} [NANOSHEL]	1.5	nm
t_{CNT} [Salvetat,1999]	0.3354	nm
ρ_g [NANOSHEL]	2500	kg/m ³
E_{11f} [TeijinCarbonEuropeGmbH]	240	GPa
ν_{12f} [Pilling]	0.2	-
ρ_f [TeijinCarbonEuropeGmbH]	1770	kg/m ³

Table 8.2: Properties of the epoxy resin, the carbon fibres and the CNTs [46, 47, 49, 81–83].

[52].

The amplitude of vibration at a point of the plate is much more difficult to define, however, since a force transducer at a point was used, we may normalize the mode shapes at that same point and try to determine its amplitude of vibration. By fitting the value of the amplitude of vibration at the excitation point to the experimental data, we can obtain an estimation of the amplitude of vibration of the force transducer, which will be equal for any mode of vibration. If the value obtained for the amplitude is reasonable, we can confirm the validity of the model.

With this last consideration, all the input variables that our models require are discussed, thus we may now compare the predictions they are able to produce against the experimental results obtained by Antunes [7]. Although interesting, a detailed presentation of the experimental methods used is out of the scope of this text.

8.2.2 Equivalent elastic properties

One of the goals of this work was to develop a more accurate model for the equivalent elastic properties of multiscale composites than the one used by Antunes [7]. For that reason, it may be interesting to compare both models, before we advance to the more complex model for the vibration of laminated composite plates. The results obtained by Antunes [7] and the respective predictions by the hierarchic model are presented in Table 8.3.

It must be noted that Exp and Num stand for, respectively, the experimental and numerical values obtained by Antunes [7], whilst HM represent the predictions by the present hierarchic model. All the experimental values of the elastic constants were determined by tensile tests on multiscale composite specimens, except for the longitudinal shear modulus, G_{12} , which was based in the rule of mixtures.

The errors shown on the hierarchic model prediction are relative to the experimental values. Also, the experimental density was obtained by the matrix digestion method. Besides that, all the numerical values were computed, including the 0.05% SWCNTs plate, for $\nu_f = 55\%$ by Antunes [7].

Specially for the 0.05% SWCNTs plate, the hierarchic model has produced values that approximate the experiments with accuracy, never having a relative error above 10%. Besides that, the transverse Young's modulus, E_{22} , and the longitudinal shear modulus, G_{12} , which was not determined experimentally as explained before, were predicted with incredible accuracy, as these are, usually, the properties that have fewer accurate models [10].

The main differences in the 0.01% SWCNTs plate are also present in the numerical model used by Antunes [7], which could mean that the experimental values contain some systematic error, for example a lower volume fraction of fibres than the one considered. This would also explain the relatively high error on the longitudinal Young's modulus, E_{11} , of the CNT-reinforced plates, as this should be the property more accurately described.

The value of the Poisson's ratio, ν_{12} , of the reference plate represented the worst approximation of the hierarchic model, however, as explained in Chapter 2, the CNTs should not have a considerable effect on the Poisson's ratio of the multiscale composite, so that value should be almost constant throughout all of the plates. The great discrepancy between the value of the Poisson's ratio for the reference plate in comparison to those of the other two plates could mean an experimental error is at play.

Finally, the density, ρ , was also better represented by the hierarchic model than the one used by

Plate		E_{11} /GPa	E_{22} /GPa	ν_{12}	G_{12} /GPa	ρ /kg m ⁻³
Reference	Exp	132	9.45	0.317	3.56	1501.4
	Num	133.49	7.21	0.26	2.72	1498.2
	HM	133.49 (1.13%)	9.46* (*)	0.259 (-18.3%)	3.56* (*)	1498.6 (-0.19%)
0.01% SWCNTs	Exp	124	8.03	0.259	3.02	1500.2
	Num	133.49	7.24	0.26	2.73	1498.2
	HM	133.49 (7.65%)	9.47 (17.9%)	0.259 (0.00%)	3.57 (18.2%)	1498.6 (-0.11%)
0.05% SWCNTs	Exp	137	8.94	0.278	3.37	1484.5
	Num	133.52	7.37	0.26	2.78	1498.3
	HM	126.41 (-7.73%)	8.97 (0.34%)	0.262 (-5.76%)	3.38 (0.30%)	1480.6 (-0.26%)

* These values were adjusted to the experimental data, so the error is meaningless.

Table 8.3: Comparison between the predictions of the hierarchic model for the equivalent elastic properties of the different plates and the experimental and theoretical values obtained by Antunes [7].

Antunes [7], but we should not forget that a different volume fraction than the one considered in the experimental analysis was also utilized by Antunes [7]. This analysis may imply the hierarchic model considered was, indeed, an improvement to the one used by Antunes [7], specially for the transverse Young's modulus and for the longitudinal shear modulus. The other properties were also well modelled, but there was no substantial improvement, because both numerical models use the rule of mixtures for the longitudinal Young's modulus, the Poisson's ratio and the density of the composite.

8.2.3 Natural frequencies of vibration

Following the equivalent elastic properties, an analysis of the numerical natural frequencies of oscillation and the corresponding mode shapes could validate the CLPT model developed for vibrating composite plates, besides giving further proof of the greater accuracy of the hierarchic model. In Table 8.4, the natural frequencies of vibration determined experimentally, Exp, and numerically, Num, by Antunes [7] and the natural frequencies computed by the dynamical model developed in this text are depicted and compared. Also, in Appendix E, the mode shapes of vibration are represented.

The natural frequencies of vibration are approximated very well by our model, with only one of the values having an error greater than 10%. Besides that, both numerical models used have the same theoretical formulation, so the divergence in results can be attributed only to the differences between the hierarchic model and the equivalent elastic properties obtained by Antunes [7]. As such, it was expected that our model, in comparison to the numerical model of Antunes [7], would approximate better the experimental results for the 0.05% SWCNTs plate, where, in fact, for its higher modes of vibration, there was a significant improvement in the numerical frequencies.

Plate		ω_1 /Hz	ω_2 /Hz	ω_3 /Hz	ω_4 /Hz	ω_5 /Hz	ω_6 /Hz	ω_7 /Hz
Reference	Exp	54.125	103.000	150.625	185.500	213.625	281.625	306.875
	Num	49.81	109.9	149.5	205.8	228.3	304.0	311.4
	CLPT	49.86	110.0	149.6	206.9	229.4	304.1	311.9
		(-7.88%)	(6.80%)	(-0.68%)	(11.5%)	(7.38%)	(7.98%)	(1.64%)
0.01% SWCNTs	Exp	49.125	97.125	139.500	180.750	203.875	267.000	287.250
	Num	42.59	93.20	127.2	186.5	204.7	257.5	272.2
	CLPT	46.28	101.3	138.2	193.6	214.3	279.9	290.2
		(-5.79%)	(4.30%)	(-0.93%)	(7.11%)	(5.11%)	(4.83%)	(1.03%)
0.05% SWCNTs	Exp	54.250	108.750	154.625	201.125	228.000	298.750	320.000
	Num	50.97	111.5	152.2	222.0	243.9	308.1	325.6
	CLPT	51.05	111.8	152.5	213.5	236.4	308.9	320.1
		(-5.90%)	(2.80%)	(-1.37%)	(6.15%)	(3.68%)	(3.40%)	(0.03%)

Table 8.4: Comparison between the natural frequencies of vibration predicted by the numerical model developed for vibrating composite plates (CLPT) and those obtained experimentally (Exp) and numerically (Num) by Antunes [7].

Finally, regarding the mode shapes of vibration, they are very similar to the ones obtained by the experimental modal analysis and the numerical model of Antunes [7]. This was expected, as the values of the properties of the plates are not very different in our model. Again, this fact helps validate the implementation of the numerical program and assure us of the results obtained by the damping model, in the next section.

8.2.4 Modal damping ratios

The last part of this chapter will provide a comparison between the experimental results obtained by Antunes [7] for the modal damping ratios and the predictions of the damping model for plates, established in this text. In Table 8.5, these results are presented, where Exp and SD represent the experimental values obtained by Antunes [7] and their respective standard deviation and DM stands for the predictions of the damping model.

Before proceeding to the analysis of these results, it must be noted that the experimental values shown were obtained by the circle-fit method, because it was considered more reliable than the other experimental method used in the work of Antunes [7]. Besides that, our damping model requires the introduction of the inherent material damping due to the epoxy matrix and the carbon fibres, as it is only capable of predicting the component of damping associated with CNT debonding. For this reason, we used the values of the damping ratio measured experimentally by Antunes [7] for the reference plate to represent this material damping, as it did not contain nanotubes.

The damping model was able to produce relatively good results, where we have adjusted the amplitude of vibration of the excitation point to $A = 1$ mm, because it seemed a reasonable amplitude for the force transducer's displacement. Obviously, the fact that we have not used the real amplitude of excitation will introduce a systematic error that must be accounted for when evaluating this comparison. For a more

Plate		ξ_1 /%	ξ_2 /%	ξ_3 /%	ξ_4 /%	ξ_5 /%	ξ_6 /%	ξ_7 /%
Reference	Exp	0.612	0.401	0.526	0.209	0.298	0.432	0.361
	SD	0.033	0.034	0.029	0.021	0.031	0.024	0.026
0.01% SWCNTs	Exp	0.677	0.446	0.644	0.120	0.255	0.553	0.414
	SD	0.030	0.007	0.021	0.022	0.004	0.035	0.014
	DM	0.626 (-7.53%)	0.434 (-2.69%)	0.540 (-16.2%)	0.247 (106%)	0.314 (23.1%)	0.449 (-18.8%)	0.384 (-7.25%)
0.05% SWCNTs	Exp	0.763	0.488	0.586	0.380	0.319	0.568	0.446
	SD	0.047	0.018	0.010	0.026	0.017	0.031	0.046
	DM	0.805 (5.50%)	0.464 (-4.92%)	0.714 (21.8%)	0.209 (-45.0%)	0.495 (55.2%)	0.624 (9.86%)	0.540 (21.1%)

Table 8.5: Comparison between the modal damping ratios predicted by the damping model developed for vibrating composite plates and those obtained experimentally by Antunes [7].

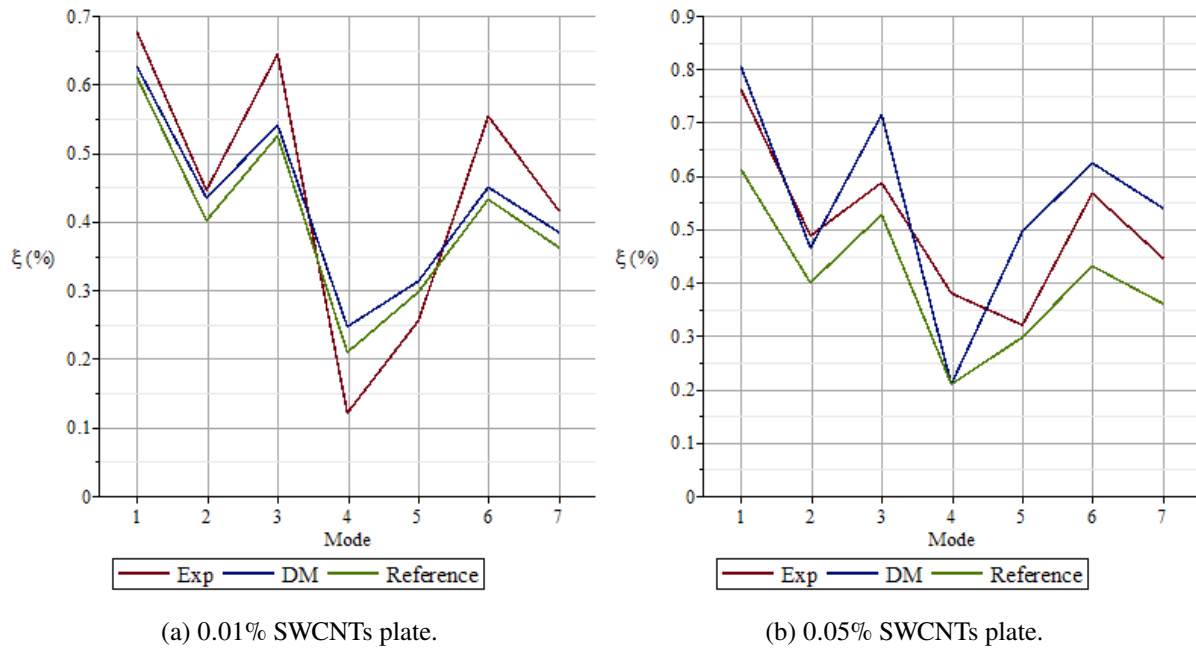


Figure 8.1: Graphical representation of the modal damping ratios predicted by the damping model and of those experimentally determined by Antunes [7].

explicit presentation of the values represented in Table 8.5 we have the same data depicted in Figure 8.1. In these figures we have the experimental and our numerical values represented, as well as the experimental data of the reference plate, which will serve as the material damping for the damping model.

From Figure 8.1 it is evident that our model produced the correct evolution of the damping ratio throughout all modes of vibration. Besides this, almost all of the predictions never had a relative error higher than 20%, with the exception of the 4th and 5th modes. Specially, the first two modes of vibration were guessed with a good accuracy, which indicate that our model may predict, sufficiently well, the damping behaviour of CNT-reinforced composite plates for structural applications, as the fundamental mode can be the most important in many dynamical systems [1].

Although the results shown above are representative of the efficiency of the damping model, it would be more useful to compare only the contribution of CNT debonding to the damping of the plates. Then, the evolution of the component of the damping ratio due to interfacial slippage of nanotubes is shown in Figure 8.2. In these plots, the experimental and numerical values of each respective plate are presented, as well as the variability of the experimental results by the dashed and dotted lines. These lines are calculated with the standard deviations of the experimental modal analysis, representing the error to within one standard deviation away from the mean. The standard deviations shown in the dashed and dotted lines are the sum of the standard deviations associated with the total modal damping ratios of the plate and those regarding the reference plate, to cancel the damping effect of the matrix and the fibres.

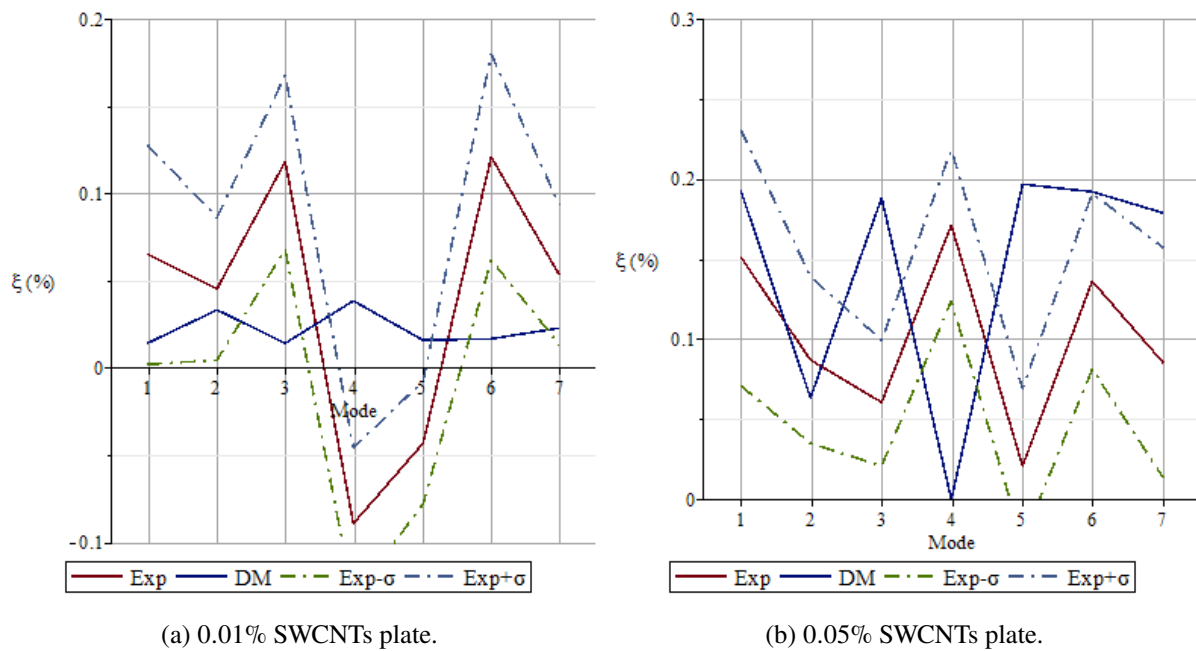


Figure 8.2: Graphical representation of the component of the modal damping ratios, due to interfacial slippage, predicted by the damping model and of those calculated by the experimental values obtained by Antunes [7].

From these graphics, it is evident that modes 4 and 5 may have experimental errors, because the contribution of CNT debonding to their damping ratios are negative for the 0.01% SWCNTs plate, which mean that the CNTs decreased the global damping behaviour of the composite. Assuming the mechanics of debonding are correctly captured by our model, it is not expected to decrease in such manner. In the 0.05% SWCNTs plate, these modes of vibration are the worst approximations as well, further proving this point. Furthermore, the first two modes are contained in the uncertainty interval of one standard deviation, while the 3th, 6th and 7th mode have greater divergences.

Although the damping model has successfully captured some of the essential features of the modal damping ratios, there are significant errors in some of the modes of vibration. These can also be explained by some rough assumptions we have made in the input variables. First of all, the modes have different contributions to the final response of the plate, so the amplitude of vibration of each should be proportional to its importance. Besides that, the amplitude of vibration of 1 mm may not be the actual amplitude when the measurements were made, leading to a systematic error, as previously stated. Also, the critical shear stresses may not be constant or may not have the values described before.

This last analysis of the results obtained in the experiments performed by Antunes [7] provided an insight on the validity of the damping model applied to laminated composite plates and the expected

behaviour of the modal damping ratios with the concentration of CNTs. A deeper analysis of the implications of the equations used in the damping model should be performed in order to understand where to refine it.

Chapter 9

Conclusion

In this dissertation, a theoretical model regarding the effect of the concentration of CNTs on the stiffness and damping characteristics of fibre-reinforced laminated composite plates was developed. Particularly, its effect on the equivalent elastic properties, the natural frequencies and mode shapes of vibration and the modal damping ratios was studied.

This model, which consists of three separate, although complementary, other models, was validated against experimental and numerical data provided by many authors and also against the results of tensile tests performed in this work. It is possible to say, with confidence, that the models described the actual behaviour of the plates, as well as the other studied systems, sufficiently well to represent, at least, a basis for a more refined model of the properties being studied.

In the following paragraphs, a brief conclusion on the results of the many chapters of this work is presented, as well as some suggestions of important future work, regarding this matter. It is in the best interest of the author that this work will serve as a starting point to a deeper understanding of the many advantages and disadvantages of the use of CNTs as an additive in fibre-reinforced composites.

9.1 Conclusions

First, the hierarchic model has produced very good results when compared against experimental and numerical evidence in the bibliography. It is adequate for the linear behaviour of the elastic properties, when low concentrations of CNTs, below 1%, are added to the matrix. Both the longitudinal Young's modulus and the Poisson's ratio have been accurately described by the model, whereas the transverse Young's modulus and the shear modulus were not approximated with the same degree of precision. In spite of this, these last two properties, which are commonly known to be worse modelled by micromechanics models, were very accurately determined in some of the comparisons, this being a point in favour of the

extended Fu model.

Although the experimental tensile tests produced results with a great degree of variability, even varying considerably amongst tests of the same laboratory, the apparent behaviour of increasing stiffness with increasing CNT concentration could be observed. Besides this, the variation in the Poisson's ratio was almost non-existent, further proving the validity of the assumption that the CNTs do not contribute to a change on the Poisson's ratio of the matrix. It was of little interest for the modelling of the composite plates, however the evolution of the tensile strength, observed in the tensile tests, also followed the general trend of increasing with the concentration of CNTs, as defended by many authors, in their works.

The damping model, although not as precise as the hierarchic model for the equivalent elastic properties, has been compared to several experimental and numerical results, on different mechanical systems, such as beams or plates, and the general shape and behaviour of the dependence curves of the loss factor, with the concentration of CNTs and the amplitude of vibration, was observed to be well captured. Mainly, the fundamental mode of vibration was modelled with a great degree of accuracy, leading to the conclusion that it is capable of predicting the interfacial interactions between nanotubes and the matrix of the composite.

However, some problems and inconsistencies appeared as a consequence of some of the assumptions in this analysis. For example, the linear vibrations model relies on a non-linearity in the damping model to produce results, which suggest that the FEM model should be extended to account for a general non-linear behaviour of the dynamical system. Also, the damping model is completely dependent on the critical shear stresses for debonding, which are difficult properties to be measured accurately. Besides this, the model is only valid, as a rule of thumb, for values of weight fraction of CNTs below 1%, as it relies on the hierarchic model, leading to a rather short spectre of values for this parameter. The damping model also encounters some difficulties when applied to fibre-reinforced composites, as it provides better results when the fibres are neglected in the analysis, which, at first, do not seem a reasonable assumption.

The p-version FEM model of vibrating composite plates also described very well the natural frequencies and mode shapes of oscillation of fibre-reinforced composite plates with carbon nanotubes. It was expected that the mode shapes would not change a lot, considering that the nanotubes should not have a large effect on the stiffness of the plates, however the natural frequencies provided were very accurately simulated, with very small errors.

Finally, all the experimental, numerical and theoretical data collected and reviewed indicate that, although the CNTs do not increase considerably the stiffness of multiscale composites, their effect on the damping behaviour of composite beams and plates is very significant, which could be of importance in future works. Perhaps, a laminated fibre-reinforced composite plate made by stacking many plies, could

use some with just resin and CNTs, so that the damping of the overall composite is increased, without a considerable decrease on its stiffness and with a very little concentration of CNTs per weight of the global composite.

9.2 Future work

Regarding the continuity of the work done in this dissertation, there are many improvements that would refine the theoretical models developed and also many other experimental results that would complete those performed in the limited amount of time, for which this thesis had lasted. Some of the suggested future work are:

- Further refine the hierarchic model for the equivalent elastic properties of multiscale composites, so that results closer to the experimental values are obtained, specially for higher concentrations of CNTs and carbon fibres;
- Develop a stiffness model for multiscale composites based on the Mori-Tanaka model and compare it with the current hierarchic model to assess if the Mori-Tanaka approach, although more complex, gives better results than the one from the Halpin-Tsai equations, which provide the foundation of the current model;
- Carry out a more profound study on the mechanisms for CNT debonding and interfacial slippage in CNT-reinforced composites, so that a more refined version of the damping model can be developed, as to predict more accurately the damping characteristics of composite dynamical systems with carbon nanotubes;
- Study the behaviour of CNT-reinforced composite dynamical systems, such as beams and plates, when a non-linear analysis of the vibrations is considered, due to the hysteretic model for damping being proportional to the amplitude of the oscillation, thus introducing non-linearities;
- Manufacture composites reinforced with MWCNTs to evaluate the differences between SWCNTs and MWCNTs experimentally, through tensile tests on specimens and modal analysis on beams and plates;
- Study optimal configurations, with different stacking sequences, of CNT-reinforced laminated composite plates, as to fine tune the damping and stiffness characteristics of such systems, for some particular practical applications.

References

- [1] Lin RM and Lu C. Modeling of interfacial friction damping of carbon nanotube-based nanocomposites. *Mechanical Systems and Signal Processing* 24, page 2996–3012, 2010.
- [2] Thostenson ET, Ren Z, and Chou T-W. Advances in the science and technology of carbon nanotubes and their composites: a review. *Composites Science and Technology* 61, page 1899–1912, 2001.
- [3] Zhou X, Shin E, Wang KW, and Bakis CE. Interfacial damping characteristics of carbon nanotube-based composites. *Composites Science and Technology* 64, page 2425–2437, 2004.
- [4] Iijima S. Helical microtubules of graphitic carbon. *Nature* 354, pages 56–58, 1991.
- [5] Kim M, Park Y, Okoli OI, and Zhang C. Processing, characterization, and modeling of carbon nanotube-reinforced multiscale composites. *Composites Science and Technology* 69, pages 335–342, 2009.
- [6] Kim M, Okoli OI, Jack D, Park Y-B, and Liang ZY. Characterisation and modelling of CNT–epoxy and CNT–fibre–epoxy composites. *Plastics, Rubber and Composites* 40, pages 481–490, 2011.
- [7] Antunes A. *Modes of Vibration of Hybrid Variable Stiffness Composite Laminated Plates: Modelling, experimental verification and analysis*. Faculdade de Engenharia da Universidade do Porto, MEng. thesis, 2019.
- [8] Jones RM. *Mechanics of Composite Materials*. Taylor & Francis, Second edition, 1999.
- [9] Aboudi J, Arnold SM, and Bednarczyk BA. *Micromechanics of Composite Materials, A generalized multiscale analysis approach*. Elsevier - Butterworth-Heinemann, First edition, 2013.
- [10] Raju B, Hiremath SR, and Mahapatra DR. A review of micromechanics based models for effective elastic properties of reinforced polymer matrix composites. *Composite Structures* 204, pages 607–619, 2018.
- [11] Thostenson ET and Chou T-W. On the elastic properties of carbon nanotube-based composites: modelling and characterization. *Journal of Physics D: Applied Physics* 36, pages 573–582, 2003.
- [12] Li C and Chou T-W. A structural mechanics approach for the analysis of carbon nanotubes. *International Journal of Solids and Structures* 40, page 2487–2499, 2003.
- [13] Wang ZL, Gao RP, Poncharal P, de Heer WA, Dai ZR, and Pan ZW. Mechanical and electrostatic properties of carbon nanotubes and nanowires. *Materials Science and Engineering C* 16, pages 3–10, 2001.

- [14] Hayashi T, Kim YA, Matoba T, Esaka M, Nishimura K, Tsukada T, Endo M, and Dresselhaus MS. Smallest freestanding single-walled carbon nanotube. *Nano Letters* 3, pages 887–889, 2003.
- [15] Rafiee M, Liu XF, He XQ, and Kitipornchai S. Geometrically nonlinear free vibration of shear deformable piezoelectric carbon nanotube/fiber/polymer multiscale laminated composite plates. *Journal of Sound and Vibration* 333, pages 3236–3251, 2014.
- [16] Tucker III CL and Liang E. Stiffness predictions for unidirectional short-fiber composites: Review and evaluation. *Composites Science and Technology* 59, pages 655–671, 1999.
- [17] Tsai S and Hahn H. *Introduction to Composite Materials*. Taylor & Francis, First edition, 1980.
- [18] Hyer MW and Waas AM. Micromechanics of linear elastic continuous fiber composites. *Comprehensive composite materials*, pages 345–375, 2000.
- [19] Hashin Z and Shtrikman S. A variational approach to the theory of the elastic behaviour of multiphase materials. *J Mech Phys Solids* 11, page 127–140, 1963.
- [20] Coleman JN, Khan U, Blau WJ, and Gun'ko YK. Small but strong: A review of the mechanical properties of carbon nanotube–polymer composites. *Carbon* 44, page 1624–1652, 2006.
- [21] Martone A, Faiella G, Zarrelli M, Antonucci V, and Giordano M. Investigation of the effective reinforcement modulus of carbon nanotubes in an epoxy matrix. 2011.
- [22] Cox HL. The elasticity and strength of paper and other fibrous materials. *Br J Appl Phys* 3, page 72–79, 1952.
- [23] Chamis C and Hopkins D. Thermoviscoplastic nonlinear constitutive relationships for structural analysis of high temperature metal matrix composites. Technical report, National Aeronautics and Space Administration, 1988.
- [24] Fu S-Y, Hu X, and Yue C-Y. A new model for the transverse modulus of unidirectional fiber composites. *Journal of Materials Science* 33, page 4953–4960, 1998.
- [25] Halpin JC. Effects of environmental factors on composite materials. Technical report, Air Force Materials Lab Wright-Patterson AFB OH, 1969.
- [26] Halpin JC and Kardos JL. The Halpin-Tsai equations: A review. *Polymer Engineering and Science* 16, pages 344–352, 1976.
- [27] Halpin JC. *Primer on Composite Materials Analysis*. Taylor & Francis, Second edition, 2007.
- [28] Lavengood RE and Goehler LA. Stiffness of non-aligned fiber reinforced composites. Technical report, Monsanto Research Corporation, 1971.
- [29] Singh S and Mohanty AK. Wood fiber reinforced bacterial bioplastic composites: Fabrication and performance evaluation. *Composites Science and Technology* 67, page 1753–1763, 2007.
- [30] Hewitt RL and De Malherbe MC. An approximation for the longitudinal shear modulus of continuous fibre composites. *Journal of Composite Materials* 4, page 280–282, 1970.
- [31] Yeh M-K, Tai N-H, and Liu J-H. Mechanical behavior of phenolic-based composites reinforced with multi-walled carbon nanotubes. *Carbon* 44, pages 1–9, 2006.

- [32] Benveniste Y. A new approach to the application of Mori-Tanaka's theory in composite materials. *Mechanics of Materials* 6, pages 147–157, 1987.
- [33] Mori T and Tanaka K. Average stress in matrix and average elastic energy of materials with misfitting inclusions. *Acta Metallurgica* 21, pages 571–574, 1973.
- [34] Eshelby J. The determination of the elastic field of an ellipsoidal inclusion and related problems. *Proc R Soc A Math Phys Eng Sci* 241, page 376–396, 1957.
- [35] Herakovich CT. *Mechanics of Fibrous Composites*. John Wiley & Sons, Inc., First edition, 1998.
- [36] Formica G, Lacarbonara W, and Alessi R. Vibrations of carbon nanotube-reinforced composites. *Journal of Sound and Vibration* 329, page 1875–1889, 2010.
- [37] Tai N-H, Yeh M-K, and Peng T-H. Experimental study and theoretical analysis on the mechanical properties of SWNTs/phenolic composites. *Composites: Part B* 39, page 926–932, 2008.
- [38] Montazeri A, Javadpour J, Khavandi A, Tcharkhtchi A, and Mohajeri A. Mechanical properties of multi-walled carbon nanotube/epoxy composites. *Materials and Design* 31, page 4202–4208, 2010.
- [39] Kulkarni M, Carnahan D, Kulkarni K, Qian D, and Abot JL. Elastic response of a carbon nanotube fiber reinforced polymeric composite: A numerical and experimental study. *Composites: Part B* 41, page 414–421, 2010.
- [40] Gupta AK and Harshaa SP. Analysis of mechanical properties of carbon nanotube reinforced polymer composites using continuum mechanics approach. *Procedia Materials Science* 6, page 18–25, 2014.
- [41] Che J, Yuan W, Jiang G, Dai J, Lim SY, and Chan-Park MB. Epoxy composite fibers reinforced with aligned single-walled carbon nanotubes functionalized with generation 0-2 dendritic poly(amidoamine). *Chem. Mater.* 21, page 1471–1479, 2009.
- [42] Dixit D, Pal R, Kapoor G, and Stabenau M. *Lightweight composite materials processing*. 2016.
- [43] EN ISO 527-1:1996 | plastics | determination of tensile properties | part 1: General principles. Technical report, European Committee for Standardization, 1996.
- [44] EN ISO 527-2:1996 | Plastics | Determination of tensile properties | Part 2: Test conditions for moulding and extrusion plastics. Technical report, European Committee for Standardization, 1996.
- [45] Paupério J. *Análise preliminar da aplicação de nanotubos de carbono para reforço mecânico de compósitos de fibra de carbono*. Faculdade de Engenharia da Universidade do Porto, MEng. thesis, 2019.
- [46] SiPreg SR 121 / KTA 31x: Epoxy systems for "in house" prepregging. Technical report, Sicomin, 2014.
- [47] Single walled nano tubes amine (NH₂) surface modified. Technical report, NANOSHEL.
- [48] Lotya M, King P J, Khan U, De S, and Coleman J N. High-concentration, surfactant-stabilized graphene dispersions. *ACS Nano* 4, page 3155–3162, 2010.

- [49] Lu JP. Elastic properties of single and multilayered nanotubes. *Journal of Physics and Chemistry of Solids* 58, pages 1649–1652, 1997.
- [50] Shan H-Z and Chou T-W. Transverse elastic moduli of unidirectional fiber composites with fiber/matrix interfacial debonding. *Composites Science and Technology* 53, pages 383–391, 1995.
- [51] Sun L, Gibson RF, Gordaninejad F, and Suhr J. Energy absorption capability of nanocomposites: A review. *Composites Science and Technology* 69, page 2392–2409, 2009.
- [52] Bhattacharya S, Alva A, and Raja S. Modeling and characterization of multiwall carbon nanotube reinforced polymer composites for damping applications. *International Journal for Computational Methods in Engineering Science and Mechanics* 15, pages 258–264, 2014.
- [53] Latibari ST, Mehrali M, Mottahedin L, Fereidoon A, and Metselaar HSC. Investigation of interfacial damping nanotube-based composite. *Composites: Part B* 50, page 354–361, 2013.
- [54] Borbón Fd, Ambrosini D, and Curadelli O. Damping response of composites beams with carbon nanotubes. *Composites: Part B* 60, page 106–110, 2014.
- [55] DeValve C and Pitchumani R. Experimental investigation of the damping enhancement in fiber-reinforced composites with carbon nanotubes. *Carbon* 63, page 71–83, 2013.
- [56] Khan SU, Li CY, Siddiqui NA, and Kim J-K. Vibration damping characteristics of carbon fiber-reinforced composites containing multi-walled carbon nanotubes. *Composites Science and Technology* 71, page 1486–1494, 2011.
- [57] Gelb A and Velde WEV. *Multi-input Describing Functions and Nonlinear System Design*. McGraw-Hill Book Company, First edition, 1968.
- [58] Li C and Chou T-W. Elastic moduli of multi-walled carbon nanotubes and the effect of van der waals forces. *Composites Science and Technology* 63, page 1517–1524, 2003.
- [59] Rajoria H and Jalili N. Passive vibration damping enhancement using carbon nanotube-epoxy reinforced composites. *Composites Science and Technology* 65, page 2079–2093, 2005.
- [60] Gou J, Minaie B, Wang B, Liang Z, and Zhang C. Computational and experimental study of interfacial bonding of single-walled nanotube reinforced composites. *Computational Materials Science* 31, page 225–236, 2004.
- [61] Rodrigues JD. *Apontamentos de Vibrações de Sistemas Mecânicos*. Faculdade de Engenharia da Universidade do Porto, 2018.
- [62] Gomes JFS. *Mecânica dos Sólidos e Resistência dos Materiais*. Edições INEGI, First edition, 2010.
- [63] Ewins DJ. *Modal Testing: Theory, Practice and Application*. Research Studies Press Ltd., Second edition, 2000.
- [64] Gu W, Wu HF, Kampe SL, and Lu G-Q. Volume fraction effects on interfacial adhesion strength of glass-fiber-reinforced polymer composites. *Materials Science and Engineering A* 277, page 237–243, 2000.
- [65] ASTM E 756-05 | standard test methods for measuring vibration-damping properties of materials. Technical report, American Society for Testing and Materials, 2005.

- [66] Bauccio M. *ASM Metals Reference Book*. ASM International, Third edition, 1993.
- [67] Fibre Glast Development Corp. 3K, Plain Weave Carbon Fiber Fabric - product data sheet. URL http://www.fibreglast.com/product/3K_Plain_Weave_Carbon_Fiber_Fabric_00530/carbon_fiber_all.html. Accessed in May 19, 2020.
- [68] Reddy JN. *Mechanics of Laminated Composite Plates and Shells: Theory and Analysis*. CRC Press, Second edition, 2003.
- [69] Ribeiro P and Akhavan H. Non-linear vibrations of variable stiffness composite laminated plates. *Composite Structures* 94, pages 2424–2432, 2012.
- [70] Ribeiro P, Akhavan H, Teter A, and Warmański J. A review on the mechanical behaviour of curvilinear fibre composite laminated panels. *Journal of Composite Materials* 48(22), pages 2761–2777, 2013.
- [71] Yazdani S, Ribeiro P, and Rodrigues JD. A p-version layerwise model for large deflection of composite plates with curvilinear fibres. *Composite Structures* 108, pages 181–190, 2014.
- [72] Gürdal Z and Olmedo R. In-plane response of laminates with spatially varying fiber orientations: Variable stiffness concept. *AIAA Journal* 31, pages 751–758, 1993.
- [73] Ramm E. From reissner plate theory to three dimensions in large deformation shell analysis. *ZAMM - Z. Angew. Math. Mech.* 80, pages 61–68, 2000.
- [74] Seabra JH, Oliveira C, Rodrigues JD, Ribeiro P, and Camanho P. *Dinâmica do ponto material e do corpo rígido*. Faculdade de Engenharia da Universidade do Porto, 2004.
- [75] Bardell NS. Free vibration analysis of a flat plate using the hierarchical finite element method. *Journal of Sound and Vibration* 151(2), pages 263–289, 1991.
- [76] Chuaqui T. *Linear and Non-Linear Vibrations of Single-Layer Graphene Sheets*. Faculdade de Engenharia da Universidade do Porto, MEng. thesis, 2016.
- [77] Reddy JN. *An Introduction to the Finite Element Method*. McGraw-Hill, Third edition, 2006.
- [78] Szabó B and Babuška I. *Finite Element Analysis*. John Wiley & Sons, Inc., First edition, 1991.
- [79] Bardell NS. The application of symbolic computing to the hierarchical finite element method. *International Journal for Numerical Methods in Engineering* 28, pages 1181–1204, 1989.
- [80] Han W, Petyt M, and Hsiao K-M. An investigation into geometrically nonlinear analysis of rectangular laminated plates using the hierarchical finite element method. *Finite Elements in Analysis and Design* 18, pages 273–288, 1994.
- [81] Pilling J. Mechanical - Thermal Properties of Selected Fibres/Matrices. URL <http://www.mse.mtu.edu/~drjohn/my4150/props.html>. Accessed May 15, 2019.
- [82] Salvétat J-P, Briggs GAD, Bonard J-M, Bacsá RR, Kulik AJ, Stöckli T, Burnham NA, and Forró L. Elastic and shear moduli of single-walled carbon nanotube ropes. *Physical Review Letters* 82(5), pages 944–947, 1999.
- [83] Tenax ® filament yarn. Technical report, Teijin Carbon Europe GmbH, 2018.

Appendix A

Materials technical data sheets

A.1 Epoxy resin: SiPreg SR 121 / KTA 315 (Sicomín)

SiPreg SR 121 / KTA 31x

Epoxy systems for "In House" Prepregging

Systems for in house prepregging.

Low viscosity systems suitable for manual or mechanical impregnation of fabrics, filaments, braids, stitched reinforcements.

Suitable for filament winding.

90 °C maximum working temperature

Post curing can be between 80 °C up to 150 °C

Two component systems without solvent, without reactive diluent, with no toxic nor CMR components

The 2 components are stable in storage for at least one year

Store the prepregged fabrics away from humidity

Epoxy Resin SR 121

Aspect		Liquid
Color		Clear to light yellow
Color Gardner		2 maximum
Viscosity (mPa.s)	@ 15 °C	24 500 ± 3 000
Rheometer	@ 20 °C	9 800 ± 1 000
CP 50 mm	@ 25 °C	4 500 ± 800
Shear gradient	@ 30 °C	2 300 ± 400
10 s ⁻¹	@ 40 °C	750 ± 200
Dry Extract		100 %
Density :	@ 20 °C	1.176 ± 0.05
Picnometer		
NF EN ISO 2811-1		
Refraction Index		1.5760
Storage Stability :		24 month, does not cristalize

Hardeners KTA 31x

		KTA 317	KTA 315	KTA 313	KTA 311
Aspect / color:		Viscous liquid	Viscous liquid	Viscous liquid	Viscous liquid
Color		White	White	White	White
Reactivity		Very fast	Fast	Slow	Very slow
Dry extract		100 %			
Storage stability		Decants, thus mix before use Do not leave exposed to air, close container after use			
Viscosity (mPa.s)					
Rheomèter	@ 15 °C	16 000 ± 3 000	10 000 ± 2 000	11 000 ± 2 000	14 000 ± 3 000
CP 50 mm	@ 20 °C	12 000 ± 2 000	6 500 ± 1 000	7 700 ± 1 500	9 000 ± 2 000
Shear gradient 10 s ⁻¹	@ 25 °C	9 000 ± 1 500	4 800 ± 1 000	5 700 ± 1 000	6 800 ± 1 500
	@ 30 °C	7 500 ± 1 500	3 800 ± 800	4 500 ± 800	6 100 ± 1 000
	@ 40 °C	5 500 ± 1 000	2 800 ± 600	3 100 ± 600	5 500 ± 1 000
Density	@ 20 °C	1.07	1.13	1.13	1.13
Picnometer					
NF EN ISO 2811-1					

Mix SR 121 / KTA 31x

	SR 121 / KTA 317	SR 121 / KTA 315	SR 121 / KTA 313	SR 121 / KTA 311
Mixing ratio by weight	100 / 21			
Mixing ratio by volume	100 / 23	100 / 22	100 / 22	100 / 22
Initial Viscosity (mPa.s)				
Rheometer @ 20 °C	5 600	6 600	7 000	5 700
PP 50 mm @ 30 °C	1 800	2 200	2 300	3 400
Shear gradient @ 40 °C 10 s ⁻¹	780	1 000	1 000	1 000
Minimum ageing required before process	24 hrs @ 23 °C	24 hrs @ 23 °C	24 hrs @ 23 °C	48 hrs @ 23 °C or 16 hrs 40 °C
Store stability of the prepregged fabrics				
@ -18 °C	6 months	6 months	1 year	1 year
@ 20 °C	7	15	60 days	> 60 days
@ 40 °C	2	5	10 days	> 20 days
Flow	None	None	Yes	Important

Mechanical properties of pure epoxy (non reinforced):

		SR 121 / KTA 315	SR 121 / KTA 313	SR 121 / KTA 311
Curing cycle		12h à 30°C + 4h à 60°C + 2h à 120°C	12h à 30°C + 4h à 60°C + 2h à 120°C	12h à 30°C + 4h à 60°C + 2h à 120°C
Traction				
Modulus	N/mm ²	3300	3700	3600
Maximum Resistance	N/mm ²	75	65	80
Breaking Strength	N/mm ²	72	65	80
Elongation at maximum load	%	3,5	2	2,8
Elongation at break	%	3,5	2	2,8
Flexion				
Modulus	N/mm ²	3300	3700	3500
Maximum Resistance	N/mm ²	129	152	153
Elongation at maximum load	%	5	5,8	5,9
Elongation at break	%	5,2	6,5	7,1
Choc Charpy				
Résilience	kJ/m ²	14	14	17
Transition vitreuse				
Tg1 / onset	°C	116	104	107
Tg1 max	°C	116	112	113

Essais réalisés sur des éprouvettes de résine pure coulée, sans dégazage préalable, entre des plaques en acier.

Mesures effectuées suivant les normes :

Traction : NF T51-034

Flexion : NF T51-001

Compression: NF T 51-101

Choc Charpy: NF T51-501

Transition vitreuse: ISO 11357-2 : 1999 -5°C/180°C sous azote

Tg1 ou Onset : 1^{er} point à 20 °C/mn

Tg1 maximum ou Onset : deuxième passage

A.2 Single-walled carbon nanotube: SA-ML-2 (NANOSHEL)

Intelligent Materials Pvt. Ltd.

Village: Sundran, Teh: Dera Bassi, Punjab (India)
 Tel: +91 9779880077, 9779550077, 9779238252
 Fax: +91 22 66459880

**SPECIFICATION CERTIFICATE**

Product: Single Walled Nano Tubes Amine (NH₂) Surface modified

Description: Sample purity of NANOSHEL SWCNT is 80-98 Vol%, as determined by Raman Spectrophotometer and SEM Analysis. Nanoshel Nano material contains no residual catalyst impurities. Tubes occur in bundles of length ~1 - 10 μ m. (\pm 1.5 μ m) Individual tube length has not been determined.

Quality Control: Each lot of NANOSHEL SWCNT's was tested successfully.

Materials	Single walled Carbon Nanotubes
Stock No.	NS6130-06-632
Category	SA-ML-2
Avg. Diameter	1-2nm
Length	8-15 μ m
Purity	90-95% (SWNT)
Amorphous carbon	<5%
Residue (calcination in air)	<5%
Amine (NH ₂) Surface Modified	2-3wt%
Special surface area	350-450* m ² /g
Bulk density	0.05-0.17 g/cm ³
Real density	2-3 g/cm ³
Charging *	2180 (Capacity: mA h/g)
Discharging*	534 (Capacity: mA h/g)
Volume Resistivity	0.1-0.15 ohm.cm (measured at pressure in powder)

This material ships as dry granules or powder. Each grade contains particles with an average thickness and surface area. All dimensions represent median sizes and there is a distribution around the mean.

A.3 Carbon fibre: Tenax®-E HTS45 12K (Teijin Carbon Europe GmbH)



Tenax® filament yarn

Product Data Sheet (EU)

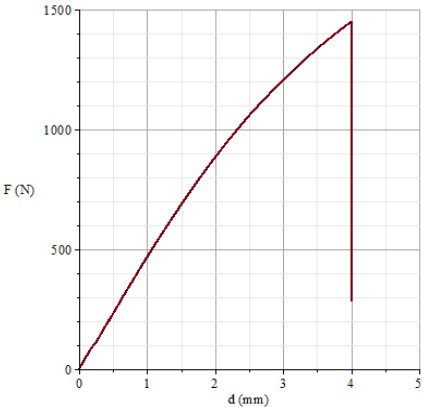
Brand name	Production site	Fiber family & tensile properties	Sizing properties	Number of filaments	Nominal linear density (without sizing)	Additional information	Tensile Strength [MPa]	Tensile modulus [GPa]	Elongation at break [%]	Filament diameter [µm]	Density [g/cm ³]	Sizing	Size level [%]
Tenax®-J	HTA40	E15	1K	67tex	15S		4100	240	1,7	7,0	1,77	EP	2,5
Tenax®-E	HTA40	E13	3K	200tex			4100	240	1,7	7,0	1,77	EP	1,3
Tenax®-E	HTA40	E13	3K	200tex	15Z		4100	240	1,7	7,0	1,77	EP	1,3
Tenax®-J/E	HTA40	E13	6K	400tex			4100	240	1,7	7,0	1,77	EP	1,3
Tenax®-E	HTA40	E13	6K	400tex	10Z		4100	240	1,7	7,0	1,77	EP	1,3
Tenax®-J	HTS40	E13	3K	200tex			4400	240	1,8	7,0	1,77	EP	1,3
Tenax®-J	HTS40	E13	6K	400tex			4400	240	1,8	7,0	1,77	EP	1,3
Tenax®-E	HTS40	F13	12K	800tex			4400	240	1,8	7,0	1,77	PU	1,0
Tenax®-E	HTS40	F13	12K	800tex	10Z		4400	240	1,8	7,0	1,77	PU	1,0
Tenax®-E	HTS40	F13	24K	1600tex			4400	240	1,8	7,0	1,77	PU	1,0
Tenax®-E	HTS40	F13	24K	1600tex	5Z		4400	240	1,8	7,0	1,77	PU	1,0
Tenax®-E	HTS45	E23	3K	200tex			4500	235	1,9	7,0	1,77	EP	1,3
Tenax®-E	HTS45	E23	3K	200tex	15Z		4500	235	1,9	7,0	1,77	EP	1,3
Tenax®-E	HTS45	E23	12K	800tex			4500	240	1,9	7,0	1,77	EP	1,3
Tenax®-E	HTS45	E23	12K	800tex	10Z		4500	240	1,9	7,0	1,77	EP	1,3
Tenax®-E	HTS45	P12	12K	800tex			4500	240	1,9	7,0	1,77	TP	0,5
Tenax®-E	STS40	E23	24K	1600tex			4300	240	1,8	7,0	1,78	EP	1,3
Tenax®-E	STS40	F11	24K	1600tex			4300	240	1,8	7,0	1,78	PU	0,17
Tenax®-J/E	STS40	F13	24K	1600tex			4300	240	1,8	7,0	1,78	PU	1,0
Tenax®-J/E	STS40	F13	48K	3200tex			4300	250	1,7	7,0	1,77	PU	1,0
Tenax®-J/E	STS40	F13	48K	3200tex	CP		4300	250	1,7	7,0	1,77	PU	1,0
Tenax®-J	UTS50	F13	12K	800tex			5100	245	2,1	7,0	1,78	PU	1,0
Tenax®-J	UTS50	F22	12K	800tex	S		5100	245	2,1	7,0	1,78	PU	0,8
Tenax®-J/E	UTS50	F24	24K	1600tex	DCP		5100	245	2,1	7,0	1,78	PU	2,0
Tenax®-E	ITS50	F23	24K	1600tex	D		5100	265	1,9	7,0	1,80	PU	1,0
Tenax®-J	IMS60	E13	24K	830tex			5800	290	2,0	5,0	1,79	EP	1,3
Tenax®-E	IMS65	E23	24K	830tex			6000	290	2,1	5,0	1,78	EP	1,3
Tenax®-E	IMS65	P12	24K	830tex			6000	290	2,1	5,0	1,78	TP	0,8
Tenax®-J	UMS40	F23	24K	800tex	S		4700	390	1,2	4,9	1,79	PU	1,0
Tenax®-J	UMS45	F22	12K	385tex			4600	425	1,1	4,7	1,83	PU	0,8
Tenax®-J	HTS40	A23	12K	1420tex	MC		2900	230	1,3	7,5*	2,70	PU	1,3

* inkl. 0,25 µm Nickel

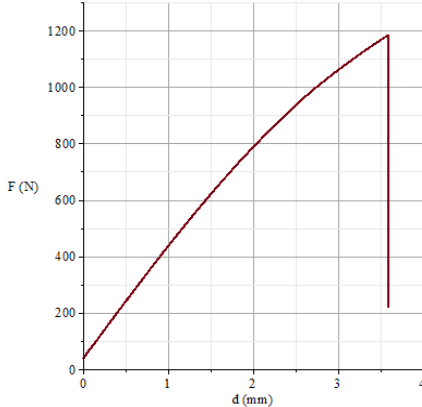
- Please contact our sales team any time, for choosing the right type. The stated numbers are typical values. For design purposes please request a fiber specification.
- Please note the application (aerospace or industry & sports) on your order.
- The export or transfer of carbon fibers can be subject to authorization, depending on end-use and final destination.

Appendix B

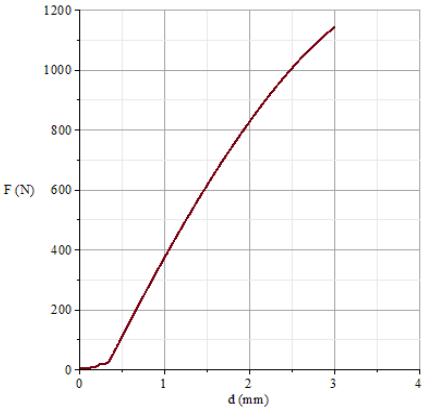
Tensile tests: load - displacement curves



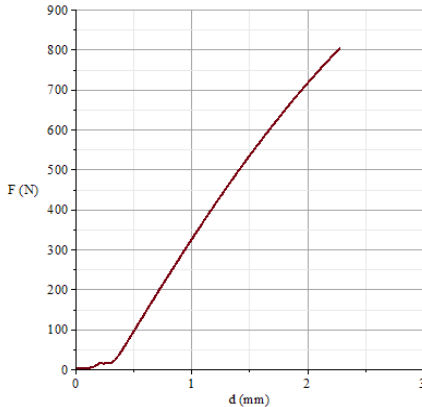
(a) Reference 1 - Specimen 1.



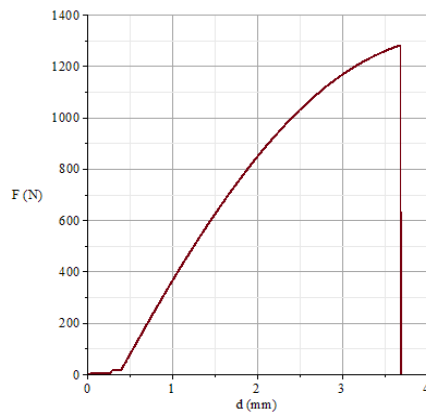
(b) Reference 1 - Specimen 2.



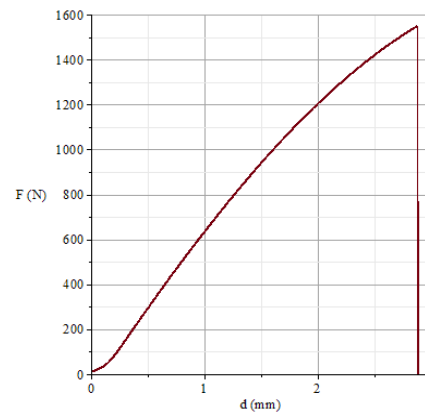
(c) Reference 1 - Specimen 3.



(d) Reference 1 - Specimen 4.

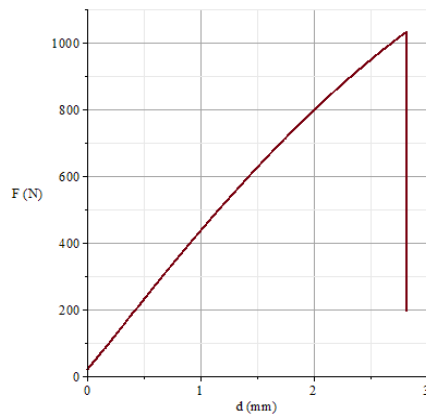


(e) Reference 1 - Specimen 5.

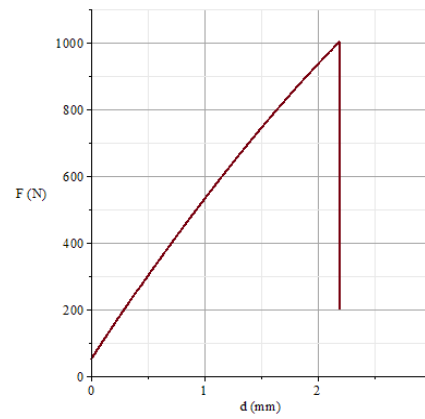


(f) Reference 1 - Specimen 6.

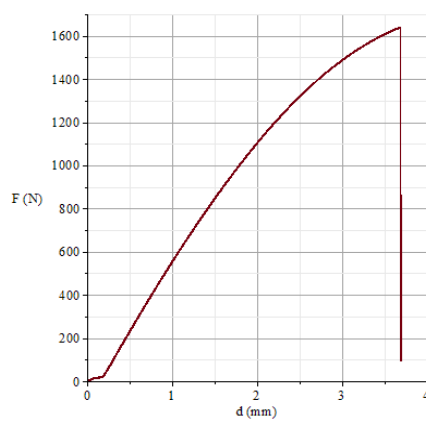
Figure B.1: Load - displacement curves of the specimens of reference 1 (Epoxy Resin).



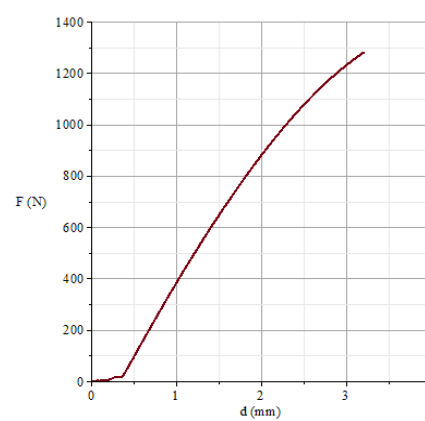
(a) Reference 2 - Specimen 1.



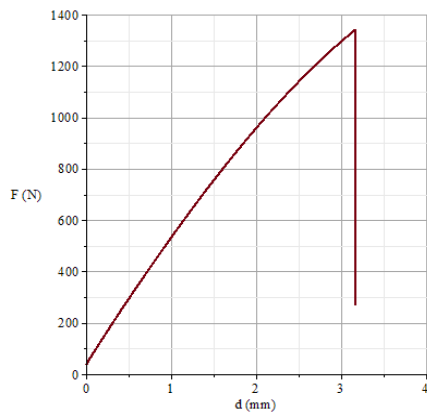
(b) Reference 2 - Specimen 2.



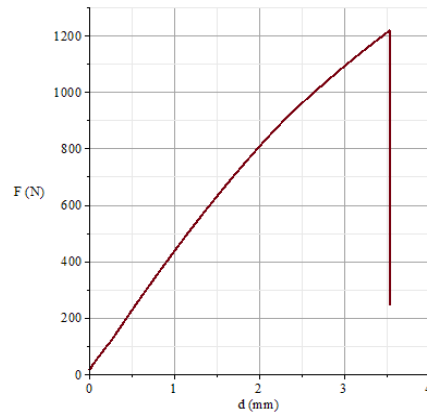
(c) Reference 2 - Specimen 3.



(d) Reference 2 - Specimen 4.

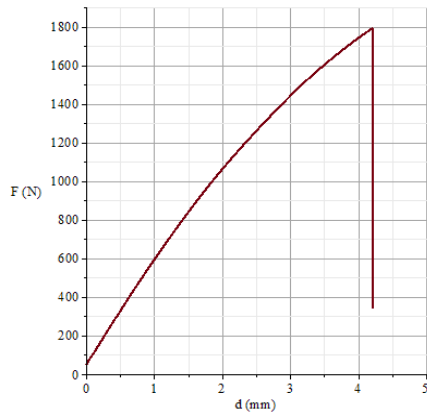


(e) Reference 2 - Specimen 5.

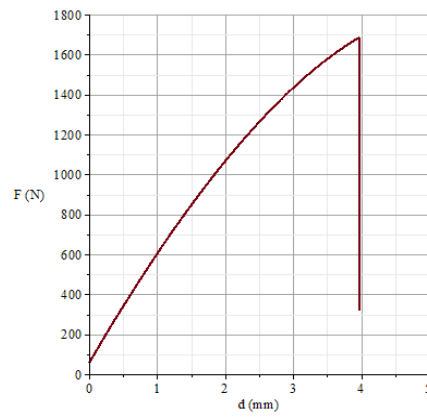


(f) Reference 2 - Specimen 6.

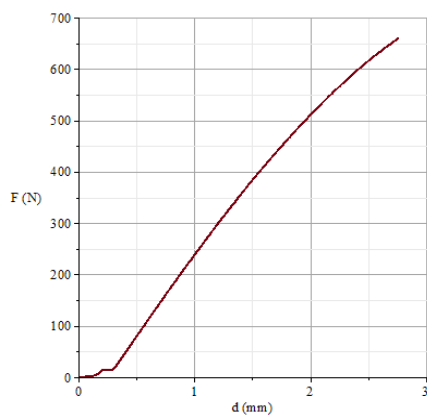
Figure B.2: Load - displacement curves of the specimens of reference 2 (0.05 CNT Normal).



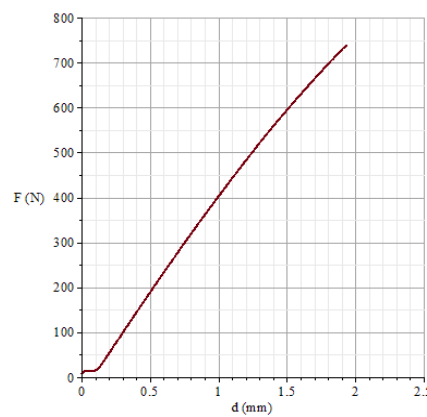
(a) Reference 3 - Specimen 1.



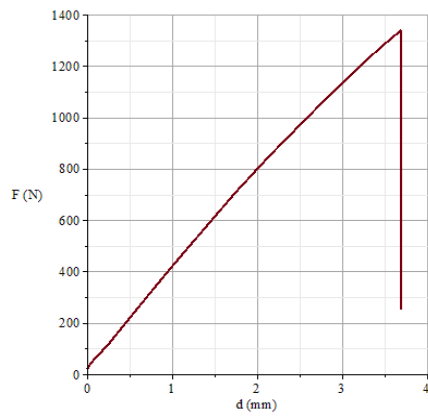
(b) Reference 3 - Specimen 2.



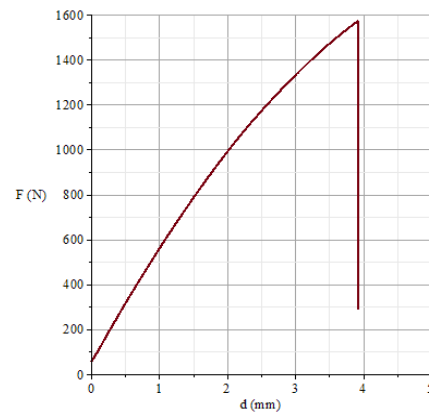
(c) Reference 3 - Specimen 3.



(d) Reference 3 - Specimen 4.

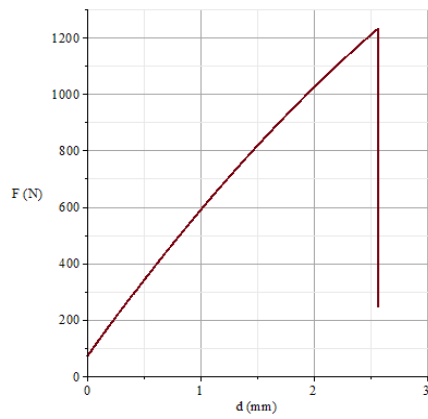


(e) Reference 3 - Specimen 5.

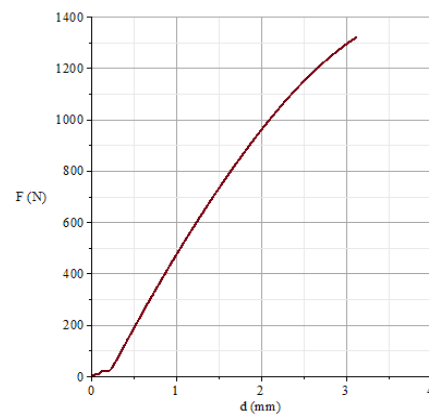


(f) Reference 3 - Specimen 6.

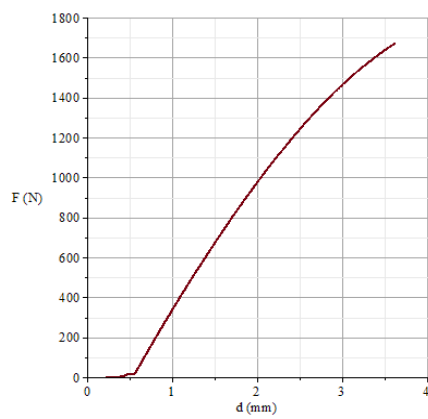
Figure B.3: Load - displacement curves of the specimens of reference 3 (0.05 CNT SDBS).



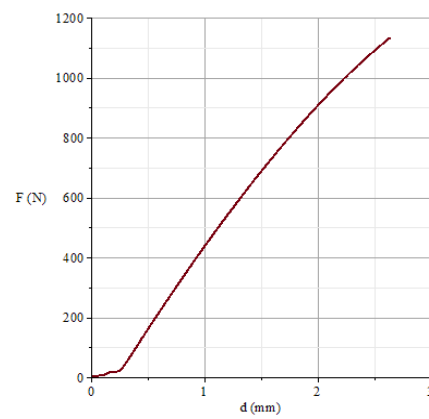
(a) Reference 4 - Specimen 1.



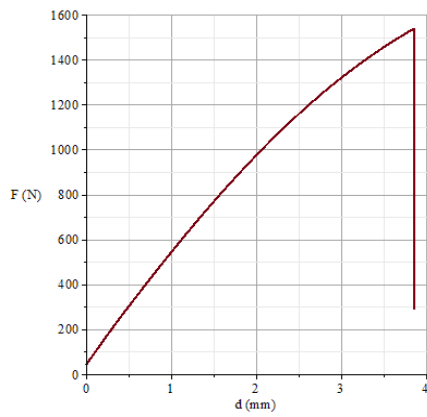
(b) Reference 4 - Specimen 2.



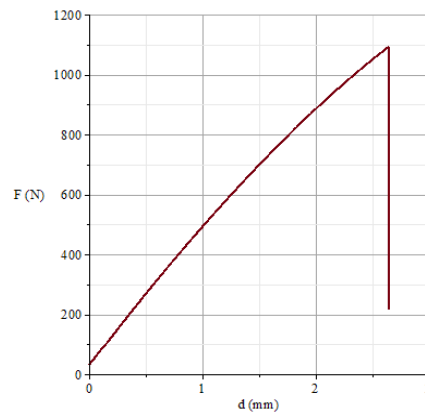
(c) Reference 4 - Specimen 3.



(d) Reference 4 - Specimen 4.

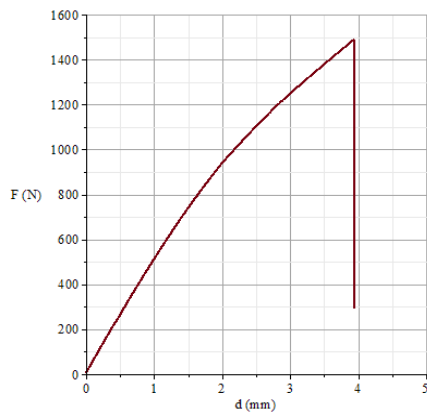


(e) Reference 4 - Specimen 5.

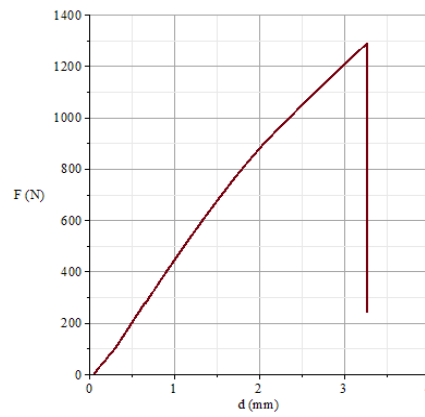


(f) Reference 4 - Specimen 6.

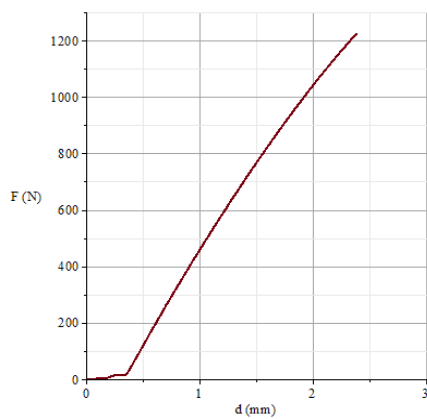
Figure B.4: Load - displacement curves of the specimens of reference 4 (0.05 CNT Triton).



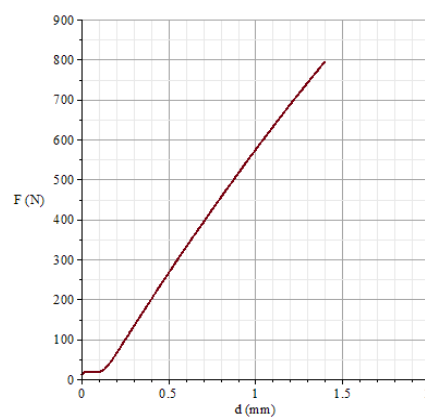
(a) Reference 5 - Specimen 1.



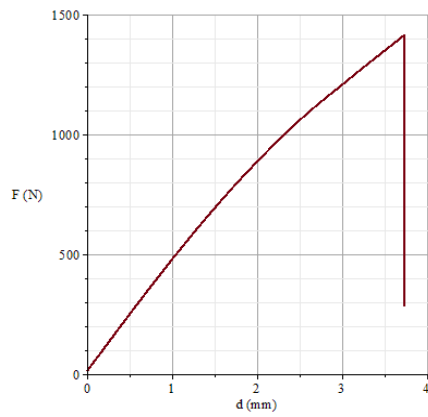
(b) Reference 5 - Specimen 2.



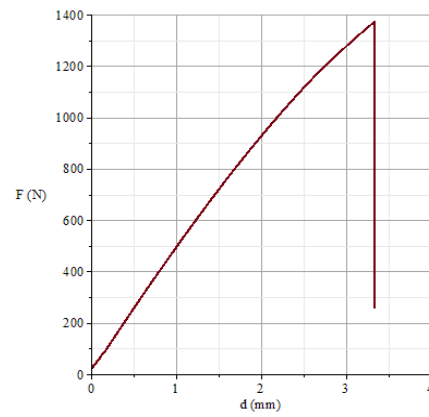
(c) Reference 5 - Specimen 3.



(d) Reference 5 - Specimen 4.

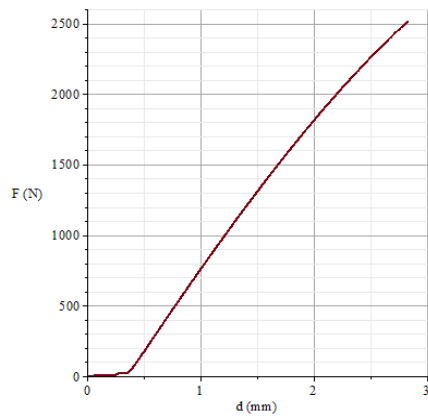


(e) Reference 5 - Specimen 5.

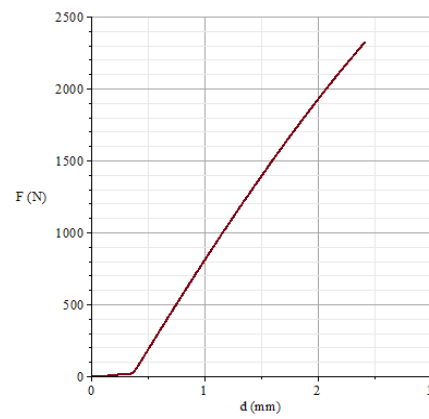


(f) Reference 5 - Specimen 6.

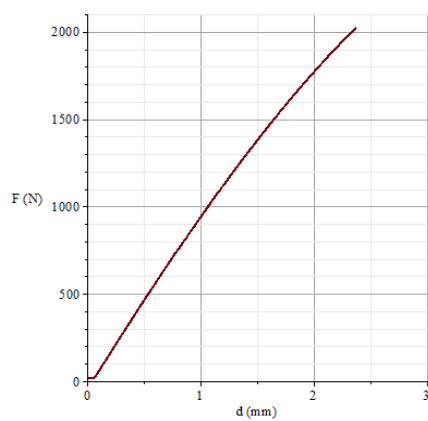
Figure B.5: Load - displacement curves of the specimens of reference 5 (0.05 CNT High).



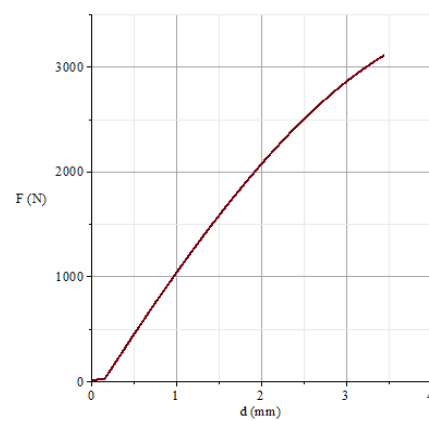
(a) Reference 6 - Specimen 1.



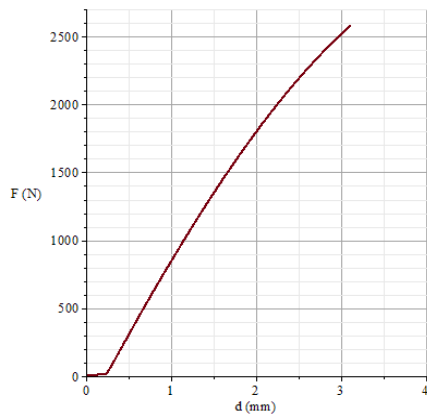
(b) Reference 6 - Specimen 2.



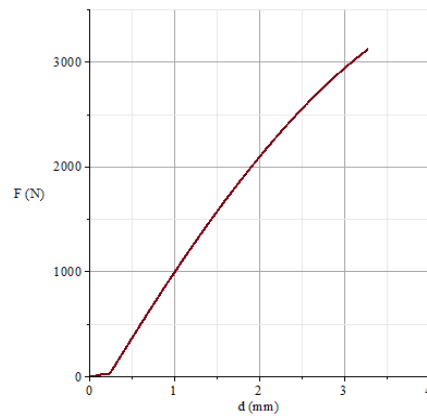
(c) Reference 6 - Specimen 3.



(d) Reference 6 - Specimen 4.

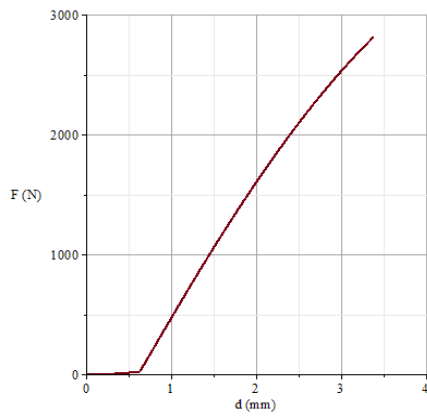


(e) Reference 6 - Specimen 5.

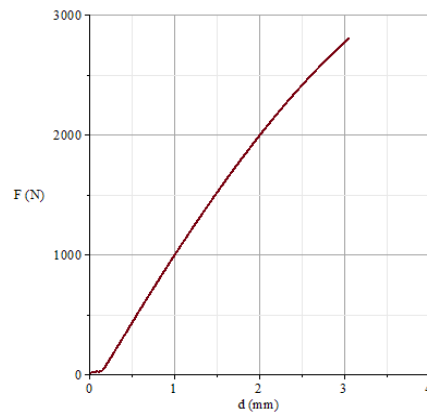


(f) Reference 6 - Specimen 6.

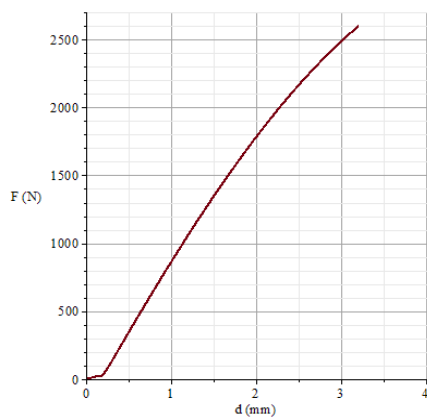
Figure B.6: Load - displacement curves of the specimens of reference 6 (0.1 CNT High).



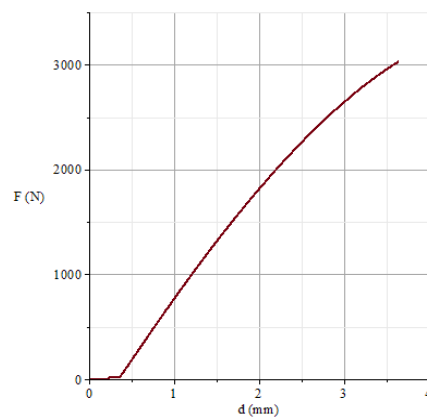
(a) Reference 7 - Specimen 1.



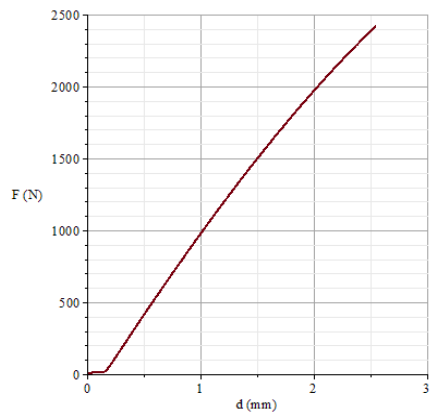
(b) Reference 7 - Specimen 2.



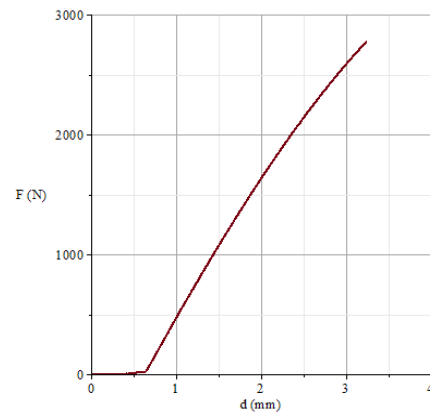
(c) Reference 7 - Specimen 3.



(d) Reference 7 - Specimen 4.



(e) Reference 7 - Specimen 5.

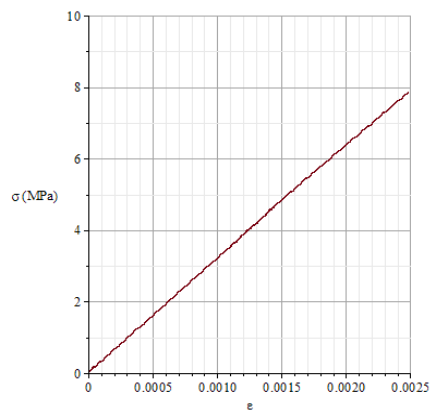


(f) Reference 7 - Specimen 6.

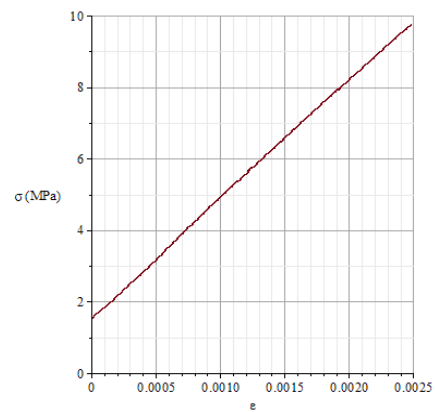
Figure B.7: Load - displacement curves of the specimens of reference 7 (0.2 CNT High).

Appendix C

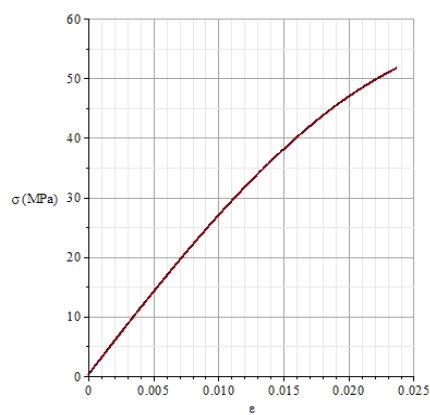
Tensile tests: stress - strain curves



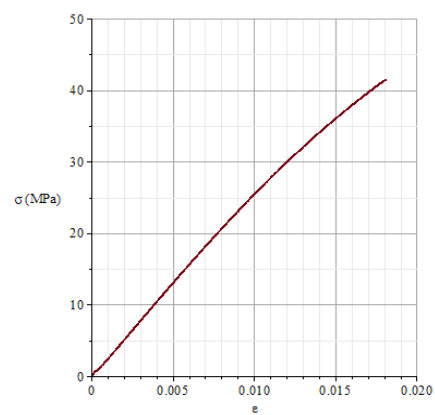
(a) Reference 1 - Specimen 1.



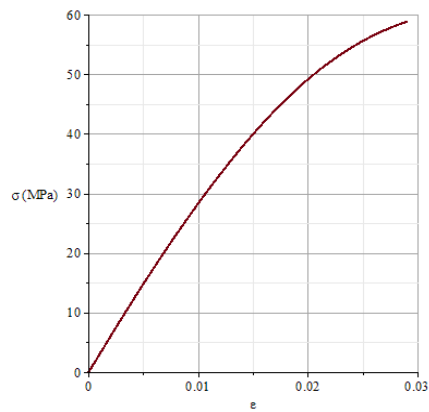
(b) Reference 1 - Specimen 2.



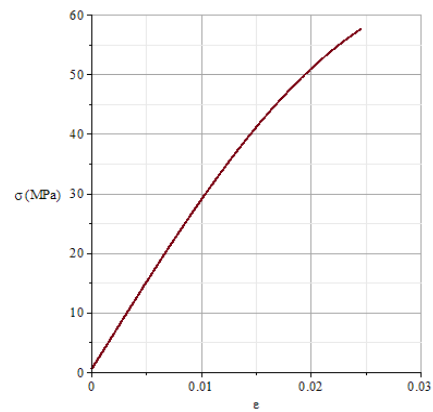
(c) Reference 1 - Specimen 3.



(d) Reference 1 - Specimen 4.

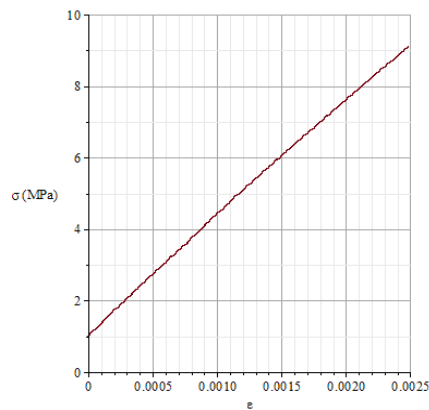


(e) Reference 1 - Specimen 5.

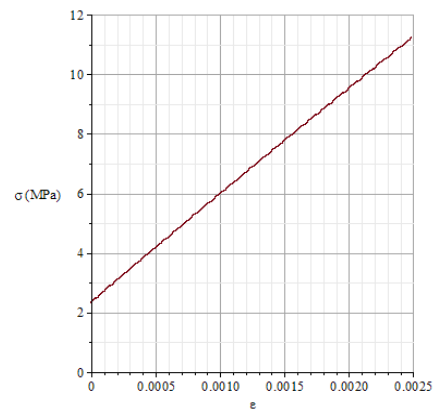


(f) Reference 1 - Specimen 6.

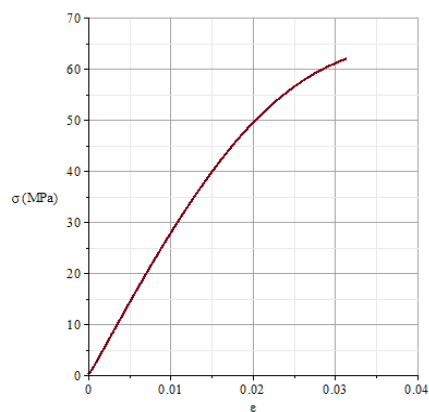
Figure C.1: Stress - strain curves of the specimens of reference 1 (Epoxy resin).



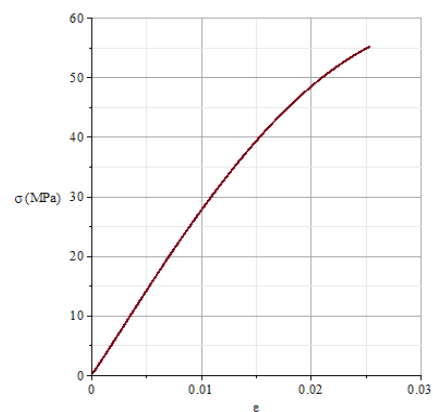
(a) Reference 2 - Specimen 1.



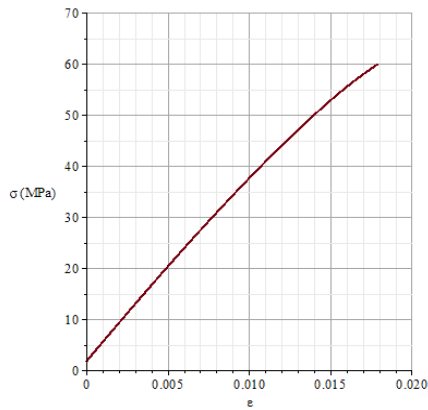
(b) Reference 2 - Specimen 2.



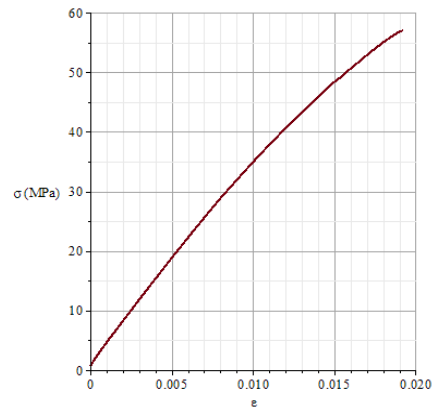
(c) Reference 2 - Specimen 3.



(d) Reference 2 - Specimen 4.

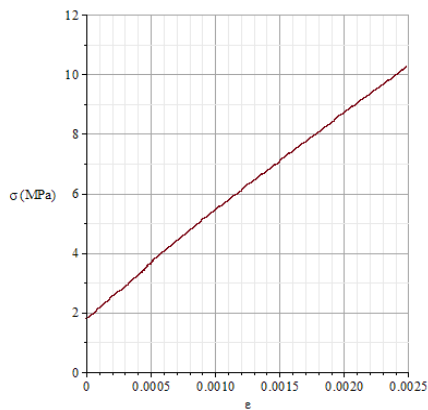


(e) Reference 2 - Specimen 5.

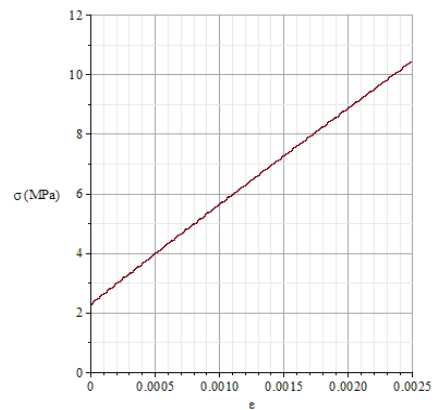


(f) Reference 2 - Specimen 6.

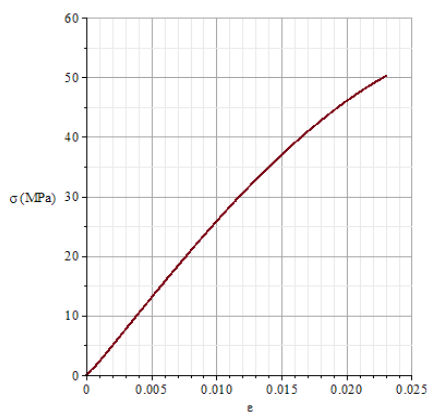
Figure C.2: Stress - strain curves of the specimens of reference 2 (0.05 CNT Normal).



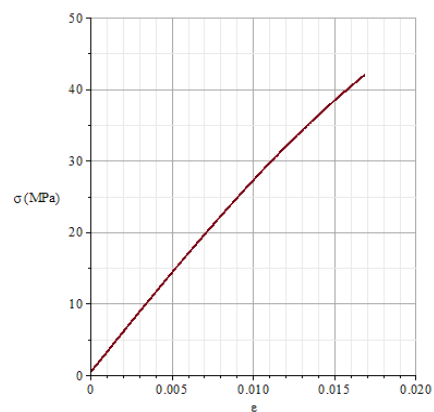
(a) Reference 3 - Specimen 1.



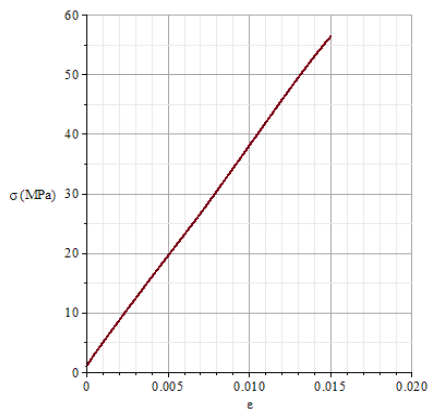
(b) Reference 3 - Specimen 2.



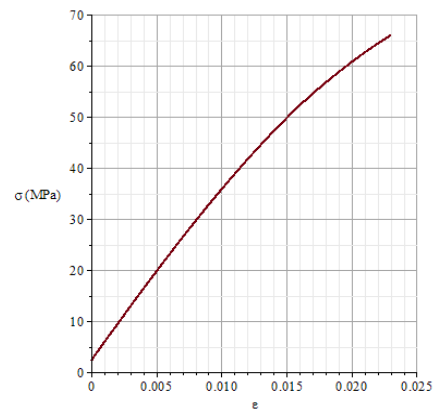
(c) Reference 3 - Specimen 3.



(d) Reference 3 - Specimen 4.

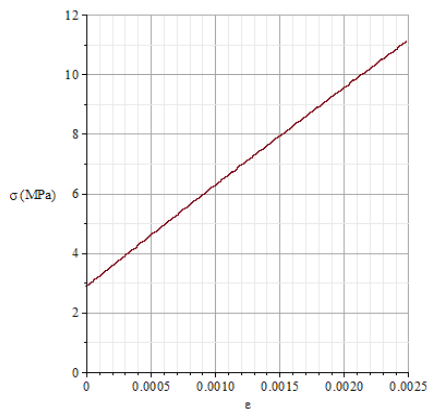


(e) Reference 3 - Specimen 5.

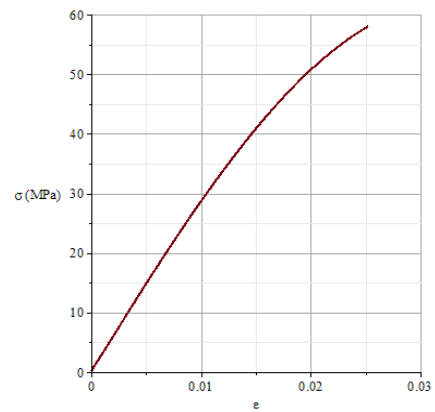


(f) Reference 3 - Specimen 6.

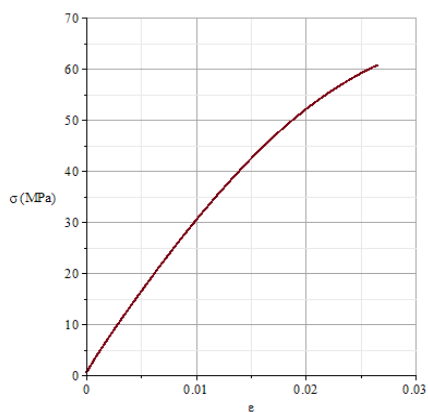
Figure C.3: Stress - strain curves of the specimens of reference 3 (0.05 CNT SDBS).



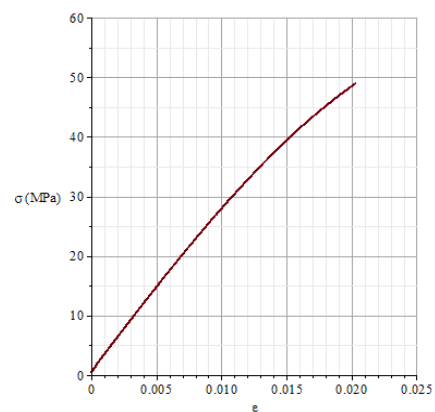
(a) Reference 4 - Specimen 1.



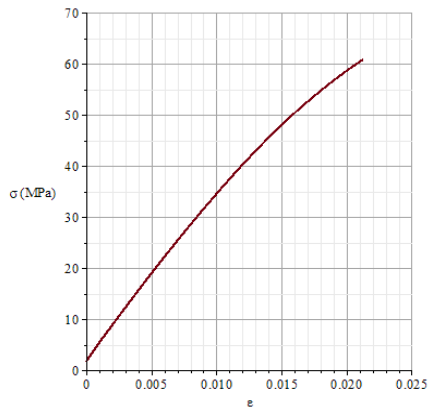
(b) Reference 4 - Specimen 2.



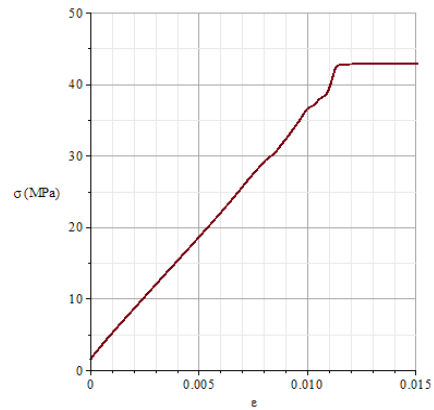
(c) Reference 4 - Specimen 3.



(d) Reference 4 - Specimen 4.

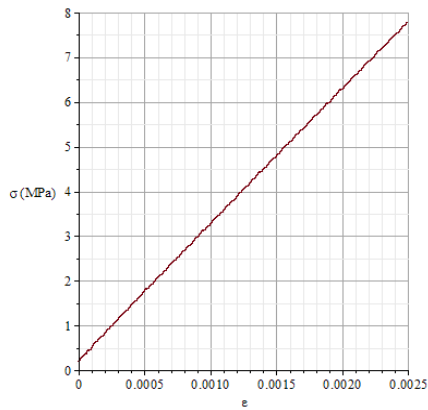


(e) Reference 4 - Specimen 5.

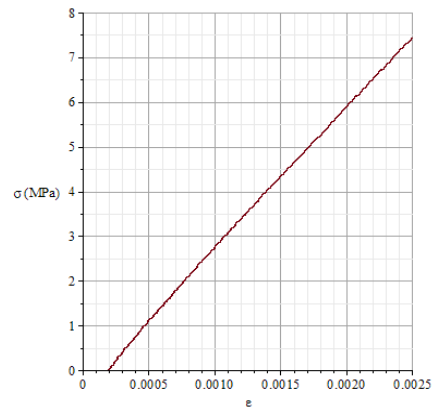


(f) Reference 4 - Specimen 6.

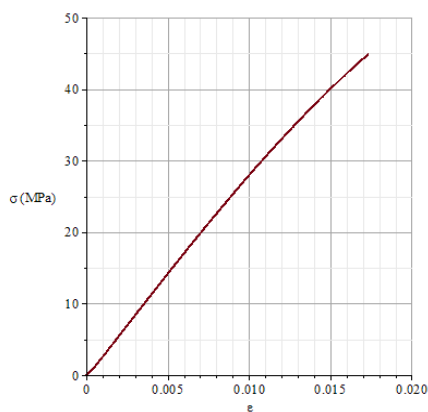
Figure C.4: Stress - strain curves of the specimens of reference 4 (0.05 CNT Triton).



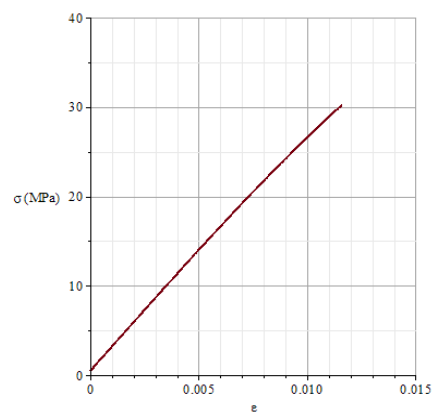
(a) Reference 5 - Specimen 1.



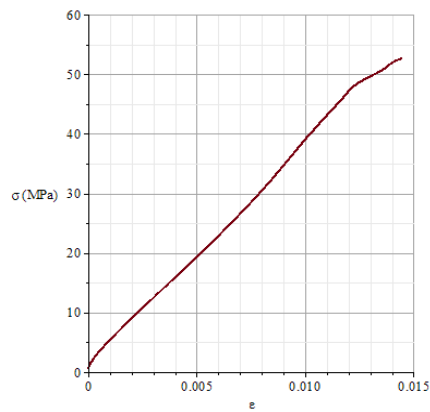
(b) Reference 5 - Specimen 2.



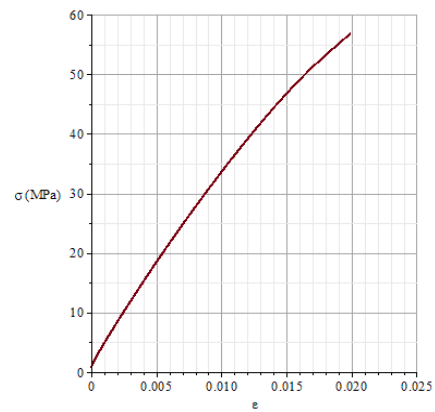
(c) Reference 5 - Specimen 3.



(d) Reference 5 - Specimen 4.

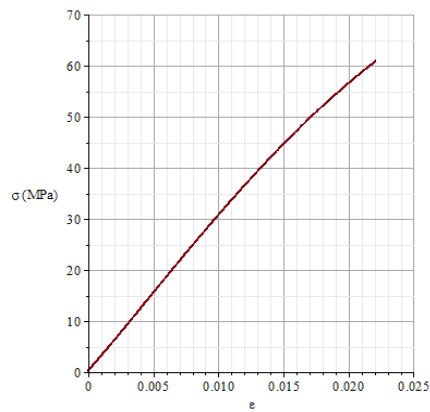


(e) Reference 5 - Specimen 5.

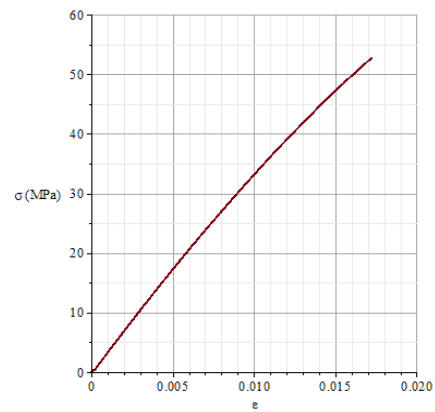


(f) Reference 5 - Specimen 6.

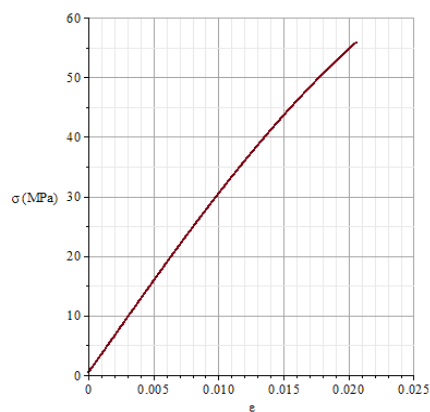
Figure C.5: Stress - strain curves of the specimens of reference 5 (0.05 CNT High).



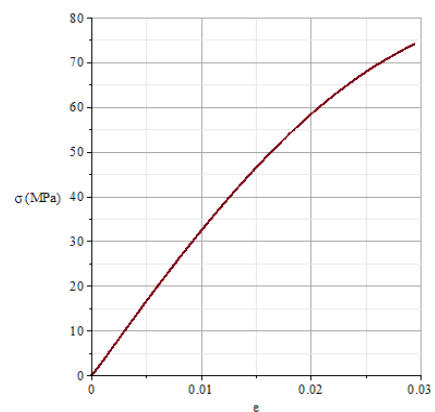
(a) Reference 6 - Specimen 1.



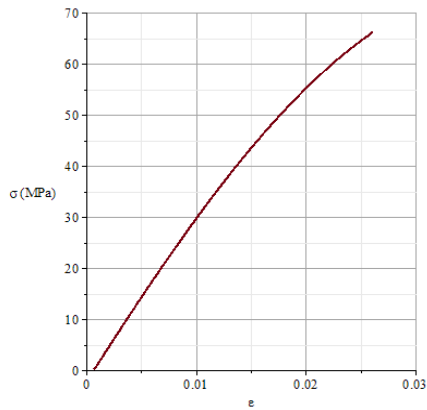
(b) Reference 6 - Specimen 2.



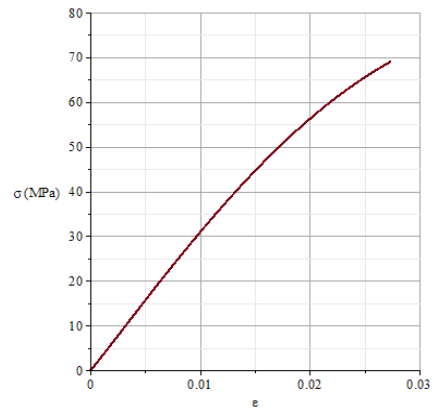
(c) Reference 6 - Specimen 3.



(d) Reference 6 - Specimen 4.

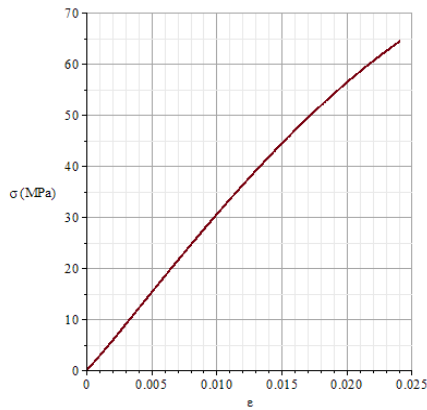


(e) Reference 6 - Specimen 5.

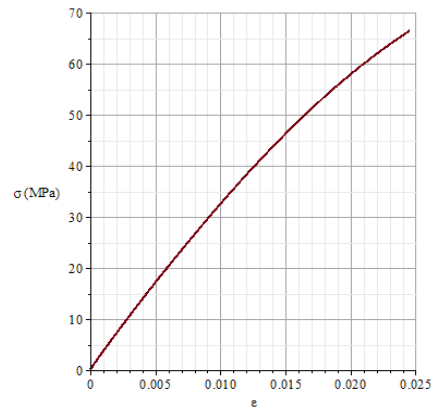


(f) Reference 6 - Specimen 6.

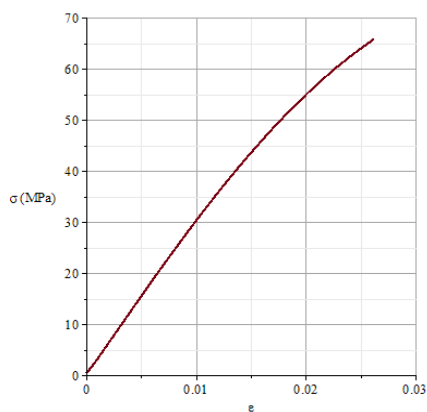
Figure C.6: Stress - strain curves of the specimens of reference 6 (0.1 CNT High).



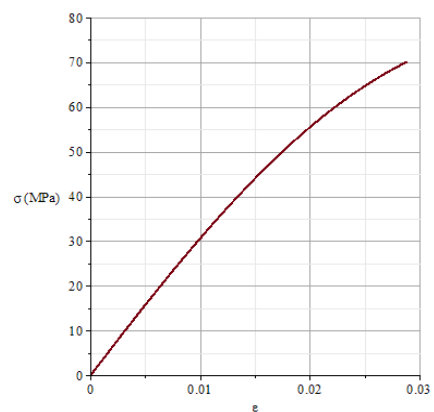
(a) Reference 7 - Specimen 1.



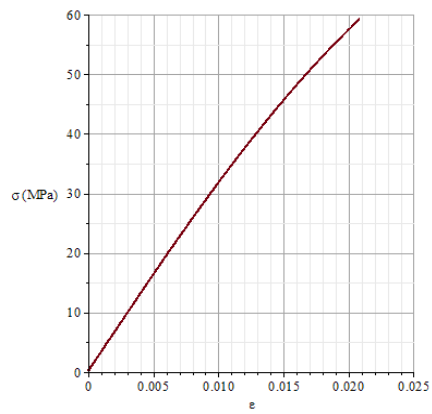
(b) Reference 7 - Specimen 2.



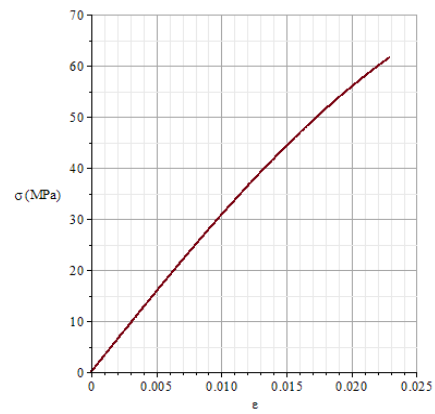
(c) Reference 7 - Specimen 3.



(d) Reference 7 - Specimen 4.



(e) Reference 7 - Specimen 5.

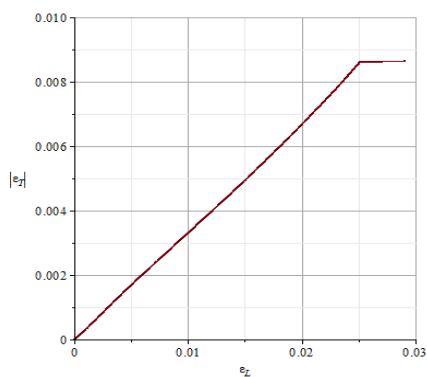


(f) Reference 7 - Specimen 6.

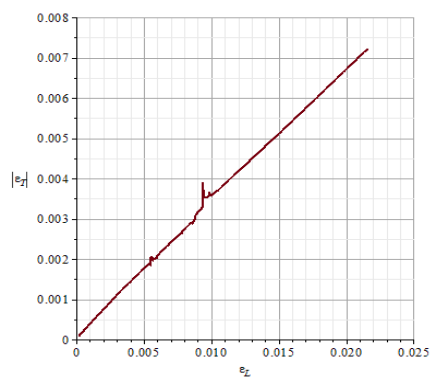
Figure C.7: Stress - strain curves of the specimens of reference 7 (0.2 CNT High).

Appendix D

Tensile tests: transversal - longitudinal strain curves

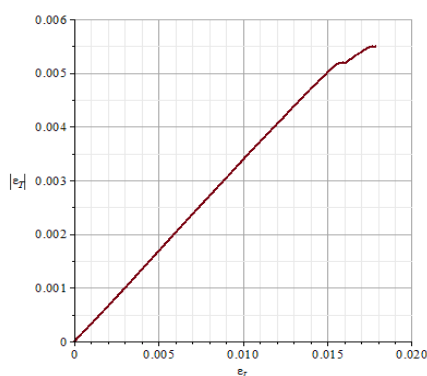


(a) Reference 1 - Specimen 5.

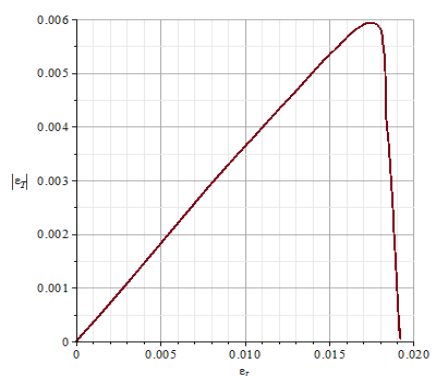


(b) Reference 1 - Specimen 6.

Figure D.1: Transversal - longitudinal strain curves of the specimens of reference 1 (Epoxy resin).

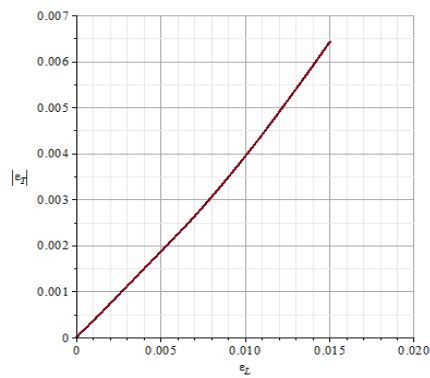


(a) Reference 2 - Specimen 5.

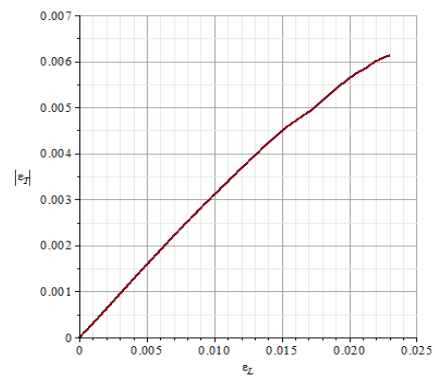


(b) Reference 2 - Specimen 6.

Figure D.2: Transversal - longitudinal strain curves of the specimens of reference 2 (0.05 CNT Normal).

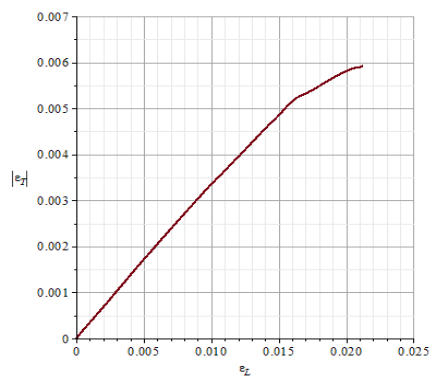


(a) Reference 3 - Specimen 5.

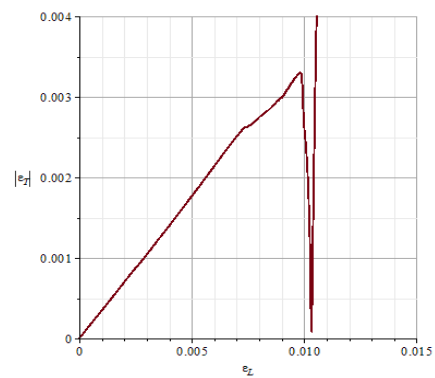


(b) Reference 3 - Specimen 6.

Figure D.3: Transversal - longitudinal strain curves of the specimens of reference 3 (0.05 CNT SDBS).

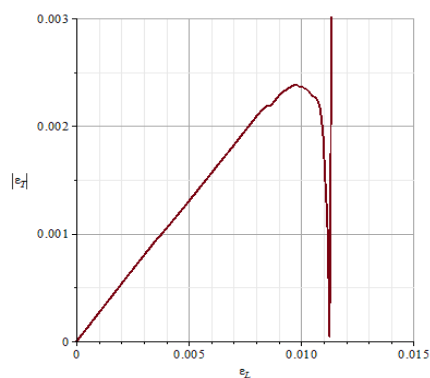


(a) Reference 4 - Specimen 5.

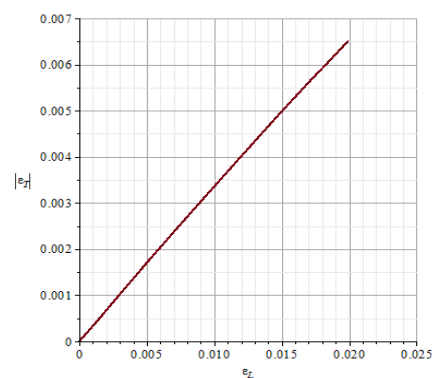


(b) Reference 4 - Specimen 6.

Figure D.4: Transversal - longitudinal strain curves of the specimens of reference 4 (0.05 CNT Triton).



(a) Reference 5 - Specimen 5.

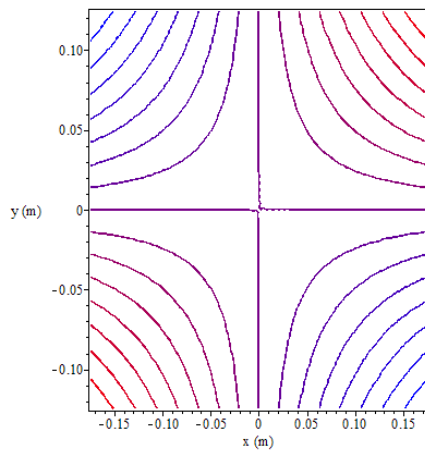


(b) Reference 5 - Specimen 6.

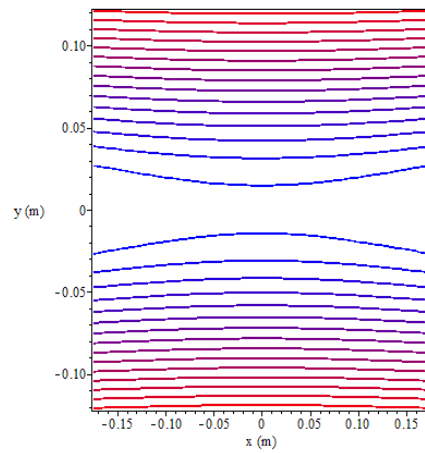
Figure D.5: Transversal - longitudinal strain curves of the specimens of reference 5 (0.05 CNT High).

Appendix E

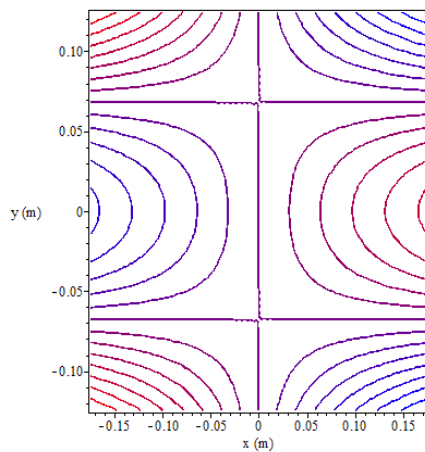
Numerical mode shapes



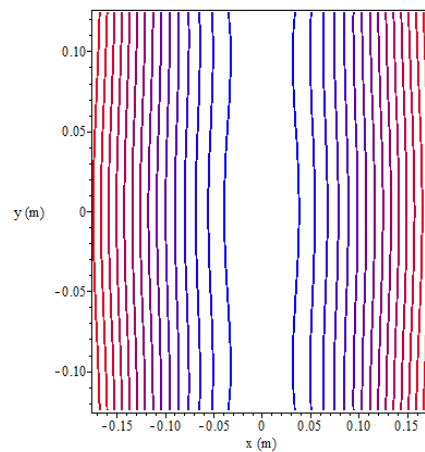
(a) Mode 1.



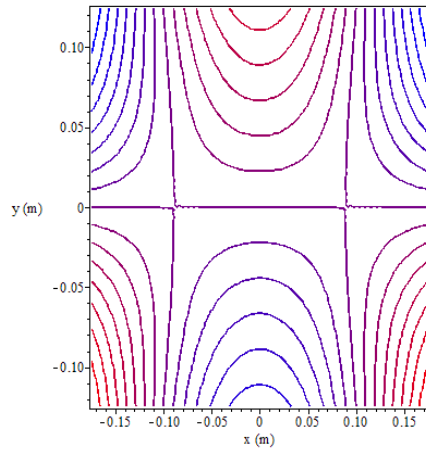
(b) Mode 2.



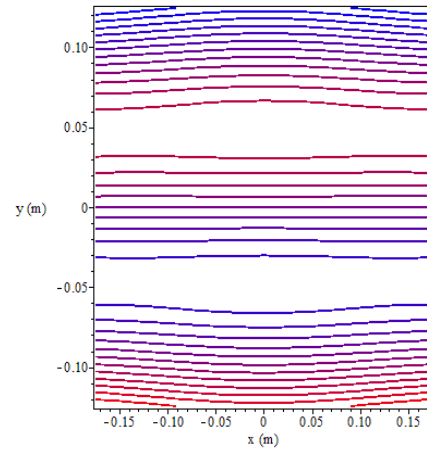
(c) Mode 3.



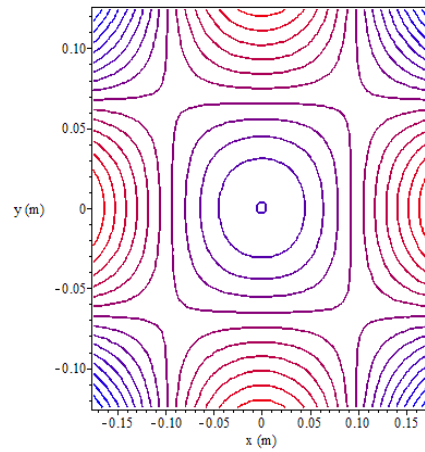
(d) Mode 4.



(e) Mode 5.

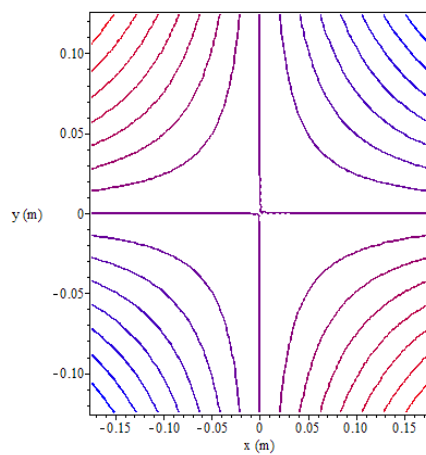


(f) Mode 6.

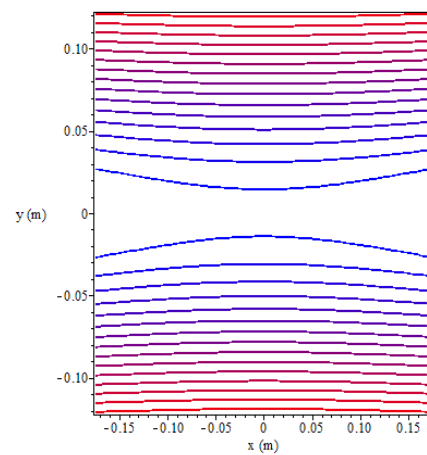


(g) Mode 7.

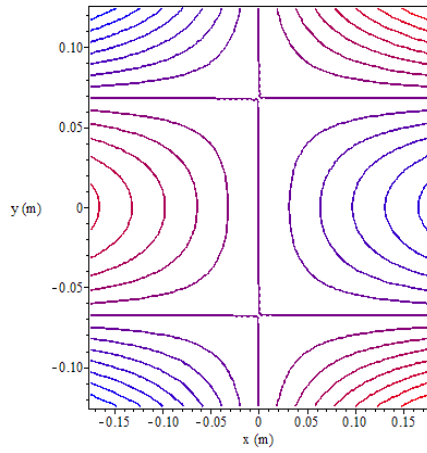
Figure E.1: Numerical mode shapes for the 0.01% SWCNTs plate.



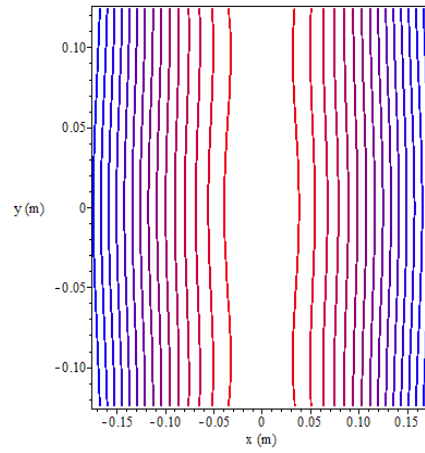
(a) Mode 1.



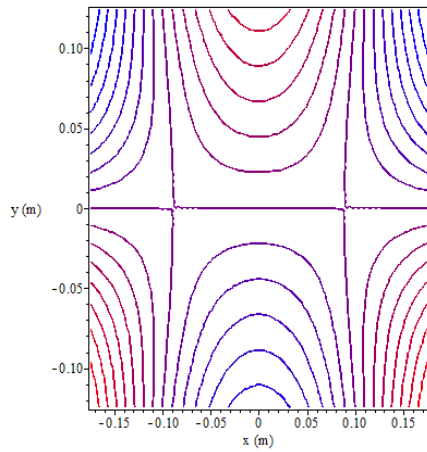
(b) Mode 2.



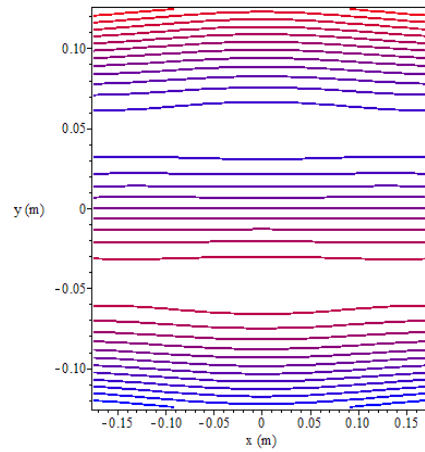
(c) Mode 3.



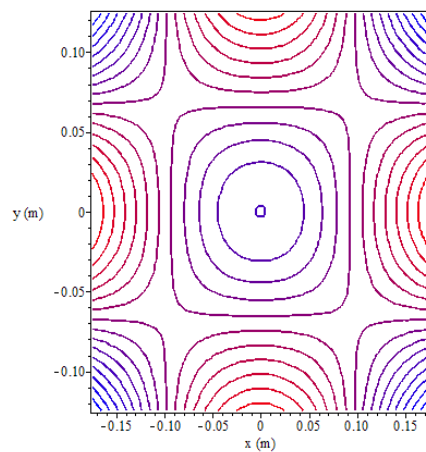
(d) Mode 4.



(e) Mode 5.



(f) Mode 6.



(g) Mode 7.

Figure E.2: Numerical mode shapes for the 0.05% SWCNTs plate.